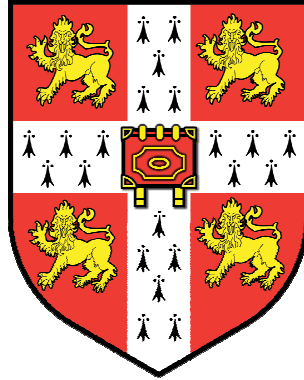


Functional characterisation of driver events in ovarian clear cell carcinoma



Ioannis Gounaris

Cancer Research UK Cambridge Institute

Dissertation Submitted For The Degree Of Doctor Of Philosophy

Corpus Christi College

May 2014

to Christina

Declaration

This dissertation is the result of my own work and includes nothing which is the outcome of work done in collaboration except where specifically indicated in the text.

I hereby declare that this dissertation is not substantially the same as any that I have submitted for a degree or diploma or any other qualification at any other University and that it does not exceed the word limit set by the Degree Committee of the Faculties of Clinical Medicine and Clinical Veterinary Medicine.

Publication from this work

Gounaris I, Charnock-Jones DS & Brenton JD, 2011. Ovarian clear cell carcinoma – bad endometriosis or bad endometrium? *Journal of Pathology*, 225(2):157-60.

Acknowledgements

I would like to express my gratitude to my supervisor, James Brenton, for his guidance and support and for giving me the opportunity to work on this exciting project. I am indebted to Helena Earl for being an excellent mentor and teacher. I am grateful to David Huntsman and Steve Charnock-Jones for the many fruitful discussions regarding my work and their helpful suggestions. I would like to thank all members of the Brenton Laboratory, past and present, for teaching me a wide range of research techniques and providing a friendly and welcoming work environment. Among them, Jian Xian and Anna Piskorz deserve special mention. The invaluable support of the Cambridge Institute core facilities members needs to be especially acknowledged.

The work contained in this thesis was funded by an MRC Clinical Research Training Fellowship and an Addenbrooke's Charitable Trust Cancer Research Fellowship – it goes without saying that I am grateful to both organisations for their support.

I am most indebted to my fantastic wife, Christina, without whom nothing would have been possible.

Summary

Ovarian clear cell carcinoma (OCCC) is a distinct subtype of epithelial ovarian cancer (EOC) characterised by glycogen accumulation. Frequently arising within endometriotic cysts, it can be conceived as an ectopic endometrial cancer. Putative driver genomic events include HNF1B overexpression and inactivating *ARID1A* mutations. Importantly, these can also be found in a significant proportion of adjacent non-malignant endometriotic lesions and, therefore, are likely early events in OCCC pathogenesis. I hypothesised that the study of the functional consequences of these driver genomic events and metabolic perturbations would provide insights into potential therapeutic targets in this difficult to treat cancer.

Gene expression arrays in normal mouse uterus, embryonic fibroblasts and human immortalised ovarian surface epithelium cells revealed that a core *ARID1A*-driven transcriptional programme, conserved across normal tissues and species, centred on regulation of mitosis and cell cycle progression-related genes, and involving potentially targetable kinases, exists. Despite this, the effect of *ARID1A* knockdown on proliferation in human cell lines and mouse cells and tissues was found to be context and tissue specific. Interestingly, *in vivo* knockout in the uterine epithelium of *Arid1a*^{fl/fl} mice was accompanied by a dramatic increase in proliferation, in support of its suggested driver-event role in uterine-derived cancers.

HNF1B overexpression has been previously reported to affect proliferation and metabolism in a variety of cell lines but studies in well characterised OCCC cells are lacking. Here, *HNF1B* was found to consistently drive proliferation in a panel of *bona fide* OCCC cell lines. Pathway analysis of *HNF1B*-regulated genes suggested that HNF1B is involved in interactions with the tumour microenvironment. Indeed, I observed that HNF1B negatively regulates migration and invasion. Additionally, I found that HNF1B overexpression drives glycogen accumulation and that its knockdown reverses the Warburg effect. These results point at trade-offs among proliferation, metabolism and metastatic capability and suggest that HNF1B overexpression may be one of the reasons that, in marked contrast to high-grade serous EOC, OCCC frequently presents as early stage disease.

Little is known about the functional consequences of glycogen accumulation in OCCC. I report that OCCC cell lines display increased expression of glycogen metabolism enzymes and that inhibiting the rate limiting phosphorylase (PYGL) and synthase enzymes markedly decreased proliferation, even in the presence of plentiful extracellular glucose. This observation suggests a role for glycogen beyond that of a glucose store. Assays performed to elucidate how *PYGL* knockdown affects proliferation suggest that this may be through G2/M phase arrest, possibly caused by inhibition of lipid breakdown or altered PKA signalling. Furthermore, preliminary evidence suggests that the effects of *PYGL* knockdown on proliferation are limited to malignant cells only.

In conclusion, this project studied the functional consequences of three driver events in OCCC: *ARID1A* mutations, HNF1B overexpression and glycogen accumulation. Targeting *ARID1A*-regulated kinases and glycogen metabolism and perturbing HNF1B function require further investigation as potential therapeutic strategies in OCCC.

Table of Contents

Declaration.....	v
Acknowledgements.....	vii
Summary	ix
Table of Contents.....	xi
List of figures	xvii
List of tables.....	xix
Abbreviations	xxi
1. INTRODUCTION	1
1.1. Origins of Epithelial Ovarian Cancer.....	1
1.2. Ovarian Clear Cell Cancer (OCCC).....	2
1.3. Molecular pathology of OCCC	3
1.3.1. <i>ARID1A</i> mutations.....	4
1.3.2. HNF1B overexpression	9
1.3.3. PIK3CA mutations and PI3K pathway activation	13
1.3.4. MET and HER2 amplifications.....	15
1.3.5. Other events in OCCC	16
1.3.6. OCCC and microsatellite instability	17
1.4. Glycogen accumulation	17
1.5. Is OCCC an endometrial cancer in the wrong place?.....	20
1.6. Model systems for OCCC	23
1.6.1. Genetically engineered mouse models (GEMM)	23
1.6.2. OCCC cell lines.....	25
1.6.3. Functional anatomy of the mouse endometrium.....	26
1.7. Specific aims of this project	27
2. MATERIALS AND METHODS	29

2.1. Animals.....	29
2.2. Estrus cycle monitoring.....	29
2.3. Mouse tissue acquisition.....	29
2.4. Estrus-timed mouse uterus series.....	30
2.5. Culture of murine uterine fragments.....	30
2.5.1. “Coin” method	30
2.5.2. Culture in CellMatrix®	30
2.5.3. Vibratome method.....	31
2.5.4. Surgispon® method	31
2.5.5. Non-adjacent co-culture method	32
2.6. Culture of dissociated uterine cells	33
2.7. Creation and expansion of Mouse Embryonic Fibroblast (MEF) cell lines.....	34
2.8. <i>In vivo Arid1a</i> ablation	35
2.9. Cell line expansion and culture	35
2.9.1. Culture under hypoxia and glucose deprivation.....	35
2.10. Immunofluorescence microscopy.....	38
2.11. Uterine Fragment Viability Microscopy.....	39
2.12. Nucleic acid extraction, quantification and quality assessment	39
2.12.1. DNA extraction and quantification	39
2.12.2. RNA extraction.....	39
2.12.3. RNA quantification and quality assessment.....	39
2.13. Protein extraction and quantification.....	40
2.14. Immunoblotting and protein band intensity quantification.....	40
2.15. Immunohistochemistry (IHC)	42
2.15.1. Quantitative IHC analysis	43
2.16. Quantitative Real Time Polymerase Chain Reaction (qRT-PCR).....	43
2.16.1. Validation of qRT-PCR for mouse uterus samples	44
2.17. Gene Expression Arrays.....	45

2.17.1. <i>ARID1A</i> expression arrays	45
2.17.2. <i>HNF1B</i> expression arrays	46
2.18. RNA sequencing (RNA-seq) in MEFs	46
2.19. Metabolic profile after <i>HNF1B</i> and <i>PYGL</i> knockdown	47
2.19.1. NMR medium and intracellular metabolites quantification	47
2.19.2. Quantitative lipid imaging after <i>PYGL</i> knockdown	48
2.20. <i>In vitro</i> gene knockdown and knockout	48
2.20.1. siRNA-mediated knockdown	48
2.20.2. Lentiviral-mediated shRNA <i>HNF1B</i> knockdown.....	49
2.20.3. Lentiviral-mediated shRNA <i>Arid1a</i> knockdown	50
2.21. <i>ARID1A</i> overexpression in SKOV3 cells	50
2.22. Glycogen metabolism inhibition	50
2.23. Proliferation assays	51
2.23.1. Bromodeoxyuridine (BrdU) assay.....	51
2.23.2. Incucyte assay	51
2.23.3. Proliferation assessment using Vi-Cell	51
2.23.4. Sulphorhodamine B (SRB) assay	52
2.23.5. Colony Forming Assay (CFA).....	52
2.24. Glycogen assays	52
2.24.1. Colorimetric glycogen assay.....	52
2.24.2. PAS and PAS-Diastase staining.....	53
2.25. Interleukin 6 (IL6) assay	53
2.26. Reactive Oxygen Species (ROS) assay.....	53
2.27. Terminal deoxynucleotidyl transferase dUTP nick end labelling (TUNEL) assay.....	54
2.28. Senescence assay	54
2.29. Cell cycle phase analysis.....	54
2.30. Migration and invasion assays.....	55
2.31. Proteomics analysis.....	55

2.32. Statistical analysis	56
3. MOUSE UTERUS ASSAY DEVELOPMENT	57
3.1. Introduction.....	57
3.2. Cultured murine uterine fragments show poor viability	57
3.3. Culture of dissociated murine uterine cells.....	61
3.3.1. Non-adjacent co-culture of dissociated uterine cells does not replicate normal hormonal regulation	61
3.3.2. Culture of dissociated uterine epithelial and stromal cells shows poor cell yields	63
3.4. Assays of gene expression in the mouse uterus	64
3.4.1. RNA quantification and quality assessment.....	64
3.4.2. Validation of qRT-PCR assay steps for mouse uterus samples	64
3.5. Discussion	66
4. FUNCTIONAL CHARACTERISATION OF <i>ARID1A</i> IN MOUSE AND HUMAN CELLS AND TISSUES	69
4.1. Introduction.....	69
4.2. <i>Arid1a</i> expression across the estrus cycle	70
4.2.1. <i>Arid1a</i> mRNA levels are stable across the estrus cycle.....	70
4.2.2. <i>Arid1a</i> protein expression in the stroma is lower than the epithelium and shows some variability	71
4.2.3. ER expression peaks in proestrus and proliferation is limited to the epithelium ..	73
4.2.4. <i>Arid1a</i> and ER expression are correlated	73
4.3. <i>Arid1a</i> expression in the uterus is associated with a transcriptional programme enriched in genes involved in cell cycle regulation	75
4.4. <i>Arid1a</i> drives a transcriptional programme enriched in genes involved in cell cycle regulation and cytoskeleton remodelling in MEFs.....	79
4.5. Mitosis regulation, cytoskeleton remodelling and chromatin modification are components of a core <i>Arid1a</i> -driven transcriptional programme in the mouse	81
4.6. <i>ARID1A</i> drives a similar transcription programme in immortalised human ovarian cells	83

4.7. A core <i>ARID1A</i> transcriptional programme which controls cell cycle progression and is conserved across species exists	84
4.8. JHOC-5 cells exhibit a different <i>ARID1A</i> -driven transcriptional programme	86
4.9. <i>Arid1a</i> regulation of <i>Smarca4</i> , <i>Smarca2</i> and other components of the SWI/SNF and polycomb complexes	90
4.10. <i>Arid1a</i> 's effect on proliferation is cell type specific	92
4.10.1. <i>Arid1a</i> knockdown does not increase proliferation in cultured mouse uterine stromal cells	92
4.10.2. Proliferation is increased in MEFs after <i>Arid1a</i> knockdown	94
4.10.3. Effect of <i>ARID1A</i> knockdown on EOC cell line proliferation	94
4.10.4. <i>ARID1A</i> overexpression does not affect proliferation in SKOV3 cells	95
4.10.5. <i>ARID1A</i> effect on proliferation is dependent on the cellular HNF1B status	95
4.11. <i>In vivo Arid1a</i> knockout increases proliferation in mouse uterine epithelium	95
4.12. <i>ARID1B</i> knockdown affects proliferation but not in a consistent direction	97
4.13. Effect of combined <i>ARID1A</i> and <i>ARID1B</i> loss on proliferation	98
4.14. Discussion	99
5. ROLE OF HNF1B IN THE OCCC PHENOTYPE	107
5.1. Introduction	107
5.2. HNF1B expression in OCCC cell lines	108
5.3. HNF1B drives proliferation in OCCC cell lines and immortalised ovarian epithelium	108
5.4. HNF1B gene expression profiling	110
5.4.1. <i>HNF1B</i> regulates EMT and cell adhesion in JHOC-5 cells	110
5.4.2. <i>HNF1B</i> regulates EMT and cell adhesion in TOV21G cells	113
5.4.3. A core <i>HNF1B</i> transcriptional programme is involved in adhesion, cytoskeleton remodelling and EMT regulation	115
5.5. <i>HNF1B</i> decreases migration and invasion in OCCC cell lines and immortalised ovarian surface epithelium	119
5.6. <i>HNF1B</i> is associated with clotting cascade genes	122
5.7. <i>HNF1B</i> regulates multiple glycolytic pathway enzymes	123

5.8. <i>HNF1B</i> knockdown reduces lactate production and leads to increased TCA intermediates and ATP accumulation	124
5.9. <i>HNF1B</i> drives glycogen accumulation in JHOC-5 and IOSE4 cells.....	125
5.10. Discussion	128
6. TARGETING GLYCOGEN METABOLISM MAY BE A NOVEL THERAPEUTIC STRATEGY IN OCCC.....	133
6.1. Introduction.....	133
6.2. OCCC cell lines are not more resistant to hypoxia or glucose deprivation	134
6.3. OCCC cell lines contain large amounts of glycogen which is utilized under glucose deprivation.....	136
6.4. <i>HIF1A</i> is constitutively expressed and contributes to glycogen accumulation in OCCC cell lines	137
6.5. The rate-limiting glycogen metabolism enzymes glycogen phosphorylase and synthase are highly expressed in OCCC	140
6.6. <i>PYGL</i> knockdown significantly decreases cellular proliferation	140
6.7. <i>GYS1</i> knockdown and small molecule inhibitors of glycogen metabolism also decrease cancer cell line proliferation	144
6.8. <i>PYGL</i> Inhibition causes G2/M arrest but not induction of apoptosis or senescence	146
6.9. <i>PYGL</i> inhibition does not have a major effect on glycolysis, the TCA cycle or ATP production	148
6.10. <i>PYGL</i> knockdown impairs lipid metabolism but does not result in ROS accumulation or induction of the unfolded protein response (UPR) pathway	152
6.11. <i>PYGL</i> knockdown does not markedly perturb the proteome but results in changes in Protein Kinase A signalling	154
6.12. Discussion	157
7. CONCLUSIONS AND FUTURE DIRECTIONS	165
Appendix.....	169
References	181

List of figures

1.1	The origins of ovarian cancer	p.2
1.2	Glycogen metabolism	p.18
1.3	Mutational events in cancers arising from the endometrium	p.20
1.4	Stepwise progression from endometriosis to OCCC	p.22
1.5	Organisation of the mouse endometrium and the stem cell niche	p.26
3.1	Murine uterine fragment culture techniques	p.58
3.2	Culture of murine uterine fragments	p.60
3.3	Dissociation of epithelial and stromal uterine cells	p.62
3.4	BrdU incorporation in co-cultured dissociated uterine cells	p.63
4.1	Arid1a during the mouse estrus cycle	p.72
4.2	ER, PgR and Ki67 during the mouse estrus cycle and correlations with stromal Arid1a	p.74
4.3	Overview of gene expression experiments	p.76
4.4	<i>Arid1a</i> gene expression array in mouse uterus	p.77
4.5	The “Spindle assembly and chromosome separation” pathway is associated with <i>Arid1a</i> expression in the mouse uterus	p.78
4.6	<i>Arid1a</i> gene expression array in MEFs	p.79
4.7	The “TGF, WNT and cytoskeletal remodelling” pathway is <i>Arid1a</i> -regulated in MEFs	p.80
4.8	The “Chromatin modification” network is <i>Arid1a</i> -regulated in MEFs	p.82
4.9	Overlap of genes regulated by <i>Arid1a</i> in mouse uterus and MEFs	p.83
4.10	<i>ARID1A</i> gene expression array in IOSE4 cells	p.84
4.11	The “Role of APC in cell cycle regulation” pathway is <i>ARID1A</i> -regulated in IOSE4 cells	p.85
4.12	Overlap of genes and pathways regulated by <i>ARID1A</i> in mouse uterus, MEFs and IOSE4 cells	p.86
4.13	The “Spindle assembly and chromosome separation” pathway is <i>ARID1A</i> -regulated in mouse and human cells	p.87
4.14	The “Mitosis” network is <i>ARID1A</i> -regulated in mouse and human cells	p.88
4.15	Overlap of genes and pathways regulated by <i>ARID1A</i> in mouse uterus, MEFs, IOSE4 and JHOC-5 cells	p.90
4.16	Effect of <i>ARID1A</i> knockdown on <i>ARID1B</i> , <i>SMARCA4</i> and <i>SMARCA2</i> expression	p.91
4.17	Effect of <i>ARID1A</i> knockdown on proliferation	p.93

4.18	<i>In vivo</i> effect of <i>Arid1a</i> knockdown on mouse uterine epithelium	p.96
4.19	Effect of <i>ARID1B</i> and combined <i>ARID1A</i> and <i>ARID1B</i> knockdown on proliferation	p.98
5.1	HNF1B expression and effect on proliferation	p.109
5.2	<i>HNF1B</i> gene expression array in JHOC-5 and TOV21G cells	p.111
5.3	The “Regulation of epithelial-to-mesenchymal transition” pathway is <i>HNF1B</i> -regulated in JHOC-5 cells	p.112
5.4	The “Chemokines and adhesion” pathway is <i>HNF1B</i> -regulated in TOV21G cells	p.114
5.5	Overlap of genes and pathways regulated by <i>HNF1B</i> in both JHOC-5 and TOV21G cells	p.115
5.6	The “Chemokines and adhesion” pathway is <i>HNF1B</i> -regulated in OCCC cell lines	p.116
5.7	Effect of <i>HNF1B</i> knockdown on EMT-related RNA and protein expression	p.119
5.8	Effect of <i>HNF1B</i> knockdown on migration and invasion of JHOC-5 and TOV21G cells	p.121
5.9	Migration and invasion of the IOSE4 and IOSE4+HNF1B cell lines	p.122
5.10	Effect of <i>HNF1B</i> knockdown on metabolites in the culture medium	p.125
5.11	Effect of <i>HNF1B</i> knockdown on intracellular metabolites	p.127
5.12	HNF1B expression drives glycogen accumulation	p.128
6.1	Effect of hypoxia and glucose deprivation on EOC cell line proliferation	p.135
6.2	Glycogen content of ovarian cell lines under normal culture conditions, hypoxia and glucose deprivation and effect of HIF1 α and interleukin-6 on glycogen accumulation	p.139
6.3	PYGL and GYS1 expression in OCCC cell lines	p.141
6.4	Effect of <i>PYGL</i> knockdown on proliferation in EOC cell lines	p.143
6.5	Effect of glycogen metabolism perturbations on proliferation	p.147
6.6	Effect of <i>PYGL</i> knockdown on apoptosis and senescence	p.149
6.7	Effect of <i>PYGL</i> knockdown on cell cycle progression	p.150
6.8	Effect of <i>PYGL</i> knockdown on metabolites in the culture medium	p.151
6.9	Effect of <i>PYGL</i> knockdown on intracellular metabolites	p.152
6.10	Effect of <i>PYGL</i> knockdown on lipid droplet, reactive oxygen species (ROS) accumulation and the unfolded protein response	p.153
6.11	Effect of <i>PYGL</i> knockdown on cellular proteomics	p.155
7.1	Models of OCCC development	p.168

List of tables

2.1	Mouse Embryonic Fibroblast cell lines	p.34
2.2	Cell lines used in experiments	p.36
2.3	List of primary antibodies used for immunofluorescence	p.38
2.4	List of secondary antibodies used for immunofluorescence	p.38
2.5	List of primary antibodies used for immunoblotting	p.41
2.6	List of primary antibodies used for IHC	p.43
2.7	List of TaqMan Gene Expression Assays used	p.44
2.8	List of siRNA products used	p.49
3.1	Culture of murine uterine fragments	p.59
3.2	RNA quantification using Nanodrop, Bioanalyzer and Qubit	p.65
3.3	PCR efficiency for TaqMan expression assays	p.66
4.1	Correlation of Arid1a, ER, PgR and Ki67 in the mouse uterus	p.75
4.2	Pathways enriched in the 177 <i>ARID1A</i> -regulated genes in all of mouse uterus, MEFs and IOSE4 cells	p.86
4.3	Process networks enriched in the 177 <i>ARID1A</i> -regulated genes in all of mouse uterus, MEFs and IOSE4 cells	p.87
4.4	<i>ARID1A</i> -regulated genes in all of mouse uterus, MEFs and IOSE4 cells	p.89
5.1	Top 25 pathways enriched in genes regulated by <i>HNF1B</i> in both JHOC-5 and TOV21G cells	p.117
5.2	Top process networks enriched in genes regulated by <i>HNF1B</i> in both JHOC-5 and TOV21G cells	p.118
6.1	Relative proliferation of 6 OCCC cell lines and PEO1 after glycogen metabolism perturbation	p.142
6.2	PYGL-regulated proteins in both JHOC-5 and TOV21G cells	p.156
A.1	Pathways enriched in “High <i>Arid1a</i> ” compared with “Low <i>Arid1a</i> ” mouse uterine samples	p.169
A.2	Process networks enriched in “High <i>Arid1a</i> ” compared with “Low <i>Arid1a</i> ” mouse uterine samples	p.169
A.3	Top 30 pathways enriched in <i>Arid1a</i> -regulated genes in MEFs	p.170
A.4	Process networks enriched in <i>Arid1a</i> -regulated genes in MEFs	p.171
A.5	Pathways enriched in <i>Arid1a</i> -regulated genes in both mouse uterus and MEFs	p.172
A.6	Process networks enriched in <i>Arid1a</i> -regulated genes in both mouse uterus and MEFs	p.172

A.7	Top 30 pathways enriched in <i>ARID1A</i> -regulated genes in IOSE4 cells	p.173
A.8	Process networks enriched in <i>ARID1A</i> -regulated genes in IOSE4 cells	p.174
A.9	Pathways enriched in <i>ARID1A</i> -regulated genes in JHOC-5 OCCC cells	p.175
A.10	Process networks enriched in <i>ARID1A</i> -regulated genes in JHOC-5 OCCC cells	p.175
A.11	Top 30 pathways enriched in <i>HNF1B</i> -regulated genes in JHOC-5 cells	p.176
A.12	Process networks enriched in <i>HNF1B</i> -regulated genes in JHOC-5 cells	p.177
A.13	Top 30 pathways enriched in <i>HNF1B</i> -regulated genes in TOV21G cells	p.178
A.14	Process networks enriched in <i>HNF1B</i> -regulated genes in TOV21G cells	p.179
A.15	Pathways enriched in <i>PYGL</i> -regulated proteins in JHOC-5 cells	p.180
A.16	Metabolic networks enriched in <i>PYGL</i> -regulated proteins in JHOC-5 cells	p.180
A.17	Pathways enriched in <i>PYGL</i> -regulated proteins in TOV21G cells	p.180

Abbreviations

aCGH	Array Comparative Genomic Hybridisation
ANOVA	Analysis Of Variance
ATP	Adenosine Triphosphate
B6	C57BL/6
BAC	Bacterial Artificial Chromosome
BCCA	British Columbia Cancer Agency
BME	Basal Medium Eagle; <i>also</i> Basement Membrane Extract (in section 5.5)
BPE	Bovine Pituitary Extract
BSA	Bovine Serum Albumin
BrdU	Bromodeoxyuridine
CARS	Coherent Anti-Stokes Raman Scattering
cDNA	Complementary DNA
CFA	Colony Forming Assay
CFU	Colony Forming Unit
ChIP	Chromatin Immunoprecipitation
CRUK CI	Cancer Research UK Cambridge Institute
DAB	1,4-Dideoxy-1,4-imino-D-arabinitol hydrochloride
DAPI	4',6-diamidino-2-phenylindole
DCFDA	2',7' –dichlorofluorescein diacetate
DEG	Differentially Expressed Genes
DES	Diethylstilboestrol
DMEM	Dulbecco's Modified Eagle Medium
DMSO	Dimethyl sulfoxide
DSS	4,4-dimethyl-4-silapentane-1-sulfonic acid
DTT	Dithiothreitol
E ₂	(O)estadiol
ECM	Extra-cellular Matrix
EDTA	Ethylenediaminetetraacetic acid
EGF	Epidermal Growth Factor
EMT	Epithelial Mesenchymal Transition
EOC	Epithelial Ovarian Cancer
ER	(O)estrogen Receptor
ERAD	Endoplasmic Reticulum Associated Degradation
F12	Ham's F12 medium

FAD	3:1 DMEM/F12 medium supplemented with EGF, hydrocortisone and cholera toxin
FBS	Fetal Bovine Serum
FC	Fold-change
FDR	False Discovery Rate
FFPE	Formalin-Fixed Paraffin-Embedded (tissue)
GEMM	Genetically Engineered Mouse Model
GM	Geometric Mean
GSEA	Gene Set Enrichment Analysis
H&E	Haematoxylin & Eosin
HBSS	Hanks Balanced Salt Solution
HEPES	2-[4-(2-hydroxyethyl)piperazin-1-yl]ethanesulfonic acid
HGS	High Grade Serous (cancer)
HKG	Housekeeping Genes
HPV	Human Papilloma Virus
IHC	Immunohistochemistry
IL6	Interleukin 6
IOSE	Immortalised Ovarian Surface Epithelium
kDa	kiloDalton
MEFs	Mouse Embryonic Fibroblasts
MEM	Minimum Essential Media
MMR	Mismatch Repair
MODY	Maturity Onset Diabetes of the Young
MOI	Multiplicity of Infection
MS	Mass Spectroscopy
MSI	Microsatellite Instability
NBF	Neutral Buffered Formalin
NC	Normal (culture) Conditions
NHEJ	Non-Homologous End Joining
NMR	Nuclear Magnetic Resonance
OCCC	Ovarian Clear Cell Cancer
OD	Optical Density
OEAC	Ovarian Endometrioid Adenocarcinoma
OPO	Optical Parametric Oscillator
OSE	Ovarian Surface Epithelium
P ₄	Progesterone

PAS	Periodic acid–Schiff
PBS	Phosphate Buffered Saline
PCA	Principal Components Analysis
PCR	Polymerase Chain Reaction
PET	Polyethylene terephthalate
PFA	Paraformaldehyde
PFU	Plaque Forming Units
PgR	Progesterone Receptor
qRT-PCR	Quantitative Real-Time Polymerase Chain Reaction
RH	Random Hexamers
ROS	Reactive Oxygen Species
RIN	RNA Integrity Number
RNA-seq	RNA sequencing
RPMI 1640	Roswell Park Memorial Institute (medium) 1640
RT	Room Temperature (15-25 °C)
shRNA	Small Hairpin RNA
siRNA	Small Interfering RNA
SNP	Single Nucleotide Polymorphism
SOP	Standard Operating Procedure
SRB	Sulforhodamine B
STIC	Serous Tubal Intraepithelial Cancer
SWI/SNF	SWItch/Sucrose NonFermentable (complex)
TBS	Tris-Buffered Saline
TCA	Tricyclic Acid (cycle); <i>also</i> Trichloroacetic Acid (in sections 2.23.5 and 2.30)
TCGA	The Cancer Genome Atlas (Research Network)
TSP	Trisodium Phosphate
TUNEL	Terminal Deoxynucleotidyl Transferase dUTP Nick End Labelling
UPR	Unfolded Protein Response
VTE	Venous Thromboembolism
X-gal	5-bromo-4-chloro-3-indolyl- β -D-galactopyranoside

1. INTRODUCTION

1.1. Origins of Epithelial Ovarian Cancer

Epithelial ovarian cancer (EOC) is a significant cause of morbidity and mortality. In 2014, it is estimated that 21,980 cases will occur in the USA, leading to 14,270 deaths (Siegel et al. 2014). In the UK, it is the fifth commonest malignancy affecting women (Cancer Statistics England 2011) and the commonest cause of death from gynaecological cancer. Despite intensive research efforts, advances in diagnostic modalities, improvements in surgical techniques and the incorporation of novel agents in systemic treatments, 5-year survival from EOC has remained constant over the past 3 decades (Vaughan et al. 2011).

Our incomplete understanding of the pathogenesis of EOC has contributed to this failure to improve outcomes for patients. For most of the 20th century, the predominant theory of ovarian carcinogenesis postulated that EOC arises from the ovarian surface epithelium with subsequent metaplasia accounting for the different histological subtypes (Dubeau 2008). Scant attention was paid to the histological subtypes themselves, as they were viewed as slightly different manifestations of a single disease process. However, the search for a putative cell of origin and precursor lesions in the ovaries has proven largely unsuccessful (Dubeau 2008). Following the discovery of the breast and ovarian cancer predisposition genes *BRCA1* and *BRCA2* (Miki et al. 1994; Wooster et al. 1994), prophylactic salpingo-oophorectomy started to be performed in germline mutation carriers. Examination of these specimens failed to show precursor lesions in the ovaries, but did reveal the frequent presence of intraepithelial neoplasia (termed STIC for serous tubal intraepithelial cancer) with serous morphology in the fallopian tubes (Lee et al. 2006). Clonal relationships, based on identical *TP53* mutations, between synchronous STIC and high-grade serous (HGS) ovarian cancer lesions have been shown (Kuhn et al. 2012), implying that a significant proportion of HGS cancers are actually fallopian tube cancers that only secondarily involve the ovaries. In addition, there is now evidence that the majority of ovarian clear cell (OCCC) and endometrioid (OEAC) cancers arise from endometriotic cysts (Kobayashi et al. 2009; Mandai et al. 2009) whereas most mucinous tumours appear to be metastatic from the gastrointestinal tract (Vaughan et al. 2011).

Based on these findings, the “Mullerian hypothesis” has been developed. This postulates that most ovarian cancers arise from Mullerian structures, such as the fallopian tube or the uterus,

and only secondarily involve the ovaries and is currently accepted by most authorities in the field (Bast et al. 2009; Dubeau 2008; Vaughan et al. 2011). Accordingly, each histological subtype, namely HGS, low-grade serous, OEAC, OCCC and mucinous, is viewed as a distinct disease entity (Fig. 1.1). It follows that advances in EOC understanding, management and outcomes will only come from subtype-specific studies. The work set out in this thesis aims to functionally characterise the main driver events in OCCC, a treatment-resistant subtype that accounts for 5-25% of all EOC (Anglesio et al. 2011a).

1.2. Ovarian Clear Cell Cancer (OCCC)

OCCC accounts for 5-13% of EOC in western populations, while, for reasons that are unclear at present, its incidence is much higher in Japan where it reaches 20-25% of all EOC (Anglesio

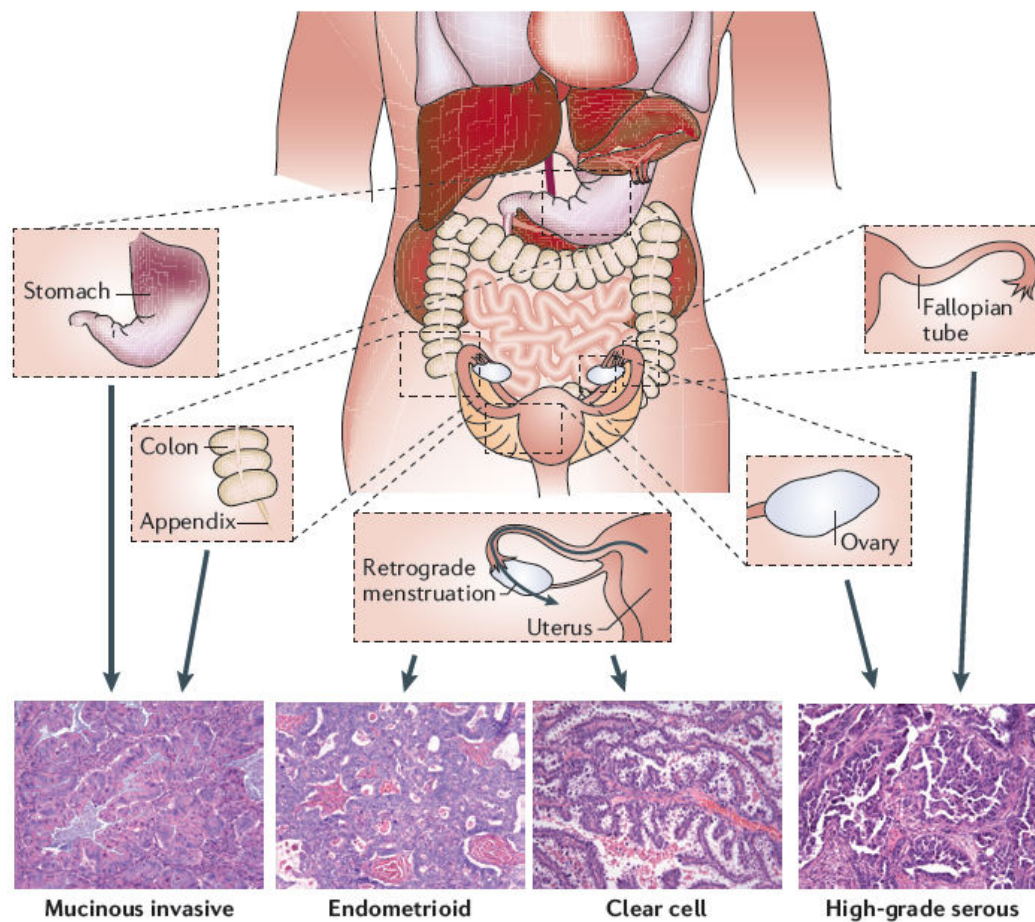


Figure 1.1. The origins of ovarian cancer

Putative sites of origin for the 4 main subtypes of EOC (from Vaughan et al. 2011).

et al. 2011a; Glasspool & McNeish 2013). Epidemiologically, histologically and clinically it differs from the commonest EOC subtype, HGS. It exhibits a strong epidemiological link to endometriosis: a self-reported history of endometriosis tripled the risk of OCCC in an analysis of 13 case-control studies as part of the Ovarian Cancer Association Consortium (Pearce et al. 2012). Histopathologically, it is characterised by the presence of clear and hobnail cells that, on electron microscopy studies, contain abundant glycogen (Ohkawa et al. 1977). Its clinical presentation is also distinct from that of HGS. Whereas the latter presents as advanced stage III-IV disease in the vast majority of cases, OCCC tends to be diagnosed as stage I-II disease and can be complicated by hypercalcaemia (Savvari et al. 2009) and venous thromboembolism (Anglesio et al. 2011a; Tan & Kaye 2007). When diagnosed at an early stage, its prognosis is at least as good, if not better, than HGS (Hoskins et al. 2012; Lee et al. 2011; Takano et al. 2008a; Takano et al. 2010). However, prognosis of advanced stage or relapsed disease is much worse (Lee et al. 2011), due to its chemo-resistant phenotype (Crotzer et al. 2007; Takano et al. 2008b). This is exemplified by response rates that range from 11-27% for single agent platinum chemotherapy in the first line setting (Ho et al. 2004; Sugiyama et al. 2000) and fall to under 2% for platinum resistant recurrent disease (Crotzer et al. 2007).

Gene expression studies support the notion that OCCC is distinct from other EOC. Schwartz *et al* (2002) analysed gene expression profiles of 113 ovarian tumours using principal components analysis (PCA) and reported that OCCC cases were readily distinguishable from HGS and OEAC tumours. Subsequently, Zorn *et al* (2005) showed, in 75 cases of ovarian and endometrial tumours analysed on a cDNA array, that clear cell cancers of both ovarian and endometrial origin clustered together and differed significantly from serous and endometrioid tumours of either ovarian or endometrial origin. Remarkably, in that study, the expression profile of the clear cell cancers was much more similar to that of renal clear cell cancer compared to the other gynaecological cancer subtypes, suggesting that the clear cell phenotype is representative of underlying biological processes that transcend the anatomical location of the tumour.

1.3. Molecular pathology of OCCC

Over the past few years, our knowledge regarding the genetic abnormalities underpinning the various EOC subtypes has markedly increased. It is now widely appreciated that HGS cancers are characterised by ubiquitous *TP53* mutations as well as defective DNA double strand break repair in at least half the cases, resulting in extensive chromosomal instability (Ahmed et al.

2010; TCGA 2011). This has led to a dualistic model of ovarian carcinogenesis where *TP53*-mutated, chromosomally unstable tumours are labelled as “Type II” and all others as “Type I” (Kurman & Shih 2011). I believe that this classification is unhelpful as it lumps together cancers, such as OCCC, low-grade serous and mucinous, with different biology, clinical behaviour and even cell of origin. Therefore, for the rest of this section, I will focus on the molecular pathology of OCCC, before comparing it with other tumours of Mullerian origin.

1.3.1. *ARID1A* mutations

ARID1A (AT Rich Interactive Domain 1A, also known as BAF250a) is a ubiquitously expressed 250kDa protein that functions as part of the mammalian SWI/SNF complex (Inoue et al. 2002). This is an ATP-dependent chromatin remodeling complex that alters chromatin structure by locally unwrapping DNA, displacing nucleosomes or ejecting histone subunits (Kasten et al. 2011). It is composed of at least 10–12 subunits, including either *ARID1A* or *ARID1B* (the latter is also known as BAF250b). These two proteins are closely related, are incorporated in the complex in a mutually exclusive fashion and may function to alter target specificity. Different combinations of ATPase (BRG1 or BRM, encoded by *SMARCA4* and *SMARCA2* respectively) and *ARID1* subunits are thought to act as a combinatorial code, causing activation or repression of transcription (Wilson & Roberts 2011). The exact composition of the complex is still a matter of debate and new subunits continue to be described (Kadoch et al. 2013). *ARID1A*-containing complexes have been implicated primarily in transcriptional repression. *ARID1A* is necessary for differentiation and cell cycle arrest in osteoblast culture models through *MYC* repression and consequent *CDKN1A* induction (Nagl et al. 2005; Nagl et al. 2006), maintenance of pluripotency of murine embryonic stem cells (Gao et al. 2008) and nuclear hormone-mediated transactivation [including estrogen (ER) receptor] (Inoue et al. 2002). Other work, although not specifically addressing the role of *ARID1A*, has also shown the importance of *ARID1/BAF57/BRG1*-containing SWI/SNF complexes in mediating ER (García-Pedrero et al. 2006) and progesterone receptor (PgR) induced transactivation (Vicent et al. 2009). Additionally, recent studies have shown that *ARID1A* is necessary for DNA repair via non-homologous end joining (NHEJ) and *TOP2A* function in mitosis (Dykhuizen et al. 2013; Watanabe et al. 2014). The role of *ARID1A* in repression of transcription and inhibition of proliferation suggests that *ARID1A* functions as a tumour suppressor gene. How this role relates to the potential growth promoting effects of ER transactivation in cancer cell line models is unclear, and the role of *ARID1A* in normal endometrial tissues needs to be determined.

1.3.1.1. Incidence of *ARID1A* mutations in OCCC and other cancers

In late 2010, *ARID1A* was reported to be frequently mutated in OCCC and OEAC. *ARID1A* mutations were found in 55 of 119 (46%) OCCC and 10 of 33 (30%) OEAC using whole transcriptome sequencing in a report from the OvCaRe tumour bank (Wiegand et al. 2010). Simultaneously, a second report showed that *ARID1A* mutations could be detected in 24 of 42 (57%) OCCC (Jones et al. 2010). In both reports, mutations were spread evenly across the 20 exons of the gene and were predominantly truncating and heterozygous. Wiegand *et al* (2010) also showed a strong, but not perfect, correlation between the presence of *ARID1A* mutations on sequencing and loss of ARID1A expression by IHC. The mechanism through which heterozygous truncating mutations result in complete loss of protein expression is not known at present but dominant-negative effects are postulated (Wiegand et al. 2010). Additionally, these authors were able to show that in 2 cases of OCCC with available adjacent atypical as well as distant endometriosis, identical *ARID1A* mutations were found in the cancer and the adjacent endometriosis but were absent in the distant endometriotic lesions (Wiegand et al. 2010), implying that *ARID1A* mutations play a role in the malignant transformation of endometriosis.

Since the start of this project in 2011, multiple additional reports have confirmed the frequent loss of ARID1A expression in OCCC (Lowery et al. 2012; Samartzis et al. 2012; Xiao et al. 2012; Yamamoto et al. 2012a; Yamamoto et al. 2012b). Additionally, in a series of 47 OCCC and OEAC from Johns Hopkins, Seirei Mikatahara and Hirosaki University Hospitals, all 31 tumours with loss of ARID1A expression showed absent ARID1A staining in the adjacent endometriosis, whereas the other 16 tumours maintained expression in both cancerous and endometriotic tissues (Ayhan et al. 2012), thus confirming the initial observations (Wiegand et al. 2010). Further support to the notion that *ARID1A* loss is an early event in OCCC pathogenesis is provided by a 54-patient series from Case Medical Centre, Cleveland, where there was a progressive increase in ARID1A protein expression loss from normal endometrium (0%), to typical endometriosis (19%), to atypical endometriosis (38%) (Xiao et al. 2012). Loss of ARID1A expression in 15% of benign endometriomas was also shown in a 71-patient Swiss series; similar to the Cleveland series, no ARID1A loss was seen in eutopic endometrium (Samartzis et al. 2012).

Over the past 2 years, *ARID1A* mutations or loss of protein expression have been reported in a wide range of gynaecological malignancies. In a series from the British Columbia Cancer Agency (BCCA), loss of ARID1A expression by IHC was seen in 29% of low grade

endometrioid, 39% of high grade endometrioid, 14% of carcinosarcoma, 18% of serous and 26% of clear cell uterine tumours (Wiegand et al. 2011). *ARID1A* mutations were also identified by whole exome sequencing in a small cohort of uterine clear cell (13%) and serous carcinomas (6%) (Le Gallo et al. 2012). The frequent presence of *ARID1A* mutations in uterine cancers was corroborated by the TCGA analysis (Kandoth et al. 2013). This integrated genomic, transcriptomic and proteomic analysis of 373 endometrial endometrioid and serous tumours classified uterine cancers into 4 subtypes: *POLE* hypermutated, microsatellite instability (MSI) hypermutated, copy-number low and copy-number high. *ARID1A* mutations were frequent in the first 3 subtypes but not in the copy-number high one which contained most of the serous cancers and showed strong expression similarity to the HGS ovarian subtype. Contrary to these findings, *ARID1A* mutations do not seem to be a feature of HGS ovarian cancer. No mutations were found in 76 HGS cancers in the initial publication describing *ARID1A* mutations in OCCC and OEAC (Wiegand et al. 2010) or in the TCGA ovarian cancer project (TCGA 2011).

ARID1A mutations have also been reported in a wide range of non-gynaecological malignancies (Wiegand et al. 2011; Wu & Roberts 2013), including a significant proportion of gastric (K. Wang et al. 2011; Wang et al. 2012; Zang et al. 2012), oesophageal (Dulak et al. 2013; Streppel et al. 2014), pancreatic (Birnbaum et al. 2011), hepatocellular (Fujimoto et al. 2012; Huang et al. 2012), colon (Jones et al. 2012), bladder (Gui et al. 2011; TCGA 2014), renal (Lichner et al. 2013) and breast cancers (Stephens et al. 2012; Zhang et al. 2012), as well as Waldenström's macroglobulinaemias (Treon et al. 2012), Burkitt's lymphomas (Giulino-Roth et al. 2012; Love et al. 2012), pulmonary carcinoids (Fernandez-Cuesta et al. 2014), cholangiocarcinomas (Ross et al. 2014) and neuroblastomas (Sausen et al. 2013).

1.3.1.2. Associations and consequences of *ARID1A* mutations in OCCC

Several studies suggest that *ARID1A* mutations are frequently present in tumours exhibiting microsatellite instability (see section 1.3.6 for details) and tend to co-exist with activating *PIK3CA* mutations. In the original description of *ARID1A* mutations in OCCC by the Johns Hopkins group, 14 out of 24 (58%) tumours with *ARID1A* mutations also carried *PIK3CA* mutations compared with 3 out of 18 (17%) without (Jones et al. 2010). Similar results were reported in a second series of 42 OCCC, with 71% of tumours without *ARID1A* expression having *PIK3CA* mutations compared to 44% of those with intact *ARID1A* expression (Yamamoto et al. 2012a). The association persisted and reached statistical significance ($p=0.013$) in an extended series of 90 cases by the same authors (Yamamoto et al. 2012b).

Additionally, it was recently reported that, in 25 OCCC and OEAC cases with *PIK3CA* mutations from the BCCA tumour bank, *ARID1A* mutations occurred in 27% of tumours with helical domain mutations but 71% of those with other mutations ($p=0.05$) (Wiegand et al. 2014a). The same pattern also seems to occur in uterine cancers with *ARID1A* mutations enriched among cases with *PIK3CA* and *PTEN* mutations in a series of 222 uterine cancers (Liang et al. 2012). In that series, *ARID1A* mutations correlated with phosphorylation of multiple members of the PI3K pathway including AKT, GSK3 (glycogen synthase kinase 3) and p70S6K. Interestingly, increased phosphorylation of AKT at Serine 473 (AKTpS473) was seen in the presence of *ARID1A* mutations even in samples with normal *PTEN* expression and absence of *PIK3CA* mutations, implying activation of the PI3K pathway by *ARID1A* that is independent of *PTEN* and *PIK3CA* aberrations (Liang et al. 2012). This is corroborated by the BCCA study (Wiegand et al. 2014a) which also showed increased AKTpS473 and AKTpT308 in OCCC and OEAC with *ARID1A* loss that was independent of the *PTEN* and *PIK3CA* status. Similar findings were recently reported in a screen of breast cancer cell lines which attempted to identify mediators of resistance to trastuzumab and PI3K pathway inhibitors (Berns et al. 2013). *ARID1A* knockdown in these cells resulted in increased AKTpS473, an effect that was mediated by induction of *ANXA1* transcription. Additionally, *ARID1A* knockdown increased AKT phosphorylation in H460 and H1299 lung cancer cells (Y. Zhang et al. 2014). Conflicting results have, however, been reported in the EOC cell lines RMG-I, ES-2 and JHOC-5 where knockdown did not have an effect on AKT phosphorylation (Wiegand et al. 2014a).

ARID1A mutations have been reported to be mutually exclusive with *TP53* mutations in EOC (Guan et al. 2011; Wu & Roberts 2013). As *TP53* mutations are ubiquitous in HGS but very rare in OCCC (Kuo et al. 2009), it is not clear if that observation reflects the different subtype distribution of mutations in these 2 genes. However, similar findings were reported in gastric cancers where 21% of samples with *ARID1A* alterations showed *TP53* mutations, compared with 52% of samples without (K. Wang et al. 2011). In contrast, no enrichment for *ARID1A* mutations was seen in *TP53* wild type bladder tumours in the recent TCGA report (TCGA 2014). Furthermore, in an immortalized ovarian surface epithelium cell line, p53 interacted directly with the C-terminus of *ARID1A* and this interaction was necessary for p21 induction (Guan et al. 2011). Therefore, it is reasonable to speculate that, in some malignancies at least, *ARID1A* mutations may confer benefits to the cancer cell, in terms of proliferation and evasion of apoptosis, similar to those conferred by *TP53* mutations. However, this hypothesis needs further experimental examination.

ARID1A exhibits evidence of haplo-insufficiency in tumours since, as has been mentioned earlier, heterozygous mutations seem to be sufficient to drive carcinogenesis. In addition, heterozygous germline *Arid1a* mutations were embryonically lethal in a mouse model with the embryos dying on day 6.5 of gestation due to failure of mesoderm formation (Gao et al. 2008). The recent report of germline *ARID1A* (and *ARID1B*) mutations as a cause of the intellectual disability Coffin-Siris syndrome in humans (Santen et al. 2012) would appear to argue against a similarly lethal haplo-insufficient phenotype in humans. However, more recent reports suggest that evidence of mosaicism can be found in all individuals with *ARID1A* mutations tested so far (Santen et al. 2013).

The functional consequences of *ARID1A* loss in OCCC are not yet clear. In agreement with its proposed tumour-suppressor role, re-expression of *ARID1A* in the OCCC cell line OWISE and the uterine endometrioid cell line HEC-1A, both of which have *ARID1A* mutations, resulted in growth inhibition. On the other hand, overexpression in the *ARID1A* wild-type OCCC cell line JHOC-5 had no further effect on growth (Guan et al. 2011). Similarly, knockdown of *ARID1A* using shRNA in 2 immortalised ovarian surface epithelium cell lines (OSE4 and IOSE-80PC) resulted in increased proliferation *in vitro* and increased tumourigenicity when implanted subcutaneously in nude mice (Guan et al. 2011). However, studies of the effects of *ARID1A* perturbations in a larger panel of OCCC cell lines and correlation with alterations in other components of the SWI/SNF complex, such as *ARID1B*, *SMARCA4* and *SMARCA2*, are necessary and may identify dependencies of *ARID1A*-mutant cells on continuing expression and function of alternative SWI/SNF complex subunits.

Clinically, there does not appear to be a distinct *ARID1A*-driven OCCC phenotype. Four series, with 149, 119, 90 and 82 patients showed no correlations between *ARID1A* expression loss and clinicopathologic characteristics or OCCC outcomes (Lowery et al. 2012; Maeda et al. 2010; Wiegand et al. 2010; Yamamoto et al. 2012b). Katagiri *et al* (2012) though, reported shorter survival in patients with *ARID1A* expression loss in their series. However, this observation was based on only 9 patients with *ARID1A* loss in a 60-patient series, limiting the strength of the authors' conclusions. Conflicting evidence exists for other cancers, particularly gastric adenocarcinomas, for which some, but not all, series show decreased survival in the presence of *ARID1A* mutations (Wang et al. 2012; Wiegand et al. 2014b; Yan et al. 2014).

To summarise, *ARID1A* mutations appear to be one of the main driver events in OCCC as well as OEAC and high-grade endometrioid uterine cancers. At present, very little is known of

the physiological role of *ARID1A* in the human endometrium and in endometriosis, the putative precursor lesion for OCCC. Based on our current understanding of the role and function of the SWI/SNF complex (Olave et al. 2002; Reisman et al. 2009; de la Serna et al. 2006; Wilson & Roberts 2011), it is very likely that the consequences of *ARID1A* alterations will be tissue and developmental-context specific. Therefore, there is an urgent need for in depth studies of *ARID1A* function in uterine, endometriotic and ovarian tissues.

1.3.2. HNF1B overexpression

1.3.2.1. Incidence of HNF1B overexpression in OCCC and precursor lesions

HNF1B (Hepatocyte Nuclear Factor 1-Beta, also known as TCF2) is a POU-homeodomain transcription factor with predominant expression in liver, pancreas and kidney (Ma et al. 2007; Tronche & Yaniv 1992). In 2003, it was first reported that, using IHC, nuclear staining for HNF1B was positive in 20 of 21 OCCC cases compared with only 1 of 61 of non-OCCC EOC (Tsuchiya et al. 2003). Subsequent reports have confirmed that >95% of OCCC stain positive for HNF1B, whereas other EOC subtypes do so extremely rarely (Higashiguchi et al. 2007; Kato et al. 2006; Kato & Toukairin 2007; Yamamoto et al. 2007). Based on that, it has been proposed that HNF1B positivity can be used as a problem solving tool in cases where the histological subtype of EOC cannot be determined by morphology alone (Anglesio et al. 2011a). Importantly, it was shown that in a series of 12 OCCC cases with available adjacent endometriosis, 9 showed positive staining for HNF1B in the non-malignant endometriotic epithelium as well (Kato et al. 2006). Furthermore, 16 of 40 benign endometriotic cysts also showed HNF1B positivity, implying that induction of HNF1B expression is an early event in OCCC pathogenesis (Kato et al. 2006). Although evidence is limited, uterine cancers seem to express HNF1B frequently. In a small series of 5 endometrial clear cell cancers, all stained positive for HNF1B (Yamamoto et al. 2007). In a second series, 9 of 15 (60%) and 7 of 20 (35%) uterine serous and endometrioid cancers were HNF1B positive, although the staining intensity for the latter was significantly lower when compared to 15 clear cell tumours (Fadare & Liang 2012). HNF1B is expressed in the normal endometrium, predominantly in glandular cells during the mid-to-late secretory phase and gestational endometrium (Fadare & Liang 2012; Yamamoto et al. 2007), but not in the ovary (Human Protein Atlas; www.proteinatlas.org/ENSG00000108753/normal). This observation further supports the uterine origin of most OCCC.

1.3.2.2. Mechanisms of *HNF1B* overexpression in OCCC

Activating mutations in *HNF1B* have not been described to date and the induction of its expression in OCCC is thought to be under epigenetic control. Using combined bisulfite restriction analysis, it was shown that methylation of CpG islands at the *HNF1B* promoter was markedly decreased in OCCC compared to HGS tumours and normal ovaries (Kato et al. 2008). Recent data confirm and extend these observations, showing that *HNF1B* is overexpressed in OCCC and that HGS cancers show increased promoter methylation compared to normal ovarian surface and fallopian tube epithelia (Pharoah et al. 2013). Additionally, a strong inverse correlation between *HNF1B* expression and promoter methylation was seen. DNA methylation analysis in 269 cases from the Ovarian Tumor Tissue Analysis Consortium also demonstrated that the majority of OCCC strongly express *HNF1B* and have unmethylated *HNF1B* promoters whereas HGS tumours exhibit the opposite features (Shen et al. 2013)

The IHC and methylation data point towards opposing roles for *HNF1B* in OCCC and HGS carcinogenesis with *HNF1B* induction in the former and repression in the latter. SNPs predisposing to EOC were analysed in 2 studies within the Ovarian Cancer Association Consortium (Pharoah et al. 2013; Shen et al. 2013). The first publication identified 2 different SNPs in the *HNF1B* locus, one (rs7405776) associated with HGS and the other (rs11651755) with OCCC risk (Shen et al. 2013). Consistent with the data already presented, the risk allele of rs7405776 was associated with increased *HNF1B* promoter methylation. Interestingly, there was also an association between unmethylated, expressed *HNF1B* promoter and a global CpG methylation phenotype (Shen et al. 2013). The second publication identified an *HNF1B* intronic SNP (rs757210) that confers increased risk for HGS cancer (Pharoah et al. 2013). The 2 HGS-predisposing SNPs in these studies are strongly correlated ($r^2=0.97$) (Shen et al. 2013). Therefore, there is now strong evidence for opposing roles of *HNF1B* in OCCC and HGS carcinogenesis. Interestingly, a further SNP in *HNF1B* (rs4430796) is associated with endometrioid uterine and prostate cancer risk as well as type 2 diabetes mellitus (Spurdle et al. 2011). This SNP correlates very strongly with the rs11651755 SNP predisposing to OCCC ($r^2=0.94$), implying a common carcinogenesis pathway for OCCC and endometrioid uterine cancer (Shen et al. 2013).

1.3.2.3. Functional implications of HNF1B overexpression

Initial studies of HNF1B function focused on its role in diabetes and kidney disease as germline *HNF1B* mutations cause Maturity Onset Diabetes of the Young Type 5 (MODY 5) as well renal dysplasia and cysts. These effects are mediated, at least partially, through de-repression of *SOCS3* expression (Ma et al. 2007) and prevention of activation of *FXRD2* expression through a dominant-negative effect (Ferrè et al. 2011). Gene expression studies support a role for *HNF1B* in carbohydrate metabolism and development. Induction of *HNF1B* expression in the human embryonic kidney cell line HEK293 resulted in differential expression of 25 genes, including genes involved in glucose metabolism (*DPP4*, encoding dipeptidyl peptidase IV) as well as bone morphogenesis and renal stone formation (*SPP1*, encoding osteopontin) (Senkel et al. 2005). The same group also reported on changes in gene expression following induction of *HNF1B* expression in the rat insulinoma cell line INS-1, which shows low constitutive *HNF1B* expression. 292 genes were differentially regulated with genes involved in development and morphogenesis being over-represented (Thomas et al. 2004). Similarly, after siRNA-mediated knockdown of *HNF1B* in a mouse hepatoma cell line, 243 genes showed >2 fold change in expression, including genes involved in insulin signaling and glucose metabolism (Tanaka et al. 2004). Over the past few years, it has become evident that germline microdeletions at 17q12, encompassing *HNF1B*, are a cause of uterine malformations, including the Mayer-Rokitanski-Kuster-Hauser syndrome (Bernardini et al. 2009; Bingham et al. 2002; Oram et al. 2010), thus implicating *HNF1B* in uterine development.

In that respect, the functional consequences of HNF1B overexpression in OCCC have only recently become the focus of investigation. Knockdown of *HNF1B* expression using siRNA in IGROV1 and SKOV3 cells resulted in reduced proliferation as assessed by a thymidine incorporation assay (Tomassetti et al. 2008). Similar results were seen in the androgen-sensitive prostate cancer cell line LNCaP and two immortalised prostate epithelial cell lines (LHSAR and RWPE1), but not in the androgen independent PC3 cell line (Grisanzio et al. 2012). Contrary to the above, increased proliferation was recently reported in the OCCC cell lines RMG-I and RMG-II after shRNA-mediated *HNF1B* knockdown (Okamoto et al. 2013). siRNA-mediated *HNF1B*-knockdown increased apoptosis in TOV21G and JHOC-5 cells, although the effect on proliferation was not reported (Tsuchiya et al. 2003). Further studies in a wider panel of OCCC cell lines are therefore needed, in order to gain a better understanding of the spectrum of *HNF1B* effects on proliferation. However, induced expression of *HNF1B* in an immortalised ovarian surface epithelium cell line, markedly increased proliferation, in accordance with the majority of studies that show a positive effect of *HNF1B* on proliferation in cancer cell lines (Tomassetti et al. 2008). The possibility that *HNF1B* may be one of the

drivers of chemotherapy resistance in OCCC was raised by a study that reported that *HNF1B* knockdown markedly improved cisplatin and paclitaxel sensitivity in TOV21G and OV207 cells through HSulf-1 de-repression (Liu et al. 2009).

In addition to its effects on proliferation, *HNF1B* appears to be one of the main drivers of gene expression programmes in OCCC. Senkel *et al* (2005) reported a significant overlap between their 25-gene *HNF1B* signature derived from overexpression in HEK293 cells (see above) and previously reported OCCC expression profiles (Schwartz et al. 2002; Tsuchiya et al. 2003) with genes such as *SPP1*, *RBPMS* and *SOX9* appearing on both lists. A gene expression signature derived from *HNF1B* knockdown in RMG-I and RMG-II cells was able to distinguish the OCCC from the other EOC in 2 publicly available ovarian cancer datasets (Okamoto et al. 2013). Furthermore, the RMG-I and RMG-II expression profiles after *HNF1B* knockdown more closely resembled the non-OCCC compared to the OCCC signature, implying that *HNF1B* is one of the major determinants of the OCCC expression signature (Okamoto et al. 2013). Also, *HNF1B* was shown to drive a gene expression profile resembling that of epithelial-to-mesenchymal transition (EMT) in SKOV3 cells, leading the authors to conclude that *HNF1B* is important for the maintenance of an E-cadherin expressing epithelial phenotype in OCCC (Tomassetti et al. 2008). Recently, Cuff *et al* (2013), using the original expression profile reported by Senkel *et al* and after performing Gene Set Enrichment Analysis (GSEA) and bioinformatics analysis of potential *HNF1B* binding sites, showed that genes related to starch metabolism and the clotting cascade were enriched among *HNF1B* targets. These authors also showed, in a series of gynaecological and renal tumours, a clear association between *HNF1B* expression and the presence of clear cytoplasm and venous thromboembolism, thus implicating *HNF1B* in both the characteristic microscopic appearance of OCCC and one of its most significant clinical associations (Cuff et al. 2013).

OCCC is characterised by glycogen accumulation and the studies referenced above suggest a role for *HNF1B* in that. However, no studies directly examining the effect of *HNF1B* alterations on the glycogen content of OCCC cells have been published. Genes involved in glucose and glycogen metabolism such as *HK1* (encoding hexokinase), *G6PC* (encoding glucose-6-phosphatase) and *DPP4* are *HNF1B*-regulated (Cuff et al. 2013; Uekuri et al. 2013). Supporting this, a recent study showed that *Hnf1b* knockdown in mouse liver caused glucose intolerance, insulin resistance and increased gluconeogenesis through *G6pc* and *Pck1* (encoding phosphoenolpyruvate carboxykinase 1) induction (Kornfeld et al. 2013). Also, shRNA-mediated *HNF1B* knockdown in RMG-I and RMG-II cells resulted in decreased

glucose uptake, glycolytic flux and lactate secretion in the medium whereas overexpression of *HNF1B* in the HGS cell line Hey, had the opposite effects (Okamoto et al. 2013). Furthermore, *HNF1B* knockdown downregulated multiple glycolytic genes, including *HK1*, *HK2*, *ALDOA* (encoding aldolase A), *ALDOB*, *ALDOC*, *PGK1* (encoding phosphoglycerate kinase 1), *PGK2*, *ENO2* (encoding enolase 2), *ENO3*, *LDHA* (encoding lactate dehydrogenase A) and *LDHB* as well as the main glucose uptake transporter GLUT1 (encoded by *SLC2A1*) (Okamoto et al. 2013). Additional circumstantial evidence for the role of *HNF1B* in glycogen accumulation is provided by the fact that *HNF1B* expression in the secretory and gestational endometrium correlates spatially and temporally with glycogen accumulation in these cells (Yamamoto et al. 2007).

In summary, *HNF1B* overexpression is a defining characteristic of OCCC. *HNF1B* seems to drive OCCC gene expression signatures and to have a major impact on OCCC proliferation and metabolic profile. However, the effects on proliferation need to be examined in a wider panel of OCCC cell lines. Much of the data regarding gene expression is derived from overexpression in HEK293 cells and limited by older microarray technology. Therefore, gene expression studies in typical OCCC cell lines would provide additional useful insights in the *HNF1B*-driven transcriptional program and complement the available knowledge. Lastly, the metabolic data from Okamoto *et al* (2013) were derived from a cell line, RMG-II, that showed an atypical increase in proliferation on *HNF1B* knockdown. Again, validation of these findings in other cell lines would be useful, especially if a direct link to glycogen accumulation can be shown. I will discuss the functional role of glycogen in OCCC in section 1.4.

1.3.3. *PIK3CA* mutations and PI3K pathway activation

The PI3K pathway is implicated in cancer cell growth, motility, survival and metabolism (Courtney et al. 2010). Mutations in components of the pathway are extremely common in a wide range of malignancies. Frequent *PIK3CA* mutations in OCCC were first reported in 2009 when, in an analysis of 87 OCCC tumours and 10 OCCC cell lines by targeted Sanger sequencing, 33% were found to harbour mutations in exons 1, 9 or 20 (Kuo et al. 2009). Further series have reported an incidence of *PIK3CA* mutations in OCCC between 29% and 42% (Jones et al. 2010; Rahman et al. 2012; Yamamoto et al. 2011). *PIK3CA* mutations appear to be more common in OCCC with visible adjacent endometriosis and prominent papillary architecture (Yamamoto et al. 2012b) and can be detected in these endometriotic lesions as well. Indeed, in 9 of 10 cases of OCCC with activating H1047R exon 20 mutations, the identical mutation could be identified in the adjacent endometriotic lesion, even in cases

where the latter lacked cytological atypia (Yamamoto et al. 2011). Therefore, and similar to what has been reported for *ARID1A* mutations and HNF1B overexpression, *PIK3CA* mutations appear to be an early event in OCCC pathogenesis.

PTEN loss, both through mutations or promoter methylation and lack of expression, is another mechanism of PI3K pathway activation and occurs at high frequency in multiple tumour types (Hollander et al. 2011). *PTEN* mutations have been reported in 5% of OCCC (Kuo et al. 2009). However, loss of immunoreactivity for PTEN has been reported in up to 37.5% of OCCC in other series (Abe et al. 2013; Hashiguchi et al. 2006; Ho et al. 2009). Furthermore, in a study of 50 OCCC using array comparative genomic hybridisation (aCGH), amplification of 19q13.2, encompassing *AKT2* and thus, potentially activating the PI3K pathway, was seen in 14% of cases (Tan et al. 2011; Tan et al. 2013). Frequent *AKT2* amplifications in OCCC were confirmed in a second study that showed their presence, again using aCGH, in 5 of 21 (24%) tumours (Yamashita et al. 2013).

It should be kept in mind that activation of the PI3K pathway is also extremely common in endometrioid uterine cancers. In the TCGA analysis, 84% of samples showed perturbations in the PI3K pathway with extremely high incidence of PTEN alterations and *PIK3CA* mutations that reached 88% and 55% respectively in the MSI subtype (Kandoth et al. 2013). An additional mechanism of PI3K pathway activation in endometrioid uterine cancers are mutations in the regulatory subunits *PIK3R1* and *PIK3R2* in 20% and 5% of cases respectively (Cheung et al. 2011). The frequency of *PIK3R1* mutations may reach 40% in the MSI subtype (Kandoth et al. 2013) but, up until now, *PIK3R1* mutations have not been reported in OCCC.

Activation of the PI3K pathway in OCCC can occur in the absence of known mutations in its core members. In a series of 87 OCCC, all of the *PIK3CA*-mutant tumour samples showed strong immunostaining for AKTpS473, but so did 85% of samples with wild type *PIK3CA*, implying alternative methods of pathway activation (Kuo et al. 2009). Similarly, absence of correlation between *PIK3CA* mutations and phosphorylated AKT and mTOR immunoreactivity was reported in a series of 56 OCCC (Rahman et al. 2012). In contrast to these two studies, a third study showed a positive correlation between *PIK3CA* overexpression by IHC and phosphorylated AKT in 62 OCCC samples (Abe et al. 2013). As already discussed (see section 1.3.1.2), *ARID1A* mutations are probably contributing to PI3K pathway activation; whether the effect of *ARID1A* loss is different in the majority of tumours with co-occurring *PIK3CA* mutations compared with those with wild type *PIK3CA* is at present unclear.

With regards to outcomes, two series of 56 and 62 OCCC cases showed improved prognosis in OCCC patients harbouring *PIK3CA* mutations (Abe et al. 2013; Rahman et al. 2012). Whether the presence of an activated PI3K pathway can predict response to mTOR inhibitors in OCCC is unclear at present. No differential activity of the PI3K inhibitors LY294002 and BEZ235 or the mTOR inhibitor temsirolimus was seen in a panel of OCCC cell lines with or without *PIK3CA* mutations (Rahman et al. 2012). However, other reports suggest that treatment with mTOR inhibitors can, at least *in vitro*, overcome OCCC resistance to cisplatin or trabectedin (Mabuchi et al. 2009; Mabuchi et al. 2011). Preliminary clinical evidence of benefit from targeting the PI3K pathway is provided by a small case series of heavily-pretreated Japanese patients with OCCC. In that series, 1 of 6 patients treated with temsirolimus showed a partial response that lasted 14 months (Takano et al. 2011).

In summary, the PI3K pathway is frequently activated in OCCC and *PIK3CA* mutations appear to be early events. Elucidation of the functional consequences of PI3K pathway activation in the context of *ARID1A* mutations and HNF1B overexpression may help identify a subgroup of patients that will benefit from treatments targeting this pathway and point towards rational therapeutic combinations.

1.3.4. *MET* and *HER2* amplifications

MET is a receptor tyrosine kinase that relays signals through both the MAPK and PI3K pathways and is considered a key driver of oncogenic transformation in a variety of cancers (Appleman 2011). *MET* appears to be the most frequently amplified gene in OCCC. Amplification was reported in 37% of patients in a 73-patient series and correlated with worse survival in early stage disease (Yamashita et al. 2013). In a study of 11 OCCC with known *MET* amplification and adjacent endometriosis, *MET* amplification could be detected in the atypical endometriotic component in 67% of the cases but not in the typical endometriotic component, implying a stepwise gain of expression during tumorigenesis (Yamamoto et al. 2012c). *MET* amplification is accompanied by increased *MET* mRNA levels as well as increased expression of its ligand, HGF, supporting the notion that *MET* is one of the key drivers of carcinogenesis, possibly in an autocrine manner, at least in a subset of OCCC (Anglesio 2011b).

HER2 amplification was found in 13 of 39 (33%) and 7 of 50 (14%) patients with OCCC using aCGH in 2 recently reported studies (Anglesio et al. 2011b; Tan et al. 2011). *HER2* mRNA

expression was increased 2.5-fold compared with the other EOC subtypes in a study of 113 ovarian tumours (Schwartz et al. 2002) and HER2 protein overexpression by IHC was shown in 43% of OCCC compared with 21% of HGS in a Japanese series (Fujimura et al. 2002). The authors of the latter study report that trastuzumab inhibited the growth of HER2-overexpressing OCCC cell lines *in vitro* (Fujimura et al. 2002) but, otherwise, the role of *HER2* in OCCC pathogenesis remains understudied.

1.3.5. Other events in OCCC

PPP2R1A is a subunit of the serine-threonine phosphatase PP2A that acts as a tumour suppressor by dephosphorylating oncogenes (Perrotti & Neviani 2013). *PPP2R1A* mutations were initially reported to occur in 7% of OCCC (Jones et al. 2010). A subsequent report confirmed their presence in 4% of OCCC but also revealed very high incidence of mutations (41%) in uterine serous carcinoma but not in ovarian HGS (McConechy et al. 2011). It appears that the mutations cluster in exons 5 and 6 of the subunit and alter its interactions with other subunits and, therefore, the stability of the holoenzyme (McConechy et al. 2011). The functional effects of *PPP2R1A* mutations in OCCC are, at present, unknown. A second phosphatase, *PPM1D*, is amplified in 10-31% of OCCC (Anglesio et al. 2011b; Tan et al. 2009) and is thought to act in a tumourigenic fashion by suppressing TP53 activation via p38 mitogen-activated protein kinase inhibition (Tan et al. 2009) and by suppressing Chk1 (Ali et al. 2012).

Other rare events in OCCC include *KRAS* and *BRAF* mutations. The former were described in 0 of 25 (Rechsteiner et al. 2013), 4 of 42 (9.5%) (Jones et al. 2010) and 7 of 97 (7.2%) (Kuo et al. 2009) OCCC cases in 3 series. *BRAF* mutations are even rarer with just 1 case reported in a 97-patient series (Kuo et al. 2009) and no mutations seen in 2 smaller series comprising of 25 and 20 patients respectively (Niskakoski et al. 2013; Rechsteiner et al. 2013). It should also be noted that *TP53* mutations have been reported in up to 10% of OCCC (Kuo et al. 2009). As *TP53* mutations are ubiquitous in HGS cancers and cells with clear cytoplasm can often be seen in these tumours (McCluggage 2008), it is unclear whether *TP53* mutations are a feature of *bona fide* OCCC or the reported cases represent instances of histological misclassification.

Interleukin 6 (IL6) expression by tumour cells (Coward et al. 2011) and plasma IL6 levels (Stone et al. 2012) are both associated with poor prognosis in patients with EOC. Inhibition of

IL6 signalling has shown preliminary evidence of benefit in preclinical models and in a small phase II study in unselected EOC patients (Coward et al. 2011). As IL6 signalling is particularly active in OCCC (Anglesio et al. 2011b) and the precursor endometriotic lesions (Bulun 2009), further evaluation of IL6 targeting therapies in OCCC is warranted (Glasspool & McNeish 2013).

1.3.6. OCCC and microsatellite instability

OCCC appears to be a frequent presentation of Lynch syndrome-associated EOC. It comprised 35% of the latter in a recently reported Finnish series and these tumours tended to show LINE-1 hypomethylation (Niskakoski et al. 2013). The frequency of *ARID1A* mutations in this series is not known but *ARID1A* expression loss appeared to be less common (14%) in uterine Lynch syndrome-associated endometrioid cancer compared with sporadic MSI tumours (75%) in a Dutch series (Bosse et al. 2013). In view of this discrepancy in *ARID1A* loss frequency, the authors postulated that *ARID1A* mutations led to *MLH1* promoter hypermethylation and the MSI phenotype, but direct experimental evidence for this is presently lacking. Co-occurrence of *ARID1A* loss and deficient mismatch repair (MMR) is supported by two Canadian series. The first showed that 39% of high-grade endometrioid tumours with deficient MMR had *ARID1A* loss compared with only 11% of MMR proficient tumours (Nelson et al. 2013). A similar pattern was seen in a second series, consisting of gastric cancer cases, with loss of *ARID1A* expression in 48% of MMR-deficient tumours compared to 19% of MMR-proficient ones (Wiegand et al. 2014b).

1.4. Glycogen accumulation

Glycogen accumulation leading to the characteristic clear cytoplasmic appearance is the defining morphological event in OCCC. Glycogen consists of glucose molecules linked linearly by $\alpha(1\rightarrow4)$ glycosidic bonds (Fig. 1.2). Glycogen synthesis begins in identical fashion to the glycolytic pathway, with phosphorylation of glucose to glucose-6-phosphate (G-6-P) by hexokinase. G-6-P is then converted to fructose-6-phosphate in the glycolytic pathway, but to glucose-1-phosphate (G-1-P) in the glycogen synthesis pathway, a reaction catalysed by phosphoglucomutase (Bouché et al. 2004). G-1-P is subsequently converted to UDP-glucose by UDP-glucose pyrophosphorylase and molecules of UDP-glucose are joined together by $\alpha(1\rightarrow4)$ glycosidic bonds by glycogen synthase around a glycogenin core (Roach et al. 2012). When chains of at least 11 glucose molecules are formed, 1,4- α -glucan branching enzyme transfers 7 glucose molecules to another chain, making an $\alpha(1\rightarrow6)$ glycosidic bond in the

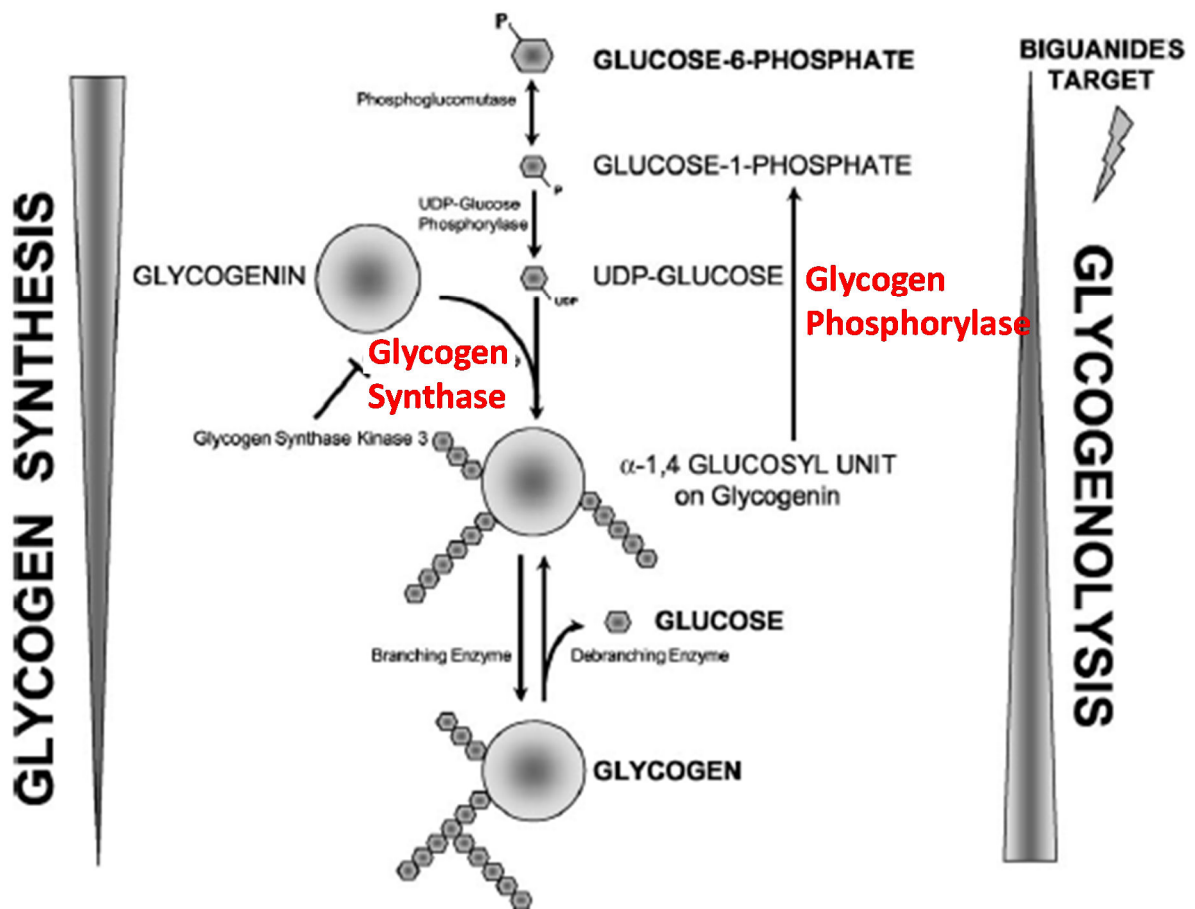


Figure 1.2. Glycogen metabolism

Key steps in glycogen synthesis and breakdown (adapted from Bouché et al. 2004).

process (Pelletier et al. 2012). Repeated cycles of this process result in large fractal structures containing, on average, 30,000 glucose molecules (Meléndez et al. 1999). Glycogenolysis, releasing G-1-P, is achieved by glycogen phosphorylase, which breaks the $\alpha(1\rightarrow4)$ bonds and the de-branching enzyme 4- α -glucanotransferase (also known as amylo- α 1,6-glucosidase and encoded by *AGL*) (Ozen 2007). G-1-P can then be converted back to G-6-P by phosphoglucomutase and enter the glycolytic or the pentose phosphate pathways (Ozen 2007).

Glycogen synthase and glycogen phosphorylase catalyse the rate-limiting steps in glycogenogenesis and glycogenolysis respectively. Glycogen synthase (GYS) phosphorylation by cAMP-dependent protein kinase A (PKA), PKC and GSK3 generally decreases its activity (Bouché et al. 2004). GYS undergoes allosteric activation by G-6-P (Roach et al. 2012). Additionally, PKA, PKB/AKT, PKC and other kinases can phosphorylate

GSK3, leading to dephosphorylation and activation of GYS (Pearce et al. 2010). This multilevel regulation of GYS allows for fine-tuning of glycogen synthesis depending on the cellular energetic state. Glycogen phosphorylase requires pyridoxal phosphate as an essential cofactor (Greenberg et al. 2006) and is activated by phosphorylation by phosphorylase kinase, which in turn is activated by PKA or phospholipase C (PLC), among others (Bouché et al. 2004).

Glycogen accumulation in OCCC is thought to represent an adaptive response to the hypoxic and oxidative environment of the endometriotic cysts from where OCCC develops (Iida et al. 2012; Yamada et al. 2011). HIF1 α is upregulated in hypoxia and has been shown to increase the expression of many genes involved in glycogen metabolism, including *PGM1* (encoding phosphoglucomutase 1) (Pelletier et al. 2012), *UGP2* (encoding UDP-glucose pyrophosphorylase) (Pescador et al. 2010), *GYS1* (encoding glycogen synthase 1) (Favaro et al. 2012; Iida et al. 2012), *GBE1* (encoding 1,4- α -glucan branching enzyme) (Pescador et al. 2010) and *PYGL* (encoding glycogen phosphorylase – liver isoform) (Favaro et al. 2012). Glycogen accumulation can be detected in a wide variety of cell lines, including mouse fibroblasts, colon, breast and renal cancer cell lines with further glycogen accumulation after exposure to hypoxia and utilisation of the stored glycogen upon glucose deprivation (Pelletier et al. 2012). Similarly, culture of U87 glioblastoma cells in hypoxic conditions (0.1% O₂) resulted in upregulation of *PYGL* and increase in cellular glycogen. *PYGL* knockdown by shRNA resulted in a further increase in glycogen levels, inhibition of proliferation and induction of senescence under both high (25mM) and physiological (5mM) glucose conditions (Favaro et al. 2012).

In OCCC, HIF1 α is activated by the IL6-JAK2-STAT3 pathway (Anglesio et al. 2011b; Coward et al. 2011). Indeed, a study using the HAC2 OCCC cell line showed HIF1 α induction by hypoxia with consequent increases in expression of many enzymes involved in glycogen metabolism including GYS1 as well as increased glycogen accumulation (Iida et al. 2012).

The role of glycogen, in cancer generally and OCCC in particular, remains understudied. It is not clear whether the glycogen stores are functionally relevant or an epiphenomenon of the malignant transformation programme or the endometrial cell of origin. The decrease in proliferation seen upon *PYGL* knockdown in the presence of adequate glucose in the medium (Favaro et al. 2012) raises the provocative hypothesis that continuous access to glycogen stores is important for sustained proliferation, even in high-glucose conditions such as those

encountered in routine cell culture. OCCC with its high glycogen content is an ideal system to examine proliferation under conditions of both high and low glucose in order to clarify whether glycogen has a role beyond that of a fuel store. Furthermore, it is not known whether other factors, besides hypoxia, contribute to the high glycogen content of OCCC. Although HNF1B has been implicated by many authors (Cuff et al. 2013; Okamoto et al. 2013; Uekuri et al. 2013), an effect of HNF1B on glycogen content has not been directly demonstrated.

1.5. Is OCCC an endometrial cancer in the wrong place?

As detailed in section 1.3, OCCC is characterised by frequent *ARID1A* mutations and activation of the PI3K pathway, two characteristics that it shares with uterine endometrioid cancer. Indeed, there is a remarkable overlap in the mutation patterns of some of the uterine and ovarian cancer subtypes (Fig. 1.3). Furthermore, as already mentioned, most OCCC arise

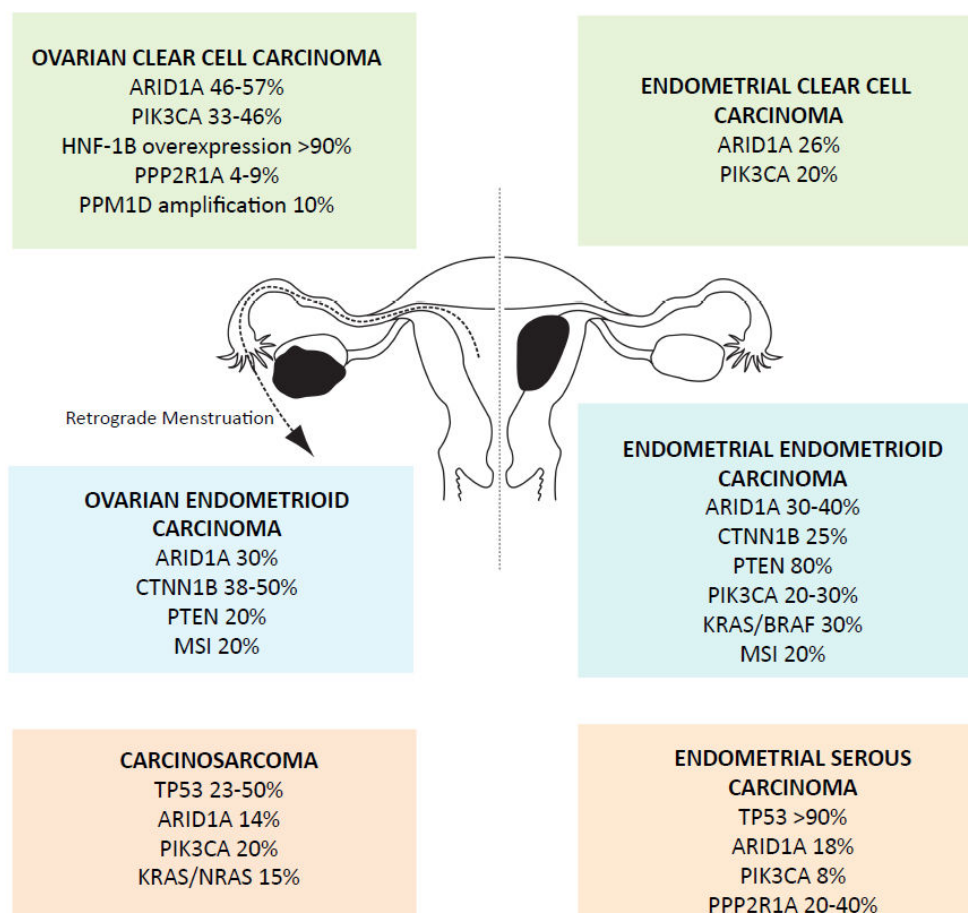


Figure 1.3. Mutational events in cancers arising from the endometrium
Frequency of common mutations in endometrium-derived cancers (from Gounaris et al. 2011).

on an endometriotic background. Endometriosis, essentially ectopic endometrial tissue, can be seen after careful histological examination in the vast majority of OCCC and a significant proportion of ovarian endometrioid tumours (McCluggage 2008). These observations have led us (Gounaris et al. 2011), and others (Mao & Shih 2013), to propose that OCCC is essentially a uterine cancer developing in the wrong environment, that of an endometriotic cyst.

Endometriosis, an inflammatory condition affecting 5-10% of reproductive age women (Giudice & Kao 2004), shares many characteristics with tumours, including evidence of clonality and tissue invasion (Barlow & Kennedy 2005). Extensive epidemiological investigations have confirmed that endometriosis is a risk factor not only for OCCC, but for OEAC and low-grade serous tumours as well (Pearce et al. 2012). The most widely accepted theory for its pathogenesis is that of retrograde menstruation through the fallopian tubes, leading to implantation of endometrial tissue on the ovaries (where they form endometriotic cysts) and other peritoneal surfaces (Bulun 2009). It is a hormonally and inflammation-driven process with multiple studies demonstrating high COX-2 and aromatase activity, leading to increased local prostaglandin E₂ (PGE₂) and oestradiol (E₂) production (Bulun 2009; Rizner 2009). Furthermore, endometriotic lesions exhibit increased local IL6 production (Bulun 2009) and evidence of oxidative stress from the release of ferric and ferrous ions from heme breakdown (Kobayashi et al. 2009). These factors contribute to extensive genomic damage, manifested as LOH in endometriotic lesions (Kobayashi et al. 2009; Xu et al. 2011) and loss of PTEN expression in up to 15% of cases (Martini et al. 2002). Additionally, as already discussed in section 1.3, mutations in genes such as *ARID1A* and *PIK3CA* as well as HNF1B expression induction can be seen in endometriosis with attendant cancer, and even in endometriotic lesions without malignancy (Samartzis et al. 2012).

Evidence has accumulated over the past few years that the eutopic endometrium of women with endometriosis differs from that of women without, exhibiting COX-2 induction and increased PGE₂ (Bulun 2009). There is also evidence of activation of the MAPK (Yotova et al. 2011) and PI3K (Laudanski et al. 2009) pathways. Therefore, a stepwise accumulation of genetic and epigenetic changes from eutopic endometrium in women destined to develop endometriosis, to endometriosis and then to OCCC can be demonstrated (Fig. 1.4).

These observations raise the important question of which, if any, of these events are responsible for the malignant transformation in 0.5-1% of endometriosis cases. If drivers of this malignant transformation can be identified, it would then be important to establish whether

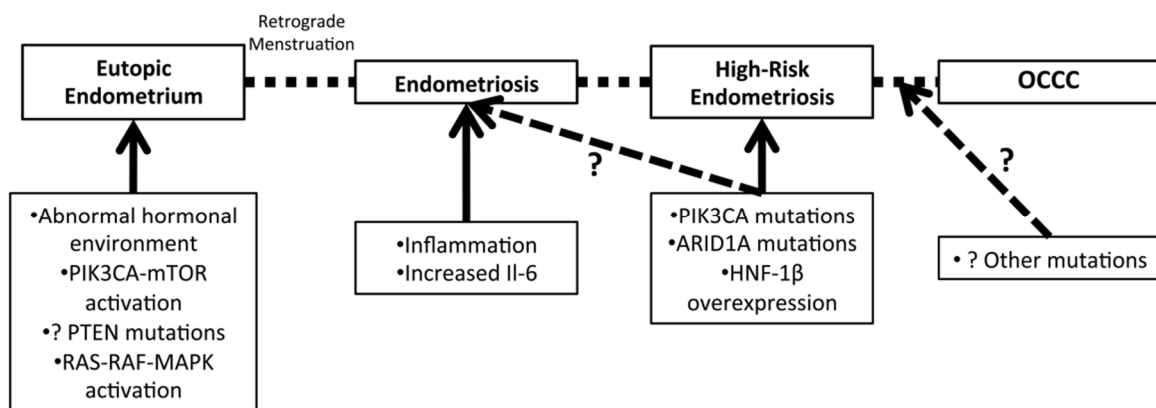


Figure 1.4. Stepwise progression from endometriosis to OCCC

Illustration of key abnormalities underlying the stepwise progression from an already abnormal eutopic endometrium to OCCC via endometriosis. The question marks refer to unknown or putative events. Specifically, it is not currently known whether *ARID1A* and *PIK3CA* mutations or HNF1B overexpression are frequent in early or typical endometriosis and whether their presence confers an increased risk of malignant progression (from Gounaris et al. 2011).

early changes in some patients with endometriosis strongly predispose them to malignancy or whether this transformation is a late stochastic event (Gounaris et al. 2011). In other words, it will be important to determine whether the appearance of putative OCCC driver events (*ARID1A* and *PIK3CA* mutations, PTEN loss, *MET* amplifications, HNF1B overexpression) in an endometriotic lesion is a common phenomenon or a harbinger of malignancy. Investigation of the functional consequences of their perturbations in endometrium and endometriosis can help elucidate interactions and temporal dependencies on the road to carcinogenesis. An important and understudied aspect of endometriosis-associated OCCC pathogenesis is the switch from a hormonally dependent state in endometriosis to a hormonally independent state in OCCC, a tumour that is almost invariably ER and PgR negative (Anglesio et al. 2011a). One theory postulates that endometriotic lesions that retain hormonal sensitivity during malignant transformation give rise to OEAC, whereas the ones that lose hormonal sensitivity develop into OCCC (Mandai et al. 2009). If a specific pattern of alterations strongly predisposing to cancer can be identified in endometriosis, then screening for endometriosis-associated cancer may become feasible, especially if such alterations can be correlated with changes in the eutopic endometrium of these women (Gounaris et al. 2011).

It should also be kept in mind, that OCCC is not necessarily genetically homogeneous. aCGH analysis of 50 OCCC cases identified two distinct clusters with different prognosis and clinical behaviour (Tan et al. 2011). Whereas the vast majority of OCCC arise from endometriotic

cysts (McCluggage 2008), some cases represent malignant transformation of the borderline tumour adenofibroma (Veras et al. 2009). Adjacent endometriosis can still be detected in up to 44% of adenofibroma-related OCCC (Veras et al. 2009) and, therefore, strong evidence for an endometriosis-independent route of OCCC pathogenesis is presently lacking. However, it would still be important to understand whether the mutational spectrum differs between cystic and adenofibroma-derived OCCC.

1.6. Model systems for OCCC

The realisation that EOC is actually a set of distinct malignancies with different tissues of origin and molecular pathogenesis has led to a reappraisal of the model systems used to study these tumours to the extent that it is no longer sufficient or acceptable to label a mouse model or cell line as “ovarian cancer”. In this section, I will briefly review some of the genetically engineered mouse models (GEMM) of endometriosis-associated ovarian cancer and established OCCC cell lines as well as the functional anatomy of the normal mouse endometrium.

1.6.1. Genetically engineered mouse models (GEMM)

Arguably, a GEMM of OCCC should reflect its uterine tissue of origin and endometriotic precursor lesions. Unfortunately, no such model exists today. Two main GEMMs have been described for the other endometriosis-related ovarian cancer, OEAC. Both models rely on intrabursal injection of recombinant adenovirus carrying the Cre recombinase (AdCre) in order to ablate genes of interest on the ovarian surface epithelium (OSE) (Dinulescu et al. 2005; Wu et al. 2007). Both models target *Pten* in addition to induction of oncogenic *Kras*^{G12D} (Dinulescu et al. 2005) or deletion of *Apc* (Wu et al. 2007) and in both models mice develop tumours with endometrioid morphology. The main concern regarding use of these models is that the transformed OSE may accurately reflect neither the real tissue of origin which is thought to be the endometrium, nor the endometriotic background.

In this respect, uterine endometrioid cancer GEMMs may provide useful insights as, at least, they reflect the putative cell of origin, albeit with the limitation that the endometriotic environment is not replicated. *PgR-Cre* has been used to selectively ablate genes of interest in tissues expressing PgR, including most female reproductive tissues but also the CNS (Soyal et al. 2005). *Pten* deletion using this system is sufficient to cause endometrial cancers (Daikoku et al. 2008; van der Zee et al. 2013), a process that is accelerated and exacerbated

when combined with either *Apc* (van der Zee et al. 2013) or *Tp53* deletion (Daikoku et al. 2008). Interestingly, when anti-Mullerian hormone type 2 receptor (*Amhr2*)-*Cre* was used to selectively ablate *Pten* in the myometrium and uterine stroma, endometrioid cancers did not develop (Daikoku et al. 2011), providing support to the notion that, although epithelial-stromal interactions may be important, the cells undergoing malignant transformation are of epithelial origin. Consistently with the above, uterine epithelial *Lkb1* ablation using small proline-rich protein 2F (*Sprr2f*)-*Cre*, was sufficient to cause endometrioid cancer (Contreras et al. 2010). A limitation of all these models is that the targeted genes are deleted in a constitutive fashion, which could be important when targeting ubiquitously expressed, developmentally crucial genes such as *Arid1a*. Similarly, although the deletion is spatially targeted to the uterus, none of the genes used to drive *Cre* expression is absolutely uterus-specific giving rise to untoward effects. This was exemplified by the reported inability to use the *Sprr2f*-*Cre* model to ablate *Pten* in the uterine epithelium because of the development of brain tumours in the targeted animals (Daikoku et al. 2011). However, temporal and spatial control of the ablation of genes of interest in the uterus can be achieved by intra-uterine injection of AdCre, a method that has been successfully used to generate endometrioid cancers by targeting *Pten* (Joshi & Ellenson 2011) or *Lkb1* (Contreras et al. 2008). Insights gained from such models, although useful, do not replicate the unique phenotype of OCCC.

Perhaps the optimal way to model OCCC would be to engineer mutations of interest (*Arid1a*, *Pik3ca*, *Hnf1b* overexpression) in a reliable model of endometriosis. Development of such models has been hampered by the fact that only primates undergo regular menstruation and spontaneously develop endometriosis. Although primate models have been developed, for obvious ethical, regulatory, financial and scientific reasons, they are not suitable for large scale carcinogenesis research (Tirado-González et al. 2010). Heterologous mouse models rely on the implantation of human endometrial tissue in immunosuppressed mice (Masuda et al. 2007; Tirado-González et al. 2010) and are, consequently, limited by the inability to fully replicate the intense inflammatory environment of endometriotic cysts. Homologous models utilise ovariectomy and oestrogen treatment to abrogate the mouse estrus cycle and induce uterine epithelial proliferation before harvesting the epithelium and implanting it in syngeneic animals (Cummings & Metcalf 1995; Tirado-González et al. 2010). An improved such model, using *Ah-Cre*^{+/+}/*Kras*^{G12V} mice has recently been described. It utilises sequential E₂ and progesterone (P₄) administration after ovariectomy in order to induce a more human-like, decidualising uterine epithelium (Cheng et al. 2011). Oncogenic *Kras*^{G12V} is subsequently induced in the uterus by topical β-naphthoflavone injection, followed by harvesting of the endometrium and subcutaneous implantation in syngeneic animals. The developing lesions have all the

characteristics of human endometriosis, including invasion and activation of fibroblasts, endothelial cells and macrophages and collagen deposition (Cheng et al. 2011). This model could serve as the basis for modelling OCCC, as it would be feasible to engineer conditional mutations in genes such as *Arid1a* and *Pik3ca* in the donor animals and activate *Cre* by intra-uterine β -naphthoflavone. Alternatively, these genes could be knocked down *ex vivo* prior to the implantation of the harvested endometrium in the recipient animals. Both methods would thus overcome the lethal haplo-insufficient phenotype exhibited by *Arid1a* loss in the germline (Gao et al. 2008).

Spontaneous peritoneal endometriotic-like lesions developed in mice after intrabursal AdCre injection that activated oncogenic *Kras*^{G12D} in the OEAC model described by Dinulescu *et al* (2005). It is unclear how local *Kras* activation could cause distant lesions in these animals that, unlike when both *Kras* and *Pten* were targeted, did not develop malignancy. A simple explanation would be bursal perforation during the injection but, even then, any lesions would be arising from transformed mesothelial cells, limiting the utility of this model.

To summarise, GEMMs of OCCC do not currently exist. Of the possible options, introducing mutations in putative OCCC driver genes in the endometriosis model described by Cheng *et al*, appears to be the most promising.

1.6.2. OCCC cell lines

Increasingly, it is realised that mis-identification and cross-contamination of laboratory cancer cell lines is a common problem with up to 15% of human cell lines shown not to be derived from the claimed source (Masters 2012). This problem is particularly acute in EOC research where accurate histological subtype information for many cell lines is lacking. Recently, it was shown that one of the commonly used OCCC cell lines, OV2008, is HPV positive and identical to the cervical adenocarcinoma cell line ME-180 (Korch et al. 2012). Another, ES-2, forms undifferentiated tumours in xenograft studies (Shaw et al. 2004) and lacks typical features of OCCC such as HNF1B overexpression, *ARID1A* or *PIK3CA* mutations (Anglesio et al. 2013), rendering it unsuitable as an OCCC model. It is also worth noting that SKOV3, commonly used as a HGS model, overexpresses HNF1B according both to mine and others' results (Anglesio et al. 2013), has *ARID1A* and *PIK3CA* mutations and accumulates large amounts of glycogen (see section 6.3). It could therefore be utilised as an OCCC model, although it is atypical as it also carries a *TP53* mutation.

Recently, research groups have integrated genomic and IHC data in order to reclassify EOC cell lines and identify lines that could be suitable experimental models for the various EOC histological subtypes (Anglesio et al. 2013; Domcke et al. 2013). It is worth noting that Anglesio's recommendation of JHOC-5 and TOV21G as the cell lines most suitable for studying OCC is entirely in agreement with my experimental approach.

1.6.3. Functional anatomy of the mouse endometrium

Both human and mouse endometria consist of luminal and glandular epithelial cells held together by a supportive stroma. There is evidence of clonal origin of individual entire glands, suggesting the presence of an endometrial stem cell niche. Label retaining and side population cells (Kyo et al. 2011) have been identified in both the epithelium and the stroma in the mouse endometrium (Fig. 1.5) but, despite cell-to-cell variability in ER and PgR expression, distinct epithelial or stromal populations have not yet been described (Gargett 2007). It has been suggested that ER α positive stromal cells provide paracrine signalling to the ER α negative luminal progenitor cells that, in turn, differentiate to the predominantly ER α positive luminal cells (Gargett et al. 2012) (Fig. 1.5). This model is supported by recombination experiments in

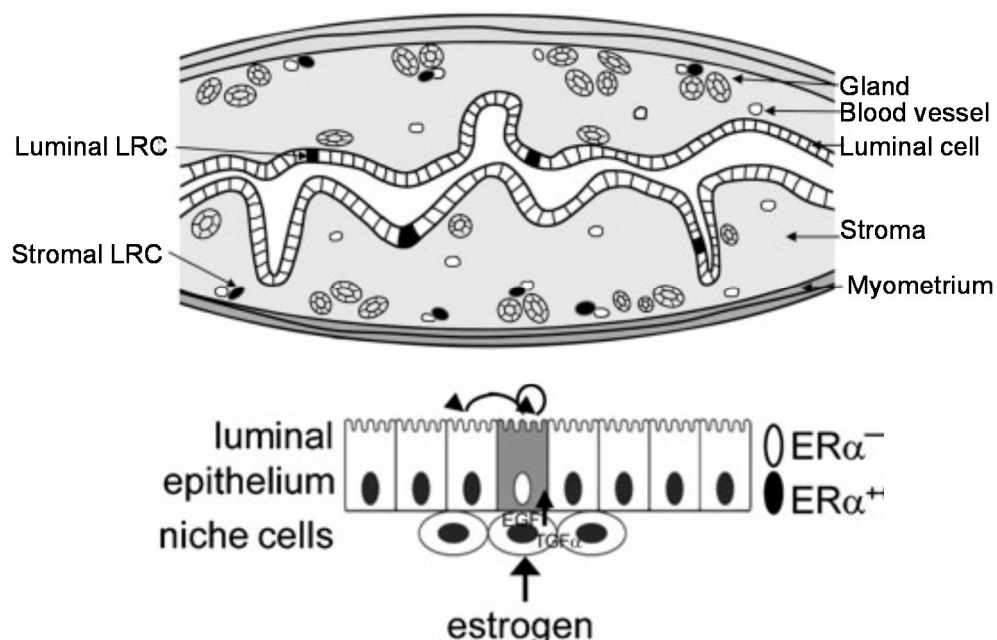


Figure 1.5. Organisation of the mouse endometrium and the stem cell niche

Position of label retaining cells (LRC) in the mouse endometrium (top panel) and paracrine interactions in the stem cell niche (bottom panel). ER α ⁺ stromal niche cells provide paracrine stimulation to ER α ⁻ progenitor cells that self-renew and differentiate to ER α ⁺ luminal cells (from Gargett 2007 and Gargett et al. 2012).

ER knockout mice that have shown that epithelial proliferation is dependent on stromal ER signalling but that epithelial ER is dispensable for proliferation (Cooke et al. 2007).

1.7. Specific aims of this project

The work presented in this thesis aims to functionally characterise the consequences of the 3 “signature” events in OCCC: *ARID1A* mutations, *HNF1B* overexpression and glycogen accumulation.

At the start of this project, in early 2011, the frequent occurrence of *ARID1A* mutations in OCCC had just been reported. Very little was, and is still, known about the physiological role of *ARID1A* in the endometrium and the consequences of its loss. From what we know about the SWI/SNF complex though in general, it was expected that *ARID1A*'s role would be tissue and context specific. Therefore, this project aimed to:

- Study the role of *Arid1a* in the hormonal regulation of the endometrium and describe the *Arid1a*-driven transcriptional programme in normal endometrium using the mouse as a model system
- Describe the *ARID1A*-driven transcriptional programme and the consequences of *ARID1A* loss in other model systems such as mouse embryonic fibroblasts (MEFs), a more easily manipulated non-cancerous model, and human immortalised ovarian surface epithelium (IOSE)
- Investigate the effect of *ARID1A* knockdown on proliferation in normal mouse uterine tissues, MEFs, IOSE and a panel of OCCC and EOC cell lines
- As *ARID1A* and *ARID1B* are mutually exclusive but essential components of the SWI/SNF complex, explore the consequences of combined *ARID1A* and *ARID1B* knockdown

HNF1B overexpression is thought to be one of the main drivers of the OCCC phenotype and contribute to OCCC proliferation. Again, in 2011, knowledge of the *HNF1B*-driven transcriptional programme was based mostly on older generation microarray studies and direct metabolic studies were lacking. Studies of *HNF1B*'s role on proliferation had given inconsistent results. With regards to *HNF1B*, this project aimed to:

- Investigate the role of *HNF1B* on proliferation in a wider panel of OCCC cell lines

- Describe the *HNF1B*-driven transcriptional programme using *bona fide* OCCC cell lines such as JHOC-5 and TOV21G
- Describe the effects of HNF1B on the metabolic profile of OCCC and show whether a direct link to glycogen accumulation exists

As detailed in section 1.4, the role of glycogen in cancer in general is understudied and only very recently studies have hinted at a role that goes beyond that of a fuel store. Aims of this project were to:

- Investigate whether the OCCC glycogen stores are functionally active
- Investigate the effects of glycogen metabolism perturbations on cell proliferation and survival in OCCC cell lines
- Investigate the consequences of glycogen metabolism perturbations on the metabolic programming of OCCC cell lines

The need for novel therapeutic approaches in OCCC is undeniable. The reports of “targetable” genomic alterations such as *MET* or *HER2* amplifications in a minority of OCCC cases, raises the hope that targeted treatments may benefit a subset a patients. However, apart from the observed correlation between *ARID1A* mutations and PI3K pathway activation, implications for therapeutic strategies arising from the 3 “signature” events in OCCC are presently unclear. It is hoped that knowledge gained from studying the roles of *ARID1A*, *HNF1B* and glycogen in OCCC will suggest avenues for future therapeutic investigations. For this, a reliable GEMM of OCCC will be indispensable. Therefore, a long-term aim, beyond the time confines of this project, is to utilise the knowledge gained in order to create an OCCC mouse model on the background of the Cheng endometriosis model.

2. MATERIALS AND METHODS

2.1. Animals

C57BL/6 (B6) and CD-1 female mice were purchased from Charles Rivers Laboratories (Margate, UK). A vasectomized male B6 mouse was a kind gift from Dr. Xiangang Zou, CRUK Cambridge Institute (CI), Cambridge, UK. *Arid1a^{fl}* mice were a kind gift from Dr. Peri Tate, Sanger Institute, Hinxton, UK. They contain LoxP sequences surrounding exon 9 of *Arid1a*, have been derived using the techniques described by Gao *et al* (2008) and were re-derived by the Transgenics Core Facility at the CI. *ROSA26^{Cre-ERT2}* mice were a kind gift from Prof. Pierre Chambon, IGBMC, France, and have previously been described (Hameyer *et al.* 2007). *Arid1a^{fl}* and *ROSA26^{Cre-ERT2}* mice were backcrossed to a B6 background under the supervision of Dr. Doug Winton, CRUK CI, to generate *ROSA26^{Cre-ERT2}-Arid1a^{fl/fl}* mice. Genotyping was performed using the following primers: TCAAGGGGGCATGATGGGAAC (forward) and CATCCCAAGGCCATCATCT (reverse). These amplify the region surrounding the LoxP sequence between exons 9 and 10 resulting in an approximately 40bp longer PCR product in its presence. After initial in-house validation, subsequent genotyping was performed by Transnetyx Inc (Cordova, TN, USA). All animals were housed in the CI Biological Resources Unit in accordance with the relevant animal care regulations.

2.2. Estrus cycle monitoring

In sexually mature mice, the estrus cycle was monitored with vaginal smears. Briefly, vaginal cells were aspirated using a sterile pastelle in ~0.5ml PBS, allowed to air-dry, fixed by immersion in acetone for 5 min, stained with Mayer's haematoxylin, cover-slipped and examined under a light microscope.

2.3. Mouse tissue acquisition

Female mice (specific ages varied according to the experimental needs) were euthanized by asphyxiation in a CO₂ chamber followed by cervical dislocation. The peritoneal cavity was opened and the uterus horns and body removed *en block* using a scalpel and scissors. Generally, the uterine horns were separated and one was fixed in 10% neutral buffered formalin (NBF) for 18-24 hours whereas the other was opened longitudinally, cut into ~5mm segments and placed in RNAlater (Qiagen) for subsequent RNA extraction.

2.4. Estrus-timed mouse uterus series

To examine the variability of *Arid1a* expression in the mouse uterus during the estrus cycle and its association to hormonal responses (Inoue et al. 2002), a cohort of 28 6-8-week-old B6 mice was used. In all mice, the phase of the estrus cycle was determined by daily vaginal smears for up to 4 days (see section 2.2) with the last one performed ~2 hours before tissue collection. One uterine horn from each mouse was preserved in RNAlater, RNA was extracted (see section 2.12.2) and used to measure *Arid1a*, *Arid1b* and *Ltf* mRNA expression by qRT-PCR (see section 2.16.1). The second uterine horn was fixed in 10% NBF and submitted for histological evaluation. Quantitative immunohistochemistry (IHC) for ARID1A, ER, PgR and Ki67 was performed and analysed as detailed in section 2.15.1. Additionally, IHC was performed for CD45.

2.5. Culture of murine uterine fragments

2.5.1. “Coin” method

This method is based on an original description by Newbold *et al* (1994) with some modifications. Three to twelve-week-old B6 and CD-1 mice were killed by asphyxiation, the uteri were removed and the uterine horns slit longitudinally. Fragments approximately 0.5-2mm in size were cut on ice, using scalpels and iris scissors, taking care to complete the procedure within 5-10 min. The fragments were subsequently placed in culture dishes with or without Matrigel (1:50 dilution) pre-coating (BD Biosciences). Media tried were a) Dulbecco's Modified Eagle Medium / Ham's F12 (DMEM/F12) 1:1 mix (Gibco), b) Basal Medium Eagle (BME) with 1% 10mM MEM non-essential amino acids, 1% 100x MEM vitamin solution, 1% 100mM MEM sodium pyruvate solution and 1% 200mM L-glutamine (all from Sigma-Aldrich) and c) 3:1 DMEM/F12 mix supplemented with 0.5µg/ml hydrocortisone (Sigma-Aldrich), 10ng/ml EGF (Peprotech) and 0.1nM cholera toxin (Enzo Life Sciences) (FAD). All media were supplemented with 10% FBS (Gibco), 50U/ml penicillin and 50µg/ml streptomycin (Gibco) with or without 1-10ng/ml diethylstilbestrol (DES - Fisher Scientific). After 5-6 days in culture, the fragments were harvested, fixed in 10% NBF overnight, paraffin embedded, sectioned and stained with H&E to assess tissue viability.

2.5.2. Culture in CellMatrix®

This is a modification of the murine intestinal fragment culture method described by Ootani *et al* (2009). Fragments were prepared as described in 2.5.1 or, alternatively, 5mm uterine

fragments were further minced using a GentleMACS Dissociator (Miltenyi Biotec) on a non-enzymatic digestion cycle. A bottom layer of collagen gel matrix consisting of CellMatrix type I-A (Nitta Gelatin) was created in a PICM03050 Millicell culture plate insert (Millipore) as described elsewhere (Ootani et al. 2009). A second layer containing a mixture of CellMatrix and the tissue fragments was added on top and the whole construct placed in 6-well plates (Corning). One-two ml medium with or without 1-10ng/ml DES was added to the outer dish. Culture media tried were DMEM/F12, RPMI 1640 (Gibco), FAD and BME supplemented as described in section 2.5.1. All media were supplemented with 10% FBS, 50Un/ml penicillin and 50µg/ml streptomycin. After 6-15 days in culture, the inserts were fixed with 4% PFA overnight and either the whole CellMatrix-tissue assembly or the retrieved tissue samples submitted for histological examination.

2.5.3. Vibratome method

Eight to fifteen-week-old CD-1 mice were killed by asphyxiation and the uteri removed. Whole uterine horns were embedded in 3% agarose (Fisher Scientific) and placed in ice for 30 min to allow the agarose to solidify. 100-200µm transverse tissue sections were cut using a VT1200S vibratome (Leica) and placed in culture dishes. Culture media tried were DMEM, DMEM/F12, RPMI 1640 and McCoy's. All media were supplemented with 10% FBS, 50Un/ml penicillin and 50µg/ml streptomycin. After 6-7 days in culture, the tissue was fixed with ice-cold methanol at -20°C for 30 min, left to air-dry overnight and stained with H&E. Alternatively, after fixation, the tissue was re-embedded in paraffin and thin sections cut for H&E and IHC (for the latter fixation was with 10% NBF overnight as this is the institutional standard for IHC). In another experiment, 150µm uterine sections from a homozygous *Arid1a^{fl/fl}* mouse were placed in wells of a 96-well plate with 200µl DMEM medium and treated with increasing titres (up to 10⁸ PFU per well) of Cre-expressing adenovirus (Ad-Cre-IRES-GFP, Vector Biolabs) to *in vitro* knockout *Arid1a*.

2.5.4. Surgispon® method

1mm uterine fragments from an 11-week-old CD-1 mouse were prepared as described in 2.5.1. The fragments were subsequently placed on 1cm³ cubes of absorbable gelatin sponge (Surgispon®, Anser Medical) pre-soaked in medium (Centenera et al. 2012) in a 24-well tissue culture plate (Corning). 500 or 1000µl RPMI 1640 medium was added, supplemented with 10% FBS, 50Un/ml penicillin and 50µg/ml streptomycin, 10µg/ml insulin (Sigma-Aldrich) and

10µg/ml hydrocortisone. After 6 days in culture, the fragments were fixed in 10% NBF overnight and submitted for histological examination.

2.5.5. Non-adjacent co-culture method

The method originally described by Chung and Das (2011) was used with modifications.¹ Six or eight-week-old pseudo-pregnant CD-1 mice were euthanised on day 4 of pseudo-pregnancy and uterine fragments prepared as described in 2.5.1. These were placed in 3ml dissociation solution consisting of a 9:1 mixture of 5mg/ml dispase (Stem Cell Technologies) and 250mg/ml pancreatin (Sigma-Aldrich) supplemented with 50Un/ml penicillin and 50µg/ml streptomycin and incubated at 4°C for 1 hour, then at 20°C for 1 hour and finally at 37°C for 10 min. Subsequently, 17ml ice-cold Hanks Balanced Salt Solution (HBSS, Gibco) and 2ml FBS were added and the fragments mixed by pipetting multiple times using a 25ml pipette. The epithelial cell-containing supernatant was collected and cells were allowed to settle by gravity. The medium was then discarded, cells were washed with 20ml HBSS, centrifuged at 1,300rpm for 3 min and re-suspended in medium (phenol red-free DMEM/F12 supplemented with 10% charcoal-stripped FBS, 50Un/ml penicillin and 50µg/ml streptomycin). The uterine fragments were washed twice with 20-30ml HBSS and then incubated in 3ml of a 19:1 mixture of HBSS and 10mg/ml collagenase (Roche Diagnostics) supplemented with 50Un/ml penicillin and 50µg/ml streptomycin at 37°C for 30 min. Subsequently, 17ml ice-cold HBSS and 2ml FBS were added and the fragments were mixed by pipetting multiple times with a 25ml pipette. The stromal cell-containing supernatant was then filtered through an 80µm nylon mesh (Millipore), centrifuged at 1,300rpm for 3 min and re-suspended in medium. The epithelial cells were plated in a 0.4µm PET cell culture insert (BD Falcon) coated with 1:50 Matrigel in medium solution, in 6-well plates. The stromal cells were plated on coverslips in different wells of 6-well plates. After 48 hours of separate culture, the inserts were placed on top of the coverslips to establish the co-culture system and the concentration of FBS in the medium reduced to 1%. 10nM oestradiol (E₂ – Sigma-Aldrich) and/or 1µM progesterone (P₄ – Sigma-Aldrich) were added after a further 24 hours followed by Bromodeoxyuridine (BrdU, Sigma-Aldrich) 48 hours later to verify, by immunofluorescence microscopy (see section 2.10), the establishment of normal hormonal responses (Chung & Das 2011). BrdU incubation times were up to 24 hours, in different experiments.

¹ It should be noted that the methods reference in this publication links to an irrelevant publication. A protocol version was obtained from the authors but it contained fundamental errors; e.g. if followed as stated, epithelial cells were discarded rather than retained. It therefore required extensive optimisation.

2.6. Culture of dissociated uterine cells

The techniques described by Ouellette *et al* (1999) and Campbell *et al* (2006) were utilized. Initial experiments were based on the Ouellette *et al* (1999) method with minor modifications. Briefly, 8-week-old B6 mice were euthanized, the uteri retrieved, the uterine horns opened longitudinally and incubated for 60 min at 37°C in 5ml DMEM/F12 with 5mg collagenase I (Invitrogen). The epithelial-cell containing supernatant was collected, spun-down briefly, re-suspended in DMEM/F12 medium supplemented with 10% FBS, 50Un/ml penicillin and 50µg/ml streptomycin and plated in 6-well plates. Meanwhile, the uterine horns were incubated for a further 60 min at 37°C at 140rpm on a shaker in fresh DMEM/F12 with 5mg/ml collagenase I. Subsequently, the horns were crushed through an 180µm metal sieve in order to collect stromal cells that were plated in a manner identical to the epithelial cells. Alternatively, the initial incubation period was extended to 20 hours and Matrigel coating (1:50 dilution) was applied to the plates. To establish baseline viability and proliferative capacity, cells were kept in culture for up to 32 days with weekly medium changes, were harvested at various time points and viable cell numbers determined using a Vi-CELL XR counter (Beckman Coulter) on days 10, 26 and 32.

Using the Campbell *et al* (2006) method, dissociation was accomplished by overnight incubation of uterine horns in a 1:1 mixture of 1.75Un/ml dispase (Sigma-Aldrich) and HBSS followed by mechanical pressure in order to squeeze the luminal epithelium out of the horn. Subsequently, epithelium and stroma were incubated separately with 10mg/ml collagenase on a shaker at 250rpm at 37°C for 2 hours and the tissue was further broken down by pipetting. The solution was centrifuged at 1,000rpm for 5 min, the pellet reconstituted and incubated with 0.5% trypsin (Gibco) for 2 min, followed by a further centrifugation step (1,000rpm/5min), reconstitution of the pellet and passing through a 30µm cell strainer (BD Biosciences). Cells were counted using the Vi-CELL XR counter and plated in 12 or 96-well plates with or without Matrigel pre-coating (1:50 dilution). Media tested were DMEM/F12, McCoy's and BME with the same additives as detailed in section 2.5.2.1. Cell numbers and viability were assessed after 7 days in culture using the Vi-CELL XR counter. Alternatively, dissociated cells from 3-week-old B6 mice were cultured in a 24-well plate with 5×10^4 irradiated feeder 3T3 fibroblasts per well, 0.5ml RPMI 1640 and 50ng/ml DES and observed for 30 days for colony formation.

2.7. Creation and expansion of Mouse Embryonic Fibroblast (MEF) cell lines

Mouse embryonic fibroblasts can be useful model systems for functional studies of putative cancer associated genes (Sun et al. 2007). To create MEF cell lines pregnant B6 mice were euthanized on day 10.5-13.5 of pregnancy. The embryos were dissected out of the implantation sites at the uterine horns, placed in separate wells of a 24-well plate and washed with sterile PBS on ice. They were subsequently incubated with 1ml 0.25% trypsin/EDTA (Gibco) at 4°C overnight. The following morning the trypsin was aspirated, 1 ml fresh 0.25% trypsin/EDTA was added to each well and the embryos incubated at 37°C for 15 min. One ml DMEM supplemented with 10% FBS was added and the embryos were gently dissociated using a wide bore glass pipette. Cells from each embryo were then plated in two 100mm culture dishes with DMEM medium supplemented with 10% FBS, 50Un/ml penicillin and 50µg/ml streptomycin. The culture dishes were inspected daily and when the cellular monolayer in a culture dish was confluent, the cells were transferred to 1 T-175 flask (passage 2). When confluent again, the cells were transferred to 3 T-175 flasks (passage 3). When the cells became confluent in passage 3, they were tested for mycoplasma infection and once confirmed mycoplasma negative, placed in a liquid nitrogen tank in freeze medium consisting of 65% DMEM, 25% FBS and 10% glycerol. A list of the MEF cell lines created as part of this project is provided in Table 2.1. Cells were taken out of liquid nitrogen and expanded up to passage 6 for individual experiments as detailed in the relevant sections.

Table 2.1. Mouse Embryonic Fibroblast cell lines

MEF Cell lines	Parental Genotype	Pregnancy day	Litter	MEF genotype	Comments
E1-E5	WT x WT	10.5	A	WT	E1 and E5 stopped growing before freezing
E6-E11	WT x WT	12.5	B	WT	
E21-E29	<i>Arid1a</i> ^{tag} x WT	12.5	C	E23, E28 & E29 <i>Arid1a</i> ^{tag} Rest WT	
E31-E36	<i>Arid1a</i> ^{tag} x WT	10.5	D	E31 & E34 <i>Arid1a</i> ^{tag} E32 WT	E33, E35 and E36 stopped growing before freezing
E41-E45	<i>Arid1a</i> ^{fl/fl} x <i>Arid1a</i> ^{fl/fl}	13.5	E	<i>Arid1a</i> ^{fl/fl}	Frozen after passage 2. Very poor growth after thawing

WT: Wild Type; *Arid1a*^{tag}: FLAG-tagged *Arid1a* allele

2.8. *In vivo* Arid1a ablation

Either 2 or 4 mg tamoxifen were injected intra-peritoneally (i.p.) to *in vivo* ablate *Arid1a* in *Arid1a*^{WT/fl}-*ROSA26*^{Cre-ERT2} or *Arid1a*^{fl/fl}-*ROSA26*^{Cre-ERT2} mice. *Arid1a*^{WT/WT}-*ROSA26*^{Cre-ERT2} mice served as negative controls². Uterine samples were collected after 4 to 28 days as described in section 2.3 and fixed in 10% NBF or preserved in RNAlater in order to establish the extent and efficiency of *Arid1a* knockout in the uterus.

2.9. Cell line expansion and culture

A list of EOC cell lines used, their presumed histological subtype, origin, and growth requirements is provided in Table 2.2. All cell lines were certified as mycoplasma-free using the Mycoprobe mycoplasma detection kit (R&D Systems) by the CI Biorepository Core Facility and their identity confirmed using Short Tandem Repeat analysis. All cell lines, unless otherwise specified, were cultured at 37°C in a 21% O₂ / 5% CO₂ environment. After initial expansion using the media detailed in Table 2.2, cell lines were maintained in DMEM medium supplemented with 10% FBS, 50Un/ml penicillin and 50µg/ml streptomycin.

Additionally, a *TERT*-immortalized ovarian surface epithelium cell line, IOSE4, and a syngeneic HNF1B overexpressing clone (*HNF1B* introduced by lentiviral transduction), IOSE4+HNF1B, were kind gifts from Prof. Simon Gayther, University of Southern California, CA, USA. These were maintained in a 1:1 mix of MCDB105 and M199 media, supplemented with 15% FBS, 10 ng/ml EGF, 0.5 µg/ml hydrocortisone, 5 µg/ml insulin, 34 µg protein/ml BPE (Life Technologies), 50Un/ml penicillin and 50µg/ml streptomycin. Selection of IOSE4+HNF1B cells was maintained by the addition to the medium of 400ng/ml puromycin (Life Technologies).

2.9.1. Culture under hypoxia and glucose deprivation

For experiments under hypoxia, cell lines were cultured at 37°C in a 1% O₂ / 5% CO₂ environment. For glucose deprivation experiments, glucose-free DMEM was used (Gibco), still supplemented with 10% FBS, 50Un/ml penicillin and 50µg/ml streptomycin.

² Tamoxifen injections performed by Dr. Anna Nicholson, Winton Laboratory, CRUK CI

Table 2.2. Cell lines used in experiments

Cell line	Histologic Subtype	Growth requirements	Supplier	Catalogue Number	Consensus STR panel	% match	Pubmed id
SKOV3	Uncertain	RPMI + 10% FBS + P/S	Prof. Russell (University of Cambridge)	ATCC HTB-77	Nil	100%	833871
ES-2	CCC	McCoy's + 10% FBS + P/S	ATCC	ATCC CRL-1978	ATCC	100%	1717140
TOV21G	CCC	MCDB105: M199 1:1 mix + 5% FBS + P/S	Prof. Huntsman (BCCA)	ATCC CRL-11730	ATCC	100%	10949993
OV2008	CCC	RPMI + 10% FBS + P/S	Prof. Huntsman		ATCC	100%	
RMG-I	CCC	RPMI + 10% FBS + P/S	Prof. Huntsman	JRCB 0172	JRCB	92%	3154025
RMG-II	CCC	RPMI + 10% FBS + P/S	Prof. Huntsman	JRCB 0172.1	JRCB	92%	1715339
OVMANA	CCC	RPMI + 10% FBS + P/S	Archive	JRCB 1045	JRCB	100%	9328139
OVTOKO	CCC	RPMI + 10% FBS + P/S	Archive	JRCB 1048	JRCB	100%	7535723

OVSAYO	CCC	RPMI + 10% FBS + P/S	Archive	JRCB 1047	JRCB	100%	9328139
OVISE	CCC	RPMI + 10% FBS + P/S	Archive	JRCB 1043	JRCB	100%	7535723
JHOC-5	CCC	RPMI + 10% FBS + P/S	Prof. Huntsman	RCB 1520	RIKEN	100%	10695020
JHOC-7	CCC	RPMI + 10% FBS + P/S	Prof. Huntsman	RCB 1688	RIKEN	100%	
JHOC-9	CCC	RPMI + 10% FBS + P/S	Prof. Huntsman	RCB 2226	RIKEN	100%	
PEO1	HGS	RPMI + 10% FBS + P/S	Dr. Langdon (University of Edinburgh)		Nil	100%	3167863
TR-175	HGS	RPMI + 10% FBS + P/S	Archive		Nil	100%	3804493

List of cell lines acquired, expanded and used in this work. Histologic subtype refers to the commonly reported and/or accepted subtype. Questions regarding the provenance of some of these cell lines have been raised and are discussed where appropriate in the text. For SKOV3 and PEO1, no publicly available STR profiles are available; these lines were checked against the profile provided by the line donors. Pubmed id is provided where an original description of the cell line derivation could be found.

HGS: High-grade serous; CCC: clear cell cancer; BCCA: British Columbia Cancer Agency; ATCC: American Type Culture Collection; JCRB: Japanese Collection of Research Bioresources; P/S: penicillin + streptomycin

2.10. Immunofluorescence microscopy

Cells growing on coverslips, Ibidi chambers (Ibidi) or 0.4µm PET membranes were fixed with methanol at -20°C for 20 min. Blocking was performed in TBS with 0.1% Triton-X (Fisher Scientific), 2% BSA (Cell Signaling Technology) and 1-10% normal goat serum (Sigma-Aldrich) at room temperature (RT) for 60 min. Primary antibody incubation was performed overnight (16-18 hours) at 4°C. After washing with TBS containing 0.1% Triton-X, the samples were incubated with secondary antibody at RT for 60 min. Primary and secondary antibodies used are presented in Tables 2.3 and 2.4. The samples were washed again, incubated with 300nM DAPI (Life Technologies) at RT for 5 min, mounted using Prolong® Gold Antifade (Life Technologies) and kept at 4°C until imaging, which was performed on a Leica TCS SP5 confocal microscope (Leica). To visualise BrdU incorporation (see 2.5.5), after fixation, the samples were permeabilised with 1.5M HCl at RT for 30 min and 5% normal donkey serum (Sigma-Aldrich) was added to the blocking solution. SKOV3 cells served as positive controls for BrdU incorporation. In all experiments samples treated with primary but not secondary antibody and *vice versa* served as negative controls.

Table 2.3. List of primary antibodies used for immunofluorescence

Antibody	Clone	Species	Manufacturer (Cat no)	Dilution
Pan-cytokeratin (PE-conjugated)	C11-PE	Mouse	Santa-Cruz (sc-8018)	1:50-1:200
Desmin	Polyclonal	Rabbit	Abcam (ab8592)	1:100-1:500
Vimentin	EPR3776	Rabbit	Abcam (ab92547)	1:100
E-cadherin	34/E	Mouse	BD Biosciences (610405)	1:50-1:400
BrdU	Polyclonal	Sheep	Abcam (ab1893)	1:50-1:200

Table 2.4. List of secondary antibodies used for immunofluorescence

Antibody	Clone	Species	Manufacturer (Cat no)	Dilution
Anti-Rabbit IgG-FITC	Polyclonal	Goat	Sigma-Aldrich (F9887)	1:500-1:1000
Anti-Sheep IgG-DyLight650	Polyclonal	Donkey	Abcam (ab96942)	1:500-1:1000
Anti-Mouse IgG-AF488	Polyclonal	Goat	Life Technologies (A-11001)	1:1000
Anti-Rabbit IgG-AF555	Polyclonal	Goat	Life Technologies (A-21428)	1:1000

2.11. Uterine Fragment Viability Microscopy

Histological examination after fixation and paraffin embedding was the primary method used to ascertain tissue viability in the uterine fragment culture experiments (section 2.5). In order to obtain a faster read-out of tissue viability in culture, the LIVE/DEAD Viability/Cytotoxicity kit (Life Technologies) was used. Tissue fragments cultured in CellMatrix were washed with Dulbecco's-PBS (Sigma-Aldrich) 3 times and placed on a microscope slide. Components A (Calcein AM) and B (Ethidium homodimer-1) were added at 2 concentrations (2 μ M/4 μ M and 4 μ M/8 μ M respectively) and allowed to incubate for 40 min. The fragments were then examined under a Leica TCS SP5 confocal microscope with laser excitation as per the assay manufacturer's instructions.

2.12. Nucleic acid extraction, quantification and quality assessment

2.12.1. DNA extraction and quantification

DNA was extracted either from cell pellets or mouse ear punch biopsies (see section 2.1), using the DNeasy Blood & Tissue kit (Qiagen) and following the manufacturer's instructions. DNA quantification was performed using a NanoDrop 1000 spectrophotometer (Thermo Scientific).

2.12.2. RNA extraction

RNA was extracted from cell pellets using the RNeasy Mini Kit (Qiagen) and following the manufacturer's instructions. On-column DNase digestion was performed for the samples used in the gene expression arrays and RNA-seq experiments (see sections 2.17 and 2.18) but was not performed routinely in other samples. For RNA extraction from murine uterine samples, uterine horns were slit longitudinally, cut into ~5mm segments and placed in RNAlater (see section 2.3). The samples were then homogenized using 2.8mm ceramic beads on a Precellys-24 homogeniser (Precellys) for two 20-sec cycles at 6,000rpm. Extraction was completed using the RNeasy Mini Kit with on-column DNase digestion.

2.12.3. RNA quantification and quality assessment

To compare the performance of different platforms, uterine RNA was extracted from 24 mice and quantified using a Nanodrop 1000 Spectrophotometer, Qubit 2.0 Fluorometer (Life Technologies) or 2100 Bioanalyzer (Agilent). Means were compared using t-tests and the

Pearson product moment correlation coefficient r calculated. Day-to-day variability in Nanodrop quantification was assessed by comparing values obtained for the same samples on 2 different days. RNA quality was assessed using the 2100 Bioanalyzer to calculate RNA Integrity Number (RIN) values³. Only samples of acceptable quality were used in the gene expression array and RNA-seq experiments as detailed in sections 2.17 and 2.18.

2.13. Protein extraction and quantification

For protein extraction, cells were incubated with 200 μ l Lysis Buffer [50mM Tris pH 8.0, 150mM NaCl, 5mM EDTA, 0.5% Igepal and 2 tablets/100ml Complete EDTA-free protein inhibitor cocktail (Roche Diagnostics)], 0.2 μ l 100mM phenylmethanesulfonyl fluoride (Sigma-Aldrich), 0.2 μ l Phosphatase inhibitor cocktail 1 (Sigma-Aldrich) and 0.2 μ l Phosphatase inhibitor cocktail 2 (Sigma-Aldrich) on ice for 3 min, transferred to a 1.5ml tube and left on ice for 30 min. The lysate was syringed 4 times with a 25G needle, centrifuged at 17,000g for 3 min at 4°C and the pellet discarded. Protein quantification was carried out on a NanoDrop 1000 spectrophotometer and from February 2013 onwards on a Direct Detect infrared system (Millipore).

2.14. Immunoblotting and protein band intensity quantification

Protein separation was performed with the NuPAGE system (Life Technologies), using NuPAGE Novex 3-8% Tris-Acetate or 4-20% Tris-Glycine Gels (Life Technologies) in an XCell Sure Lock chamber (Life Technologies) according to the manufacturer's instructions. Tris-Acetate gels were used when assaying ARID1A and ARID1B; for all other proteins, Tris-Glycine gels were used. The HiMark® pre-stained protein standard (Life Technologies) and the Rainbow® molecular weight protein marker (Fisher Scientific) were used for protein size estimation with the Tris-Acetate and the Tris-Glycine gels respectively. For blotting, the XCell II Blot Module (Life Technologies) was used with the Immobilon FL PVDF Membrane (Millipore). Membranes were blocked in Odyssey Blocking Buffer (LI-COR) at RT for 60 min. Primary antibody incubation was performed overnight (16-18 hours) at 4°C with the antibodies listed in Table 2.5. For protein detection, the Odyssey Infrared Imaging System (LI-COR) and associated secondary antibodies (goat anti-mouse or anti-rabbit conjugated with either IR Dye

³ RIN is a robust measurement of RNA quality, derived from assessing the RNA electrophoregram and ranging from 0-10.

Table 2.5. List of primary antibodies used for immunoblotting

Antibody	Clone	Species	Manufacturer (Cat no)	Dilution
ARID1A	PSG3	Mouse	Santa Cruz (sc-32761)	1:1000
	Polyclonal	Rabbit	Sigma-Aldrich (HPA005456)	1:500
	AT1188a	Mouse	Abgent (discontinued)	1:1000
ARID1B	KMN1	Mouse	Santa Cruz (sc-32762)	1:500
	Polyclonal	Rabbit	Sigma-Aldrich (HPA016511)	1:300-1:1000
β-Catenin	6B3	Rabbit	Cell Signaling (#9582)	1:1000
Cdc2	P34	Mouse	Santa Cruz (sc-54)	1:1000
Cdc25C	5H9	Rabbit	Cell Signaling (#4688)	1:1000
Chk1	2G1D5	Mouse	Cell Signaling (#2360)	1:1000
Cyclin B1	V152	Mouse	Cell Signaling (#4135)	1:1000
E-cadherin	34/E	Mouse	BD Biosciences (610405)	1:150
GAPDH	14C10	Rabbit	Cell Signaling (#5014)	1:1000-1:5000
GLUT1	Polyclonal	Rabbit	Santa Cruz (sc-7903)	1:200
	Polyclonal	Rabbit	Abcam (ab15309)	1:100-1:300
GYS1	EP817Y	Rabbit	Abcam (ab40810)	1:1000
HIF1α	EP1215Y	Rabbit	Abcam (ab51608)	1:500-1:2000
HNF1B	Polyclonal	Rabbit	Sigma-Aldrich (HPA002083)	1:500-1:1000
IL6	Polyclonal	Rabbit	Abcam (ab6672)	1:500
IL6R	Polyclonal	Rabbit	Abcam (ab85105)	1:200
Nonphosphorylated β-Catenin	D13A1	Rabbit	Cell Signaling (#8814)	1:1000
PhosphoCdc2(Y15)	Polyclonal	Rabbit	Cell Signaling (#9111)	1:1000
PYGL	Polyclonal	Rabbit	Sigma-Aldrich (HPA000962)	1:500-1:1000
α-tubulin	DM1A	Mouse	Sigma-Aldrich (T6199)	1:5000

680 or IR Dye 800, 1:10,000) were used following the manufacturer's instructions. For protein band intensity quantification, the relevant bands were selected manually on the Odyssey

Imaging System, intensity was calculated using the manufacturer's software and normalized against the intensity of the GAPDH or tubulin loading control band.

2.15. Immunohistochemistry (IHC)

IHC assays were optimized manually in mouse uterine tissue for ARID1A (PSG3 and HPA005456 antibodies), ARID1B (KMN1) and PgR (HPA004751, Sigma-Aldrich). FFPE slides were de-waxed and rehydrated followed by heat-mediated antigen retrieval using either EDTA or Citrate pH 6.0 buffers for 20 min at 100°C. Endogenous peroxidase activity was quenched with 0.3% H₂O₂ in methanol for 20 min. The slides were then sequentially treated with 1% normal donkey serum (Sigma-Aldrich) for 30 min followed by the Vector Avidin/Biotin blocking kit (Vector Laboratories). For the PSG3 and KMN1 antibodies, which are raised in mouse, mouse IgG was then blocked using the Vector Mouse IgG blocking kit (Vector Laboratories) followed by application of the primary antibody (dilution range 1:50-1:400) for 60 min. Subsequently, secondary (and tertiary in the case of mouse primary) antibody incubation [rat anti-mouse and donkey anti-rat (Jackson Laboratories) for PSG3 and KMN1 and donkey anti-rabbit (Jackson Laboratories) for HPA005456 and HPA004751] was performed for 30 min at 1:250 dilution and the Vectastain ABC kit (Vector Laboratories) was applied for 30 min. Slides were then incubated with the DAB chromogen system (DAKO) for 2 min, washed and counter-stained with H&E. Cancer cell lines with ARID1A mutations served as negative controls for ARID1A staining and mouse spleen tissue for PgR staining. ARID1A/B staining is ubiquitous in normal tissues and therefore the stained uterine tissues served as internal positive controls. For PgR staining mouse mammary tissue served as positive control. In all cases, samples where the primary antibody incubation step was replaced with incubation in PBS only served as additional negative controls.

Following demonstration that the HPA00456 anti-ARID1A and the HPA004751 anti-PgR antibodies were performing satisfactorily, they were placed on the automated platform operated by the CI Histopathology Core Facility. Using this platform, de-waxing and rehydration are performed on a ST5020 Multistainer (Leica) and the blocking and staining on a Bond Max robot (Leica) using the Vector Biotin/Avidin and IgG blocking kits detailed above. Antigen retrieval is heat-mediated, using citrate pH 6.0 buffer for 20 min at 100°C. Post IHC dehydration and cleaning is again performed on a ST5020 Multistainer and a CV5030 Coverslipper (Leica) is used for mounting. Primary antibodies used in this project are summarized in Table 2.6. Secondary antibody incubation times and dilutions are identical to those detailed above for manual IHC staining.

Table 2.6. List of primary antibodies used for IHC

Antibody	Clone	Species	Manufacturer (Cat no)	Dilution
ARID1A	Polyclonal	Rabbit	Sigma-Aldrich (HPA005456)	1:200
Caspase-3	Polyclonal	Rabbit	R&D Systems (AF835)	1:100
Caspase-8	11B6	Mouse	Novocastra (NCL-CASP-8)	1:50
CD45	RA3-6B2	Mouse	R&D Systems (MAB1217)	1:2000
ER	6F11	Mouse	Novocastra (ER-6F11-L)	1:70
Ki67	TEC-3	Mouse	DAKO (M7249)	1:500
	Polyclonal	Rabbit	Bethyl Laboratories (IHC-00375)	1:1000
PgR	Polyclonal	Rabbit	Sigma-Aldrich (HPA004751)	1:200

2.15.1. Quantitative IHC analysis

Quantitative analysis of IHC staining for ARID1A, Ki67, ER and PgR was undertaken in the estrus-timed mouse uterus samples (see section 2.4). Stained slides were digitized and uploaded onto the eSlide Manager Platform (Aperio). Areas of interest encompassing the luminal and glandular epithelia as well as the uterine stroma were drawn, and an algorithm trained with the help of Dr. Will Howat, Head of the CI Histopathology Core Facility, to segment the epithelia from the stroma and subsequently to count and grade on a 0-3 scale all stained nuclei in each compartment. One transverse 5µm uterine section was analyzed for each mouse in its entirety, obviating the need for random sampling within each section. Two measurements were obtained for each antibody, in each of the 2 compartments (epithelium or stroma) and for each mouse: the percentage of positive cells, irrespective of intensity and an H-score calculated as $1 \times (\% \text{ cells staining } 1+) + 2 \times (\% \text{ cells staining } 2+) + 3 \times (\% \text{ cells staining } 3+)$. ANOVA and t-tests were used to compare percentages or H-scores and the Pearson product moment correlation coefficient r to examine correlations.

2.16. Quantitative Real Time Polymerase Chain Reaction (qRT-PCR)

qRT-PCR was used for relative quantification of RNA expression. Briefly, RNA was converted to cDNA using the TaqMan® Reverse Transcription Kit (Applied Biosystems) according to the manufacturer's instructions and with random hexamer (RH) primers. qRT-PCR was performed

using the TaqMan® Fast Advanced Master Mix (Applied Biosystems) and TaqMan® Gene Expression Assays with FAM dye labels for 40 cycles in a 7900HT Fast Real-Time PCR System (Applied Biosystems) according to the manufacturer's instructions. Table 2.7 lists all the TaqMan® Gene Expression Assays used. Relative expression of the RNA of interest was quantified using the $\Delta\Delta C_T$ method, where the amount of target RNA present is given by the formula $2^{-\Delta\Delta C_T}$ where $\Delta\Delta C_T$ is the difference in ΔC_T between samples. ΔC_T in turn is defined as the difference in cycle threshold between the transcript of interest and a reference transcript ($\Delta C_T = C_T \text{ Target} - C_T \text{ Reference}$). *GAPDH* was used as the reference transcript in experiments using cell line-derived samples.

2.16.1. Validation of qRT-PCR for mouse uterus samples

Formal validation of all the steps in RNA expression quantification was undertaken for mouse uterus samples in preparation for the estrus-timed mouse series experiment (see section 2.4).

Table 2.7. List of TaqMan Gene Expression Assays used

Gene	Species	Assay Number
ARID1A	Human	Hs00195664_m1
	Mouse	Mm00473838_m1
		Mm00473848_m1
		Mm00473841_m1
ARID1B	Human	Hs01128043_m1
	Mouse	Mm01338353_m1
ATF6	Human	Hs00232586_m1
CDH1	Human	Hs01023894_m1
CTNNB1	Human	Hs00355049_m1
GAPDH	Human	Hs02758991_g1
	Mouse	Mm99999915_g1
HIF1A	Human	Hs00153153_m1
Hmbs1	Mouse	Mm01143545_m1
HNF1B	Human	Hs01001602_m1
Hprt1	Mouse	Mm00446968_m1
HSP90B1	Human	Hs00427665_g1
HSPA5	Human	Hs00607129_gH
IL6	Human	Hs00985639_m1
IL6R	Human	Hs01075666_m1
Ltf	Mouse	Mm00434787_m1
PBRM1	Human	Hs00216838_m1
PDIA3	Human	Hs00607126_m1
Rpl32	Mouse	Mm02528467_g1
SLC2A1	Human	Hs00892681_m1
SMARCA2	Human	Hs01030846_m1
SMARCA4	Human	Hs00231324_m1
SNAI1	Human	Hs00195591_m1
XBP1	Human	Hs00231936_m1

First, as the transcripts of interest (*Arid1a*, *Arid1b*, *Ltf*) exhibit large differences in length, both oligo-dT and RH primers were tested and their relative efficiency for reverse transcription assessed. Then, for each TaqMan® Gene Expression Assay used, efficiency and the slope of ΔC_T vs. log input were calculated for 0.01-100ng input RNA, as relative quantification using the $\Delta\Delta C_T$ method requires that the PCR efficiency is similar for all transcripts of interest. A literature review was undertaken to identify putative housekeeping genes (HKG) for qRT-PCR normalisation in the mouse uterus and the performance of the selected genes assessed using the freely available NormFinder (Andersen et al. 2004) and BestKeeper (Pfaffl et al. 2004) algorithms.

2.17. Gene Expression Arrays

Gene expression arrays were performed using the BeadArray microarray platform (Illumina) by the CI Genomics Core Facility and initial analysis generating differentially expressed gene lists by the CI Bioinformatics Core Facility using the Bioconductor package on R (Gentleman et al. 2004). I performed the downstream analysis using MetaCore (www.portal.genego.com). Individual experiment details are provided below:

2.17.1. ARID1A expression arrays

ARID1A was knocked down using siRNA (see section 2.20.1 for knockdown details) in MEFs, IOSE4 and JHOC-5 cells. In MEFs, 3 cell lines derived from the same litter (E6, E8 and E9) were used as biological replicates. For IOSE4 and JHOC-5 cells, knockdown was performed independently in 3 flask replicates per cell line. Additionally, gene expression was analysed in 6 mouse uterus samples, all from late diestrus/early proestrus; 3 with high and 3 with low *Arid1a* expression. *ARID1A* knockdown efficiency was confirmed by qRT-PCR (see section 2.16). Mean *ARID1A* mRNA levels after knockdown were 71%, 49% and 75% lower in MEFs, IOSE4 and JHOC-5 cells respectively. Similarly the “low *Arid1a*” uterus samples had 73% lower *Arid1a* mRNA levels compared to the “high *Arid1a*” ones. In all cases, RNA was extracted using the RNeasy Mini Kit (see 2.12.2) and RNA quality was assessed by calculating the RIN value. RIN values ranged from 8.5-9.7, 9.7-10 and 6.8-9.4 in MEFs, IOSE4 and uterus samples respectively. RIN value was 10 for all JHOC-5 samples. Samples were run on MouseWG-9 v2.0 and HumanHT-12 v4.0 BeadChip arrays (Illumina) as appropriate and differentially expressed gene lists generated using false discovery rate (FDR) thresholds of 0.01 and 0.05.

Lists of *ARID1A*-regulated genes in the 4 experiments detailed above were compared using the Venny tool (<http://bioinfogp.cnb.csic.es/tools/venny/>) and overlapping genes were selected for further downstream analysis using MetaCore. To establish whether the lists showed a larger number of overlapping genes than expected by chance alone, representation factors and the corresponding p values were calculated using a calculator provided online (http://nemates.org/MA/progs/overlap_stats.html) by the Lund Laboratory, University of Kentucky, KY, USA.

2.17.2. *HNF1B* expression arrays

Lentiviral vectors were used to stably knock down *HNF1B* in JHOC-5 and TOV21G cells (see section 2.20.2 for details). Gene expression was compared between the JHOC-5 202 (non-target shRNA) and JHOC-5 577 and JHOC-5 583 (*HNF1B* shRNA) clones and between the TOV21G 202 (non-target shRNA) and TOV21G 578 and TOV21G 582 (*HNF1B* shRNA) clones. Four flask replicates for each clone were used for this experiment. Knockdown efficiency, as determined by qRT-PCR (see section 2.16) was 30%, 43%, 0% and 49% for JHOC-5 577, JHOC-5 583, TOV21G 578 and TOV21G 582 respectively at the time of RNA extraction, despite constant puromycin selection. RNA was extracted using the RNeasy Mini Kit (see 2.12.2) and RNA quality was assessed by calculating the RIN value; this ranged from 9.3-10. RNA expression was compared on a HumanHT-12 v4.0 BeadChip (Illumina), separately for each cell line. Differentially expressed gene lists at FDR 0.01 and 0.05 were generated for each knockdown clone compared to its respective non-target control. In accordance with the qRT-PCR results, the data generated by the arrays showed that only JHOC-5 583 and TOV21G 582 exhibited statistically significant reduction in *HNF1B* expression. Therefore, downstream analysis was performed for the gene lists generated by the JHOC-5 202 – JHOC-5 583 and TOV21G 202 – TOV21G 582 comparisons only. Additionally, differentially expressed gene lists from the 2 cell lines were compared using the tools described in section 2.17.1.

2.18. RNA sequencing (RNA-seq) in MEFs

RNA sequencing was performed in MEFs after siRNA *Arid1a* knockdown using the samples described in section 2.17.1. Library preparation was performed by the CI Genomics Core Facility using the TruSeq® RNA Sample Prep Kit-v2 (Illumina) according to the manufacturer's instructions; samples were pooled and run on a single lane on a HiSeq 2000 Sequencing System (Illumina). Single end reads were trimmed to 50 base pairs and aligned using Tophat

v.2.0.4 to the mouse genome v.GRCm38.68. Gene-level read counts were then carried out using HT-Seq-count v.0.5.3p9.

Differentially expressed gene lists at FDR 0.01 derived from the microarray (see section 2.17.1) and the RNA-seq analysis, were compared using the tools described in section 2.17.1. Genes that were concordantly up- or down-regulated in both the microarray and RNA-seq experiments underwent further downstream analysis using MetaCore.

2.19. Metabolic profile after *HNF1B* and *PYGL* knockdown

2.19.1. NMR medium and intracellular metabolites quantification

Medium and intracellular metabolites were quantified in JHOC-5 cells stably transfected with non-targeting shRNA (clone 202) or shRNA targeting *HNF1B* (clones 577 and 583) and in JHOC-5 and TOV21G cells treated with non-targeting or anti-*PYGL* siRNAs. In each experiment, 5×10^5 cells were plated in 100mm cell culture dishes in DMEM medium supplemented with 10% FBS, 50U/ml penicillin and 50 μ g/ml streptomycin. Three technical replicates were performed per sample. After 72 (shRNA-treated cells) or 96 (siRNA-treated cells) hours in culture, 600 μ l medium was aspirated and frozen at -80°C until analysis. Cells were then harvested, counted on a Vi-Cell XR counter, and incubated with 2ml ice-cold 6% perchloric acid for 10 min to extract their water-soluble intracellular metabolites (Madhu et al. 2006). Samples were neutralised to pH 7.0 with 10M KOH, lyophilised and stored at -80°C until analysis. For ^1H NMR analysis, cell extracts were re-suspended in 1 ml D_2O ⁴. 600 μ l of the sample (medium or cell extract) was taken in a 5mm Wilmad standard NMR tube (Sigma-Aldrich) and 10 μ l 10mM 4,4-dimethyl-4-silapentane-1-sulfonic acid (DSS) was added as an external standard. Additionally, 10 μ L 10mM TSP was added as external standard for the cell extract samples. ^1H NMR spectroscopy data was acquired on a 600 MHz Avance NMR spectrometer (Bruker). A water pre-saturation sequence with 128 averages, repetition time of 5 sec and 64K time domain data points was used. Pre-processing of the time domain data included exponential multiplication (line broadening 0.3 Hz), Fourier transformation, zero and first order phase correction. DSS was used for chemical shift calibration and metabolite quantification. Intracellular metabolite concentrations were estimated using the Chenomx Software package (Chenomx) and then normalized to the protein content in the cell sample, as determined using the Direct Detect infrared system. Metabolites in the medium were

⁴ All processing and analysis after the extraction step performed by Dr. Madhu Basetti, CRUK CI NMR Core Facility

measured as differences in concentration between fresh fully-supplemented and used medium and normalised to the number of cells at 72 or 96 hours as appropriate.

2.19.2. Quantitative lipid imaging after *PYGL* knockdown

PYGL was knocked down using siRNA as detailed in section 2.20.1 in JHOC-5 and TOV21G cells, in 3 replicates per cell line. Coherent Anti-Stokes Raman Scattering (CARS) imaging was performed by the CI Microscopy Core Facility. Briefly, a Chameleon Ultra Ti-sapphire laser (Coherent) was used to produce a pump beam ($\lambda=835\text{nm}$) with 100fs pulse duration and 80MHz repetition rate. 3W of the output power was used to generate a Stokes beam using a Levante optical parametric oscillator (OPO) (APE GmbH). To match the frequency for the CH_2 lipid vibrational mode (2845 cm^{-1}) the OPO was tuned to 1096nm whilst temporally overlaying the two beams using a delay stage. For spatial overlay and scanning, the galvanometer stage of a TriM Scope II (Lavision Biotec GmbH) was used. The overlaid beams were directed into a BX51 upright microscope (Olympus), from which the sample was excited and blue shifted CARS light detected (Steuwe et al. 2013). Highly CARS active voids were used as control samples for optimised CARS resonance. The laser power at the sample was 30 mW. Cells were washed with PBS, fixed in cold 4% PFA in PBS for 15 minutes, washed three times with PBS and kept in PBS at 4°C until CARS images were taken. Images were acquired randomly from 10 individual locations within the sample for each time point using a pixel dwell time of 30 μs , a scanning area of 75 μm x 75 μm and a pixel resolution of 500 x 500. The lipid droplets were observed as bright spots, which were quantified using an in-house code written in MATLAB (Mathworks); shot noise occurring in the images was smoothed out using average filtering and the number of pixels with intensities exceeding a threshold defined by the cellular CARS background (the dispersed CARS signal from the cells) were counted as previously described (Steuwe et al. 2013). The lipid area in pixels was measured in each image from the total area of cells. Lipid droplet content of non-target and *PYGL* siRNA treated cells were then compared using the paired samples t-test.

2.20. *In vitro* gene knockdown and knockout

2.20.1. siRNA-mediated knockdown

siRNA technology was used to knock-down transcripts of interest in cell lines (see section 2.9) and dissociated mouse uterine cells (see sections 2.5.5 and 2.6). Briefly, siRNA was resuspended in siRNA buffer (Thermo Scientific) to a final concentration of 20 μM . For transfection in 96-well plates, 0.125 μl siRNA and 0.2 μl DharmaFECT DF1 transfection reagent

(Thermo Scientific) were added to 19.675µl Opti-MEM medium (Gibco) and plated together with the appropriate number of cells suspended in 80µl medium, thus giving a final siRNA concentration of 25nM. siGENOME non targeting siRNA Pool 2 (Thermo Scientific) was used as a non-targeting control in all experiments. For experiments in 6-well plates, a scaling factor of 25 was used. For combined *ARID1A* and *ARID1B* knock-down experiments, each siRNA was used at a final concentration of 12.5nM for a total siRNA concentration in the experimental wells of 25nM. A list of targets and siRNAs used is provided in Table 2.8. Generally, ON-TARGETplus SMARTpool (Thermo Scientific), which consists of a pool of 4 different siRNAs was the preferred reagent; when one targeting the gene of interest was not available, Silencer Select (Life Technologies) products, consisting of a single siRNA each, were used instead. Following knockdown, samples were collected at 72 or 96 hours, unless otherwise specified, to ascertain the efficiency of knockdown by qRT-PCR (see 2.16) or immunoblots (see 2.14). Details of the assays performed after knockdown are provided in the relevant sections in this chapter.

2.20.2. Lentiviral-mediated shRNA *HNF1B* knockdown

TRC2-pLKO vectors (Sigma-Aldrich) carrying shRNA targeting *HNF1B* were packaged into lentiviruses by Ms. Mareike Wiedmann, Brenton Laboratory, CRUK CI. The following MISSION shRNA plasmids were used: TRCN0000255577 (referred to as “577”), TRCN0000255578 (“578”), TRCN0000255582 (“582”) and TRCN0000255583 (“583”). SHC202 (“202”) was used as a non-targeting control and SHC003, expressing TurboGFP, as a positive control for transfection efficiency (all from Sigma-Aldrich). Briefly, plasmids were expressed in *E. coli*, their identity confirmed by restriction digestion with PvuII and then packaged into lentiviruses in HEK293 cells using a 3rd generation packaging system (pMDL/pRRE, pRSV-REV, pVSG-V). The calculated viral titre was 2.3x10⁸ CFU/ml. JHOC-5 and TOV21G cells were infected at Multiplicity of Infection (MOI) 1.0 and underwent selection

Table 2.8. List of siRNA products used

Target	Species	Product	Supplier
ARID1A	Human	ON-TARGETplus SMARTpool	Thermo Scientific
	Mouse	ON-TARGETplus SMARTpool	Thermo Scientific
ARID1B	Human	ON-TARGETplus SMARTpool	Thermo Scientific
	Mouse	Silencer Select	Life Technologies
GYS1	Human	ON-TARGETplus SMARTpool	Thermo Scientific
HIF1A	Human	ON-TARGETplus SMARTpool	Thermo Scientific
HNF1B	Human	Silencer Select	Life Technologies
IL6R	Human	ON-TARGETplus SMARTpool	Thermo Scientific
PYGL	Human	Silencer Select	Life Technologies

with 1 µg/ml puromycin. Knockdown efficiency was determined by immunoblotting (see 2.14) after 7 days puromycin selection. Compared to cells transfected with clone 202, HNF1B levels were 2%, 92%, 18% and 0% using clones 577, 578, 582 and 583 in JHOC-5 cells; the corresponding values in TOV21G cells were 37%, 13%, 3% and 10% respectively. Details of the assays performed after knockdown are provided in the relevant sections in this chapter.

2.20.3. Lentiviral-mediated shRNA *Arid1a* knockdown

Lentiviruses carrying shRNA targeting *Arid1a* were prepared by Dr. Lorraine Levy, Brenton Laboratory, as described above (section 2.20.2). The *Arid1a*-targeting vectors used were: TRCN0000238303 (“303”), TRCN0000238304 (“304”) and TRCN0000238305 (“305”). SHC202 and SHC003 were used as non-targeting and transfection efficiency controls respectively. The calculated viral titre was 5.8×10^8 CFU/ml and 5 µl virus was used to knock down *Arid1a* expression in 2.5×10^4 E21 MEFs in 12-well plates for a sulforhodamine B (SRB) proliferation assay (see section 2.23.4).

2.21. ARID1A overexpression in SKOV3 cells

ARID1A was overexpressed in SKOV3 cells using a 129 kb BAC vector (Cat No: RP24-339K10, Life Technologies) and Lipofectamine 2000 transfection reagent (Life Technologies) according to the manufacturer’s instructions by Dr. Jian Xian, Brenton Laboratory. These cells were used in proliferation assays as detailed in section 2.23.4.

2.22. Glycogen metabolism inhibition

Glycogen phosphorylase was inhibited in PEO1, TOV21G, SKOV3, JHOC-5, JHOC-7, JHOC-9 and OVISE cells with R3401 (Sigma-Aldrich) at concentrations up to 150 µM and sc-203975 (Santa Cruz) at concentrations up to 10 µM with DMSO at the appropriate concentrations used as vehicle control. Additionally, PEO1, JHOC-5, TOV21G and SKOV3 cells were treated with 0.78-800 µM 1,4-Dideoxy-1,4-imino-D-arabinitol hydrochloride (DAB – Sigma-Aldrich) or 0.004-5 mM Metformin (Abcam) dissolved in water. Proliferation and glycogen assays were performed as detailed in sections 2.23.4 and 2.24.1.

2.23. Proliferation assays

2.23.1. Bromodeoxyuridine (BrdU) assay

The BrdU Cell Proliferation Assay Kit (Cell Signaling Technology) was used, following the manufacturer's instructions, to assess proliferation in dissociated mouse uterus stromal cells after *Arid1a* knockdown. Stromal cells from five 7-11-week-old CD-1 mice were prepared as described in section 2.5.5. From each mouse, stromal cells derived from a whole uterus ($115-185 \times 10^3$ in 5 different experiments) were divided equally into wells of a 96-well plate. After 2 days in culture, *Arid1a* or non-target siRNA was added (see 2.20.1) followed by hormonal manipulation 24 hours later as described in section 2.5.5. The final conditions, therefore were *Arid1a* or non-target siRNA treatment with no hormones, 10nM E₂ only, 1 μ M P₄ only or both hormones together; 3 technical replicates were performed for each condition. After a further 48 hours, BrdU was added according the Assay Kit instructions and BrdU incorporation was measured using a PHERAstar FS plate reader (BMG Labtech) 24 hours later. BrdU incorporation was compared between *Arid1a* knockdown and controls using the t-test, and among the different hormonal manipulations using ANOVA. In a further experiment, stromal cells from a single CD-1 mouse, treated as above, were incubated with BrdU for 15, 30, 60, 120 and 240 min to establish a time profile for BrdU incorporation.

2.23.2. Incucyte assay

The Incucyte kinetic imaging system (Essen BioScience) was used to assess proliferation after *Arid1a* knockdown using siRNA (see 2.20.1) in MEFs. Four MEF cell lines (E7, E8, E10 and E11) were used with 3 flask replicates per cell line. 8,000 cells were plated in each well of a 96-well plate together with *Arid1a* or non-targeting siRNA and images of the wells were taken every 3 hours for 7 days. Changes in proliferation, demonstrated by differences in the surface area of each well covered by cells, were analysed using the Incucyte software. An identical experiment was performed using 4 flask replicates of the RMG-I cell line. Two-way ANOVA with post-hoc t-tests were used to compare confluency.

2.23.3. Proliferation assessment using Vi-Cell

ES-2 (2×10^6), SKOV3 (1×10^6) and RMG-II (1×10^6) cells were cultured under normoxic (21% O₂) and hypoxic (1% O₂) conditions for 96 hours, at which point viable cell numbers were counted again using Vi-CELL XR. The experiment was repeated 4-6 times for each cell line and differences in proliferation were tested using a paired samples t-test.

2.23.4. Sulforhodamine B (SRB) assay

The SRB assay was the main assay used to assess proliferation in cell lines. The assay protocol has been previously published (Vichai & Kirtikara 2006). The cell lines listed in Table 2.2, IOSE4, IOSE4+HNF1B cells as well as MEFs were used, and changes in proliferation were assessed after manipulations such as culture under hypoxia and glucose deprivation (see section 2.9.1), siRNA (2.20.1) or shRNA (2.20.2) knockdown or treatment with PYGL inhibitors (2.22). In most experiments, 1,000 cells were plated per well in a 96-well plate, manipulated using one of the techniques above and allowed to proliferate for up to 168 hours. Plates were fixed at 168 hours and, sometimes, at intermediate time points, and after staining with SRB, optical density (OD) was determined at 510nm using the PHERAstar FS plate reader. Instances where the conditions differed from the above (e.g. different time points or seeding cell numbers) are highlighted in the relevant results sections where appropriate. The statistical significance of differences in proliferation was tested using the appropriate paired or unpaired t-tests.

2.23.5. Colony Forming Assay (CFA)

CFA was performed to further examine the effects of *PYGL* knockdown on proliferation. Briefly, siRNA was used to knock down *PYGL* in PEO1, SKOV3, JHOC-5 and TOV21G cells as described above (see 2.20.1). 72 hours after knockdown, the cells were plated in limiting dilutions (25,000→12,500→6,250→3,125→1,565→782) in 6-well plates and cultured under normal tissue culture conditions, hypoxia or glucose deprivation (see 2.9.1) for 14 days. The colonies were then fixed with 3.3% TCA and photographed on a GelCount scanner (Oxford Optronix). Quantification of proliferation was then performed using the SRB assay.

2.24. Glycogen assays

2.24.1. Colorimetric glycogen assay

A Glycogen Assay Kit (Abcam) which employs glucoamylase to break down glycogen into glucose with subsequent oxidation of the latter to produce a product that reacts with OxiRed probes to produce colour was used to measure the glycogen content of cell lines under experimental manipulations such as culture under hypoxia, glucose deprivation, *PYGL*, *GYS1*, *HIF1a*, *IL6R* siRNA knockdown or treatment with *PYGL* inhibitors. PEO1, TOV21G, SKOV3, JHOC-5, JHOC-7, JHOC-9, OVISE, IOSE4 and IOSE4+HNF1B cells were cultured under normal conditions, hypoxia or glucose deprivation (see 2.9.1) and glycogen content per 1×10^5

cells was assessed at various time points following the kit's instructions. In experiments involving siRNA knockdown, due to the limited number of cells available, the assay was performed using all available cells and then normalised to the cell count as determined by using the Countess® Cell Counter (Life Technologies). In all assays, wells containing buffer only served as negative controls and wells with sample but no hydrolysis enzymes were used to correct for background glucose content.

2.24.2. PAS and PAS-Diastase staining

PAS and PAS-Diastase staining was performed by the CI Histopathology Core Facility to assess glycogen content under normal culture conditions in PEO1, SKOV3, TOV21G and JHOC-5 cell pellets, following fixation with 10% NBF and embedding in paraffin. It was also performed on TOV21G, SKOV3 and JHOC-5 cell pellets 96 hours after *PYGL* siRNA knockdown (see 2.20.1) under normal culture conditions.

2.25. Interleukin 6 (IL6) assay

IL6 secretion in culture medium was quantified using the Human IL-6 ELISA Ready-SET-Go!® kit (Affymetrix eBioscience). Briefly, 8×10^5 PEO1, TOV21G, SKOV3, JHOC-5, JHOC-7, JHOC-9 and OVISE cells were plated in 60mm dishes in 4ml medium. After 72 hours, the cells were counted, the medium collected and IL6 content quantified following the kit instructions. Results were normalised to cell number and medium volume.

2.26. Reactive Oxygen Species (ROS) assay

The generation of ROS after *PYGL* siRNA knockdown was assayed with the DCFDA Cellular Reactive Oxygen Species Detection Assay Kit (Abcam) according to the manufacturer's instructions. Briefly, 72 hours after non-target or *PYGL* siRNA treatment (see 2.20.1 for details), 25×10^3 JHOC-5 and TOV21G cells were plated per well in dark-sided, clear-bottomed 96-well plates (Corning) and allowed to adhere overnight. The following morning, the cells were fixed using 25µM DCFDA for 45 min at 37°C and fluorescence measured with a PHERAstar FS plate reader at Ex485/Em520nm. Each experiment was repeated 4 times.

2.27. Terminal deoxynucleotidyl transferase dUTP nick end labelling (TUNEL) assay

The TUNEL assay was performed by the CI Histopathology Core Facility to assess apoptosis 96 hours after *PYGL* siRNA knockdown (see 2.20.1) in TOV21G, SKOV3 and JHOC-5 cells. The DeadEnd Colorimetric TUNEL System (Promega) was used according to the manufacturer's instructions but with the biotinylated nucleotide mix used at 1:1,000 dilution and the wash steps adapted to the requirements of the Bond automated systems. Appropriate positive and negative controls were used with each run following the facility's SOPs.

2.28. Senescence assay

The Senescence Cells Histochemical Staining Kit (Sigma-Aldrich) was used to assess senescence after *PYGL* siRNA knockdown in PEO1, TOV21G, SKOV3 and JHOC-5 cells (see 2.20.1). 5×10^4 cells were plated in each well of 12-well plates, siRNA was added and the cells left in culture for 168 hours before being fixed and stained as per the kit's instructions. The cells were imaged 3 and 24 hours after X-gal staining.

2.29. Cell cycle phase analysis

The cell cycle phase distribution after *PYGL* siRNA knockdown (see 2.20.1) was assessed. Briefly, 2.5×10^5 TOV21G, SKOV3 and JHOC-5 cells were plated in 6-well plates and *PYGL* or non-target siRNA added. After 72 hours, the medium was replaced by FBS-free medium for 24 hours to effect a G₁ block. Following 24 hours of serum starvation, the medium was changed again to DMEM with 10% FBS and cells fixed using ice-cold 70% ethanol at 0, 4, 8 and 24 hours. The pellets were then frozen at -20°C until analysis. For analysis, the pellets were resuspended in 500µl PBS and 20µg/ml propidium iodide added. The samples were run on a FACSCalibur flow cytometer (BD Biosciences) and analysed using the FlowJo X software (Tree Star) with manual gating. There was no difference in the cell cycle phase distribution across the time points in each treatment condition, meaning that 24 hours of serum starvation failed to induce cell cycle arrest. Therefore the 4 time points were treated as flask replicates in the analysis.

2.30. Migration and invasion assays

For the migration assay, 72 hours after non-target or *HNF1B* siRNA treatment, 1×10^4 JHOC-5 and TOV21G cells, as well as untreated IOSE4 and IOSE4+HNF1B cells, were plated per well in ImageLock 96-well plates (Essen Bioscience) and allowed to proliferate until they were confluent. The plates were then scratched using a WoundMaker (Essen Bioscience) and the plates were imaged every 3 hours on an Incucyte kinetic imaging system. Wound width was analysed using the device's software. The assay was performed using 4 biological replicates per condition run in technical triplicates.

Two different invasion assays were performed. In the first, 3×10^4 JHOC-5 and TOV21G cells treated as above were suspended in 300 μ l medium without FBS and placed in Matrigel-coated 8 μ m invasion chambers (BD Biosciences) in 24-well plates. 800 μ l fully supplemented medium on the bottom of the wells was used as chemo-attractant. After 24 hours, cells adherent to the insert face of the membrane were removed using a cotton bud and the membranes were fixed in 3.3% TCA and stained with SRB. Invading cells were then counted manually on a microscope. The assay was performed using 4 biological replicates per cell line. The second assay used was the CultreCoat® 96-Well BME-Coated Cell Invasion Optimization Assay (Trevigen) following the manufacturer's instructions. Briefly, 72 hours after siRNA-mediated *HNF1B*-knockdown, 25×10^3 JHOC-5 and TOV21G cells in a final volume of 50 μ l serum-free medium were transferred to invasion chambers with high, medium, low or no basement membrane extract (BME) coating. 150 μ l fully supplemented medium was added to the bottom chambers. After 24 hours, cells still in the top chambers were washed away and the chambers transferred to an opaque 96-well receiving plate. Calcein AM/Dissociation solution was added to remove invading cells from the membrane and cells were quantified on a PHERAstar FS plate reader at Ex485/Em520nm. The assay was performed using 4 biological replicates run in technical triplicates.

2.31. Proteomics analysis

Proteomics analysis was undertaken in JHOC-5 and TOV21G cells following siRNA *PYGL* knockdown. 1×10^6 cells were plated in 60mm tissue culture plates and treated with non-target or *PYGL* siRNA in 3 independent experiments. After 72 hours, cells were lysed with 250 μ l Urea buffer (9M urea + 20mM HEPES pH8.0) and flash-frozen in a dry ice / ethanol bath. Samples were shipped to Prof. Moran's Laboratory (Hospital for Sick Children, Toronto, ON, Canada) where they were processed and analysed as previously described (W. Zhang et al. 2014).

Briefly, the samples were treated with DTT and iodoacetamide, followed by trypsin digestion and purified in a Pierce C18 spin column (Thermo Scientific). Eluted peptides were then run on an Orbitrap Elite Mass Spectrometer (Thermo Fisher Scientific). Data were analysed with MaxQuant (www.maxquant.org) and Perseus software (www.perseus-framework.org) and FDR-corrected differentially expressed protein lists created. I then performed further downstream analysis using the Scaffold (www.proteomesoftware.com/products/scaffold/) and MetaCore tools.

2.32. Statistical analysis

Graphpad Prism 6.0 (GraphPad) and Excel 2010 (Microsoft) were used to summarise data and perform statistical analysis. Descriptive statistics were used to summarise data and proportions were compared using the χ^2 or Fisher's exact test as appropriate. Paired or unpaired t-tests and ANOVA were used to compare outcomes measured on continuous scales. The bioinformatics analysis was performed by the CI Bioinformatics Core Facility using Bioconductor packages on R. In all graphs, "*" denotes $0.01 < p \leq 0.05$, "**" denotes $0.001 < p \leq 0.01$ and "***" $p \leq 0.0001$.

3. MOUSE UTERUS ASSAY DEVELOPMENT

3.1. Introduction

Epithelial-stromal interactions are important for oestrogen-mediated responses in the normal uterus with oestrogen-induced epithelial proliferation being controlled by stromal ER through paracrine mechanisms (Cooke et al. 1997; Cunha et al. 2004). Establishing an *in vitro* uterine fragment culture system that maintains normal hormonal regulation and allows genetic manipulation would be extremely useful for the study of early events in the pathogenesis of potentially uterus-originating cancers. Insights gained from such a system could then be applied *in vivo* in order to eventually create a GEMM of OCCC. In this initial part of my project, I attempted to set up such a system and I also selected and validated the reagents and techniques used in assessing *Arid1a*-driven transcriptional programmes in the uterus.

3.2. Cultured murine uterine fragments show poor viability

Four conceptually related techniques were used to establish *in vitro* cultures of uterine fragments: the “coin”, “CellMatrix”, “Surgispon” and “Vibratome” methods (Fig. 3.1). I first attempted to replicate the “coin” culture system described by Newbold *et al* (1994) that shows epithelial proliferation in the cultured uterine fragments in response to DES. Multiple fragments were cultured from each of 5 mice using DMEM/F12, BME or FAD medium with or without Matrigel coating of the culture dishes to provide support and DES, as detailed in Table 3.1. After 5-6 days in culture, the fragments were fixed and stained with H&E to assess viability. In all cases there was extensive necrosis with only a rim of viable tissue in the periphery and scattered cells in the middle of the “coin” (Fig. 3.2B-D, compare with the immediately fixed, non-cultured uterine section in Fig. 3.2A).

Poor nutrient and oxygen diffusion to the centre of the fragment could be an explanation for the results observed above. Therefore, I subsequently used the “CellMatrix” intestinal organoid culture method reported by Ootani *et al* (2009). Using this method, medium diffuses through the collagen layer from below, allowing an air-tissue interface, and consequently oxygenation, to be maintained (Fig. 3.1). Multiple fragments were cultured from each of 16 mice using DMEM, RPMI 1640, BME or FAD media with or without DES (Table 3.1). After 6 to 15 days in culture, the fragments were fixed and stained with H&E to assess viability. Again,

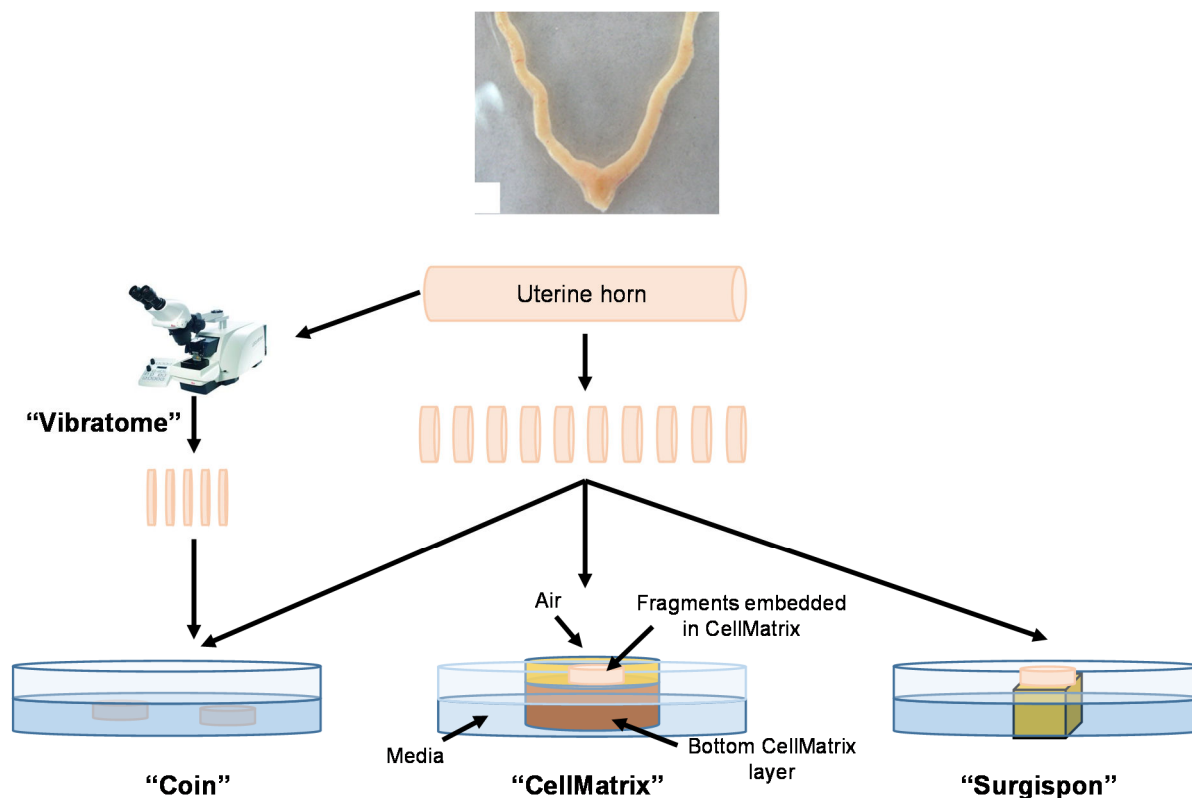


Figure 3.1. Murine uterine fragment culture techniques

Schematic diagram illustrating the four uterine fragment culture techniques. The mouse uterus picture is from Zhang et al (2008).

there was extensive necrosis with loss of tissue architecture (Fig. 3.2E-F, J), although, for some fragments, viability appeared better compared with the “coin” method.

A recent publication reported on the ability to culture *ex vivo* prostatic cancer tissue using a pre-soaked gelatin sponge to provide tissue support (Centenera et al. 2012). I therefore tried this method, using “Surgispon” sponges, to culture uterine fragments from a single mouse in RPMI 1640 medium (Table 3.1). After 6 days in culture the sponge had started to disintegrate and viability remained poor (Fig. 3.2G).

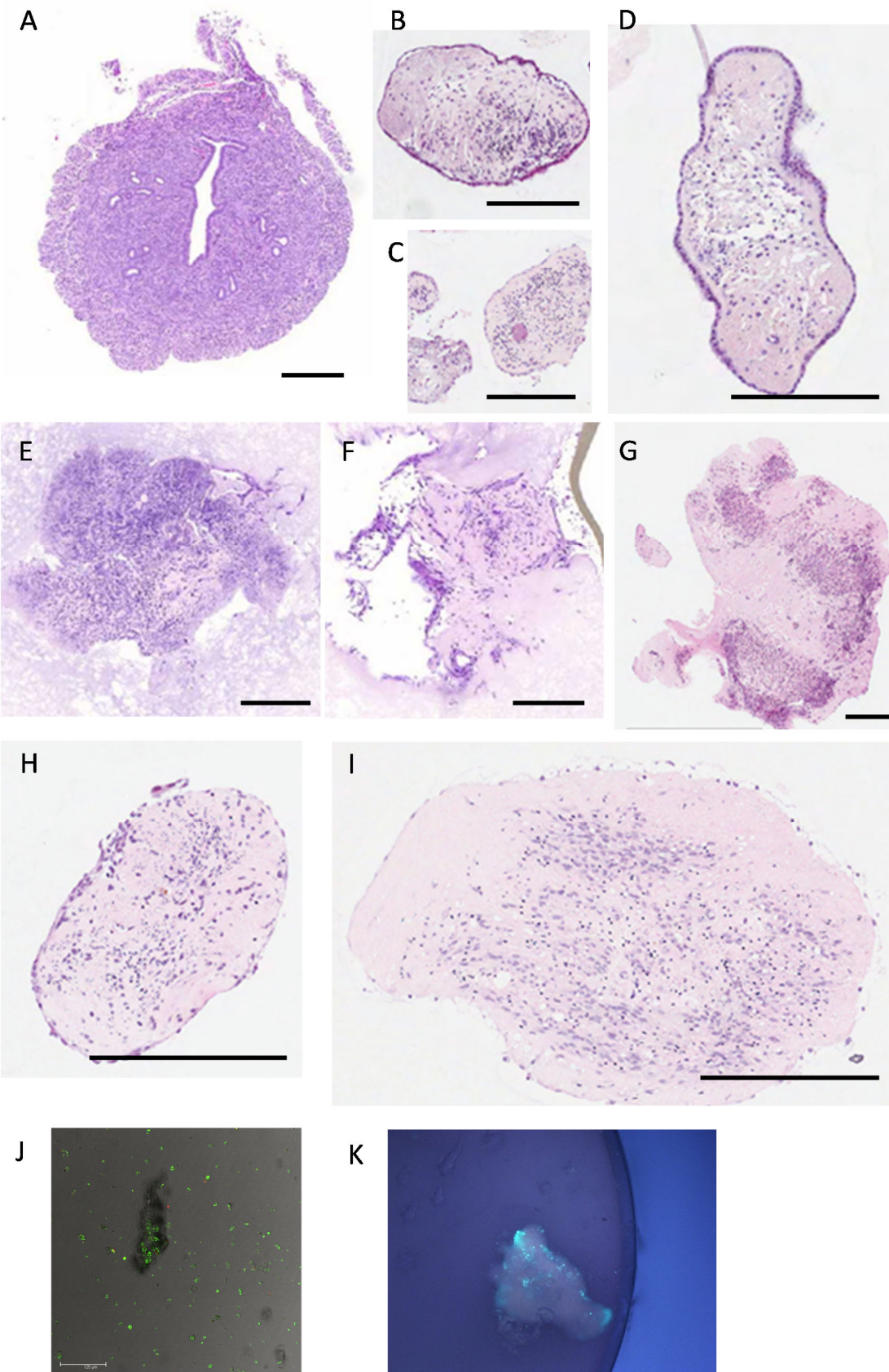
To address the concern that excessive thickness of the manually cut fragments contributed to their poor viability, I used a Leica Vibratome to cut thick (100-200 μ m) sections from just harvested, agarose-embedded uteruses. Sections from 4 mice were subsequently cultured using DMEM, DMEM/F12, RPMI and McCoy’s media for 6-8 days (Table 3.1). H&E staining revealed that viability remained poor with loss of tissue architecture (Fig. 3.2H-I), an

Table 3.1. Culture of murine uterine fragments

Experiment	Strain	Age (weeks)	Fragment preparation technique	Culture Conditions	Time in culture (days)
01	B6	8	Coin	DMEM/F12 +/- DES	5
02	B6	8	Coin	DMEM/F12 +/- DES	5
				Matrigel + DMEM/F12 +/- DES	5
03	B6	12	Coin	BME	5
				FAD	5
04	CD-1	12	Coin	BME	5
				FAD	5
05	CD-1	3	Coin	BME	6
				FAD	6
06	CD-1 (2 mice)	3	CellMatrix	DMEM	12
				BME	12
				RPMI 1640	12
07	CD-1 (3 mice)	3	CellMatrix	BME +/- DES	9
				RPMI 1640 +/- DES	9
				DMEM +/- DES	9
08	B6 (4 mice)	3	CellMatrix	BME +/- DES	7, 15
				RPMI +/- DES	7, 15
09	B6	8	CellMatrix	BME +/- DES	8
10	B6	8	CellMatrix	RPMI 1640	6
11	CD-1	8	CellMatrix	RPMI 1640	6
12	B6	8	CellMatrix	RPMI 1640	8
13	CD-1	8	CellMatrix	RPMI 1640	8
14	CD-1 (2 mice)	3	CellMatrix	BME	6
				FAD	6
15	CD-1	11	Surgispon	RPMI 1640	6
16	CD-1	11	Vibratome	RPMI 1640	7
17	CD-1	8	Vibratome	DMEM	6
				DMEM/F12	6
				McCoy's	6
				RPMI 1640	6
18	CD-1	8	Vibratome	DMEM	7
19	CD-1	15	Vibratome	DMEM	7

B6: C57BL/6; Culture media composition detailed in section 2.5. Multiple fragments were cut from each uterine horn.

observation supported by IHC for ARID1A that showed only few scattered positive cells (data not shown).



Taking all the results together, there were no observed differences in viability according to the mouse strain (CD-1 or B6), mouse age (range 3-15 weeks), use of Matrigel or CellMatrix support, type of medium used or the addition of DES. Because of the poor viability exhibited in these experiments, further development of the method to *in vitro* assay the effects of *Arid1a* knockdown was abandoned. This decision was informed by a further experiment, where treatment of 150µm uterine sections from a homozygote *Arid1a^{fl/fl}* mouse, prepared with the Vibratome method, in wells of a 96-well plate with 0.5×10^6 - 1×10^8 PFUs of Ad-Cre-IRES-GFP adenovirus showed only patchy, peripheral transfection after 24 hours incubation (Fig. 3.2K). This suggests that even if the fragment viability problems were overcome, *in vitro* *Arid1a* knockout was likely to be technically and financially unsustainable and it would be preferable to ablate *Arid1a* *in vivo*.

3.3. Culture of dissociated murine uterine cells

3.3.1. Non-adjacent co-culture of dissociated uterine cells does not replicate normal hormonal regulation

In view of the poor viability of uterine fragments in culture, I investigated alternative *in vitro* assays that replicate the *in vivo* epithelial-stromal interactions. Relevant to this, a co-culture method of dissociated uterine cells that utilises tissues from pseudo-pregnant CD-1 mice was recently published (Chung & Das 2011). This method reportedly maintains the normal epithelial-stromal interactions as evidenced by proliferation, detected by BrdU incorporation, of the epithelial cells in response to E₂ and of the stromal cells in response to combined E₂ and P₄ treatment (Chung & Das 2011). Unfortunately, the publication did not contain the dissociation protocol and it referenced an irrelevant previous publication in its methods section. A version of the protocol was obtained after contacting the authors but it contained

Figure 3.2. Culture of murine uterine fragments

A) Uterine section from an 8-week-old B6 mouse (not cultured). B-I) Murine uterine fragments cultured as indicated (H&E stains): B) 3-week-old CD-1, prepared with the “coin” method, in culture for 6 days with BME medium. C) 12-week-old B6, prepared with the “coin” method, in culture for 5 days with BME medium. D) 12-week-old CD-1, prepared with the “coin” method, in culture for 5 days with FAD medium. E) 8-week-old B6, prepared with the “CellMatrix” method, in culture for 8 days with RPMI 1640 medium. F) 8-week-old CD-1, prepared with the “CellMatrix” method, in culture for 8 days with RPMI 1640 medium. G) 11-week-old CD-1, prepared with the “Surgispon” method, in culture for 6 days with RPMI 1640 medium. H) 8-week-old CD-1, prepared with the “Vibratome” method, in culture for 7 days with DMEM medium. I) 8-week-old CD-1, prepared with the “Vibratome” method, in culture for 6 days with RPMI 1640 medium. J) LIVE/DEAD Viability Kit staining showing viable (green) and dead (red) cells in tissue fragments from an 8-week-old B6, prepared with the “CellMatrix” method, in culture for 8 days with BME medium. K) Photomicrograph of a 150µm section from an *Arid1a^{fl/fl}* mouse, prepared with the “Vibratome” method and cultured for 24 hours in the presence of 10^8 PFUs of Ad-Cre-IRES-GFP adenovirus (bar=300µm).

fundamental errors, as detailed in section 2.5.5. Eventually, the protocol was optimised and reliable separation of cytokeratin-positive, desmin-negative epithelial (Fig. 3.3A-C) and cytokeratin-negative, desmin-positive stromal cells (Fig. 3.3D-F) was achieved. SKOV3 cells were, as expected, cytokeratin-positive and desmin-negative (Fig. 3.3G-I), showing the specificity of the immunofluorescence staining protocol, which was further supported by the absence of fluorescence when primary antibodies were omitted in control slides (data not shown). Additionally, SKOV3 cells showed extensive BrdU incorporation (Fig. 3.3J),

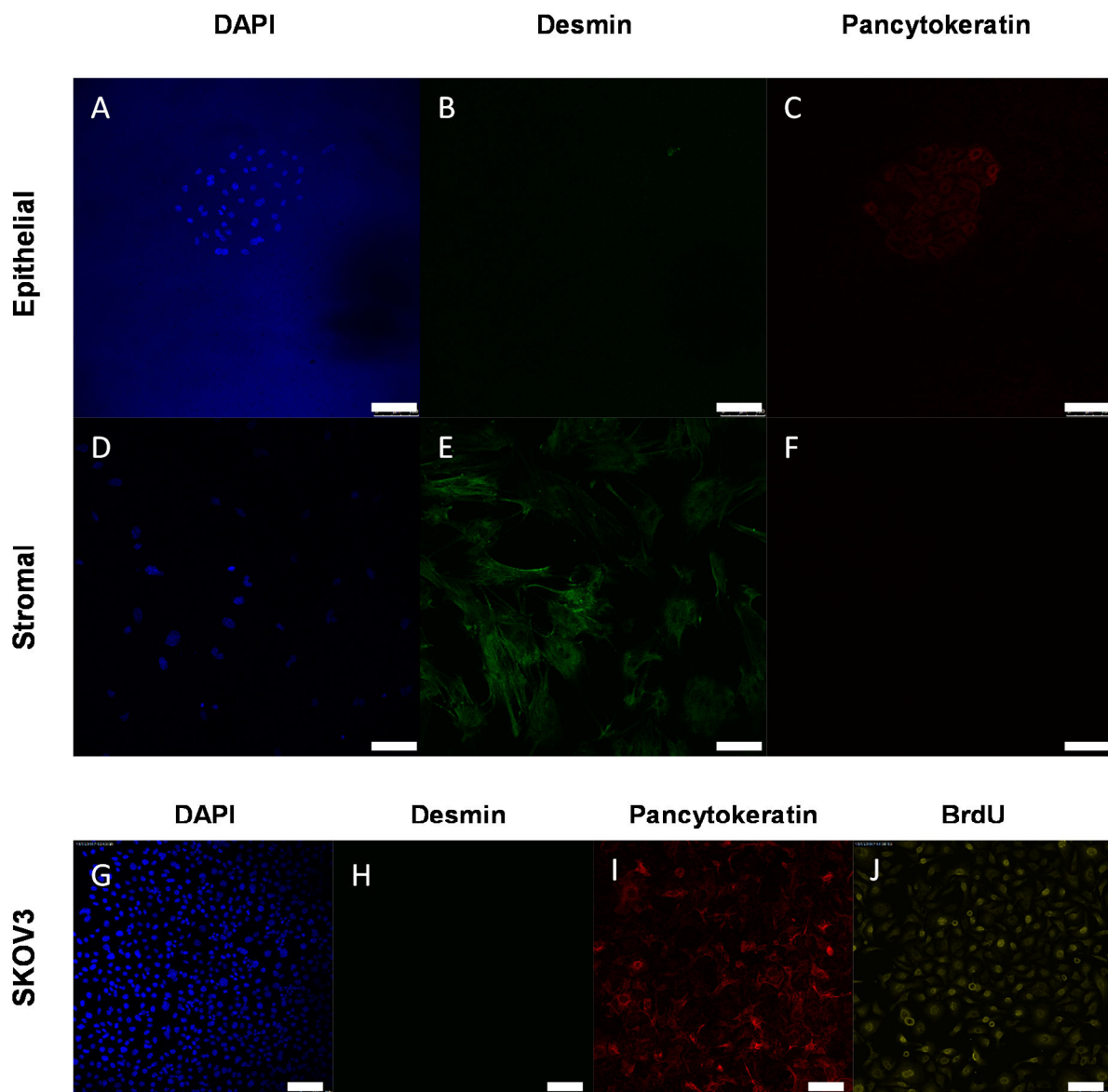


Figure 3.3. Dissociation of epithelial and stromal uterine cells

A-C) Epithelial cells in cell culture inserts demonstrating positive DAPI (A) and pancytokeratin (C) and negative desmin (B) staining. D-F) Stromal cells cultured on coverslips demonstrating positive DAPI (D) and desmin (E) and negative pancytokeratin (F) staining. G-J) SKOV3 cells demonstrating positive DAPI (G) and pancytokeratin (I), negative desmin (H) staining and BrdU incorporation (J). The increased background in (A) is due to DAPI-induced fluorescence in the cell culture insert membrane (bar=100 μ m).

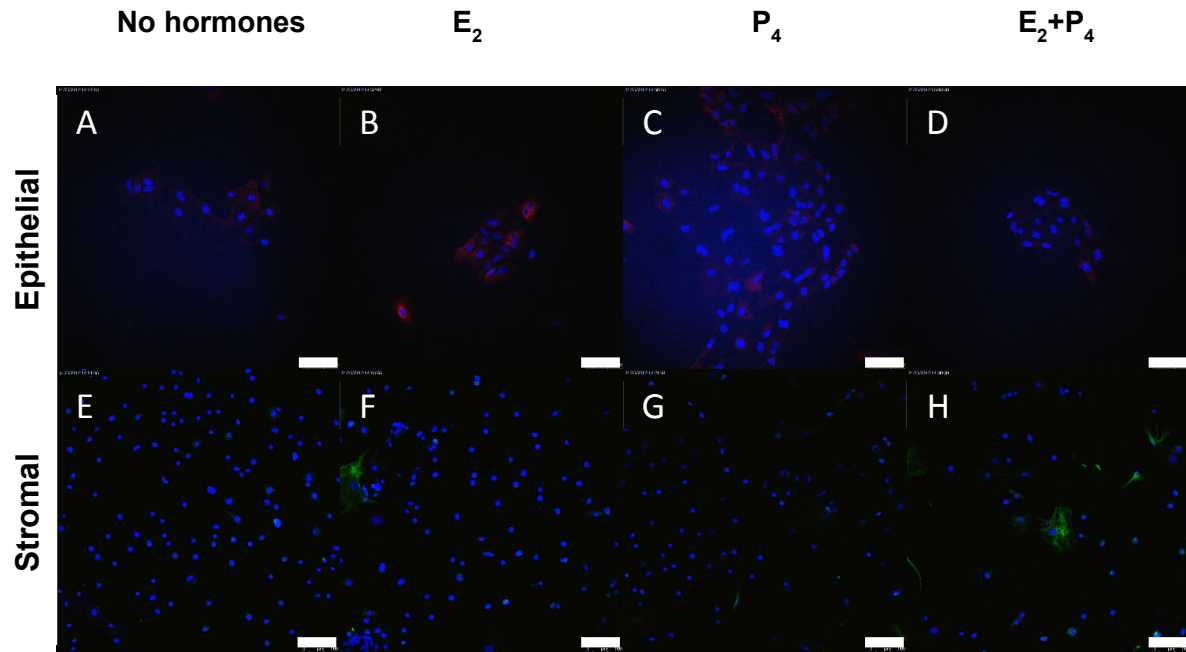


Figure 3.4. BrdU incorporation in co-cultured dissociated uterine cells

A-D) Composite images showing no BrdU incorporation in epithelial cells under baseline conditions (A), treatment with 10nM E₂ (B), 1μM P₄ (C) or both E₂ and P₄ (D). E-H) Composite images showing no BrdU incorporation in stromal cells under baseline conditions (E), treatment with 10nM E₂ (F), 1μM P₄ (G) or both E₂ and P₄ (H). I) Composite image showing BrdU incorporation in SKOV3 cells. Note that the HCl treatment necessary for BrdU immunofluorescent staining interferes with, resulting in attenuation of, the pancytokeratin and particularly the desmin stains (bar=100μm).

confirming the successful optimisation of the BrdU staining protocol. However, in 3 separate experiments, no BrdU incorporation was seen in either the epithelial or the stromal cells, irrespective of hormonal treatment (Fig. 3.4). Thus, I could not replicate the original publication (Chung & Das 2011). Whether this is because of subtle differences in the dissociation protocol is presently uncertain. Therefore, the co-culture system could not be used as a substitute for uterine fragments in order to *in vitro* ablate *Arid1a* while maintaining hormonal regulation.

3.3.2. Culture of dissociated uterine epithelial and stromal cells shows poor cell yields

Even without replicating the epithelial-stromal interactions, primary cultures of dissociated epithelial and stromal uterine cells could still be a valuable experimental resource. Therefore, I initially dissociated harvested uteri using collagenase I (Ouellette et al. 1999). Cells from one uterus were split into 9 wells of a 12-well plate and cultured in DMEM/F12 medium, with or without Matrigel and DES. This protocol showed low cell yields with no evident proliferation as

cell numbers did not increase between 10 and 32 days in culture. At all timepoints, total live cell counts were between 500 and 15000 cells, with more live cells in Matrigel-coated wells but overall viability being poor at 25-72% (mean 55%). Next, I tried a dispase-collagenase-trypsin method, as reported by Campbell et al (2006). Cells were cultured in DMEM/F12, McCoy's or BME media, with or without Matrigel and DES. Despite plating 37500 epithelial and 67500 stromal cells per well, less than 5000 cells remained viable after 7 days in culture as assayed using the Vi-CELL counter. Viability was not improved when, in a separate experiment, irradiated 3T3 fibroblasts were used to provide stromal support (data not shown).

3.4. Assays of gene expression in the mouse uterus

3.4.1. RNA quantification and quality assessment

Uterine RNA was extracted from 24 estrus-timed mice and quantified using the Nanodrop, Qubit and Bioanalyzer platforms (Table 3.2). There was excellent correlation between the Nanodrop and Qubit measurements ($r=0.85$, $p<0.0001$) but not between the Nanodrop and the Bioanalyser ($r=0.36$, $p=0.08$) or the Bioanalyzer and Qubit ($r=0.35$, $p=0.1$). Repeating the Nanodrop quantification on a different day showed excellent test-retest correlation ($r=0.97$, $p<0.0001$), although there was some variability in the absolute recorded concentrations (mean difference between samples 14.5%). As is evident from Table 3.2, despite the excellent correlation between Nanodrop and Qubit, there were large differences in the absolute RNA concentration as assayed with these two platforms. Mean calculated RNA concentration was 358ng/ μ l using Nanodrop and 1684ng/ μ l using Qubit ($p<0.0001$). As the ultimate purpose of the assay was to study changes in *Arid1a* expression across samples, accurate relative quantification is more important, in order to ensure similar input RNA quantities for all samples in the qRT-PCR reactions. Therefore, for most experiments, I elected to proceed with the more conservative Nanodrop quantification, using the mean of 2 measurements on different days. However, Qubit was used for quantification of samples submitted for RNA-seq to conform to institutional SOPs.

3.4.2. Validation of qRT-PCR assay steps for mouse uterus samples

Formal validation of all steps in RNA expression quantification was undertaken for mouse uterus samples in preparation for the estrus-timed mouse series experiment (see section 4.2). Using RH, compared to oligo-dTs, reverse transcription for *Arid1a* and *Arid1b* was more efficient with lower Ct at qRT-PCR (e.g. for 100ng input RNA mean *Arid1a* Ct with RH was 21.8 vs. 26.9 with oligo-dTs, $n=6$). Also, using RH but not oligo-dTs, PCR efficiencies were

Table 3.2. RNA quantification using Nanodrop, Bioanalyzer and Qubit

Mouse ID	Nanodrop 1 (ng/ μ l)	Nanodrop 2 (ng/ μ l)	Qubit (ng/ μ l)	Bioanalyzer (ng/ μ l)
101	91	187	494	366
102	469	448	577	720
103	360	300	492	504
104	328	282	741	528
105	294	260	757	366
106	101	206	801	312
107	457	459	2984	714
108	333	207	1212	348
109	121	120	532	186
110	227	259	1484	546
111	430	414	2672	690
112	456	448	2832	840
113	548	537	2920	762
114	844	771	4224	786
115	302	293	1194	342
116	599	601	3256	672
117	315	309	1530	2178
118	219	219	775	240
119	455	458	2720	534
120	104	99	446	132
121	213	209	573	312
122	553	561	2992	570
123	346	361	1582	414
124	424	413	2616	486

Nanodrop 1 and 2 refer to 2 measurements, performed on different days. The Nanodrop 1 value was used for the calculation of correlation co-efficient with Qubit and Bioanalyzer as described in the text.

within 10% of those of the putative HKGs (Table 3.3) and the slopes of Δ Ct vs. log input were acceptable (all <0.1), thus fulfilling the manufacturer-suggested constraints. Three different *Arid1a* expression assays were tested. Mm00473838_m1 resulted in very poor amplification with Ct values >32 and was discarded. Both Mm00473848_m1 and Mm00473841_m1 were acceptable with similar PCR efficiencies (Table 3.3) and resulting Ct values. Mm00473841_m1 was used in all subsequent experiments.

There is a paucity of publications regarding appropriate HKGs for qRT-PCR normalisation in the mouse uterus, although *Gapdh* is most commonly used for this purpose. After a literature review encompassing studies in mice (Schroder et al. 2009), humans (Vestergaard et al. 2011), horses (Kayis et al. 2011) and pregnant pigs (S. Wang et al. 2011), 4 putative HKGs

Table 3.3. PCR efficiency for TaqMan expression assays

Expression assay	Random Hexamers	Oligo-dTs
<i>Gapdh</i>	98.1%	100.4%
<i>Rpl32</i>	89.7%	93.8%
<i>Hprt1</i>	96.8%	97.3%
<i>Hmbs</i>	87.2%	97.0%
<i>Arid1a</i> Mm00473848_m1	90.5%	95.4%
<i>Arid1a</i> Mm00473841_m1	91.3%	108.6%
<i>Arid1b</i>	95.7%	97.0%
<i>Ltf</i>	94.8%	96.9%

were selected for further evaluation: *Gapdh*, *Rpl32*, *Hprt1* and *Hmbs* (see Table 2.7 for assay details). The stability of gene expression across the estrus cycle was assessed in 24 estrus-timed uterus samples (diestrus n=9; proestrus n=9; estrus n=4; metestrus n=2) with acceptable RNA quality (mean RIN 8.1, range 5.5-9.9) using the NormFinder (Andersen et al. 2004) and BestKeeper (Pfaffl et al. 2004) algorithms. Using BestKeeper (Pfaffl et al. 2004), Ct values for suitable HKGs must exhibit <3-fold difference across all samples and have SD<1. In a preliminary experiment, *Hmbs* showed high SD (2.5) and was not tested further. Testing across the 24 samples, the Ct SDs for *Gapdh*, *Rpl32* and *Hprt1* were 0.92, 1.18 and 0.8 respectively. All 3 putative HKGs exhibited <3-fold difference across the samples (*Gapdh* 2.15, *Rpl32* 1.97 and *Hprt1* 1.86). An advantage of the NormFinder algorithm (Andersen et al. 2004) is that it takes the grouping of the samples into account and reports a stability value. Using NormFinder, *Gapdh* and *Hprt1* showed the most stable expression across the 4 phases of the cycle (stability value for the combination 0.228) and *Gapdh* was the single most stable gene. Taking both algorithm results in consideration, the geometric mean of *Gapdh* and *Hprt1* was used for normalisation when performing qRT-PCR in mouse uterus samples.

3.5. Discussion

In this section, I have described in detail my attempts to establish an *in vitro* uterine organoid culture system. Despite testing multiple protocols, two of which specifically were developed for mouse uterus (Chung & Das 2011; Newbold et al. 1994), I was not successful. Irreproducibility of research, even when carefully peer-reviewed and published in high-impact journals, is a well-publicised phenomenon (Begley & Ellis 2012). It is exacerbated by the cursory attention paid to the Methods section (and often its relegation to online-only supplementary information) in many scientific papers, as exemplified by my experience with non-adjacent co-culture of dissociated uterine cells. Obviously, it raises concerns regarding the validity of any conclusions based on an experimental method that is only shown to work

in the hands of its developers. However, the problem is more pervasive, as even well characterised and commercially available assays, such as those assaying ERCC1 expression to guide lung cancer treatment, can prove irreproducible and flawed (Friboulet et al. 2013; Schneider et al. 2014).

Despite the above, the eventually optimized dissociation protocol based on the Chung and Das (2011) publication consistently produced adequate numbers of viable stromal cells, whose identity could be confirmed by immunofluorescence microscopy. Therefore, stromal cells prepared using this protocol were used to assess the effects of *Arid1a* knockdown on proliferation (see section 4.10.1). Additionally, I was able to develop a robust qRT-PCR protocol to assess gene expression in the mouse uterus.

4. FUNCTIONAL CHARACTERISATION OF *ARID1A* IN MOUSE AND HUMAN CELLS AND TISSUES

4.1. Introduction

Truncating or frameshift *ARID1A* mutations, generally leading to loss of protein expression, are the most frequently occurring mutational event in OCCC (Jones et al. 2010; Wiegand et al. 2010). Their frequency, as well as their presence in precursor endometriotic lesions (Wiegand et al. 2010), imply that disruption of *ARID1A* is an early event in OCCC pathogenesis. Functioning as part of the chromatin remodelling SWI/SNF complex, ARID1A exhibits diverse roles in differentiation and cell cycle control (Nagl et al. 2005; Nagl et al. 2006), maintenance of stem cell pluripotency (Gao et al. 2008; Krosi et al. 2010) and steroid hormone mediated transactivation (Inoue et al. 2002). Furthermore, different configurations of the SWI/SNF complex can occupy the same gene promoter region (Nagl et al. 2007) and are associated with either activation or repression of transcription in a context-specific manner (Euskirchen et al. 2011).

From the above it follows that insights gained by perturbing ARID1A function in established OCCC cell lines, although useful, will be limited by the extensive genetic and epigenetic abnormalities already present in these lines. It cannot be assumed that the effects of ARID1A loss will be the same in situations where it is an early event and in cell lines that managed to achieve all the hallmarks of malignancy while maintaining normal ARID1A expression. Therefore, in order to understand how *ARID1A* mutations contribute to OCCC pathogenesis, functional characterisation of ARID1A in normal endometrial and ovarian tissues, as well as in endometriosis, is necessary.

The first question I asked, pertinent in view of the high frequency of *ARID1A* mutations in uterus-derived cancers, was whether *Arid1a* itself is hormonally regulated in the mouse uterus. In view of *ARID1A*'s reported role in steroid hormone receptor transactivation and the importance of epithelial-stromal interactions in uterine regulation, I then tested the hypothesis that *Arid1a* expression would correlate with ER, PgR or Ki67 expression in the uterine epithelium and stroma. I subsequently performed a microarray study in order to answer the question of what pathways and processes are *Arid1a*-regulated in the mouse uterus in an agnostic manner. Having thus established a transcriptional profile in the uterus, I tested the

hypothesis that a core *ARID1A*-driven transcriptional programme, operative in normal tissues, exists by investigating transcription in MEFs and IOSE cells. Following that, I asked whether similar conclusions could be reached by studying *ARID1A* function in an established OCCC cell line. Next, I tested the hypothesis that *ARID1A* effects on proliferation are context specific by performing proliferation assays in a variety of non-malignant and cancerous cells, including *in vivo* ablation in the mouse uterine epithelium. Finally, I asked whether *ARID1B* loss affects proliferation in EOC cell lines and specifically whether its loss is detrimental in the presence of *ARID1A* mutations.

4.2. *Arid1a* expression across the estrus cycle

Cyclical changes in oestrogen and progesterone exposure globally affect gene transcription and protein expression in the mouse uterus (Bronson & Hamilton 1971; Tan et al. 2003). Changes in *Arid1a* expression during the estrus cycle would imply that it, too, is hormonally regulated. To study this, I created a cohort of 28 B6 mice in which the estrus cycle phase was determined with daily vaginal smears prior to uterine tissue collection (diestrus n=9; proestrus n=9, estrus n=7; metestrus n=3).

4.2.1. *Arid1a* mRNA levels are stable across the estrus cycle

24 estrus-timed uterine samples yielded RNA of acceptable quality (mean RIN 8.1, range 5.5-9.9). Due to smaller sample numbers, estrus and metestrus were analysed together and, therefore, the analysis dataset comprised 9 diestrus, 9 proestrus and 6 estrus/metestrus samples. Δ Ct values for *Arid1a* and *Arid1b* showed considerably less variability compared to the classical oestrogen-regulated gene *Ltf*, which encodes lactotransferrin (Fig. 4.1A). As a measure of dispersion, the SDs for *Arid1a* and *Arid1b* were statistically significantly smaller than that of *Ltf* (both $p < 0.0001$ using the f-test), whereas there was no difference between *Arid1a* and *Arid1b* ($p = 0.76$). Compared to diestrus, *Arid1a* mRNA levels were not significantly different in proestrus [mean (\pm S.E.) fold-change (FC) 0.96 (0.82-1.13)] or estrus/metestrus [mean (\pm S.E.) FC 0.88 (0.70-1.11)] (Fig. 4.1B). Similarly, *Arid1b* mRNA levels did not differ between diestrus and proestrus [mean (\pm S.E.) FC 0.85 (0.71-1.03)] or estrus/metestrus [mean (\pm S.E.) FC 0.94 (0.77-1.15)]. As expected (Newbold et al. 1992), *Ltf* mRNA levels increased in proestrus [mean (\pm S.E.) FC 1.99 (1.27-3.13)] and even more so in estrus/metestrus [mean (\pm S.E.) FC 19.76 (12.01-32.49)] (Fig. 4.1B).

4.2.2. *Arid1a* protein expression in the stroma is lower than the epithelium and shows some variability

RNA expression levels reflect the contributions of both the epithelial (luminal and glandular) and stromal compartments whereas IHC allows protein expression to be separately assessed in each of these two compartments. Visual inspection of the slides (diestrus n=8; proestrus n=8; estrus n=6; metestrus n=3) showed ubiquitous epithelial *Arid1a* expression (Fig. 4.1C) whereas stromal expression varied with most samples showing ubiquitous strong expression (Fig. 4.1C left panel) but others having a mixture of positive and negative stromal cells (Fig. 4.1C right panel). On visual inspection, samples in the latter group seemed to be mainly in the estrus and metestrus phases of the cycle. In order to more robustly assay *Arid1a* protein expression, quantitative IHC was undertaken, separately for the epithelial and stromal compartments as detailed in section 2.15.1 (Fig. 4.1D). Quantitative IHC showed that 5 of 8 samples with <70% *Arid1a* positive stromal cells were from estrus or metestrus compared with only 4 of 17 with $\geq 70\%$ positive cells (Fig. 4.1F). However, this did not reach statistical significance ($p=0.087$). Across all samples, more epithelial (87.2%) than stromal cells (73.6%) were *Arid1a* positive ($p<0.0001$), a difference that was maintained when staining intensity was taken into account by using H-scores [mean (\pm S.E.) 199.6 (± 12.35) vs. 160.2 (± 13.49), $p<0.0001$]. However, there was no difference in the mean percentage of positive cells across the estrus cycle phases either for the epithelium ($p=0.26$) or stroma ($p=0.3$) (Fig. 4.1E). Substituting H-scores for percentages of positive cells did not modify this observation ($p=0.36$ and $p=0.38$ respectively) (Fig. 4.1E). There was only moderate correlation between *Arid1a* mRNA levels and either epithelial ($r=0.41$, $p=0.066$) or stromal ($r=0.48$, $p=0.026$) *Arid1a* protein expression (Fig. 4.1G).

The RNA and protein expression data together show that average *Arid1a* expression does not vary during the estrus cycle, and do not support hormonal regulation of *Arid1a*. However, *Arid1a* protein expression can be relatively low in the stroma in a subset of samples, preferentially in estrus or metestrus. The functional relevance of this observation, if any, is presently unclear. Staining for CD45 showed only very occasional positive cells and, therefore, leukocytic infiltration was excluded as a significant contributor to the observed stromal appearances (data not shown).

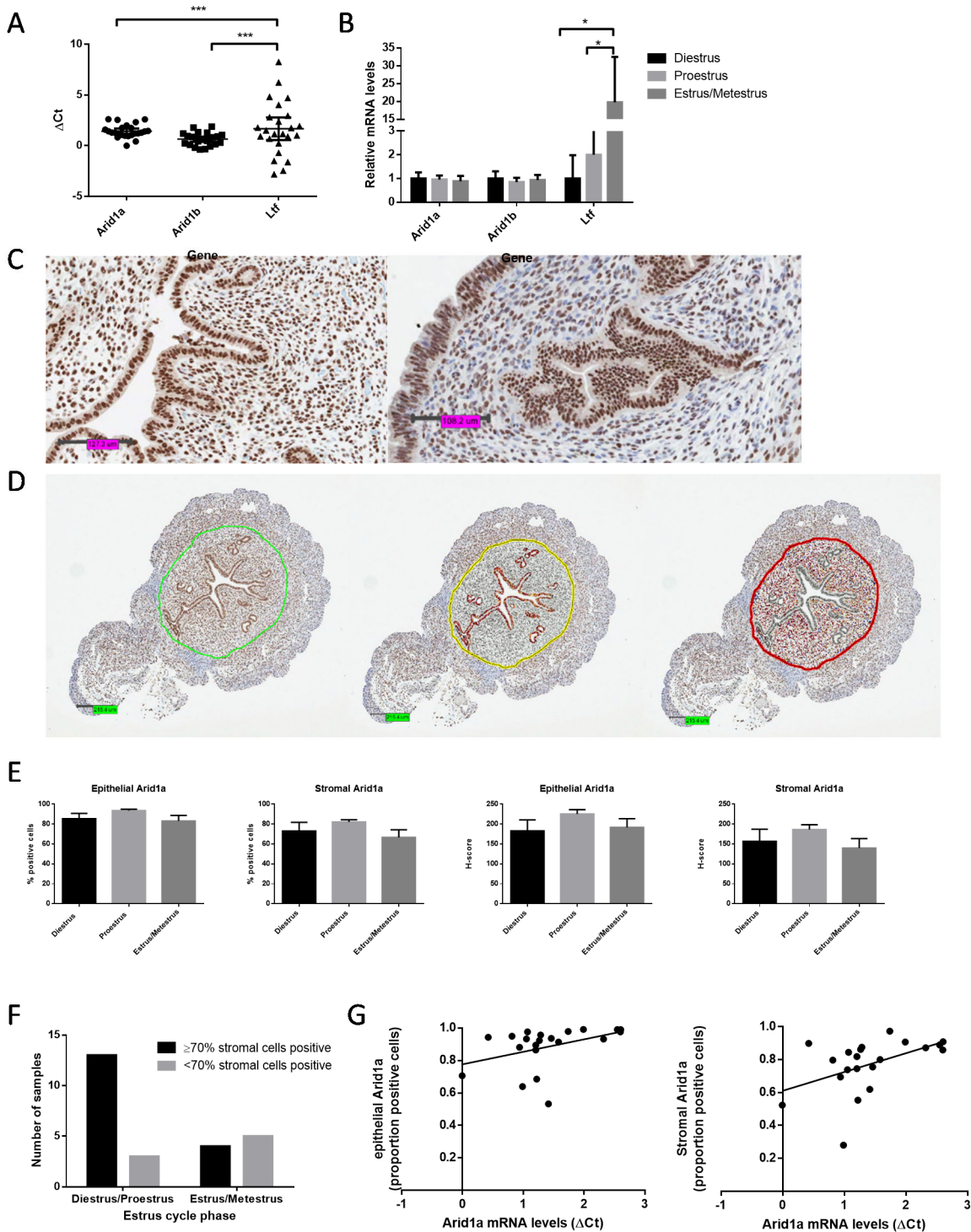


Figure 4.1. *Arid1a* during the mouse estrus cycle

Arid1a expression determined in 24 (RNA) and 25 (protein) 6-8-week-old B6 mice: A) Δ Ct values for *Arid1a*, *Arid1b* and *Ltf*, calculated relative to the GM of *Gapdh* and *Hprt1*. B) Mean \pm S.E. *Arid1a*, *Arid1b* and *Ltf* mRNA levels across the mouse estrus cycle normalised to diestrus. C) Examples of strong (left) and weak (right) *Arid1a* stromal staining by IHC. D) Example of the set-up for quantitative IHC: area of interest (left), luminal and glandular epithelial compartment (centre) and stromal compartment (right). After an area of interest is drawn by hand (green level), the algorithm counts and scores separately the epithelial (yellow level) or stromal (red level) cells. E) Mean \pm S.E. epithelial and stromal *Arid1a* positive cells and H-scores across the estrus cycle. F) Distribution of strong ($\geq 70\%$ cells positive) and weak ($< 70\%$) *Arid1a* stromal expression across the estrus cycle. G) Correlation between *Arid1a* mRNA and *Arid1a* protein expression in the epithelium (left) and stroma (right).

4.2.3. ER expression peaks in proestrus and proliferation is limited to the epithelium

ER and PgR expression show cyclical changes in the mouse uterus (Bergman et al. 1992; Mote et al. 2006) and ARID1A has been reported to be necessary for ER-mediated transactivation in breast cancer cell lines (Inoue et al. 2002). If ER and PgR are Arid1a-regulated in the uterus, their expression should be correlated. In order to study these relationships, I first performed quantitative IHC for ER, PgR and Ki67 in the estrus-timed uterine samples. As determined by the percentage of positive cells, ER expression (Fig. 4.2A) in both epithelium and stroma was higher in proestrus. This difference in expression approached statistical significance in the epithelium ($p=0.078$) and reached it in the stroma ($p=0.005$). Substituting H-scores (Fig. 4.2A) slightly increased the strength of the observed associations ($p=0.061$ and $p=0.002$ respectively). Similar numbers of cells were ER positive in the epithelium (31%) and stroma (33%, $p=0.37$) (Fig. 4.2D). PgR expression showed less variability, although epithelial expression tended to be lower in estrus/metestrus, especially when H-scores were calculated ($p=0.043$) (Fig. 4.2B). More stromal than epithelial cells were PgR positive ($p=0.016$), although the difference was small (64% vs. 58%) (Fig. 4.2D). Proliferation seemed to be confined to the epithelium where 23% cells were Ki67 positive, compared to 8% in the stroma ($p<0.0001$) (Fig. 4.2D). No differences in Ki67 staining across the estrus cycle were seen (Fig. 4.2C). These results are generally in agreement with previous reports (Bergman et al. 1992; Mote et al. 2006) and, therefore, provide a robust base on which to study correlations between steroid hormone receptors, proliferation and Arid1a expression.

4.2.4. Arid1a and ER expression are correlated

I then calculated pairwise correlation coefficients r for Arid1a and ER, PgR or Ki67 expression, separately in the epithelium and stroma (Table 4.1). There were no statistically significant correlations of either epithelial or stromal Arid1a and epithelial or stromal PgR or Ki67 (Table 4.1 and Fig. 4.2E-F). The correlations between epithelial or stromal Arid1a and stromal ER but not epithelial ER were statistically significant when the number of positive cells was used as the basis for the calculations (Table 4.1 and Fig. 4.2E-F). All 4 pairwise correlations between epithelial or stromal Arid1a and epithelial or stromal ER were statistically significant when calculated using H-scores (Table 4.1 and Fig. 4.2G). Using conventional thresholds for interpretation of r (Zou et al. 2003), the observed correlations between Arid1a and ER are moderate. Furthermore, 24 different correlation coefficients were calculated. As calculations based on positive cell numbers and H-scores are not independent, an appropriate correction for statistical significance would be to divide the 0.05 threshold by 12 (i.e. apply a Bonferroni correction). The p value threshold for significance then becomes 0.0042 and only the

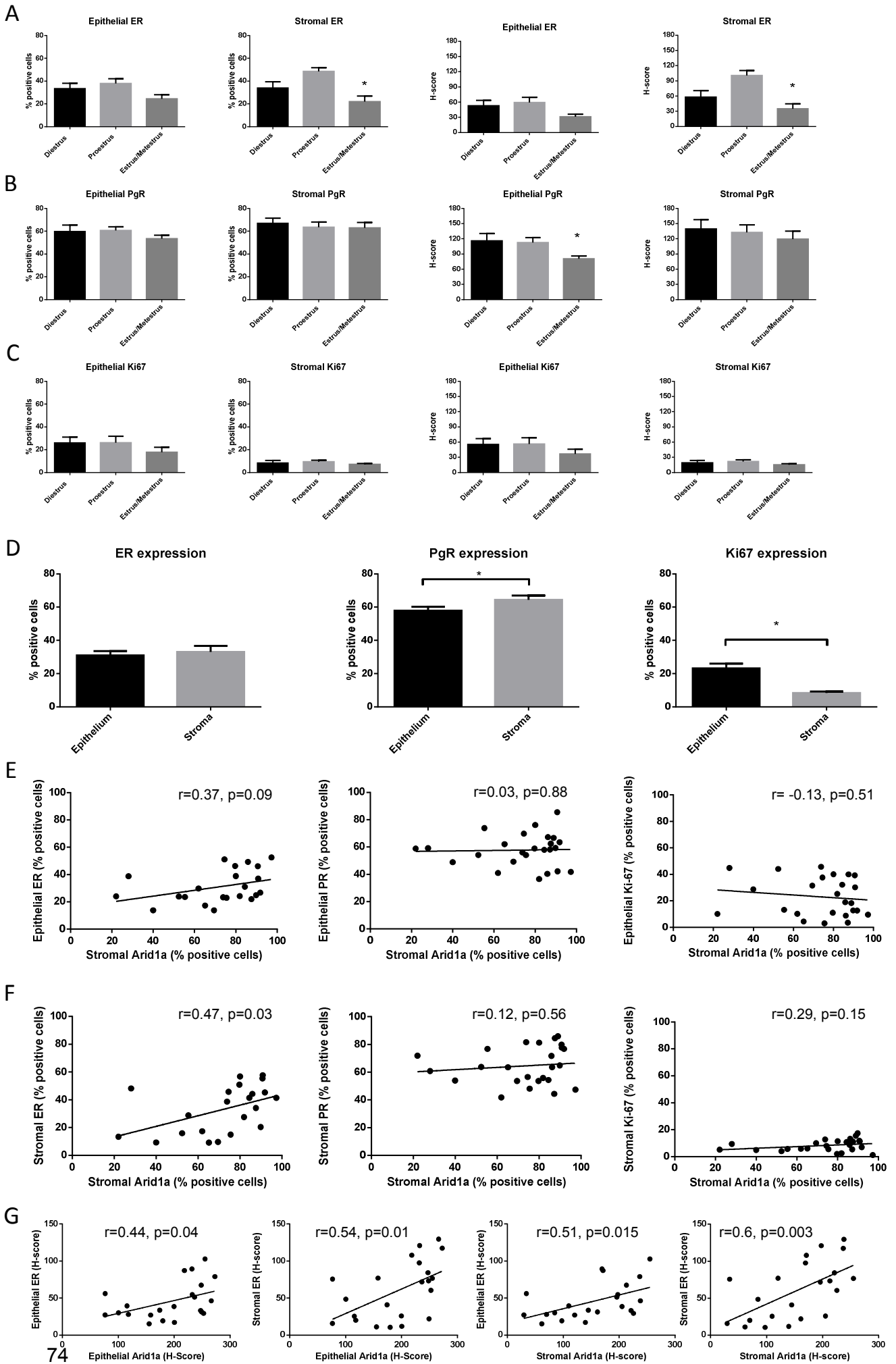


Table 4.1. Correlation of Arid1a, ER, PgR and Ki67 in the mouse uterus

Comparison	Cell number correlation coefficient r	p value	H-score correlation coefficient r	p value
Epithelial Arid1a – epithelial ER	0.32	0.17	0.44	0.04
Epithelial Arid1a – stromal ER	0.49	0.02	0.54	0.01
Stromal Arid1a – epithelial ER	0.37	0.09	0.51	0.015
Stromal Arid1a – stromal ER	0.47	0.03	0.60	0.003
Epithelial Arid1a – epithelial PgR	0.12	0.56	-0.03	0.89
Epithelial Arid1a – stromal PgR	0.27	0.20	0.27	0.19
Stromal Arid1a – epithelial PgR	0.03	0.88	-0.01	0.98
Stromal Arid1a – stromal PgR	0.12	0.56	0.33	0.11
Epithelial Arid1a – epithelial Ki67	-0.03	0.9	-0.09	0.68
Epithelial Arid1a – stromal Ki67	0.34	0.09	0.29	0.16
Stromal Arid1a – epithelial Ki67	-0.13	0.51	-0.11	0.60
Stromal Arid1a – stromal Ki67	0.29	0.15	0.34	0.10

correlation between stromal Arid1a and stromal ER remains significant. The observed correlations could be consistent with a model of Arid1a-dependent ER transactivation (Inoue et al. 2002). However, regulation of both by a third factor, cannot be excluded from this cross-sectional dataset.

4.3. *Arid1a* expression in the uterus is associated with a transcriptional programme enriched in genes involved in cell cycle regulation

Having established a potential correlation between Arid1a and ER expression, I asked what other genes may be *Arid1a*-regulated in the mouse uterus. To answer this in an unbiased manner, I exploited the fact that although *Arid1a* mRNA levels do not systematically vary

Figure 4.2. ER, PgR and Ki67 during the mouse estrus cycle and correlations with stromal Arid1a

IHC performed in uterine samples from 25 6-8-week-old B6 mice: A-C) Mean \pm S.E. epithelial and stromal ER (A), PgR (B) and Ki67 (C) positive cells and H-scores across the estrus cycle. D) Mean \pm S.E. ER, PgR and Ki67 expression in epithelium and stroma. E-F) Correlation between positive stromal Arid1a and epithelial (E) or stromal (F) ER, PgR and Ki67 cells. G) Correlation between epithelial or stromal Arid1a and ER H-scores.

across the estrus cycle and the dynamic range of *Arid1a* mRNA expression is much smaller than that of oestrogen-regulated genes such as *Ltf* (see section 4.2.1), there can still be significant between-sample variability. Gene expression arrays were performed using Illumina Beadchip arrays in 6 uterine samples with high (n=3) and low (n=3) *Arid1a* mRNA expression as determined by qRT-PCR (an overview of all gene expression experiments contained in this chapter can be found in Fig. 4.3). All samples came from mice in late diestrus / early proestrus (presence of lymphocytes with a few nucleated cells on the vaginal smears), minimising the impact of the estrus cycle phase on the global expression profile. The mean *Arid1a* mRNA expression in the “Low *Arid1a*” group was 73% lower than in the “High *Arid1a*” group. Hierarchical clustering showed that all “High *Arid1a*” samples clustered together, along with one of the “Low *Arid1a*” samples which necessitated weighing down the contribution of that sample and limited the power of the array (Fig. 4.4A). Despite this, 1358 unique genes were differentially expressed at a FDR 0.05 cut-off (Fig. 4.4B) with similar numbers of genes showing lower (n=745) and higher (n=612) expression in an *Arid1a* high context. As there was no experimental manipulation of *Arid1a*, these genes are best regarded as genes whose expression is correlated with *Arid1a* rather than genes directly regulated by it.

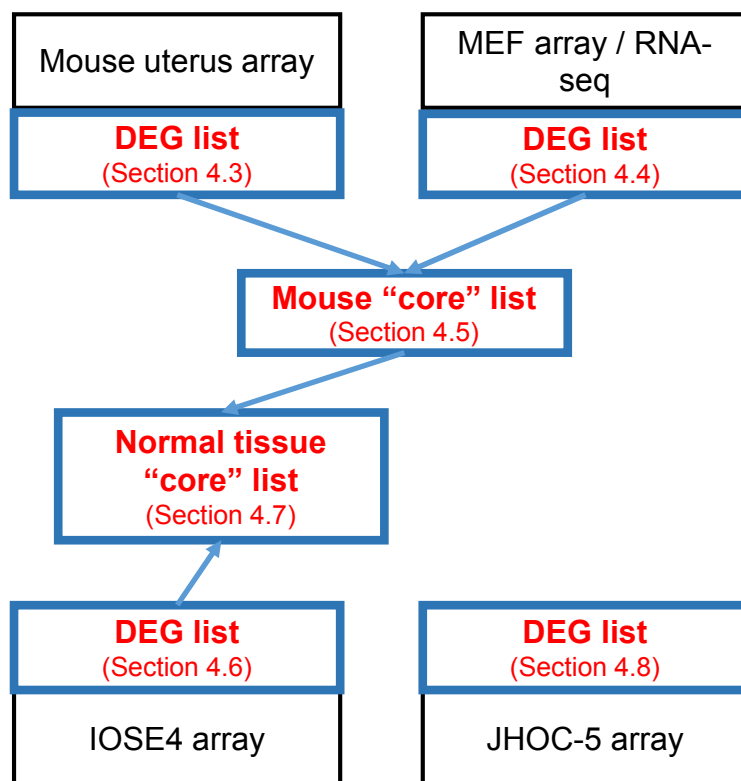


Figure 4.3. Overview of gene expression experiments

Schematic depicting the relationships of the 4 gene expression experiments and the corresponding text sections where they are discussed (DEG=Differentially Expressed Genes).

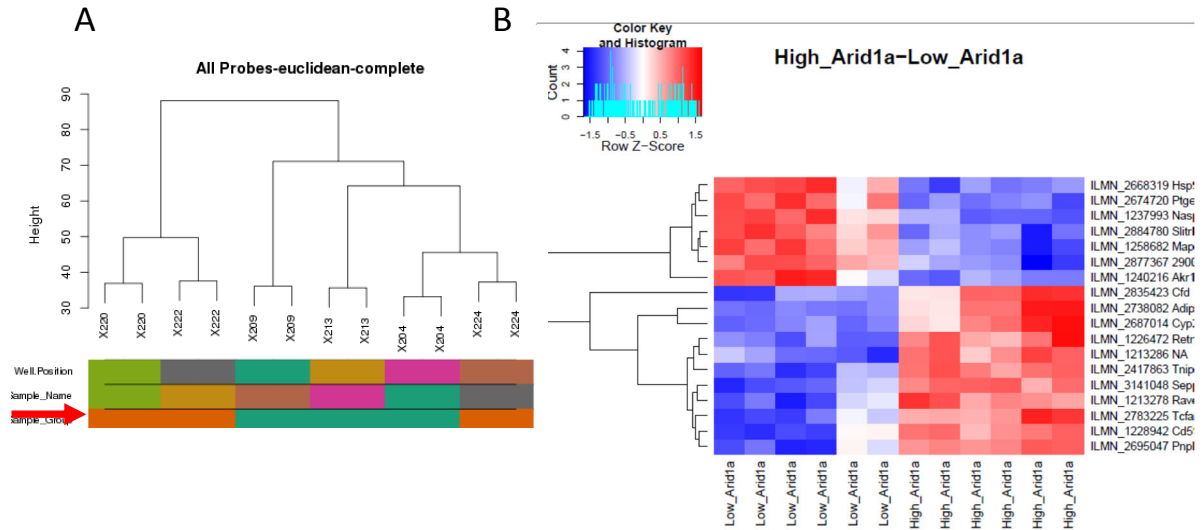


Figure 4.4. *Arid1a* gene expression array in mouse uterus

Uterus samples with high (n=3) and low (n=3) *Arid1a* mRNA levels by qRT-PCR were compared using BeadChip arrays. A) Hierarchical clustering (red arrow) shows that all *Arid1a* high samples (green) cluster together, whereas the *Arid1a* low samples (brown) are split into 2 groups. B) Heatmap of the high vs. low *Arid1a* comparison.

Pathway analysis of the 1358 differentially expressed genes using MetaCore, revealed 19 enriched pathways at FDR<0.05 (Table A.1 in the Appendix). Five of the top 6 differentially regulated pathways are related to cell cycle, of which four are involved in regulation of mitosis [“Role of Nek in cell cycle regulation”, “Spindle assembly and chromosome separation” (Fig. 4.5), “Role of APC in cell cycle regulation” and “The metaphase checkpoint”]. Differentially expressed genes involved in these pathways included some encoding cell cycle-related kinases (*Aurka*, *Plk1*, *Cdk2*) and regulatory proteins (*Ccnb1*, *Cdc20*, *Cdc6*, *Cdc25a*, *Mad211*), tubulin isoforms (*Tuba1a*, *Tuba1b*, *Tuba1c*, *Tubb5*, *Tubb6*, *Tubb2c*) and PI3K pathway components (*Pik3r3*, *Pik3cb*). Additionally, pathways related to apoptosis, cytoskeleton remodelling and development were also represented (Table A.1). Process network analysis of the same gene list, revealed 8 enriched networks at FDR<0.05 (Table A.2 in the Appendix). Similarly to the pathway analysis, cell cycle-related networks comprised 4 of the 8 significantly enriched networks with “Mitosis” representing the top hit, driven by differential expression of many of the genes mentioned above. Networks related to protein folding were also enriched, due to differential expression of genes such as *Atf6b*, *Atf4*, *Hsp90aa1*, *Hsp90b1*, *Hspa2*, *Hspd1* and *Hspe1*.

Using MetaCore, steroid hormone pathways and networks were not enriched among the differentially expressed genes. Additionally, *Esr1* (encoding ER α) and *Pgr* (encoding PgR)

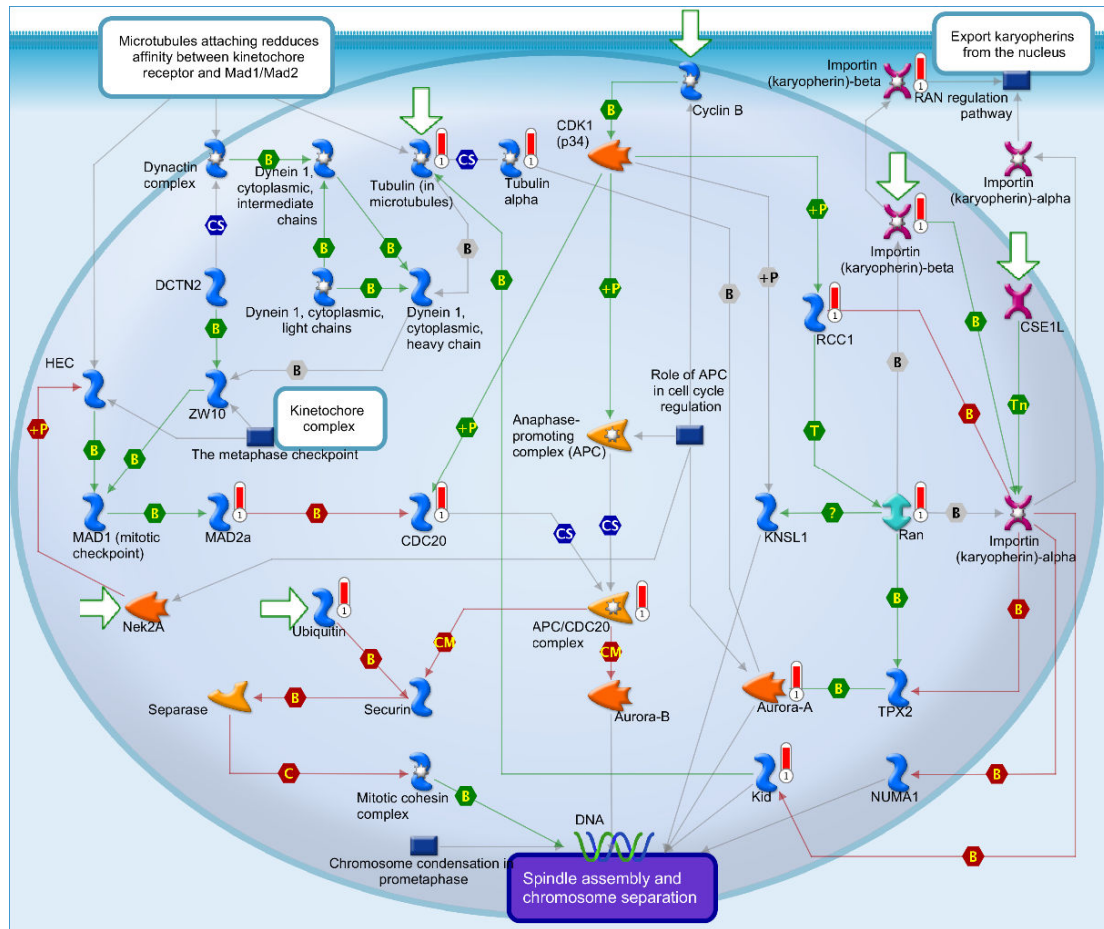


Figure 4.5. The “Spindle assembly and chromosome separation” pathway is associated with *Arid1a* expression in the mouse uterus

“Spindle assembly and chromosome separation” was one of the most enriched pathways when uterus samples with high (n=3) and low (n=3) *Arid1a* mRNA levels were compared using BeadChip arrays (FDR = 0.002). Differentially expressed gene (DEG) lists (n=1358) were created at FDR 0.05. Red “thermometer” bars highlight the DEG that drive pathway enrichment. Analysis performed and graph created using MetaCore (www.genego.com).

were not differentially expressed (Log₂-fold change of 0.05 and -0.53 respectively). I then tested the overlap of the 1358 differentially expressed genes and 27 core ER-signalling genes (*Ahr*, *Adora1*, *Bcar1*, *Brca1*, *Cav1*, *Ccnd1*, *Efna5*, *Esr1*, *Esr2*, *Hsp90aa1*, *Igf1*, *Med1*, *Mta1*, *Ncoa1*, *Ncoa2*, *Ncoa3*, *Ncor1*, *Ncor2*, *Nr0b1*, *Nr0b2*, *Nrip1*, *Pelp1*, *Pgr*, *Phb2*, *Safb*, *Tff1*, and *Vdr*)⁵. Only 2 genes (*Ccnd1* and *Hsp90aa1*) overlapped (p=0.46) and therefore, the microarray data do not support regulation of the ER pathway by *Arid1a* in the uterus.

The enrichment of mitosis and apoptosis associated pathways in this analysis would be in agreement with the tumour suppressor role of *ARID1A* in uterus-derived cancers. However,

⁵ These are the genes analysed in the “Estrogen Receptor Signaling RT² Profiler PCR Array” kit (Qiagen).

as already stated, the experimental design used cannot provide assurances that *Arid1a* really regulates these genes as other factors could cause differential expression of both *Arid1a* and the 1358-gene set. To mitigate against this limitation, an experimental setup with direct modulation of *Arid1a* expression is needed.

4.4. *Arid1a* drives a transcriptional programme enriched in genes involved in cell cycle regulation and cytoskeleton remodelling in MEFs

In order to obtain a more robust insight into *Arid1a*-driven transcriptional programmes, I utilised siRNA to knock down *Arid1a* expression in 4 different MEF cell lines and analysed gene expression with BeadChip microarrays and RNA-seq (see sections 2.17.1 and 2.18 for details). siRNA treatment reduced *Arid1a* expression by 68-76% as assessed by qRT-PCR (Fig. 4.6A). The MEF cell lines E6, E8 and E9 were tested, in technical duplicates, on BeadChip microarrays. Hierarchical clustering revealed that the cell lines clustered according to treatment with *Arid1a* or non-target siRNA (Fig. 4.6B) and 2971 genes were differentially expressed using a FDR 0.01 cut-off. The same samples, with the addition of a fourth MEF cell line, E10, were also tested with RNA-seq. The increased power of this technique (Hitzemann et al. 2013), combined with the larger sample size, resulted in 5288 genes being designated as differentially expressed at FDR 0.01. 2210 genes (50.5% up-regulated and 49.5% down-regulated), were significantly differentially expressed at FDR 0.01 with both methods ($p < 1 \times 10^{-100}$ for the overlap) and formed a cross-validated high-confidence gene set that was used for downstream analysis.

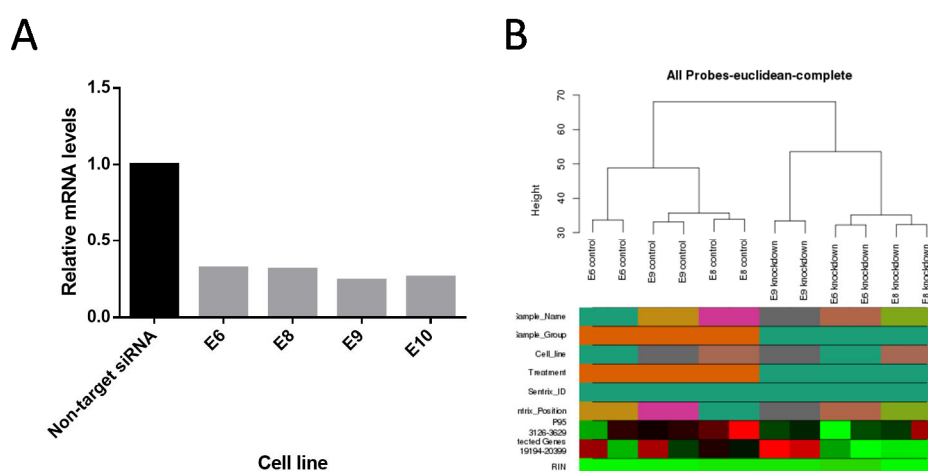


Figure 4.6. *Arid1a* gene expression array in MEFs

Arid1a was knocked down using siRNA and gene expression was assayed using BeadChip arrays and RNA-seq in 4 MEF cell lines (E6, E8, E9 and E10). A) qRT-PCR shows 68-74% *Arid1a* knockdown after siRNA treatment B) Hierarchical clustering shows that samples used in the microarray experiment (E6, E8 and E9) cluster by *Arid1a* treatment status into 2 groups.

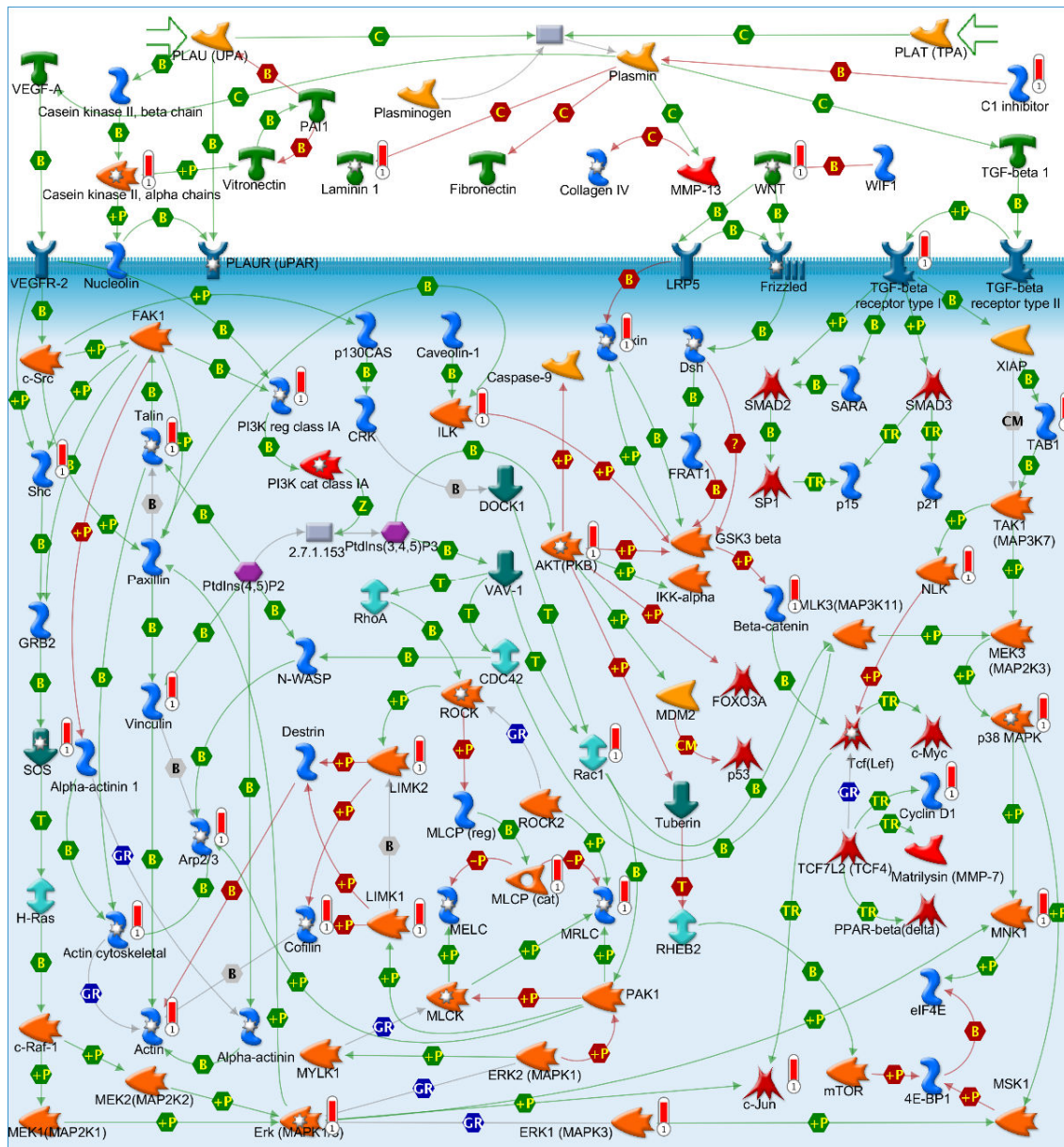


Figure 4.7. The “TGF, WNT and cytoskeletal remodelling” pathway is *Arid1a*-regulated in MEFs

“TGF, WNT and cytoskeletal remodelling” was the most enriched pathway (FDR = 2.8×10^{-6}) following siRNA knockdown of *Arid1a* in MEFs (n=3). High-confidence differentially expressed gene (DEG) lists (n=2210) were created using the overlap between the lists generated by BeadChip array and RNA-seq experiments, both at FDR 0.01. Red “thermometer” bars highlight the DEG that drive pathway enrichment. Analysis performed and graph created using MetaCore (www.genego.com).

MetaCore pathway analysis of the 2210 genes revealed more than 50 pathways as being enriched at FDR<0.01 (Table A.3 in the Appendix lists the top 30 enriched pathways, all with FDR< 7.5×10^{-4}). Similar to the uterus samples (see section 4.3), 6 of the 10 most enriched pathways are involved in cell cycle control and predominantly mitosis (“Spindle assembly and

chromosome separation”, “The metaphase checkpoint”, “Role of Nek in cell cycle regulation”, “Initiation of mitosis”, “Chromosome condensation in prometaphase” and “Regulation of G1/S transition”). As was the case with the uterus samples, cytoskeleton remodelling pathways were also significantly enriched with 3 of the top 10 pathways [“TGF, WNT and cytoskeletal remodelling” (Fig. 4.7), “Cytoskeleton remodelling” and “Regulation of actin cytoskeleton by Rho GTPases”] related to the cytoskeleton. Developmental and immune response pathways were also significantly enriched (Table A.3), whereas, contrary to the uterus samples, apoptosis-related pathways were not. Process network analysis revealed 33 significantly enriched networks at FDR<0.05 (Table A.4 in the Appendix). Again, cell cycle-related, cytoskeleton and developmental networks were prominent as was a “chromatin modification” network driven by components of the swi/snf complex, histone, histone deacetylase and polycomb group members (Fig. 4.8). Similar to the uterus experiment, genes such as *Aurka*, *Ccnb1*, *Ccnd1*, *Cdk1*, *Cdc20*, *Pik3r3*, *Tuba1a*, *Tuba1c*, *Tubb5*, *Tubb6*, *Kif22*, *Shc1* and *Sos2* were *Arid1a*-regulated in the MEFs.

4.5. Mitosis regulation, cytoskeleton remodelling and chromatin modification are components of a core *Arid1a*-driven transcriptional programme in the mouse

There exists a remarkable overlap between the pathways and networks enriched after *Arid1a* knockdown in MEFs and in “High *Arid1a*” vs. “Low *Arid1a*” mouse uterus samples (Tables A.1-A.4). In both datasets, 4 of the top 6 enriched pathways are identical (“TGF, WNT and cytoskeletal remodelling”, “Spindle assembly and chromosome separation”, “The metaphase checkpoint” and “Role of Nek in cell cycle regulation”) as are 3 of the top 6 enriched process networks (“Mitosis”, “Cell cycle – Core” and “Spindle microtubules”). The implications of this observation are two-fold: first, it increases the confidence that many of the genes identified from the mouse uterus microarray are *Arid1a*-regulated and not just correlated. Second, it supports the concept of a core *Arid1a*-driven transcriptional programme that is conserved across cell types and developmental stages. With that in mind, it should be noted that *Cdkn1a*, a gene reported to be a direct target of *ARID1A* in osteoblasts (Nagl et al. 2006) and immortalised ovarian surface epithelium (Guan et al. 2011), was not differentially expressed in either the uterus or the MEFs. Similarly, *Myc*, previously reported as *ARID1A*-regulated (Nagl et al. 2006), was not detected as differentially expressed in either of the microarrays. Therefore, even if a core transcriptional programme exists, it is likely that it does so in parallel to cell and tissue-specific ones.

To detect a putative *Arid1a*-driven core transcriptional programme in the mouse, the differentially expressed gene lists generated from the microarray experiments in the uterus (n=1358) and the MEFs (n=4291), both at a FDR 0.05 cut-off, were compared. I chose the 0.05 FDR cut-off for the MEFs, using the microarray data only, to ensure consistency of the methods used to generate the 2 lists. The overlap between the 2 lists, consisting of 556 genes, was highly statistically significant ($p=2.4 \times 10^{-68}$) (Fig. 4.9). Seven pathways (Table A.5 in the Appendix) were significantly differentially regulated at $FDR < 0.05$, with mitosis-related ones being prominent (“Role of Nek in cell cycle regulation”, “Spindle assembly and chromosome separation”, “The metaphase checkpoint” and “Role of APC in cell cycle regulation”) and cytoskeleton remodelling, apoptosis and cell adhesion also represented. Similarly, 8 process networks were differentially regulated at $FDR < 0.05$ (Table A.6 in the Appendix), with cell cycle-related ones (“Mitosis”, “Cell cycle – Core”, “G2-M” and “Meiosis”) being prominent and cytoskeleton and chromatin modification-related ones also making the list.

4.6. *ARID1A* drives a similar transcription programme in immortalised human ovarian cells

Having established that *Arid1a* regulates, through a common set of genes, similar pathways and processes in 2 different mouse tissues, I then tested whether that observation could be extended to a third cell type in a different species. For that, *ARID1A* was knocked down in human IOSE cells, a model commonly used in ovarian cancer research. siRNA treatment reduced *ARID1A* mRNA levels by 42-56% (Fig. 4.10A). Hierarchical clustering revealed that the cell lines were clustering according to siRNA treatment (Fig. 4.10B) and 2738 genes were

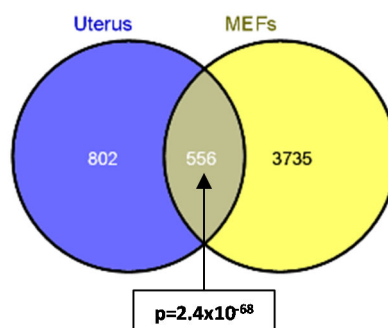


Figure 4.9. Overlap in genes regulated by *Arid1a* in mouse uterus and MEFs

Overlap of genes regulated by *Arid1a* in mouse uterus (n=1358) and MEFs (n=4291). Differentially expressed gene lists were created using BeadChip arrays at FDR 0.05.

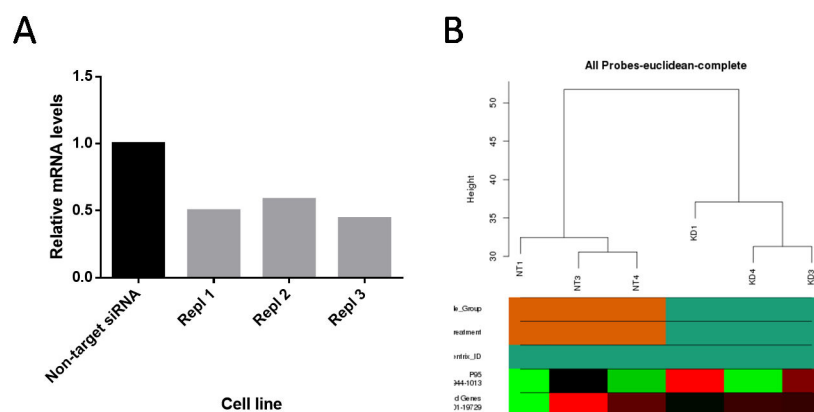


Figure 4.10. *ARID1A* gene expression array in IOSE4 cells

ARID1A was knocked down using siRNA and gene expression was assayed using BeadChip arrays in IOSE4 cells (n=3 flask replicates) A) qRT-PCR shows 42-56% *ARID1A* knockdown after siRNA treatment B) Hierarchical clustering shows that the samples cluster by *ARID1A* treatment status into 2 groups.

differentially expressed using a FDR 0.01 cut-off. As was the case with the mouse uterus and MEF samples, cell cycle-related pathways (Table A.7 in the Appendix) and process networks (Table A.8 in the Appendix) related to mitosis and the G2/M checkpoint, were significantly enriched among *ARID1A*-regulated genes using MetaCore (Fig. 4.11). Similar to the mouse data, cytoskeleton remodelling and EMT regulation were also regulated by *ARID1A* in IOSE4 cells. Additionally, DNA damage response pathways were significantly enriched in IOSE4 cells. As has been previously reported in IOSE, *SMAD3* transcription was repressed and that of *MYC* induced upon *ARID1A* knockdown (Guan et al. 2011). In agreement with the mouse uterus data, no enrichment for core ER-signalling pathway genes (see section 4.3 for gene list) was seen after knockdown in IOSE4 cells ($p=0.15$).

4.7. A core *ARID1A* transcriptional programme which controls cell cycle progression and is conserved across species exists

It is evident from looking at Tables A.1 to A.8 that *ARID1A* regulates the same pathways and network processes in mouse uterus, MEFs and human IOSE cells and that these pathways are mostly related to the G2/M checkpoint, mitosis and cytoskeleton remodelling (Fig. 4.12B). I then asked whether this is achieved through regulation of a common core set of genes, conserved across species. To answer that, I looked for genes that were *ARID1A*-regulated at FDR 0.05 in all 3 model systems. 177 genes fulfilled these criteria ($p=1.7 \times 10^{-13}$) (Fig. 4.12A). This p value is conservative as it assumes that all genes represented in the mouse array are present in the human one and *vice versa*, something unlikely to be true. MetaCore analysis of

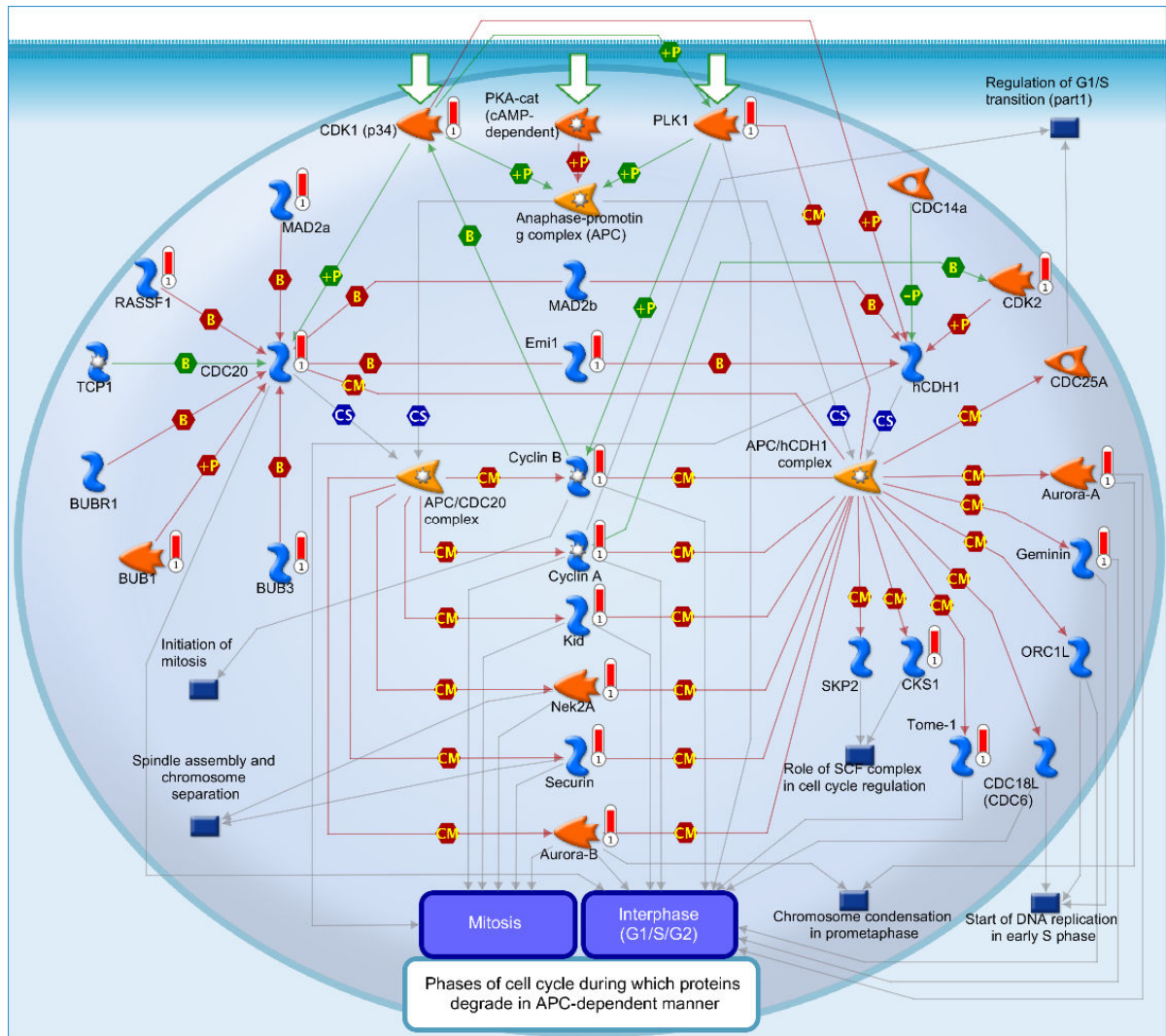


Figure 4.11. The “Role of APC in cell cycle regulation” pathway is *ARID1A*-regulated in IOSE4 cells

“Role of APC in cell cycle regulation” was the most enriched pathway (FDR = 4.3×10^{-8}) following siRNA knockdown of *ARID1A* in IOSE4 cells (n=3). Differentially expressed gene (DEG) lists (n=2738) were created at FDR 0.01. Red “thermometer” bars highlight the DEG that drive pathway enrichment. Analysis performed and graph created using MetaCore (www.genego.com).

the “core” 177-gene set, again revealed enrichment of cell cycle-related pathways (Table 4.2) with the 4 most enriched pathways being “Spindle assembly and chromosome separation” (Fig. 4.13), “The metaphase checkpoint”, “Role of Nek in cell cycle regulation” and “Role of APC in cell cycle regulation”. Similarly, the 5 most enriched process networks were “Cell cycle - Mitosis” (Fig. 4.14), “Cell cycle - Core”, “Spindle microtubules”, “Cell cycle - G2-M” and “Cell cycle - S-phase” (Table 4.3). Looking at the gene list (Table 4.4), these pathways and networks are driven by changes in targetable genes such as *CCNB1*, *CCND1*, *AURKA* (encoding Aurora kinase A), *PLK1* (encoding Polo-like kinase 1) and *PLK4*.

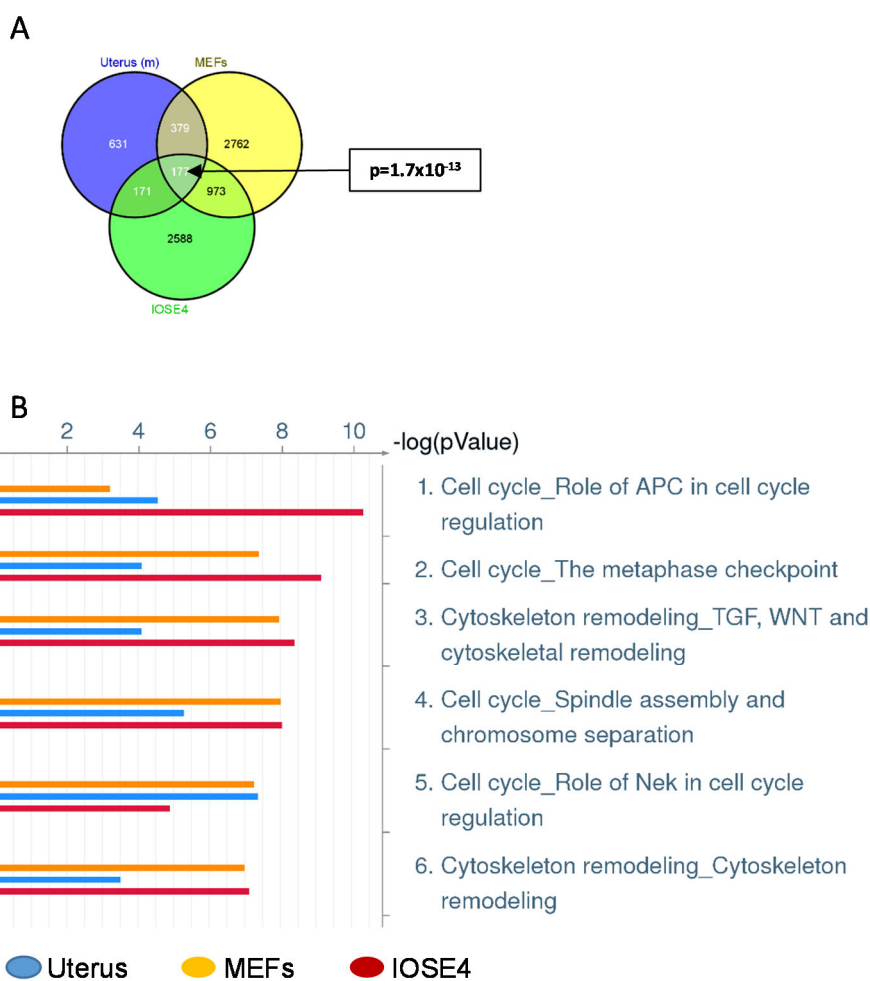


Figure 4.12. Overlap of genes and pathways regulated by *ARID1A* in mouse uterus, MEFs and IOSE4 cells

A) Overlap of genes regulated by *ARID1A* in mouse uterus (n=1358), MEFs (n=4291) and IOSE4 cells (n=3909). Differentially expressed gene lists were created using BeadChip arrays at FDR 0.05. B) Pathways enriched in *ARID1A*-regulated genes with $p < 10^{-4}$ in all 3 datasets.

Table 4.2. Pathways enriched in the 177 *ARID1A*-regulated genes in all of mouse uterus, MEFs and IOSE4 cells

Pathway	p value	FDR
Cell cycle - Spindle assembly and chromosome separation	8.809E-12	3.180E-09
Cell cycle - The metaphase checkpoint	8.165E-10	1.474E-07
Cell cycle - Role of Nek in cell cycle regulation	1.115E-08	1.007E-06
Cell cycle - Role of APC in cell cycle regulation	1.115E-08	1.007E-06
Cell cycle - Start of DNA replication in early S phase	1.886E-04	0.0136
Cell cycle - Nucleocytoplasmic transport of CDK/Cyclins	2.459E-04	0.0148
Reproduction - Progesterone-mediated oocyte maturation	4.536E-04	0.0234
Cell cycle - Chromosome condensation in prometaphase	8.580E-04	0.0387

Pathways list created and statistical analysis performed using MetaCore

Table 4.3. Process networks enriched in the 177 *ARID1A*-regulated genes in all of mouse uterus, MEFs and IOSE4 cells

Process Network	p value	FDR
Cell cycle - Mitosis	2.612E-16	3.265E-14
Cell cycle - Core	9.946E-12	6.216E-10
Cytoskeleton - Spindle microtubules	8.416E-10	3.507E-08
Cell cycle - G2-M	1.736E-06	5.425E-05
Cell cycle - S phase	1.752E-05	4.379E-04
Cell cycle - Meiosis	5.548E-05	0.00116

Process networks list created and statistical analysis performed using MetaCore

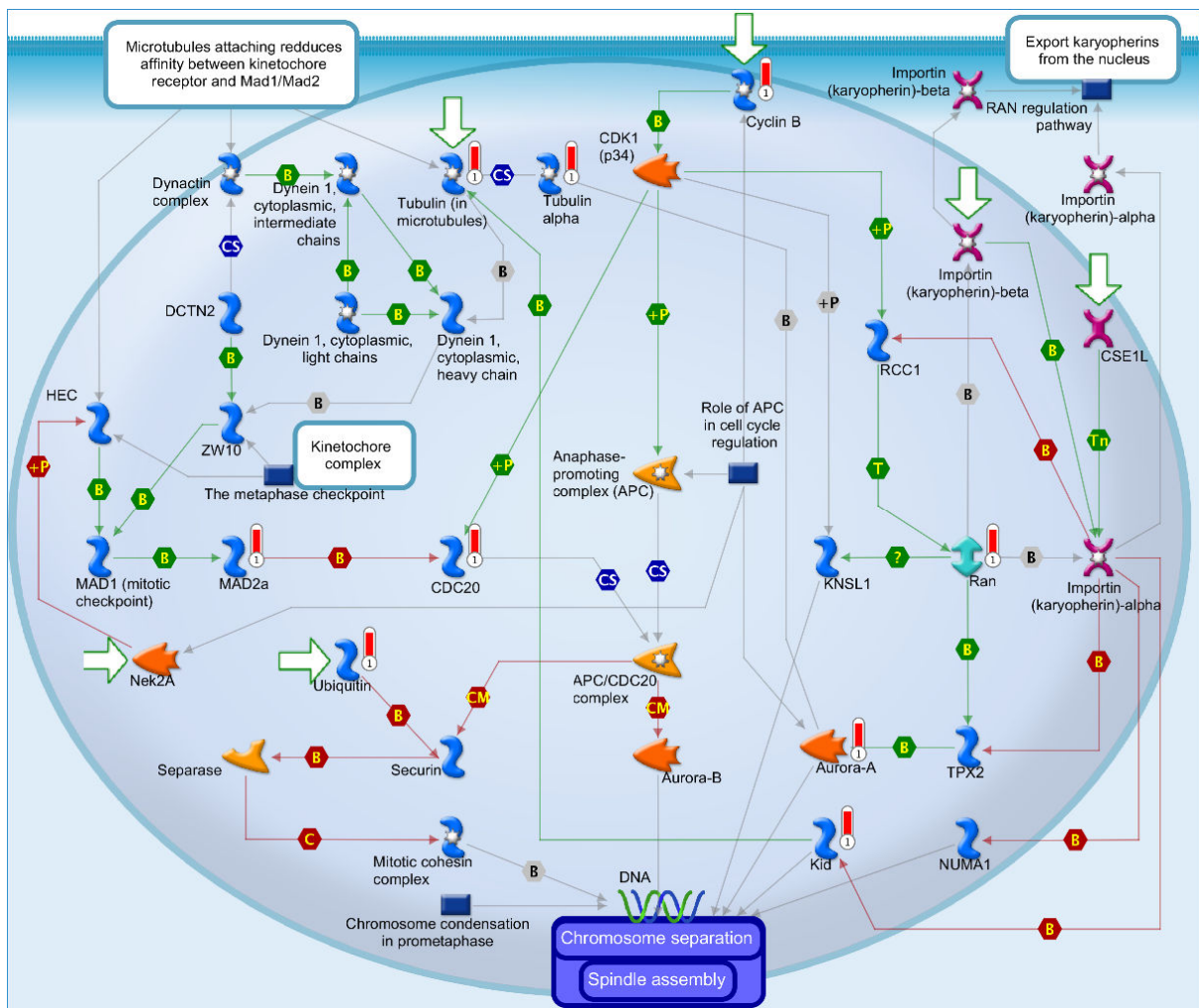


Figure 4.13. The “Spindle assembly and chromosome separation” pathway is *ARID1A*-regulated in mouse and human cells

“Spindle assembly and chromosome separation” was the most enriched pathway (FDR = 3.2×10^{-9}) among the 177 genes that were *ARID1A*-regulated in mouse uterus, MEFs and IOSE4 cells. Red “thermometer” bars highlight the DEG that drive pathway enrichment. Analysis performed and graph created using MetaCore (www.genego.com).

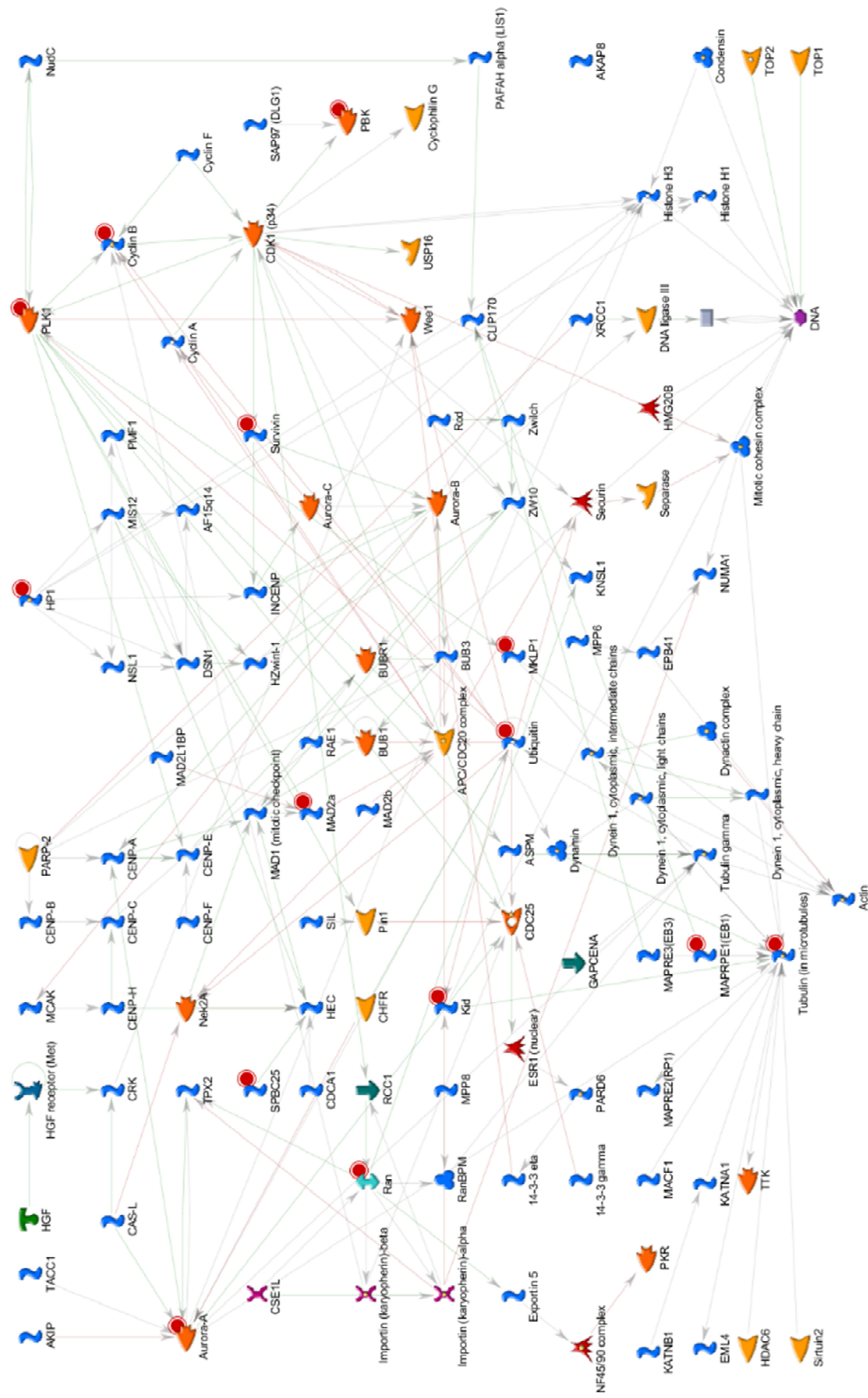


Figure 4.14. The “Mitosis” network is ARID1A-regulated in mouse and human cells

“Mitosis” was the most enriched process network ($FDR = 3.3 \times 10^{-14}$) among the 177 genes that were ARID1A-regulated in mouse uterus, MEFs and IOSE4 cells. Red circles highlight the DEG that drive network enrichment. Analysis performed and graph created using MetaCore (www.genego.com).

Table 4.4. *ARID1A*-regulated genes in all of mouse uterus, MEFs and IOSE4 cells

Gene Name						
ABHD4	CDC20	FBXW2	KIF22	NME4	RASSF4	TMEM150A
ACADM	CDCA3	FEN1	KIF23	NOMO1	RAVER2	TMEM48
ACER3	CDCA8	FHDC1	KLHL24	NSF	RHOBTB3	TMEM97
AKAP12	CDR2	FHL1	LAMP2	NTN4	RNF167	TPI1
AKIRIN1	CENPI	FIGNL1	LANCL1	NUSAP1	RPL22	TSC22D3
ALG1	CENPW	FNBP1	LMNA	PA2G4	RPS27A	TSHZ1
ANKRD10	CIB1	FRAT2	LRP8	PAMR1	RPS6KA5	TUBA1A
ANLN	CLDN1	GALE	LRRC49	PBK	RRM1	TUBB6
ANTXR2	CRELD2	GCAT	LSM2	PDGFRA	RRP12	TXNIP
ANXA3	CTGF	GCLM	MAD2L1	PELI2	RTN3	TYMS
AP1S1	DBF4	GINS2	MAPRE1	PIK3IP1	SERINC2	UBE2K
ARHGEF6	DBI	GLIPR2	MARS	PLEKHA1	SERPING1	UBE2Q1
ARPC5L	DCAF7	GOLM1	MCM10	PLK1	SETD8	UCK2
ATF4	DENND2A	GSG2	MCM4	PLK4	SFXN4	UFC1
ATIC	DEPTOR	GSTA4	MMGT1	POMT2	SH3PXD2B	UHRF1
AURKA	DHCR24	HDLBP	MORF4L2	PPFIBP1	SLC22A5	ULK1
BBS4	DOLPP1	HMGB2	MORN4	PROS1	SLC25A5	USE1
BIRC5	ECHDC2	HN1L	MRPL17	PRRX1	SLC35A2	USP4
BVES	EFTUD2	ID3	MRPS12	PRSS23	SLC35B1	WDR1
CACNB3	ENDOD1	IFIT2	MRPS7	PSAT1	SLC39A11	YIF1A
CBX3	ERLIN2	IFT20	MTHFD2	PSMB2	SLC6A15	ZCRB1
CBX5	FAM83D	IGFBP3	NCAPH2	PUS1	SPC25	
CCNB1	FAM98A	IKBIP	NCKAP5	PVRL3	SRXN1	
CCND1	FAM98C	IRF7	NDRG1	RAD54L	ST5	
CCNDBP1	FBLN1	ITPR2	NFIX	RAN	TCEA2	
CD200	FBXO4	KCNK1	NHP2	RASL11B	TMED10	

4.8. JHOC-5 cells exhibit a different *ARID1A*-driven transcriptional programme

Subsequently, I assessed the effects of *ARID1A* knockdown in JHOC-5 cells, an OCCC cell line with wild type *ARID1A*. My hypothesis was that the effects of *ARID1A* on transcription would be different in a cell line that acquired the hallmarks of malignancy without needing to mutate *ARID1A* compared to normal cells and tissues. siRNA treatment decreased *ARID1A* expression by 75% (see section 2.17.1) and 435 genes were differentially expressed at FDR 0.01. Contrary to the observations in non-malignant cells and tissues, enrichment in cell cycle-related pathways and process networks was not observed (Tables A.9 and A.10 in the

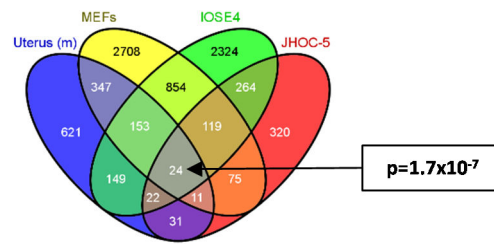


Figure 4.15. Overlap of genes and pathways regulated by ARID1A in mouse uterus, MEFs, IOSE4 and JHOC-5 cells

Overlap of genes regulated by ARID1A in mouse uterus (n=1358), MEFs (n=4291), IOSE4 (n=3909) and JHOC-5 (n=866). Differentially expressed gene lists were created using BeadChip arrays at FDR 0.05.

Appendix). The sole significantly enriched pathway at FDR<0.05 was “ECM remodelling”, driven by changes in expression in genes such as *MMP10*, *MMP7* and *IL8*. The 2 enriched process networks at the same significance level were “Blood Coagulation” (driven by changes in fibrinogen, plasminogen activator and collagen IV) and “Cell-matrix interactions”. Only 24 genes overlapped when the “core” 177-gene list derived from normal cells and tissues was compared with the 866 *ARID1A*-regulated genes at FDR 0.05 in JHOC-5 cells ($p=1.7 \times 10^{-7}$) (Fig. 4.15). MetaCore analysis did not identify any pathways or networks as significantly enriched in this 24-gene set.

4.9. *Arid1a* regulation of *Smarca4*, *Smarca2* and other components of the SWI/SNF and polycomb complexes

There exist well known interactions between the SWI/SNF and polycomb complexes (Wilson et al. 2010); in fact the drosophila *swi/snf* complex was initially discovered during a screen for polycomb repressors (Reisman et al. 2009). As “chromatin modification” was one of the process networks significantly differentially regulated by *Arid1a* in MEFs, I assessed the effect of *Arid1a* knockdown on the expression of core components of the two complexes using the high-confidence list of 2210 genes regulated by *Arid1a* in both the microarray and RNA-seq MEF experiments. Expression changes in 21 *swi/snf* components (Kadoch et al. 2013) and the 3 core polycomb subunits (*Ezh2*, *Suz12* and *Eed*) were compiled. *Smarca2*, *Bcl7a*, *Bcl7b* and *Suz12* were significantly down-regulated whereas *Smarce1*, *Smarcd3* and *Actb* were up-regulated. The enrichment in *swi/snf* and polycomb components (7/24) in the 2210-gene list reached statistical significance ($p=0.024$). I then checked the same 24-gene list in the 1358-

gene uterus and 2738-gene IOSE datasets. *Smarca2* showed concordant changes in the uterus, having significantly higher expression in the “High *Arid1a*” samples. Additionally, *Smarca5*, *Smarca1* and *Eed* showed lower expression in those samples. The only 2 SWI/SNF components showing change in expression upon *ARID1A* knockdown, decrease in both cases, in IOSE4 cells were *BCL7B* and *SMARCC1*.

To further investigate the effects of *ARID1A* loss on the expression of the SWI/SNF complex ATPases and components that could compensate for *ARID1A* (*ARID1B* and *PBRM1*), I knocked down *ARID1A* in PEO1, SKOV3 and JHOC-5 cells and performed qRT-PCR. siRNA treatment successfully depleted *ARID1A* by 73-80% (Fig. 4.16A). *ARID1B* and *PBRM1* expression did not change in any of the cell lines (Fig. 4.16B-C). In contrast, *SMARCA4* mRNA was significantly decreased in PEO1 (21%, $p=0.017$) and JHOC-5 cells (27%, $p=0.015$) (Fig. 4.16D) and *SMARCA2* in PEO1 only (31%, $p=0.009$) (Fig. 4.16E). Taken together, the cell line and microarray results show no changes in the expression of the potentially complementing subunits *ARID1B* and *PBRM1* upon *ARID1A* knockdown in any of the non-malignant or

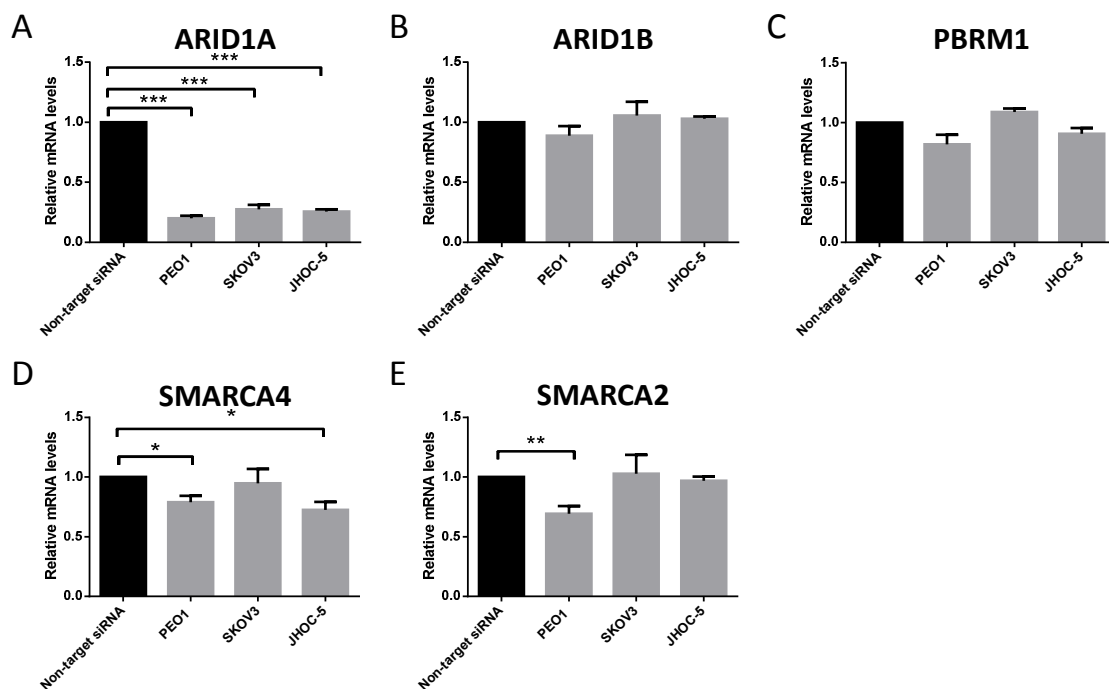


Figure 4.16. Effect of *ARID1A* knockdown on *ARID1B*, *SMARCA4* and *SMARCA2* expression

ARID1A was knocked down using siRNA and RNA collected after 72 hours for qRT-PCR (n=5 biological replicates). A) Mean \pm S.E. *ARID1A* mRNA levels after knockdown. B-E) Mean \pm S.E. *ARID1B* (B), *PBRM1* (C), *SMARCA4* (D) and *SMARCA2* (E) mRNA levels after *ARID1A* knockdown.

malignant cells tested. However, in some, but not all, cases, reduction in *ARID1A* expression leads to suppression of expression of the core ATPases and other members of the complex, at least at the mRNA level and in a cell context-specific manner.

4.10. *Arid1a*'s effect on proliferation is cell type specific

Pathways and networks related to cell cycle control emerged as enriched in *ARID1A*-regulated genes in my gene expression experiments. However, there was no correlation between *Arid1a* and Ki67 expression in the estrus-timed mouse uterus samples (see section 4.2.4). Therefore, I then investigated the effects of *ARID1A* knockdown on proliferation in mouse tissues and cells and human cell lines, hypothesising that these will be tissue and context-specific.

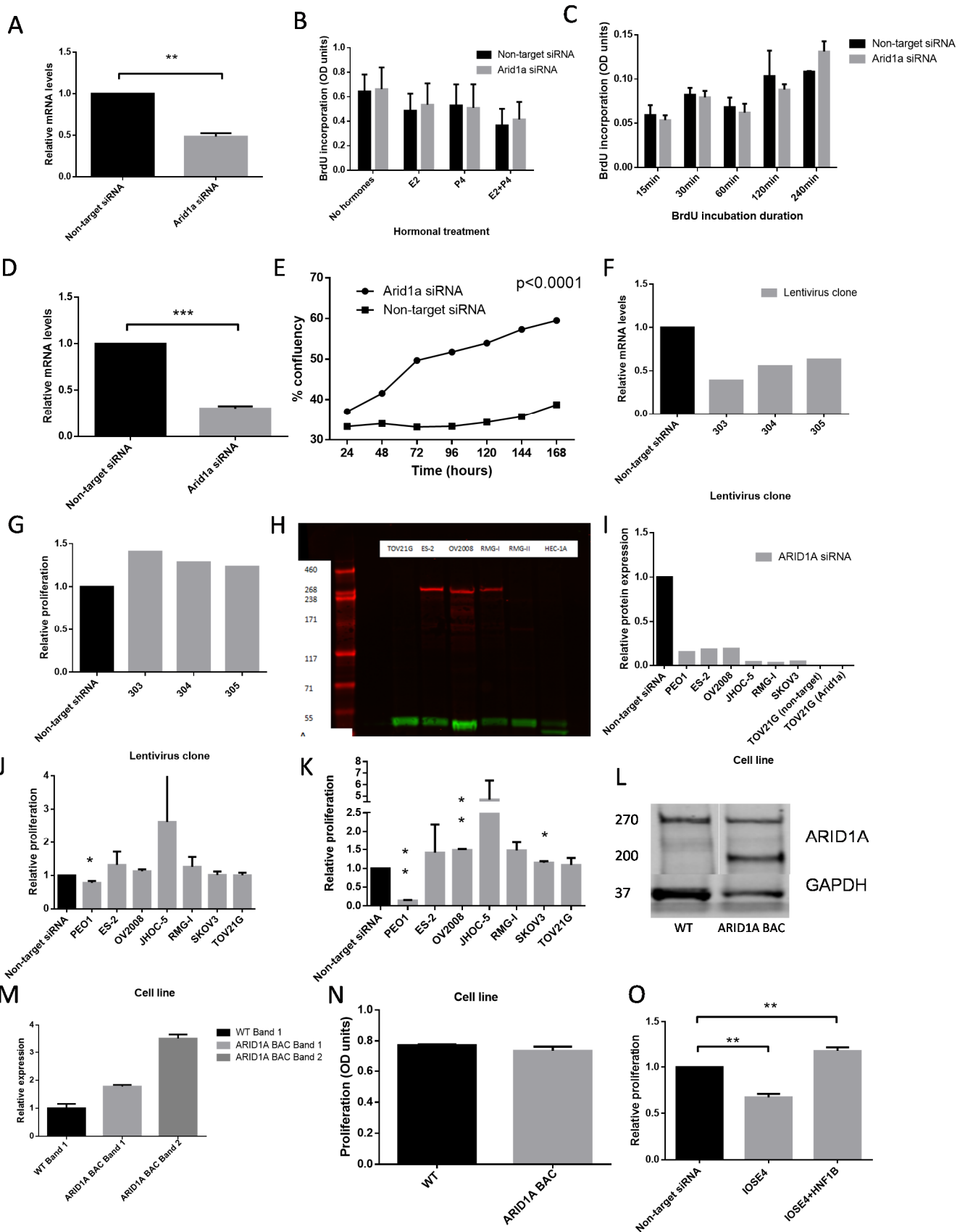
4.10.1. *Arid1a* knockdown does not increase proliferation in cultured mouse uterine stromal cells

First, I utilised siRNA to knock down *Arid1a* in cultured dissociated uterine stromal cells from CD-1 mice. In 5 separate experiments, a mean 52% reduction in *Arid1a* mRNA levels by qRT-PCR was achieved (Fig. 4.17A). There was no effect on proliferation, as assessed by a BrdU incorporation assay after 24 hours of incubation with BrdU (Fig. 4.17B). This observation was

Figure 4.17. Effect of *ARID1A* knockdown on proliferation

ARID1A was knocked down using siRNA (except for panels F-G) for the mouse and human sequences as appropriate: A) Mean \pm S.E. *Arid1a* mRNA levels in primary mouse uterine stromal cells 72 hours after knockdown (n=5). B) Mean \pm S.E. BrdU incorporation 72 hours after *Arid1a* knockdown in cultured primary mouse uterine stromal cells (n=5). Cells have been treated with 10nM E₂ and/or 1 μ M P₄ and incubated with BrdU for 24 hours. C) Mean \pm S.E. BrdU incorporation 72 hours after *Arid1a* knockdown in cultured primary mouse uterine stromal cells (n=3 technical replicates). Cells have received no hormonal treatment and incubated with BrdU for 15-240min. D) Mean \pm S.E. *Arid1a* mRNA levels in MEFs 72 hours after knockdown (n=4). E) Mean confluency, assessed on Incucyte, of MEFs over 168 hours after *Arid1a* knockdown. 8,000cells/well, 4 technical replicates for each MEF cell line (n=4). F) Mean *Arid1a* mRNA levels in E21 MEFs 168 hours after transfection with lentiviruses delivering 3 different shRNAs against *Arid1a* (303, 304 and 305; n=1). G) Relative proliferation by the SRB assay in E21 MEFs 168 hours after transfection with lentiviruses delivering shRNA against *Arid1a* (n=1). H) *ARID1A* expression by immunoblot in TOV21G, ES-2, OV2008, RMG-I, RMG-II and HEC-1A cells. Red bands correspond to *ARID1A* and green to GAPDH. I) Relative *ARID1A* protein expression 96 hours after knockdown in EOC cell lines. J) Relative mean \pm S.E. proliferation by the SRB assay of 7 EOC cell lines 96 hours after *ARID1A* knockdown. 4,000cells/well, 4 technical replicates per each flask replicate (n=4). K) Relative mean \pm S.E. proliferation by the SRB assay of 7 EOC cell lines 168 hours after *ARID1A* knockdown. 1,000 cells/well, 4 technical replicates per each flask replicate (n=4). L) *ARID1A* protein expression in SKOV3 cells transfected with empty vector (WT) and an *ARID1A* expressing BAC. Introduction of the *ARID1A* BAC gives rise to two products: Band 1 at the expected WT *ARID1A* size (~270kDa) and Band 2 which is slightly smaller (~200kDa). M) Quantification (Mean \pm S.E.) of *ARID1A* protein expression in transfected SKOV3 cells (n=3). N) Mean \pm S.E. proliferation by the SRB assay of transfected SKOV3 cells after 168 hours. 1,000cells/well, 4 technical replicates per each flask replicate (n=4). O) Relative mean \pm S.E. proliferation by the SRB assay of IOSE4 and IOSE4+HNF1B cells 168 hours after *ARID1A* knockdown. 8,000cells/well, 4 technical replicates per each flask replicate (n=4).

consistent across cells that received no hormonal treatment, or were treated with 10nM E₂, 1μM P₄ or both (Fig. 4.17B). Consistently, no difference in proliferation was seen at earlier timepoints, with BrdU incubation times ranging from 15 min to 4 hours (Fig. 4.17C).



4.10.2. Proliferation is increased in MEFs after *Arid1a* knockdown

Arid1a was also knocked down using siRNA in 4 MEF cell lines (E7, E8, E10 and E11) in triplicate and a mean reduction of 70% in *Arid1a* mRNA expression was seen (Fig. 4.17D). As assessed using the Incucyte imaging system, *Arid1a* knockdown resulted in increased proliferation ($p < 0.0001$ by 2-way ANOVA) (Fig. 4.17E). The absolute difference in confluency was 16.5% ($p = 0.012$) at 72 hours and reached 20.8% ($p = 0.008$) at 168 hours. Consistent results were obtained using the SRB assay to assess proliferation, as siRNA-mediated *Arid1a* knockdown in E21 MEFs ($n = 4$) resulted in a 23% increase in proliferation ($p = 0.047$) (Fig. 4.19B). Similarly, using lentiviral delivery of 3 different shRNAs against *Arid1a* (see section 2.20.3 for details) in E21 MEFs ($n = 1$), a 37-61% reduction in *Arid1a* mRNA expression was seen (Fig. 4.17F), with a concomitant 23-41% increase in proliferation (Fig. 4.17G).

4.10.3. Effect of *ARID1A* knockdown on EOC cell line proliferation

Expression of ARID1A by immunoblotting was tested in the EOC cell lines listed in Table 2.2 and the endometrial cell line HEC-1A which is known to have a truncating *ARID1A* mutation (Guan et al. 2011) (Fig. 4.17H shows examples). The only “OCCC” cell lines expressing ARID1A were ES-2, OV2008, RMG-I and JHOC-5, results consistent with recent publications (Anglesio et al. 2013; Domcke et al. 2013). The histological subtype of ES-2, OV2008 and RMG-I is disputed: ES-2 is undifferentiated with an IHC staining pattern inconsistent with OCCC (Anglesio et al. 2013; Shaw et al. 2004), OV2008 is identical to the cervical adenocarcinoma ME-180 cell line (Korch et al. 2012) and RMG-I is probably HGS (Anglesio et al. 2013). Therefore, the only *bona fide* OCCC cell line expressing ARID1A from this panel is JHOC-5. Additionally, SKOV3, as detailed in section 1.6.2, has characteristics of OCCC and retains expression of ARID1A (Fig. 4.17L) despite having a heterozygous truncating *ARID1A* mutation (Anglesio et al. 2013).

I then performed siRNA knockdown in 5 ARID1A expressing “OCCC” cell lines, the HGS cell line PEO1, as well as in the ARID1A non-expressing TOV21G OCCC cell line as negative control ($n = 4$ per cell line). The knockdown resulted in an 81-97% reduction in ARID1A protein expression compared to non-target siRNA in the 6 ARID1A-expressing cell lines (Fig. 4.17I). SRB assay after 96 hours (Fig. 4.17J) showed reduced proliferation in PEO1 cells (22%, $p = 0.03$), non significant trends towards increased proliferation in ES-2 (32%, $p = 0.62$), OV2008 (13%, $p = 0.12$), RMG-I (26%, $p = 0.54$) and JHOC-5 (162%, $p = 0.41$) and no difference in SKOV3 (2%, $p = 0.97$) and TOV21G cells (1%, $p = 0.94$). The results were similar at 168 hours

(Fig. 4.17K), with PEO1 showing a significant reduction in proliferation (86%, $p=0.0005$). In contrast, proliferation was increased in OV2008 (49%, $p=0.001$) with non-significant changes in ES-2 (42%, $p=0.77$), RMG-I (48% $p=0.11$) and JHOC-5 cells (370%, $p=0.11$). SKOV3 cells showed a numerically small but significant increase in proliferation (15%, $p=0.04$) whereas, as expected, there was no difference in TOV21G cells (9%, $p=0.63$). When RMG-I proliferation was assayed using the Incucyte system, there was a 16.8% increase in proliferation at 96 hours ($p=0.001$), entirely consistent with the SRB assay results (data not shown). In summary, *ARID1A* knockdown shows trends towards increased proliferation in many EOC cell lines but the opposite effect was seen in PEO1 cells.

4.10.4. *ARID1A* overexpression does not affect proliferation in SKOV3 cells

An *ARID1A* BAC was introduced to over-express *ARID1A* in SKOV3 cells as detailed in section 2.21. Immunoblotting showed 2 *ARID1A* bands in the overexpressing cells, one of which was smaller (~200kDa) than the expected (~270kDa) size (Fig. 4.17L) and, therefore, its functionality is uncertain. Quantitative analysis showed that even if that band was disregarded, *ARID1A* expression was increased by 77% (Fig. 4.17M). However, when proliferation was assayed using the SRB assay ($n=4$), no difference was noted (difference in proliferation -5%, $p=0.24$) (Fig. 4.17N). Whether this is because *ARID1A* supra-physiologic concentrations have no incremental proliferation-suppressing effect or because the introduced *ARID1A* was not fully functional due to re-arrangement is unclear.

4.10.5. *ARID1A* effect on proliferation is dependent on the cellular HNF1B status

HNF1B is universally overexpressed in OCCC (Tsuchiya et al. 2003). To investigate whether the effects of *ARID1A* knockdown differ according to the cellular HNF1B status, siRNA was used to knock down *ARID1A* in immortalised ovarian surface epithelium IOSE4 cells and isogenic cells overexpressing HNF1B (IOSE4+HNF1B). Remarkably, *ARID1A* knockdown decreased proliferation by 33% in the former ($p=0.005$) and increased it by 18% in the latter ($p=0.01$) (Fig. 4.17O).

4.11. *In vivo Arid1a* knockout increases proliferation in mouse uterine epithelium

I then tested the effects of *Arid1a* knockout in the mouse uterus in mice carrying *floxed Arid1a* alleles and tamoxifen responsive Cre driven by the *ROSA26* locus. Mice were killed 28 days

after tamoxifen administration and the uteruses harvested. IHC for Arid1a showed ablation in the luminal and glandular epithelium but not consistently in the stroma in *Arid1a^{fl/fl}* mice (Fig. 4.18B). As expected, Arid1a expression was maintained in *Arid1a^{fl/+}* and wild-type mice. There is considerable physiological variability in Ki67 expression in the epithelium in untreated wild type mice (Fig. 4.18A) and the same variability was seen following tamoxifen administration.

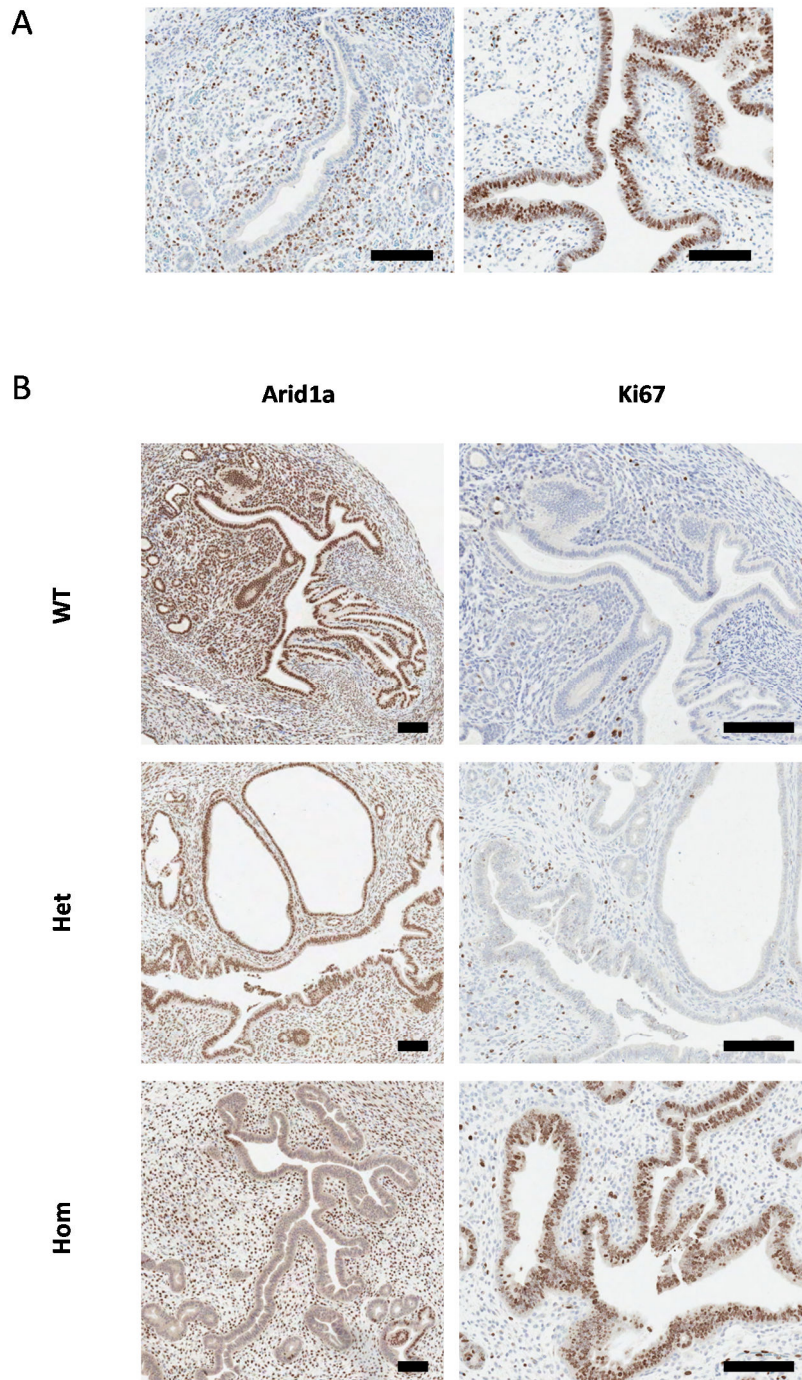


Figure 4.18. *In vivo* effect of *Arid1a* knockdown on mouse uterine epithelium

A) Spectrum of Ki67 staining in untreated, wild type mice. B) Arid1a and Ki67 staining in representative wild type (WT), *Arid1a^{fl/+}* (Het) and *Arid1a^{fl/fl}* (Hom) mice, 28 days after 2mg Tamoxifen was administered i.p. All mice were homozygous for *ROSA26^{Cre-ERT2}* (bar=100µm).

Remarkably however, three of four *Arid1a*^{fl/fl} showed strong, almost ubiquitous Ki67 staining in the uterine epithelium; this was seen in two of four *Arid1a*^{fl/+} mice but only in 1 of 5 wild type ones. Representative photomicrographs are shown in Fig. 4.18B. Similarly, no epithelial Ki67 staining was seen in 3 wild-type mice when, in a different experiment, uteruses were harvested 14 days after tamoxifen administration whereas patchy staining was seen in both *Arid1a*^{fl/fl} mice tested (data not shown).

4.12. ARID1B knockdown affects proliferation but not in a consistent direction

ARID1A and ARID1B are mutually exclusive components of the SWI/SNF complex. ARID1B mutations have been reported in a variety of cancers (Shain & Pollack 2013) but their effect on proliferation is unknown and potentially depends on the ARID1A status of the cells. Using siRNA, I knocked down *Arid1b* in E21 MEFs. qRT-PCR showed that *Arid1b* mRNA expression was reduced by 82% with a compensatory, non-significant 49% increase in *Arid1a* expression (Fig. 4.19A). Proliferation, as assessed by the SRB assay, did not change significantly (24% decrease, p=0.51, n=4) (Fig. 4.19B).

I then determined *ARID1B* expression in EOC cell lines using qRT-PCR as, despite trying multiple different antibodies (see section 2.14 for details), no bands corresponding to ARID1B were seen at immunoblotting. All cell lines tested expressed *ARID1B* at comparable levels with the exception of SKOV3 that had 4-fold higher mRNA expression (Fig. 4.19C). I used siRNA to knock down *ARID1B* in 10 EOC cell lines (n=4 per cell line) with good knockdown efficiency (range 67-87%) (Fig. 4.19D). *ARID1B* knockdown resulted in significant decrease in proliferation after 168 hours in 5 cell lines [PEO1 (32%, p=0.0005), SKOV3 (24%, p<0.0001), TOV21G (31%, p=0.01), JOHC-9 (34%, p=0.001) and OVISE (15%, p=0.01)], no change in 1 cell line [JHOC-5 (0%, p=0.85)] and a significant increase in 4 cell lines [ES-2 (16%, p=0.03), OV2008 (46%, p=0.001), RMG-I (70%, p=0.005) and JHOC-7 (178%, p=0.0003)] (Fig. 4.19E). There was no entirely consistent relationship to *ARID1A* status as of the 4 ARID1A non-expressing cell lines, 3 showed decreased proliferation and one increased. Of the 6 ARID1A expressing lines, 2 showed decreased proliferation, 1 no change and 3 increased proliferation. There was however a trend towards a reduction in proliferation when both ARID1A and ARID1B expression was impaired.

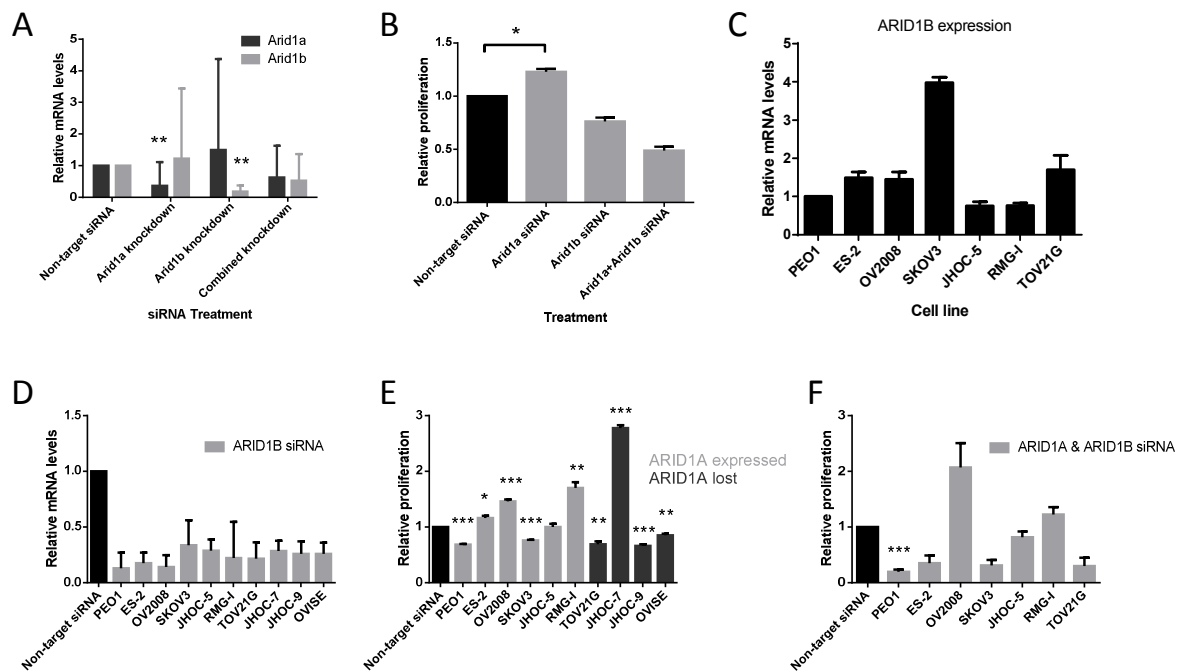


Figure 4.19. Effect of *ARID1B* and combined *ARID1A* and *ARID1B* knockdown on proliferation

ARID1B and both *ARID1A* and *ARID1B* simultaneously were knocked down using siRNA for the mouse and human sequences as appropriate: A) Mean \pm S.E. *Arid1a* and *Arid1b* mRNA in E21 MEFs 96 hours after knockdown (n=2). B) Mean \pm S.E. proliferation by the SRB assay of E21 MEFs 168 hours after knockdown. 8,000cells/well, 4 technical replicates per each flask replicate (n=4). C) Mean \pm S.E. *ARID1B* expression in EOC cell lines, normalised to levels in PEO1 (n=3). D) Relative mean \pm S.E. *ARID1B* mRNA levels 72 hours after knockdown in EOC cell lines (n=3). E) Relative mean \pm S.E. proliferation by the SRB assay of 10 EOC cell lines 168 hours after *ARID1B* knockdown. 1,000 cells/well, 4 technical replicates per each flask replicate (n=4). F) Relative mean \pm S.E. proliferation by the SRB assay of 7 EOC cell lines 168 hours after combined *ARID1A* and *ARID1B* knockdown. 1,000cells/well, 4 technical replicates per each flask replicate (n=4).

4.13. Effect of combined *ARID1A* and *ARID1B* loss on proliferation

To further investigate the consequences of combined *ARID1A* and *ARID1B* loss, I used siRNA to simultaneously knock down *ARID1A* and *ARID1B*. In MEFs, combined knockdown reduced *Arid1a* and *Arid1b* levels by 37% and 47% respectively (Fig. 4.19A), resulting in a non-significant 51% reduction in proliferation (p=0.19, n=4) (Fig. 4.19B). I then knocked down both *ARID1A* and *ARID1B* in the 7 cell lines used for the *ARID1A* knockdown experiment (4.10.3). SRB assay 168 hours after simultaneous knockdown (n=4 per cell line) showed reduced proliferation in PEO1 (mean decrease: 80%, p=0.0003), with trends towards reduction in ES-2 (66%, p=0.11), SKOV3 (69%, p=0.06), JHOC-5 (19%, p=0.18) and TOV21G (70%, p=0.08). The opposite trend was seen in OV2008 (mean increase: 107%, p=0.07) and RMG-I (23%, p=0.18) (Fig. 4.19F). Comparing the results of *ARID1A* (Fig. 4.17K) and combined *ARID1A*

and *ARID1B* (Fig. 4.19F) knockdown, it is evident that combined knockdown was able to reverse the pro-proliferative effect of *ARID1A* loss in ES-2, SKOV3 and JHOC-5 cells but not in RMG-I and OV2008 cells, implying that modulation of *ARID1B* may have therapeutic value in a subset of *ARID1A* mutated tumours.

4.14. Discussion

In this part of my project, I investigated aspects of *ARID1A*'s functional role in normal cells and tissues, including the putative OCCC tissue of origin, the uterus. I have found limited evidence for hormonal regulation of *Arid1a* and describe an *ARID1A*-driven transcriptional programme, conserved across tissues and species, centred on G2/M phase regulation. Knockdown experiments, in a variety of cell types, revealed cell context specific effects of *ARID1A* on proliferation as well as interactions with other components of the SWI/SNF complex such as *ARID1B* and *SMARCA2*.

My data show that there is no systematic variation in *Arid1a* mRNA levels or protein expression during the estrus cycle and, therefore, *ARID1A* expression in the uterus is unlikely to be hormonally regulated. A limitation of my analysis is that I had to combine estrus and metestrus samples due to small numbers. However, when I analysed them separately, the overall pattern did not change, although confidence intervals became wider (data not shown). My observations are supported by the absence of *Arid1a* from a recently published list of 2428 genes with differential expression between proestrus and estrus in CD-1 mice (Yip et al. 2013). If *Arid1a* were hormonally regulated, a potential mechanism for the frequent *ARID1A* mutations in endometriosis-associated cancer could be sought in the abnormal hormonal environment of these lesions (Bulun 2009).

Conversely, prior knowledge would suggest that *Arid1a* regulation of uterine hormonal responses is likely, as components of the SWI/SNF complex, including BAF53 (Jeong et al. 2009), BAF57 (García-Pedrero et al. 2006) and *ARID1A* itself (Inoue et al. 2002) have been shown to be necessary for ER transactivation. My results show that *Arid1a* stromal protein expression can be variable and that it is correlated with ER expression. This observation, which cannot be made from the mRNA data that represents the aggregate expression in epithelium and stroma, provides some limited support for *Arid1a* regulation of oestrogen responses in the uterus. However, my gene expression studies showed no difference in *Esr1* mRNA levels when uterine samples with high and low *Arid1a* mRNA levels were compared.

Moreover, genes implicated in ER signalling do not appear to be *Arid1a*-regulated in the mouse uterus or in human IOSE cells. The observations implicating ARID1A in ER transactivation were made in breast cancer cell lines. It is therefore unclear whether the discrepancy between those and my results reflect differences in ARID1A role in ER regulation in the breast compared to the ovary or uterus or differences in regulation between normal and malignant cells. The differences in ARID1A-driven transcriptional programmes between non-malignant and JHOC-5 cells that I describe, make the latter explanation plausible. Clarification of *Arid1a*'s role in the hormonal regulation in the uterus may be possible by examining the effects of *Arid1a* knockout on ER and PgR expression in a large cohort of mice, work that is being planned. However, in the current GEMM, tamoxifen administration only ablated *Arid1a* in the epithelium (Fig. 4.18). Alternative methods of Cre activation such as intra-uterine adenovirus injection, may successfully ablate *Arid1a* in the stroma as well and facilitate the study of epithelial-stromal interactions. Another unanswered question is whether ARID1A mutations play a role in the transition from the oestrogen-dependent endometriosis state to the oestrogen-independent OCCC state. This question could be answered by manipulating *Arid1a* in the Cheng endometriosis model (Cheng et al. 2011). It would then be important to explore cell-context specific differences in the consequences of ARID1A mutations in oestrogen-independent OCCC and oestrogen-dependent ovarian and endometrial endometrioid carcinomas.

I describe a core ARID1A-driven transcriptional programme that is conserved across non-malignant cells and tissues of different developmental origins and across species. Before discussing the implications of this any further, it is important to note some of the limitations of my analysis. As I have already mentioned, the experimental set-up used to generate the uterus gene expression data (see section 4.3) essentially provides correlational data. However, the remarkable overlap in enriched pathways and networks between uterus, MEFs and IOSE cells provides some assurance that the uterus expression data is enriched with genes regulated by and not just correlated with *Arid1a*. Additionally, the knockdown in IOSE cells, despite leading to the identification of 2938 differentially regulated genes at FDR 0.01, at approximately 50%, was suboptimal. A further limitation is that, whereas the gene expression data generated by using microarrays in MEFs were cross-validated by RNA-seq, no such procedure was performed for the uterus or IOSE data. However, approximately 75% of the genes (2210 of 2971) identified as differentially expressed in MEFs by the microarray were confirmed as such by RNA-seq, and there is no reason to suppose that this proportion would differ significantly for the other microarray experiments. Of course, functional validation of the transcriptome analysis predictions is extremely important, as will be discussed later.

Several observations from the gene expression experiments deserve mention. To the best of my knowledge, no published *ARID1A*-driven transcriptome data exists yet. My data show that *ARID1A* regulates an extensive array of genes with 1358 genes differentially expressed in the mouse uterus (FDR 0.05), 2210 validated genes in MEFs and 2938 in human IOSE cells (both FDR 0.01). These numbers are much higher than the ~150 genes reported to be regulated by *ARID1A* in the hepatocellular carcinoma cell line HEPG2 in unpublished data presented by Dr. J Raab, University of North Carolina, USA.⁶ I found that 435 genes were *ARID1A*-regulated in JHOC-5 OCCC cells at FDR 0.01 in my data. Examination of a larger panel of non-malignant and malignant cells will help clarify whether *ARID1A*-regulates a more restricted subset of genes when modulated in established malignant cell lines compared to normal cells. Furthermore, although *ARID1A* has been described to be associated predominantly with transcriptional repression (Nagl et al. 2007), approximately equal numbers of genes were up- and down-regulated in all my experiments. Second and further-order effects could explain this discrepancy with *ARID1A* directly repressing transcription regulators, the consequences of which could be either repression or expression of their target genes. Analysis of *Arid1a* binding sites in MEFs using ChIP-seq is being planned and could provide important information.

Pathways and networks related to mitotic cell cycle regulation were among the most significantly enriched in mouse uterus, MEFs and IOSE cells when each experiment was analysed independently, despite their different developmental origins. I was able to define a “core” set of 177 genes that showed *ARID1A* regulation in all 3 experiments. Remarkably, the 4 most enriched pathways among these genes were all related to mitosis (“Spindle assembly and chromosome separation”, “The metaphase checkpoint”, “Role of Nek in cell cycle regulation” and “Role of APC in cell cycle regulation”). Of course, this is partly due to overlapping genes defining these pathways, but this does not negate the observation that *ARID1A* appears to play an important role in G2/M regulation. Previous reports have implicated the SWI/SNF complex in kinetochore organisation and regulation of mitosis (Varga-Weisz 2001; Xue et al. 2000). Furthermore, disruption of mitotic checkpoints has been reported to accompany BAF47 (also known as Snf5) (Vries et al. 2005) and SMARCA4 loss (Bourgo et al. 2009). A recent publication shows that SMARCA4 and *ARID1A* are necessary for Topoisomerase II α -mediated DNA decatenation and that disruption of either SWI/SNF component promotes the formation of anaphase bridges and aneuploidy, thus directly

⁶ Presented at the AACR Chromatin and Epigenetics in Cancer Conference (June 19-22, 2013, Atlanta, GA, USA).

implicating ARID1A in the mitotic mechanism (Dykhuisen et al. 2013). My data also point towards further inter-dependencies between Topoisomerase II α and ARID1A as *Top2a* expression was significantly downregulated (log₂-fold change -0.66 in the microarray, -0.79 in RNA-seq) in MEFs following *Arid1a* knockdown. However, this was not seen in the mouse uterus and IOSE datasets. The observation that, in 3T3 cells, *Arid1a* expression is down-regulated at prophase and completely disappears by metaphase (Flores-Alcantar et al. 2011), is consistent with my data and, together, suggest a model where *ARID1A* loss abrogates the G2/M checkpoint. These predictions require validation at the protein level and by cell-cycle analysis. An expedient way to perform these experiments would be to create MEFs from - *ROSA26^{Cre-ERT2}-Arid1a^{fl/fl}* mice and use tamoxifen to ablate *Arid1a* expression *in vitro*, work that is being planned.

As detailed in section 1.3.1.2, *ARID1A* mutations tend to co-occur with PI3K pathway aberrations in many tumours, including OCCC (Jones et al. 2010; Yamamoto et al. 2012b) and endometrial cancers (Liang et al. 2012). Additionally, studies in endometrial cancer (Liang et al. 2012) have shown functional activation of the PI3K pathway in the presence of *ARID1A* mutations even in the absence of PI3K pathway mutations. Conversely, *ARID1A* overexpression in the glioblastoma U87 cell line decreased expression of pAKT and pS6K (Zeng et al. 2013). My gene expression data did not show differential expression of the major PI3K pathway genes (*Pten*, *Pik3ca*, *Pik3r1*, *Akt*, *Torc1*, *Rps6kb1*, *Tsc1*, *Tsc2*, *Gsk3b*) in either the MEFs or the uterus (data not shown). Of these genes, only *TSC1* was down-regulated after knockdown in IOSE and none was in JHOC-5 cells. Whether this is because of differences between mRNA expression and stabilisation or activation of protein products is unclear. However, some accessory components (*Pik3r3*, *Pik3ip1*, *Pik3cb*, *Pik3cd*), appear to be *Arid1a*-regulated in at least one of the normal tissues studied. Detailed functional studies are needed to examine whether *ARID1A* loss in normal tissues activates the PI3K pathway. It is possible that other co-operating events are needed for this activation to occur; these could be present in malignant but not normal cells.

Differences in *Arid1a* transcriptional programmes between different tissues also exist. Taking the mouse uterus and MEF data as an example, pathways related to apoptosis were prominent among the former but not the latter (Table A.1). Additionally different developmental pathways were enriched in the two datasets (Tables A.1 and A.3). This points towards tissue and cell-type specific *Arid1a*-driven transcriptional programmes on top of its more generic effects on the cell cycle. However, pathway and network analysis using the list of 802 genes

that were *Arid1a*-regulated in the uterus, but not the MEFs, did not show any enriched pathways or networks at FDR<0.05 (data not shown), implying that *Arid1a*-driven cell type specific transcriptional programmes rely more on variations of the core programme than on regulation of entirely different sets of genes.

Examination of *ARID1A*-regulated genes in the OCCC JHOC-5 cells did not show enrichment for the cell cycle or cytoskeleton-related genes that predominated in normal cells and tissues. In fact, despite 435 genes being reported as differentially regulated, very few specific pathways and networks were identified as enriched. This underscores the fact that, when studying putative early events in carcinogenesis, examination of gene function in normal and pre-malignant tissues can provide more valuable insights compared with aggressive malignant cell lines that have achieved the hallmarks of malignancy without the need to mutate the gene of interest.

ARID1A knockdown resulted in decreased *SMARCA4* and *SMARCA2* mRNA levels in 2 EOC cell lines (PEO1 and SKOV3) as well as in MEFs. Additionally, *Smarca2* mRNA levels were lower in the “Low *Arid1a*” compared with the “High *Arid1a*” uterine samples. These observations imply regulation of the SWI/SNF complex ATPases by *ARID1A*. A preferential association of *ARID1A* with either *SMARCA4* or *SMARCA2* is not thought to exist (Nagl et al. 2007). However, my results are consistent with unpublished observations from our group (Ms. Charlotte Sutherland) that show *SMARCA2* protein expression is not detected in 7 out of 8 OCCC cell lines with absent *ARID1A* expression and warrant further confirmation.

My results show that in the majority of cancer cell lines tested (5 of 6), *ARID1A* knockdown increases proliferation and the same effect was seen in MEFs. This is consistent with observations in hepatocellular carcinoma cell lines (Huang et al. 2012) and immortalised ovarian epithelium lines (Guan et al. 2011). However, I show that this is not a universal phenomenon as PEO1 cells exhibited decreased proliferation following knockdown. PEO1 is a HGS cell line that carries *TP53* and *BRCA2* mutations (Ng et al. 2012). However, knockdown of *ARID1A* increased proliferation in other cell lines that are probably HGS (RMG-1) or carry *TP53* mutations (SKOV3). Examination of a larger panel of cell lines is needed to clarify whether PEO1 is a rare exception to a rule of increased proliferation after *ARID1A* knockdown in cancer cell lines. Supporting this notion, re-expression of *ARID1A* in mutated cell lines (OVISE and HEC-1A) decreased proliferation (Guan et al. 2011). Consistently with results in JHOC-5 cells (Guan et al. 2011), I found no change in proliferation when *ARID1A* was

overexpressed in SKOV3, a cell line with normal ARID1A expression. In contrast, reduction in proliferation was reported after ARID1A overexpression in U87 cells (Zeng et al. 2013); again overexpression in a wider range of cell lines will be needed to clarify the frequency of such phenomena. It should be noted however that, on average, the changes in proliferation upon *ARID1A* knockdown are modest compared to the effects of *HNF1B* knockdown (see section 5.3) or glycogen metabolism perturbations (see sections 6.6 & 6.7). Additionally, the effect of *ARID1A* knockdown on proliferation was modified by HNF1B in at least one pair of isogenic cell lines, a matter that will be further discussed in the next chapter.

Contrary to the observations in cell lines, siRNA targeting of *Arid1a* did not increase proliferation in cultured mouse uterus stromal cells, despite efficient gene knockdown. A limitation of this experiment is that a different assay, based on BrdU incorporation, was used to assess proliferation rather than the SRB assay used in the cell line experiments. However, the assay was able to detect different proliferation rates after hormonal treatments of the cells (Fig. 4.17B) and therefore, lack of assay sensitivity is an unlikely explanation for these results. Also, the lack of negative correlation between stromal *Arid1a* and Ki67 expression (Fig. 4.2E-F) provides support for the BrdU assay results. It would be interesting to know the effects of *Arid1a* knockdown in uterine epithelial cells, since they are the most likely source of the cells that eventually undergo malignant transformation. However, the dissociation protocol only produced small numbers of epithelial cells in strips and clumps (compare Fig. 3.3C and 3.3E) that made accurate proliferation assays difficult to perform.

Impressively, *in vivo Arid1a* knockout resulted in almost ubiquitous epithelial staining for Ki67 28 days later in 75% of the mice examined compared to 20% of wild type mice, with heterozygous mice showing intermediate results. This very important observation suggests the possibility of a proliferative advantage for an endometrial epithelium clone with early ARID1A loss that could contribute to malignant transformation and needs to be further verified in a larger series. In this regard, a recent conference report showed that isolated *Arid1a* ablation in the ovarian epithelium via intrabursal adeno-Cre injection did not result in tumour formation. However, undifferentiated tumours formed in 40% of mice after combined *Arid1a* and *Pten* ablation (Guan et al 2013).

Nevertheless, in their totality, the proliferation assays described above once more highlight the fact that the effects of knocking down a specific gene may be different in cells that have already achieved all the hallmarks of malignancy via other routes, compared with genomically

normal cells. This is particularly relevant in the study of putative early events in carcinogenesis such as *ARID1A* loss.

Until very recently, the effects of *ARID1B* knockdown on proliferation had not been reported. I knocked down *ARID1B* in a panel of 10 EOC cell lines and found decreased proliferation in 5 cell lines, increased in 4 and no change in 1. Three of 4 cell lines with no *ARID1A* expression showed reduction in proliferation after *ARID1B* knockdown. This was supported by the results of simultaneous knockdown of both *ARID1A* and *ARID1B* in cell lines expressing both proteins. Simultaneous knockdown in that experiment was able to reverse the pro-proliferative effect of *ARID1A* knockdown in 3 of 5 cell lines, suggesting that most cells need at least one of the 2 *ARID1* components for survival and that targeting *ARID1B* may be a therapeutic strategy in cells with *ARID1A* mutations. However, this is not a universal phenomenon as simultaneous knockdown markedly accelerated proliferation in OV2008 cells (compare Fig. 4.17K and 4.19E-F) and mutations in both *ARID1A* and *ARID1B* have been reported in some tumours (Shain & Pollack 2013). Very recently, it was reported that *ARID1B* was required for survival of *ARID1A*-mutated cell lines, in agreement with my results (Helming et al. 2014). It appears therefore, that a synthetically lethal relationship between *ARID1A* and *ARID1B* may exist. A similar relationship has been reported for the 2 ATPases of the complex, *SMARCA4* and *SMARCA2* (Hoffman et al. 2014), and data from our laboratory point towards interactions between *ARID1A* and the ATPases as many OCCC cell lines concomitantly lack expression of *ARID1A* and *SMARCA2*. It is important to identify whether that renders them particularly reliant on *SMARCA4* and work to clarify this is ongoing in our group.

An important premise of my project was that functional characterisation of *ARID1A* may identify potential therapeutic vulnerabilities of OCCC. The “core” transcriptional programme I describe is driven by activation of cell cycle and mitotic kinases such as Cyclin B, Cyclin D, Polo like kinases and Aurora Kinase A. Drugs targeting these kinases are in various states of development (Li et al. 2013; Rocca et al. 2014; Umene et al. 2013). Additionally, *PDGFRA* (Table 4.4), targeted by drugs such as sunitinib, imatinib and nintedanib, is part of the “core” *ARID1A* transcriptional programme. It will be important to test the effect of these drugs in *ARID1A*-mutant OCCC cell line models.

In conclusion, the observations presented in this chapter, for the first time, describe *ARID1A*-driven transcriptional programmes and point towards a pro-proliferative role for *ARID1A* mutations in the majority of cases. An immediate priority is to study in much greater depth the

consequences of *Arid1a* knockout in the uterus, by performing gene expression studies and ChIP-seq in samples from the *ROSA26^{Cre-ERT2}-Arid1a^{fl/fl}* mice. Additionally, we have already begun preparatory work (in collaboration with the Charnock-Jones laboratory, led by Dr. Claire Dawson) in order to conditionally knock out *Arid1a* in the Cheng endometriosis model. Detailed description of the consequences of *Arid1a* loss in an endometriotic background holds great promise in identifying novel drivers and therapeutic targets in OCCC. Furthermore, *Arid1a* mutations in the Cheng model may lead, alone or in combination with introduction of mutations in further genes such as *Pik3ca* and overexpression of *Hnf1b*, to a much needed GEMM of OCCC.

5. ROLE OF HNF1B IN THE OCCC PHENOTYPE

5.1. Introduction

HNF1B is overexpressed, through epigenetic mechanisms (Pharoah et al. 2013), in the vast majority of OCCC (Kato et al. 2006; Kato & Toukairin 2007; Tsuchiya et al. 2003) and is one of the signature characteristics of this malignancy. As detailed in section 1.3.2.3, *HNF1B* has been reported to be one of the main drivers of a gene expression profile that distinguishes OCCC from other ovarian cancers (Okamoto et al. 2013; Senkel et al. 2005). Germline *HNF1B* mutations are the cause of a rare form of diabetes, MODY 5 (Ma et al. 2007), and *HNF1B* regulation of multiple genes involved in glucose metabolism and glycolysis has been convincingly shown (Cuff et al. 2013; Okamoto et al. 2013; Uekuri et al. 2013). These observations have led to the conclusion that HNF1B underpins glycogen accumulation in OCCC, although this has not been directly demonstrated.

As discussed in section 1.3.2.3, a limitation of our understanding of the *HNF1B*-driven transcriptional programme is that most data were derived following *HNF1B* overexpression in embryonic kidney (HEK293) cells (Cuff et al. 2013; Senkel et al. 2005). Until very recently, the only data derived from a putative OCCC cell line utilised SKOV3 cells (Tomassetti et al. 2008) and showed regulation of EMT-related genes by *HNF1B*. While this project was underway, a study reported on gene expression profiles following *HNF1B* knockdown in RMG-I and RMG-II cells (Okamoto et al. 2013). However, these authors reported that *HNF1B* knockdown increased proliferation in these 2 cell lines (Okamoto et al. 2013), a finding that contradicts observations in IGROV1 and SKOV3 cells (Tomassetti et al. 2008) and is inconsistent with the induction of apoptosis after *HNF1B* knockdown in TOV21G and JHOC-5 cells (Tsuchiya et al. 2003).

In this part of my project, I tested the hypothesis that HNF1B drives proliferation in OCCC, and that the reported findings in RMG-I and RMG-II cells (Okamoto et al. 2013) are atypical, by studying the effects of *HNF1B* knockdown in a panel of 6 OCCC cell lines. I then investigated in detail the *HNF1B*-driven gene expression programme in 2 *bona fide* OCCC cell lines, JHOC-5 and TOV21G, as previous gene expression profiles have been derived from cell lines that are either not widely accepted as representative of OCCC (SKOV3), are probably not OCCC [RMG-I (Anglesio et al. 2013)], or show an atypical increase in proliferation after *HNF1B* knockdown [RMG-I and RMG-II (Okamoto et al. 2013)]. Guided by the results of the

expression profiling, I hypothesised that HNF1B overexpression decreases migration and invasion and tested this, using scratch wound and Boyden chamber assays. Spurred on by the associations of *HNF1B* mutations and diabetes and the recently published data using RMG-II cells (Okamoto et al. 2013), I next asked whether HNF1B drives the Warburg effect and glycogen accumulation in JHOC-5 cells.

5.2. HNF1B expression in OCCC cell lines

I first confirmed HNF1B expression by immunoblots in 6 OCCC cell lines (TOV21G, SKOV3, JHOC-5, JHOC-7, JHOC-9 and OVISE) whereas, as expected, the HGS cell line PEO1 did not express HNF1B (Fig. 5.1A). Quantification of protein expression showed that there was only limited variation in expression among the 6 cell lines, with the highest expressing one, OVISE, showing two-fold higher expression than the lowest, TOV21G (Fig. 5.1A). qRT-PCR confirmed expression at the mRNA level in OVISE, TOV21G and RMG-I cells, whereas PEO1, ES-2 and OV2008 did not show expression (data not shown). This observation casts further doubt on the provenance of the last two lines that have commonly been used as OCCC cell models.

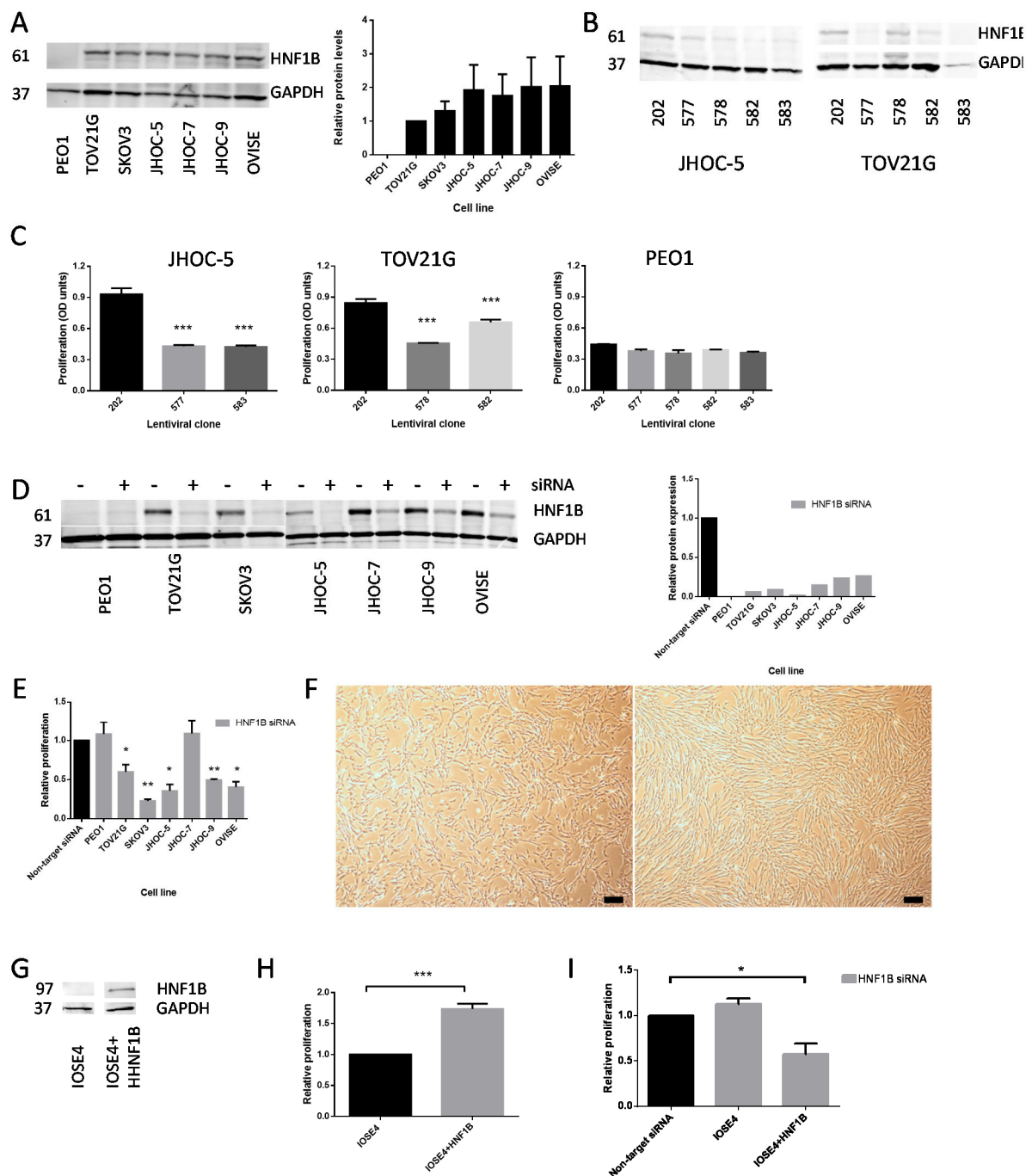
5.3. HNF1B drives proliferation in OCCC cell lines and immortalised ovarian epithelium

I then used lentiviruses expressing shRNA targeting *HNF1B* (clones 577, 578, 582 and 583) or non-targeting shRNA (clone 202) to stably knock down *HNF1B* expression in JHOC-5 and

Figure 5.1. HNF1B expression and effect on proliferation

A) HNF1B expression in cell lines. The left side panel shows a representative immunoblot whereas the right side panel shows mean \pm S.E. protein expression quantification relative to TOV21G (n=3). B) Representative immunoblot after shRNA *HNF1B* knockdown in JHOC-5 and TOV21G cells (202: Non-targeting shRNA; 577, 578, 582 and 583: shRNAs targeting *HNF1B*). C) Mean \pm S.E. proliferation by the SRB assay of JHOC-5, TOV21G and PEO1 cells stably transfected with *HNF1B*-targeting shRNAs (transient transfection for PEO1) after 168 hours in culture. 1,000cells/well, 4 technical replicates per each flask replicate (n=4). D) HNF1B protein expression 72 hours after siRNA-mediated *HNF1B* knockdown. The left side panel shows the immunoblot and the right side panel quantification of protein expression relative to non-targeting siRNA. E) Relative mean \pm S.E. proliferation by the SRB assay of 7 EOC cell lines 168 hours after *HNF1B* knockdown. 1,000cells/well, 4 technical replicates per each flask replicate (n=4). F) Morphological appearance of parental IOSE4 (left) and IOSE4 cells overexpressing HNF1B (right) (bar=100 μ m). G) HNF1B protein expression by parental IOSE4 and overexpressing IOSE4+HNF1B cells. The increase in the apparent HNF1B size is due to the GFP tag. H) Relative mean \pm S.E. proliferation by the SRB assay of IOSE4 and IOSE4+HNF1B cells after 168 hours in culture. 1,000cells/well, 4 technical replicates per each flask replicate (n=4). I) Relative mean \pm S.E. proliferation by the SRB assay of IOSE4 and IOSE4+HNF1B cells 168 hours after siRNA *HNF1B* knockdown. 1,000cells/well, 4 technical replicates per each flask replicate (n=4).

TOV21G cells as detailed in section 2.20.2. Protein expression was assessed after puromycin selection for 7 days (Fig. 5.1B). The effect of knockdown on proliferation was then assayed in 4 separate experiments in 2 clones per cell line, by the SRB assay. Knockdown resulted in significant decrease in proliferation after 168 hours in both JHOC-5 and TOV21G cells (both $p < 0.0001$ by 1-way ANOVA) (Fig. 5.1C). Compared to clone 202, proliferation was decreased by 57% and 58% using clones 577 and 583 in JHOC-5 and by 55% and 34% using clones 578 and 582 in TOV21G cells. Transient shRNA *HNF1B* knockdown, using all 4 clones, did not decrease proliferation in the non-*HNF1B* expressing PEO1 cells (Fig. 5.1C). I then assayed the effect of transient *HNF1B* knockdown using siRNA in a wider panel of cell lines,



including PEO1 as a negative control. Treatment with *HNF1B*-targeting siRNA resulted in a 74-98% reduction in protein expression at 72 hours (Fig. 5.1D). Proliferation was then assayed in a manner identical to the shRNA-mediated knockdown. There was a significant decrease in proliferation in 5 of the 6 OCCC cell lines tested (Fig. 5.1E). Proliferation decreased by 40% ($p=0.04$) in TOV21G and 64% ($p=0.03$) in JHOC-5 cells, mirroring the results obtained by shRNA treatment. Furthermore, it decreased by 77% ($p=0.01$) in SKOV3, 51% ($p=0.007$) in JHOC-9 and 60% ($p=0.02$) in OVISE cells. JHOC-7 proliferation was not affected by *HNF1B* knockdown (9% difference, $p=0.78$) nor was, as expected, PEO1 proliferation (8% difference, $p=0.46$).

Next, I investigated the effects of HNF1B overexpression in the immortalised ovarian surface epithelium IOSE4 cell lines. Compared to the parental IOSE4 cells, IOSE4+HNF1B cells assume a more elongated shape (Fig. 5.1F) and express HNF1B (Fig. 5.1G). Using an identical set-up for the SRB assay to that utilised for the OCCC cell lines, induction of *HNF1B* expression in IOSE4 cells increased proliferation by 74% ($p=0.0005$) (Fig. 5.1H). As expected, siRNA-mediated *HNF1B* knockdown decreased proliferation back to baseline levels in IOSE4+HNF1B cells, but had no effect on IOSE4 cells (Fig. 5.1I).

These results support a proliferation-promoting role for *HNF1B* in both OCCC and IOSE, in accordance with previous observations (Tomassetti et al. 2008; Tsuchiya et al. 2003).

5.4. HNF1B gene expression profiling

I then asked whether pathways and genes reported to be *HNF1B*-regulated in the literature were indeed so in the *bona fide* JHOC-5 and TOV21G OCCC cell lines. As detailed in section 2.17.2, cells stably transfected with lentiviruses carrying non-targeting or *HNF1B*-targeting shRNA were assayed with Beadchip arrays, using four flask replicates per cell line. I first analysed results for each cell line separately, to gain an understanding of the variability of the *HNF1B*-driven transcriptional programme across different cell lines.

5.4.1. HNF1B regulates EMT and cell adhesion in JHOC-5 cells

Hierarchical clustering of the array samples showed that they clustered by treatment type, indicating that the type of shRNA used (*HNF1B* vs. non-targeting) was the most significant driver of the differences in the expression profiles (data not shown). Volcano plots and

heatmaps based on 2919 genes differentially expressed at FDR 0.01 are shown in Fig. 5.2A-B. Approximately equal numbers of genes were up (1452) and down-regulated (1467) after *HNF1B* knockdown. I then carried out pathway analysis, using MetaCore, which showed that more than 50 pathways were enriched in differentially regulated genes at FDR<0.01 (Table A.11 in the Appendix). Pathways related to EMT, WNT signalling and cell adhesion [“Regulation of EMT (Fig. 5.3)”, “WNT signaling pathway”, “Chemokines and adhesion”, “ECM remodelling”, “TGF, WNT and cytoskeletal remodelling” and “TGF-beta-dependent induction of EMT via RhoA, PI3K and ILK”] occupy 6 of the top 7 places. Among others, genes involved in these pathways that were *HNF1B*-regulated are 3 WNT ligands (*WNT2B*, *WNT7A* and *WNT7B*), 3 Frizzled receptors (*FZD2*, *FZD7* and *FZD8*) and growth factor receptors (*EGFR*,

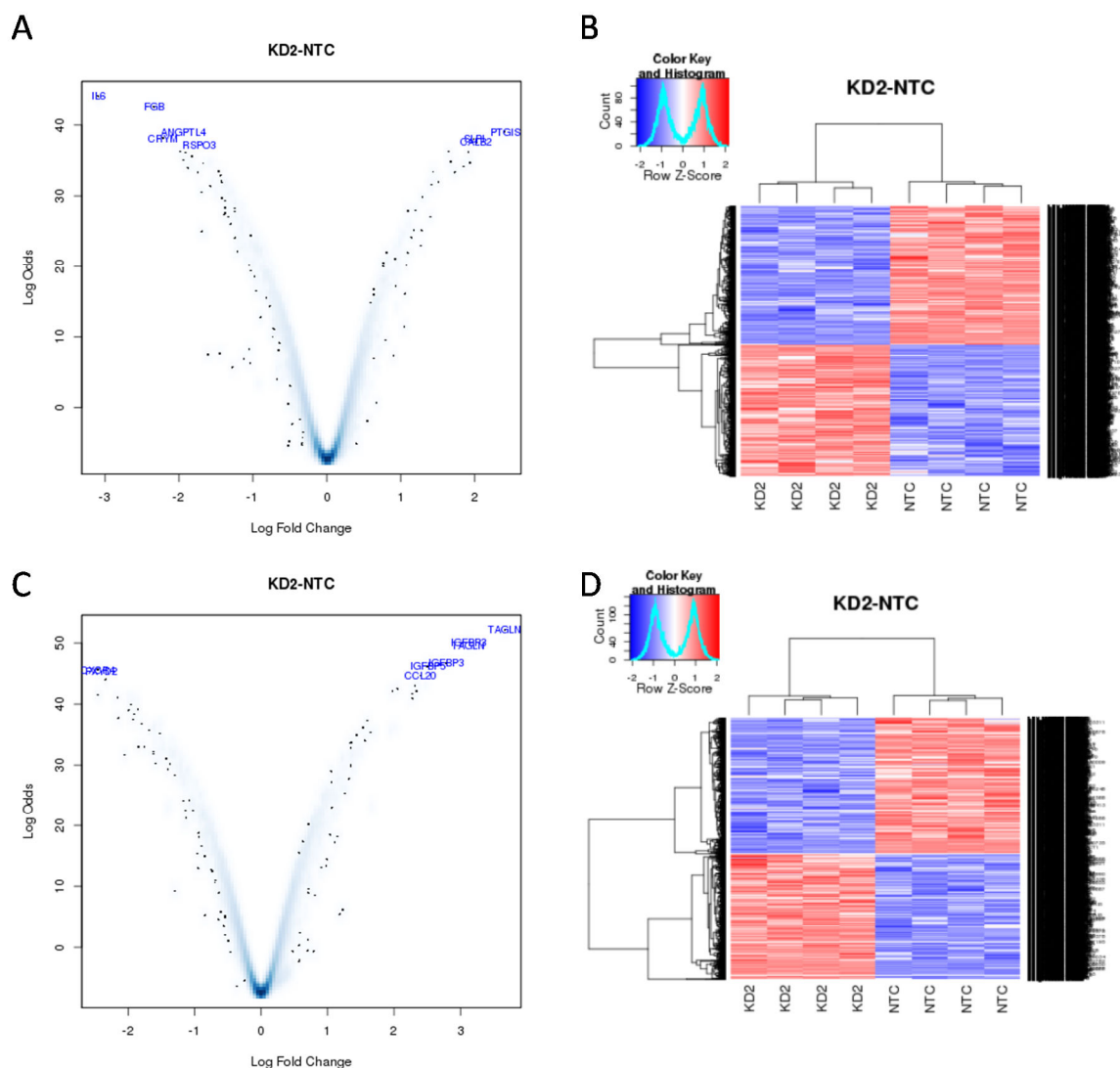


Figure 5.2. *HNF1B* gene expression array in JHOC-5 and TOV21G cells

Gene expression was assayed using BeadChip arrays in JHOC-5 and TOV21G cells stably transfected with non-targeting shRNA (NTC) or shRNA targeting *HNF1B* (KD2). (n=4 flask replicates per clone). A, C) Volcano plots (log₂-fold change vs. log odds) showing the top 8 differentially expressed genes in JHOC-5 (A) and TOV21G (C) cells. B, D) Heatmaps for the KD2 vs. NTC comparisons in JHOC-5 (B) and TOV21G (D) cells.

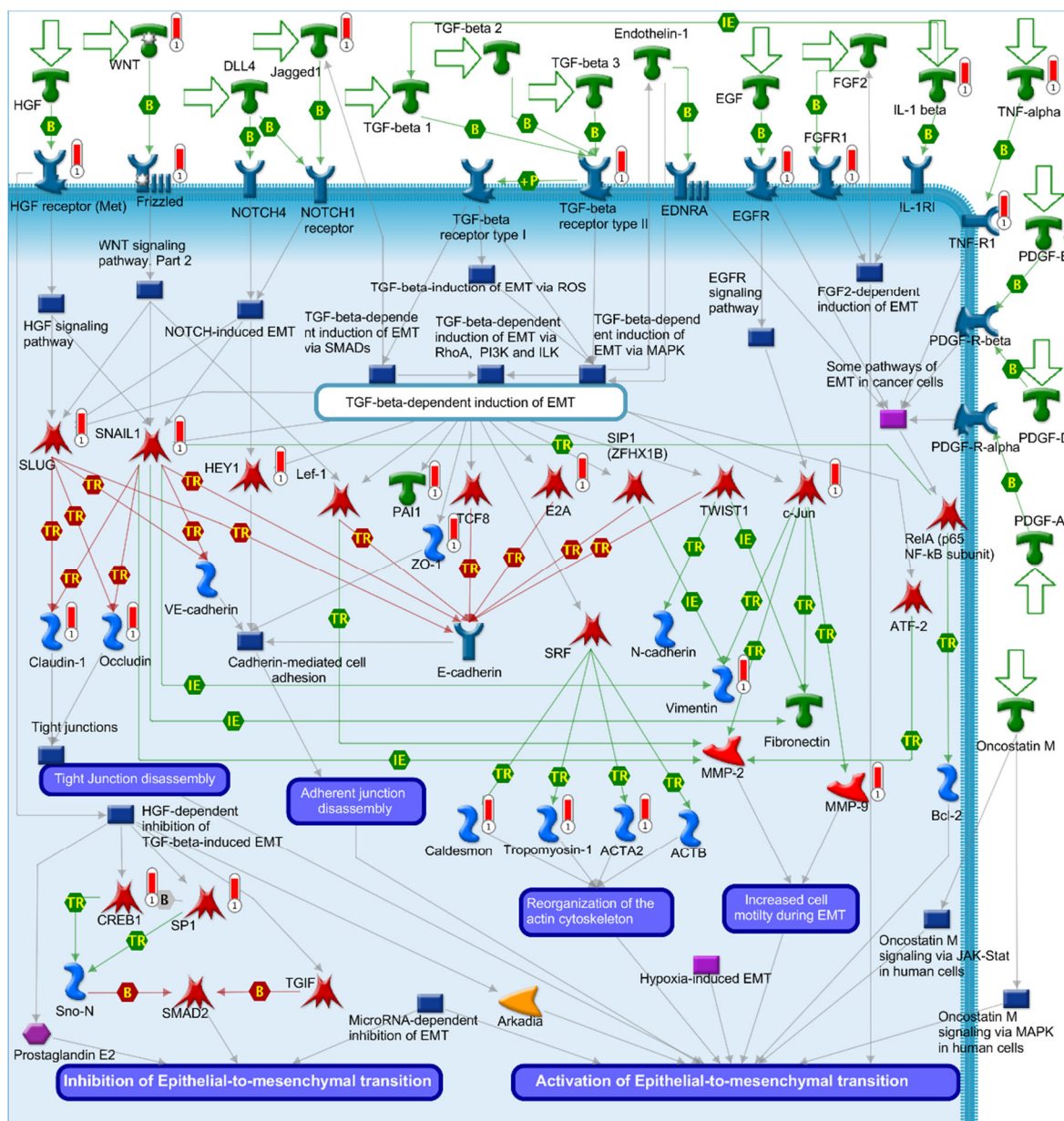


Figure 5.3. The “Regulation of epithelial-to-mesenchymal transition” pathway is *HNF1B*-regulated in JHOC-5 cells

“Regulation of epithelial-to-mesenchymal transition” was the most enriched pathway (FDR = 6.35×10^{-8}) following shRNA knockdown of *HNF1B* in JHOC-5 cells (n=4). Differentially expressed gene (DEG) lists (n=2919) were created at FDR 0.01. Red “thermometer” bars highlight the DEG that drive pathway enrichment. Analysis performed and graph created using MetaCore (www.genego.com).

FGFR1, *MET* and *TGFBR2*). Genes encoding downstream transcription factors such as *TCF3*, *TCF4*, *JUN*, *SP1*, *CREB*, *MYC*, *SP1*, *SNAIL1* (encoding SNAIL) and *SNAIL2* (encoding SLUG) as well as proteins involved in EMT [e.g. *MMP9*, *VIM* (encoding Vimentin), *CLDN1* (encoding Claudin-1) and *CTNNB1* (encoding β -catenin)] also showed expression changes. *HNF1B* also appeared to positively regulate the expression of multiple members of the interleukin family (e.g. interleukin 1 α , 1 β , 6, 8 and 23 α) and regulate members of the NF- κ B

pathway (e.g. *NFKB2*, *NFKB1A*, *NFKB1B* and *IKBKG*), which was reflected in the presence of multiple pathways related to immune response among the enriched pathways in Table A.11. In fact, *IL6* was the single most down-regulated gene following *HNF1B* knockdown, showing an 8.5-fold reduction in expression.

Process network analysis showed that 34 networks were enriched in *HNF1B*-regulated genes at FDR<0.01 (Table A.12 in the Appendix). “Mitosis” was the most enriched network, driven by changes in expression in *CCNA1* (encoding Cyclin A), *CCNB1*, *CCNB2*, *CDC25B* and *CDC25C*. Interestingly, an “ESR1-nuclear pathway” network was also enriched (FDR=0.0005), driven by changes in expression of ER-associated transcription factors such as *FOS*, *JUN* and *FOXA1* and ER chaperones such as *FKBP2*. Furthermore, a “Chromatin modification” network was significantly enriched (FDR=0.0005). SWI/SNF components (*ARID1B*, *SMARCA4*, *SMARCB1*, *SMARCC1* and *SMARCD3*) were negatively regulated by *HNF1B*, raising the possibility of an interaction between HNF1B and ARID1A in OCCC carcinogenesis.

5.4.2. *HNF1B* regulates EMT and cell adhesion in TOV21G cells

Similarly to JHOC-5 cells, hierarchical clustering after *HNF1B* knockdown in TOV21G cells showed clustering by treatment arm (data not shown). 3630 genes (1917 down-regulated and 1713 up-regulated) showed change in expression at FDR 0.01 (Fig. 5.2C-D). More than 50 pathways were enriched at FDR<0.01 on pathway analysis using MetaCore (Table A.13 in the Appendix). Similarly to JHOC-5 cells, 6 of the 7 most enriched pathways were related to EMT, cytoskeleton and adhesion [“Chemokines and adhesion” (Fig. 5.4), “Cytoskeleton remodelling”, “TGF, WNT and cytoskeletal remodelling”, “Regulation of epithelial-to-mesenchymal transition (EMT)”, “Histamine H1 receptor signaling in the interruption of cell barrier integrity” and “Cadherin-mediated cell adhesion”]. Again, WNT ligands (*WNT2B*, *WNT5A*, *WNT7B*, *WNT10A* and *WNT11*), Frizzled receptors (*FZD1*, *FZD2*, *FZD3*, *FZD7*, *FZD8* and *FZD9*), TGF β ligands (*TGFB2* and *TGFB3*), growth factor receptors (*EGFR*, *MET* and *FGFR1*) and downstream transcription factors (*JUN*, *SP1*, *TCF3*, *SNAI1* and *TWIST1*) were *HNF1B*-regulated. Additionally, multiple genes encoding cadherins [*CDH1* (encoding E-cadherin), *CDH2* (N-cadherin), *CDH5* (VE-cadherin)] were *HNF1B*-regulated in TOV21G cells, something that was not seen in JHOC-5.

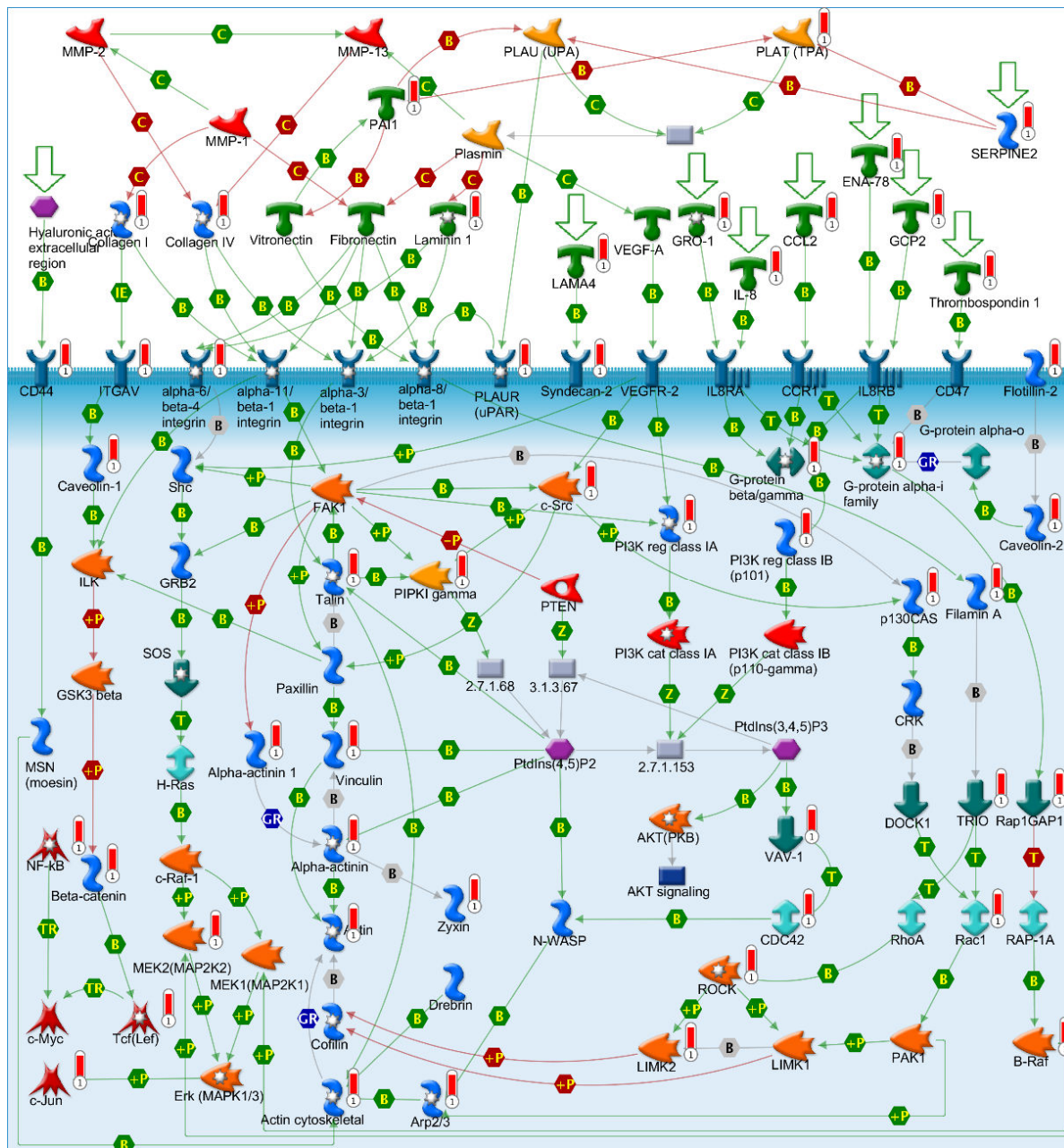


Figure 5.4. The “Chemokines and adhesion” pathway is *HNF1B*-regulated in TOV21G cells

“Chemokines and adhesion” was the most enriched pathway (FDR = 7.7×10^{-13}) following shRNA knockdown of *HNF1B* in TOV21G cells (n=4). Differentially expressed gene lists (n=3630) were created at FDR 0.01. Red “thermometer” bars highlight the DEG that drive pathway enrichment. Analysis performed and graph created using MetaCore (www.genego.com).

31 process networks were significantly enriched at FDR<0.01 using MetaCore (Table A.14 in the Appendix). Consistent with the above, networks related to adhesion, EMT and cytoskeleton remodelling predominated. Multiple genes encoding collagen subunits, including subunits of Collagen Type I (*COL1A1*, *COL1A2*), IV (*COL4A1*, *COL4A2*, *COL4A5*) and V (*COL5A1*) underlie the enrichment in adhesion-related networks. The same Collagen Type IV,

but not Type I or V, genes were regulated by *HNF1B* in JHOC-5 cells too. Intriguingly, mitosis-associated kinases did not appear to be *HNF1B*-regulated in TOV21G cells. However, genes encoding Cyclin D isoforms (*CCND1*, *CCND2* and *CCND3*) were negatively and those encoding Cyclin E isoforms (*CCNE1* and *CCNE2*) positively regulated by *HNF1B*. Additionally, *HNF1B* positively regulated multiple DNA polymerase genes (*POLA2*, *POLB*, *POLD3* and *POLE2*). This could imply different mechanisms for proliferation regulation by *HNF1B* depending on the cellular context and needs to be further investigated.

5.4.3. A core *HNF1B* transcriptional programme is involved in adhesion, cytoskeleton remodelling and EMT regulation

Gene expression analysis in JHOC-5 and TOV21G cells, separately in each cell line, revealed some common themes such as regulation of WNT pathways and EMT but also differences

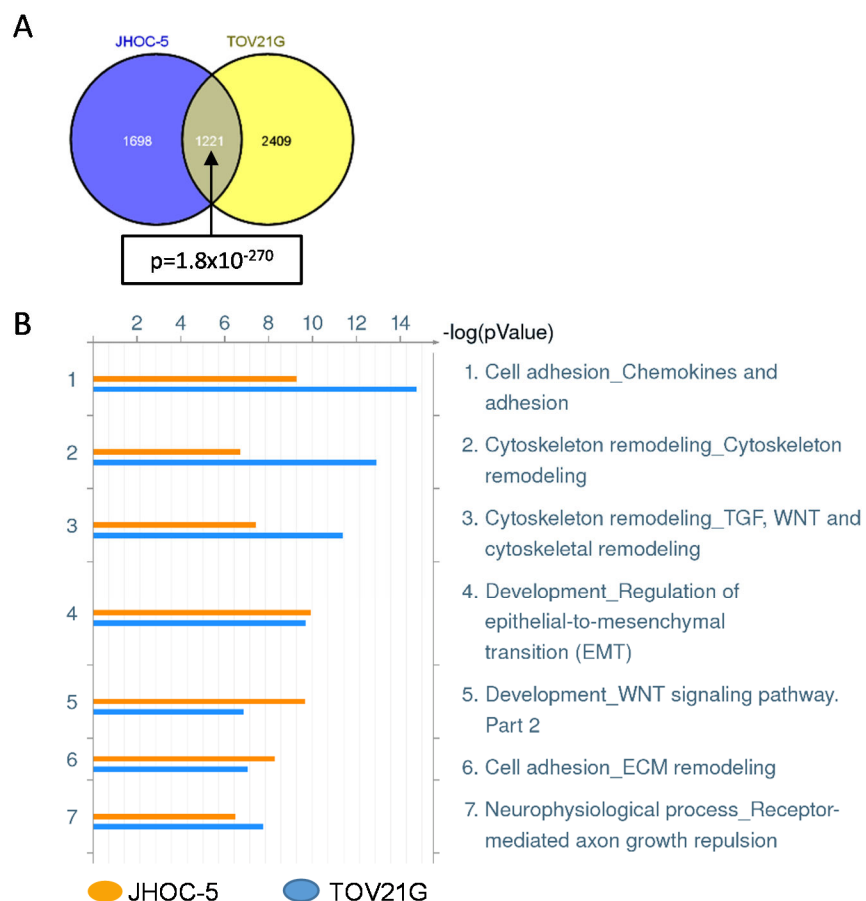


Figure 5.5. Overlap of genes and pathways regulated by *HNF1B* in both JHOC-5 and TOV21G cells

A) Overlap of genes regulated by *HNF1B* in JHOC-5 and TOV21G cells. Differentially expressed gene lists were created using BeadChip arrays at FDR 0.01. B) Pathways enriched in *HNF1B*-regulated genes with $p < 10^{-7}$ in both JHOC-5 and TOV21G cells.

such as the enrichment in immune response, SWI/SNF and mitosis regulation genes in JHOC-5 and in S-phase and angiogenesis regulation genes in TOV21G cells. Genes that are *HNF1B*-regulated in both cell lines could provide insights into a “core” *HNF1B*-driven transcriptional programme. 1221 genes showed differences in expression after *HNF1B* knockdown in both cell lines (Fig. 5.5A), an overlap that was highly statistically significant ($p=1.8 \times 10^{-270}$).

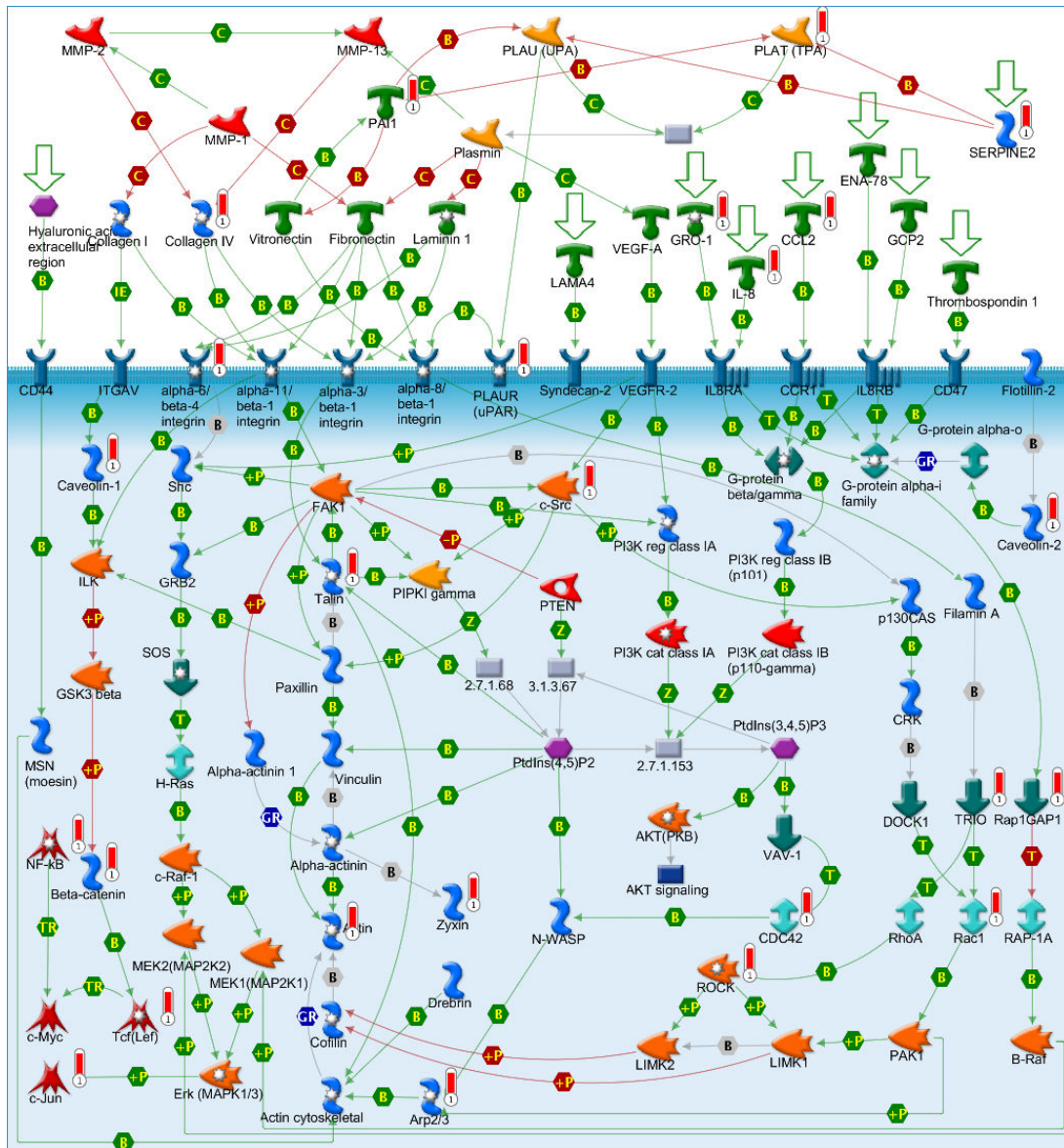


Figure 5.6. The “Chemokines and adhesion” pathway is *HNF1B*-regulated in OCC cell lines

“Chemokines and adhesion” was the most enriched pathway ($FDR = 6.62 \times 10^{-7}$) in the 1221 genes that were *HNF1B*-regulated in both JHOC-5 and TOV21G cells. Red “thermometer” bars highlight the DEG that drive pathway enrichment. Analysis performed and graph created using MetaCore (www.genego.com).

Table 5.1. Top 25 pathways enriched in genes regulated by *HNF1B* in both JHOC-5 and TOV21G cells

Pathway	p value	FDR
Cell adhesion - Chemokines and adhesion	1.01E-09	6.62E-07
Cytoskeleton remodelling - TGF, WNT and cytoskeletal remodelling	4.36E-08	9.64E-06
Cytoskeleton remodelling - Cytoskeleton remodeling	4.43E-08	9.64E-06
Development - Regulation of epithelial-to-mesenchymal transition (EMT)	1.07E-07	1.74E-05
Cell adhesion - ECM remodeling	2.49E-07	3.25E-05
Immune response - MIF-induced cell adhesion, migration and angiogenesis	3.62E-07	3.94E-05
DNA damage - Brca1 as a transcription regulator	1.54E-06	1.44E-04
Neurophysiological process - Receptor-mediated axon growth repulsion	2.03E-06	1.55E-04
Immune response - HMGB1/RAGE signaling pathway	2.14E-06	1.55E-04
DNA damage - ATM/ATR regulation of G1/S checkpoint	3.01E-06	1.97E-04
Development - Role of IL-8 in angiogenesis	4.6E-06	2.73E-04
Immune response - C5a signaling	6.76E-06	3.68E-04
Immune response - MIF-mediated glucocorticoid regulation	8.45E-06	4.25E-04
Mucin expression in CF airways	9.63E-06	4.49E-04
Immune response - CCL2 signaling	1.58E-05	6.8E-04
Cell cycle - Regulation of G1/S transition (part 1)	1.67E-05	6.8E-04
Development - VEGF signaling via VEGFR2 - generic cascades	2.36E-05	9.06E-04
Development - Thromboxane A2 pathway signaling	3.23E-05	0.001171
G-protein signalling - RhoA regulation pathway	4.21E-05	0.001449
Immune response - IL-18 signaling	4.85E-05	0.001508
Immune response - IL-17 signaling pathways	4.85E-05	0.001508
Development - VEGF signaling and activation	5.34E-05	0.001586
Immune response - IL-1 signaling pathway	6.6E-05	0.001874
Cell adhesion - Tight junctions	6.89E-05	0.001876
Reproduction - GnRH signaling	7.29E-05	0.001905

Pathways list created and statistical analysis performed using MetaCore

Pathway analysis of these 1221 gene using MetaCore, showed that more than 50 pathways were enriched in *HNF1B*-regulated genes at FDR<0.01 (Table 5.1 and Fig. 5.5B). The 5 most enriched pathways were again related to adhesion, WNT signalling and EMT regulation [“Chemokines and adhesion” (Fig. 5.6), “TGF, WNT and cytoskeletal remodelling”, “Cytoskeleton remodelling” “Regulation of EMT” and “ECM remodelling”]. Genes that were *HNF1B*-regulated in both cell lines included WNT ligands (*WNT2B* and *WNT7B*) and receptors (*FZD2*, *FZD7* and *FZD8*), other growth factor receptors (*MET*, *EGFR*, *FGFR1* and *IGF1R*),

Table 5.2. Top process networks enriched in genes regulated by *HNF1B* in both JHOC-5 and TOV21G cells

Process Network	p value	FDR
Development - Regulation of angiogenesis	4.75E-09	7.55E-07
Development - Blood vessel morphogenesis	8.27E-08	6.58E-06
Development – EMT - Regulation of epithelial-to-mesenchymal transition	3.15E-06	1.67E-04
Reproduction - FSH-beta signaling pathway	1.32E-05	5.25E-04
Immune response - Antigen presentation	2.66E-05	8.46E-04
DNA damage - Checkpoint	1.26E-04	0.003338
Cell adhesion - Integrin-mediated cell-matrix adhesion	1.53E-04	0.003478
Development – Neurogenesis - Axonal guidance	3.02E-04	0.006011
Signal transduction - ESR1-nuclear pathway	3.98E-04	0.006205
Cardiac development – Wnt - beta-catenin, Notch, VEGF, IP3 and integrin signalling	4.26E-04	0.006205
Cytoskeleton - Regulation of cytoskeleton rearrangement	4.29E-04	0.006205
Inflammation - Protein C signaling	8.17E-04	0.009898
Inflammation - MIF signaling	8.25E-04	0.009898
Development - Ossification and bone remodeling	8.72E-04	0.009898

Process networks list created and statistical analysis performed using MetaCore

downstream transcription factors (*TCF3*, *JUN*, *FOS*, *SP1*, *NFKB2* and *SNAI1*), interleukins (*IL6* and *IL8*) and integrins (*ITGA6*).

Process network analysis suggested that 14 networks were enriched in *HNF1B*-regulated genes at FDR<0.01 (Table 5.2). The top 2 networks were “Regulation of angiogenesis” and “Blood vessel morphogenesis”. Inspection of the gene lists revealed that this network enrichment was driven mostly by pleiotropic transcription factors (e.g. *NFKB2*, *SP1*, *JUN*, *FOS*) and protein kinases (e.g. *SRC*, *PRKCH*, *PRKCQ*) as well two ephrin isoforms (*EFNA1* and *EFNAB2*). There was no differential expression of VEGF isoforms of their receptors and, therefore, whether *HNF1B* directly regulates angiogenesis requires further mechanistic *in vivo* studies. Similar considerations apply to the enriched “ESR1-nuclear pathway”, with differentially regulated genes in this network including *SP1*, *FOS*, *CDKN1A*, *CCND1* and *CCNE1*.

5.5. *HNF1B* decreases migration and invasion in OCCC cell lines and immortalised ovarian surface epithelium

The combined gene expression profiling results suggested a role for *HNF1B* in the regulation of migration and invasion, in agreement with findings in SKOV3 cells where *HNF1B* was shown to promote an epithelial phenotype and repress EMT markers (Tomassetti et al. 2008). Therefore, I hypothesised that *HNF1B* overexpression suppressed migration and invasion. I first replicated the microarray results using qRT-PCR to assay changes in *SNAI1*, *CTNNB1* and *CDH1* after siRNA-mediated *HNF1B* knockdown. As predicted, knockdown increased *SNAI1* and decreased *CDH1* expression (the latter only in TOV21G cells, in accordance with the array results); *CTNNB1* showed a trend towards increase that was not significant due to the small number of replicates (n=2) in this experiment (Fig. 5.7A). At the protein level, knockdown did not seem to affect total or non-phosphorylated, active, β -catenin expression (Fig. 5.7B). E-cadherin expression could not be detected by immunoblotting or

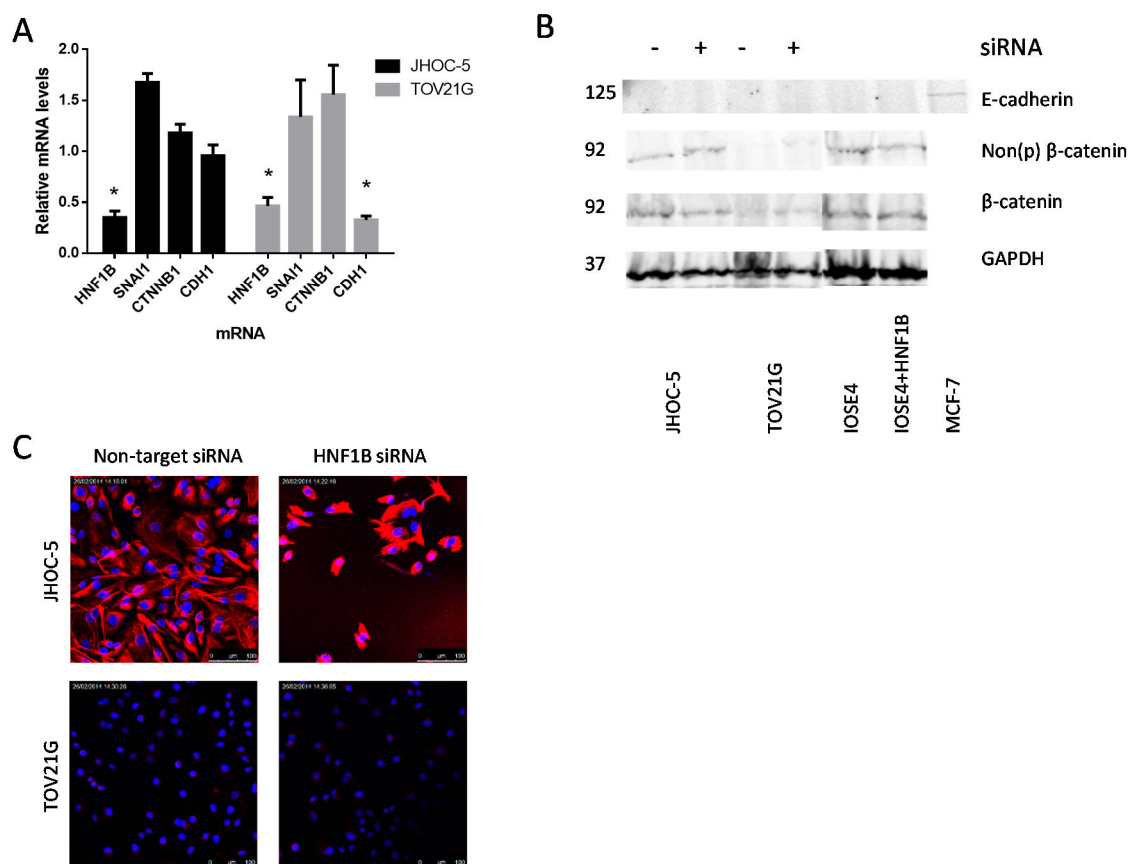


Figure 5.7. Effect of *HNF1B* knockdown on EMT-related RNA and protein expression
 A) Relative mRNA expression levels of EMT-related genes 72 hours after siRNA *HNF1B*-knockdown in JHOC-5 and TOV21G cells (n=2). B) Protein expression of total and non-phosphorylated β -catenin and E-cadherin in JHOC-5 and TOV21G cells 72 hours after siRNA *HNF1B* knockdown and in IOSE4 cells stably overexpressing *HNF1B*. MCF-7 cells are positive control for E-cadherin expression. C) Changes in vimentin expression by immunofluorescence in JHOC-5 and TOV21G cells 96 hours after *HNF1B* siRNA treatment.

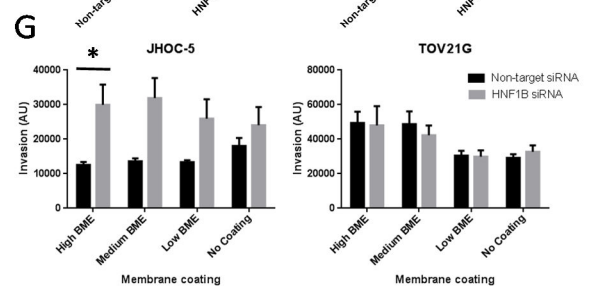
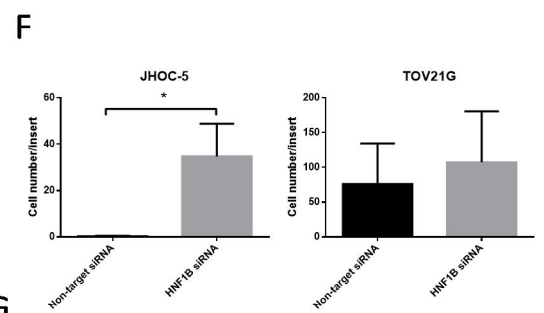
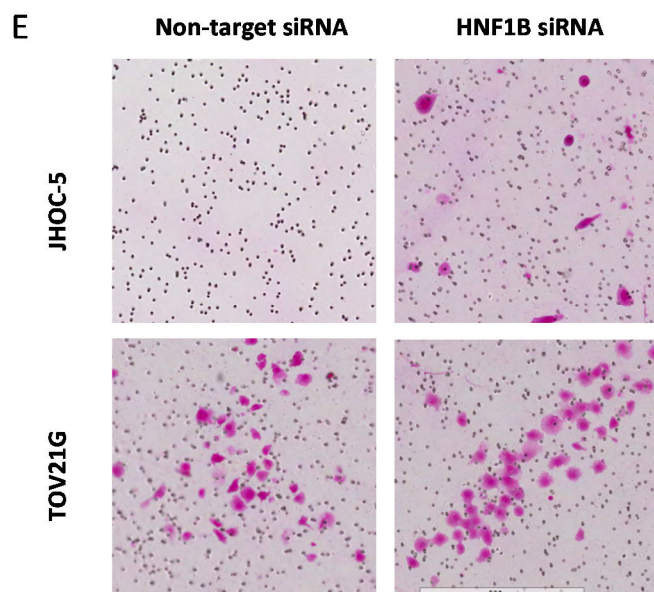
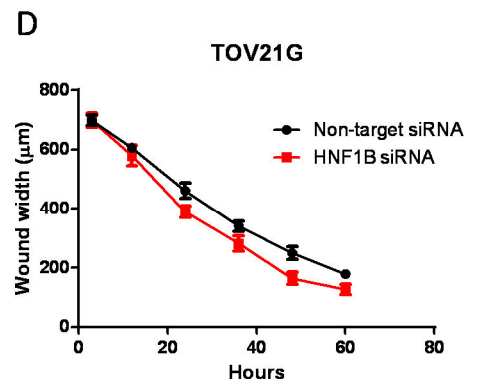
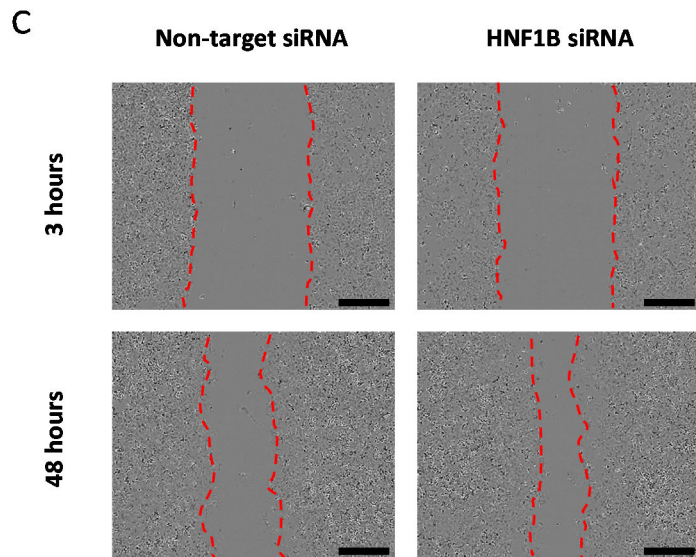
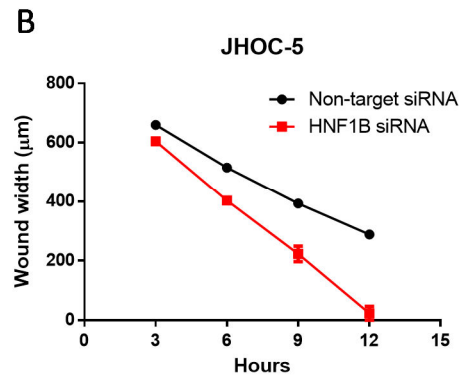
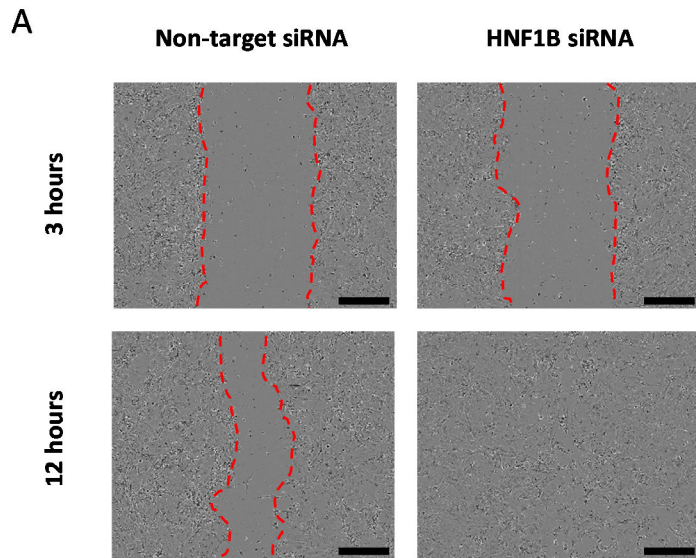
immunofluorescence in JHOC-5 and TOV21G cells treated with either non-target or *HNF1B* siRNA, whereas a faint band was seen in MCF-7 cells (positive control) (Fig. 5.7B). JHOC-5 cells strongly expressed vimentin under baseline conditions and showed a further increase in expression after *HNF1B* knockdown (Fig. 5.7C). Conversely, TOV21G cells showed low baseline vimentin expression with no further induction upon knockdown (Fig. 5.7C). In accordance with these results, induction of HNF1B expression in IOSE4 cells did not affect total or non-phosphorylated β -catenin expression (Fig. 5.7B).

To test the hypothesis that *HNF1B* negatively affects migration and invasion, I performed scratch wound and invasion assays in JHOC-5 and TOV21G cells. The scratch wound assay was performed with 4 flask replicates, each in technical quadruplicates, and showed that siRNA-mediated *HNF1B* knockdown markedly increased migration in JHOC-5 cells (Fig. 5.8A-B). After 12 hours, the mean wound width was 23 μ m in the *HNF1B* siRNA treated cells compared with 288 μ m in non-target siRNA treated ones ($p < 0.0001$). Two-way ANOVA showed that the knockdown had a significant effect on migration ($p < 0.0001$) and also revealed a time by treatment interaction ($p < 0.0001$) with the effect of knockdown becoming greater over time (Fig. 5.8B). TOV21G cells showed much slower migration (Fig. 5.8D). *HNF1B* knockdown significantly increased migration ($p = 0.0004$ by 2-way ANOVA) but the magnitude of the effect was smaller than in JHOC-5 cells.

Subsequently, I repeated the migration assays in IOSE4 and IOSE4+HNF1B cells. Similarly to the results in the OCCC cell lines, *HNF1B* expression in IOSE4 cells, confirmed by qRT-PCR, resulted in a dramatic decrease in migration (Fig. 5.9A-B). 24 hours after scratching, the mean wound width was 136 μ m in the parental IOSE4 cells compared with 474 μ m in the IOSE4+HNF1B ones ($p < 0.0001$). Two-way ANOVA showed that wound width was significantly different between the 2 cell lines ($p < 0.0001$) and also revealed a time by treatment interaction ($p < 0.0001$).

Figure 5.8. Effect of *HNF1B* knockdown on migration and invasion of JHOC-5 and TOV21G cells

A, C) Representative photomicrographs depicting JHOC-5 (A) and TOV21G (C) cell migration in the scratch wound assay (bar=300 μ m). B, D) Time course of wound width in JHOC-5 (B) and TOV21G cells (D) ($n=4$ for each cell line). E) Representative photomicrographs depicting JHOC-5 and TOV21G cell invasion after 24 hours in culture using BD Biocoat Matrigel Invasion chambers F) Quantification of cell invasion depicted in (E) ($n=4$ for each cell line). G) Quantification of cell invasion in the CultureCoat Cell Invasion Assay Basement Membrane Extract (BME) system ($n=4$ for each cell line)



I then performed an invasion assay using Matrigel-coated cell inserts, again with 4 flask replicates for each cell line. In agreement with the scratch wound assay, *HNF1B* knockdown resulted in increased invasion (Fig. 5.8E-F), which was statistically significant for JHOC-5 (mean number of invading cells 34.75 vs. 0.25, $p=0.05$) but not TOV21G (mean number of invading cells 107.33 vs. 76.25, $p=0.75$). I repeated the invasion assay using the CultureCoat® assay that contains wells coated with 3 different concentrations of Basement Membrane Extract (BME) and provides a quantitative readout based on the fluorescence exhibited by invading cells following dissociation and Calcein AM incubation (Fig. 5.8G). Again, invasion of JHOC-5 cells was increased after *HNF1B* knockdown and reached statistical significance ($p=0.05$) for the “High BME” coating. Conversely, there was no difference in TOV21G invasion, irrespective of the invasion chamber coating ($p=0.29-0.92$). It is interesting to note that JHOC-5 and TOV21G cells exhibited discordant behaviours in the 2 assays with the former showing very rapid migration but little invasion and the latter the reverse pattern.

5.6. *HNF1B* is associated with clotting cascade genes

OCCC is characterised by increased risk of VTE (Anglesio et al. 2011b) and a recent publication reported enrichment for clotting cascade genes among the genes regulated by *HNF1B* in HEK293 cells, a finding that was confirmed in an independent EOC dataset that included 8 OCCC cases (Cuff et al. 2013). Therefore, I investigated whether 36 clotting

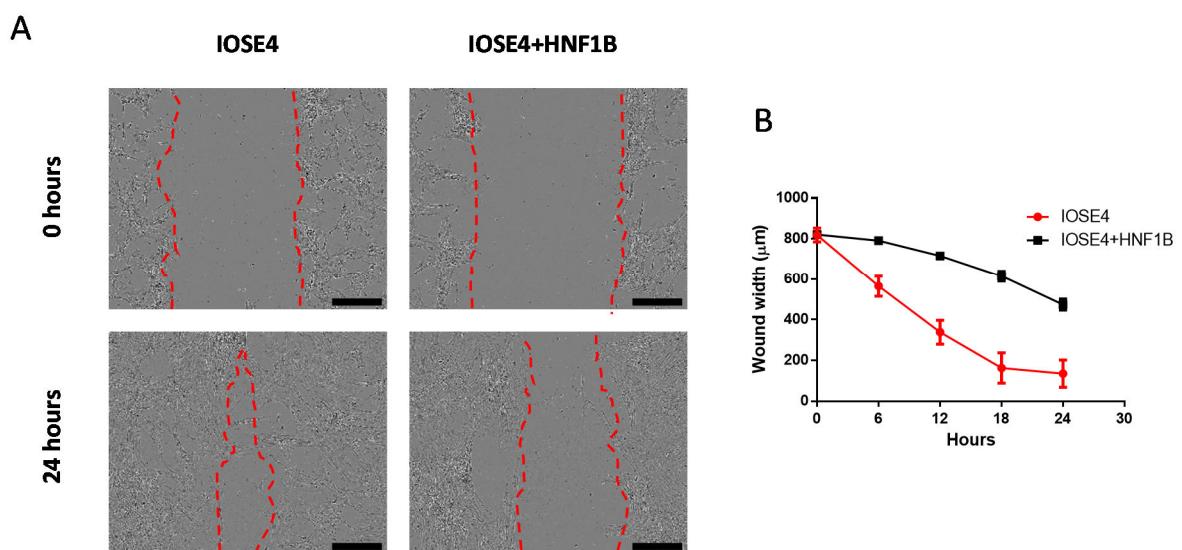


Figure 5.9. Migration and invasion of the IOSE4 and IOSE4+HNF1B cell lines

A) Representative photomicrographs depicting parental IOSE4 and IOSE4 cells overexpressing HNF1B (IOSE4+HNF1B) cell migration in the scratch wound assay (bar=300μm). B) Time course of wound width in IOSE4 and IOSE4+HNF1B cells ($n=4$ for each cell line).

cascade genes were over-represented among *HNF1B*-regulated genes in JHOC-5 and TOV21G cells. Eight genes (*FGB*, *F12*, *PLAT*, *PLAU*, *SERPINE1*, *SERPINA1*, *F2R* and *PLAUR*) were regulated by *HNF1B* in JHOC-5, whereas 10 (*FGA*, *FGB*, *BDKRB2*, *VWF*, *F3*, *PROS1*, *PLAT*, *TFPI*, *SERPINE1* and *PLAUR*) were in TOV21G cells. Of these, *FGA* and *FGB* were 2 of the 4 genes referred by name in the report by Cuff *et al* (2013). However, the overlap between the 36-gene clotting cascade gene set and the 2919 and 3630 *HNF1B*-regulated genes in JHOC-5 and TOV21G cells did not reach statistical significance ($p=0.102$ and $p=0.067$ respectively).

5.7. *HNF1B* regulates multiple glycolytic pathway enzymes

HNF1B has been shown to be important for glucose homeostasis (Wang *et al.* 2004) and the regulation of glycolysis in OCCC (Okamoto *et al.* 2013). Surprisingly, glucose metabolism related pathways and networks did not appear among the top hits in the agnostic MetaCore analysis of the core 1221 *HNF1B*-regulated genes. However, “Bile acids regulation of glucose and lipid metabolism via FXR” and “Regulation of lipid metabolism via LXR, NF-Y and SREBP” were among the enriched pathways (FDR=0.002 for both). Three transcription factors involved in glucose homeostasis, *FOXA1*, *FOXO1* and *FOXO4*, were *HNF1B*-regulated in both cell lines as were the lipid metabolism-associated genes *SREBF1*, *CREB1*, *PRKAG2*, *ACLY* and *SCD*.

Very recently, it was reported that 16 of 19 genes encoding enzymes involved in glycolysis were down-regulated following *HNF1B* knockdown in RMG-II cells (Okamoto *et al.* 2013). Seven of these genes (*HK1*, *HK2*, *PFKP*, *PFKL*, *ENO2*, *ENO3* and *LDHA*) were significantly differentially expressed in JHOC-5 cells as well, with all except *ENO3* showing reduced expression after *HNF1B* knockdown. The overlap in differentially expressed genes between this 19-gene list and the 2919 *HNF1B*-regulated genes in JHOC-5 cells was significant ($p=0.009$). Similarly, 6 genes (*HK2*, *PFKL*, *PGK1*, *ENO2*, *LDHA* and *GAPDH*) were differentially expressed in TOV21G cells. However, only *PFKL*, *PGK1* and *ENO2* were down-regulated. The overlap was not significant in TOV21G cells ($p=0.084$). Notably, *GAPDH* expression was modestly but significantly increased after *HNF1B* knockdown by 18%. A consequence of this is that *HNF1B* knockdown efficiency is slightly underestimated in these cells as *GAPDH* expression was used for normalisation in qRT-PCR and immunoblots. In accordance with published results in RMG-I and RMG-II cells (Okamoto *et al.* 2013), *HNF1B* knockdown resulted in significant reduction in *SLC2A1* (encoding GLUT1) expression in

JHOC-5 but not TOV21G cells. It appears therefore, that the effects of *HNF1B* knockdown on glycolysis are fairly similar between RMG-II and JHOC-5, but not TOV21G, cells.

5.8. *HNF1B* knockdown reduces lactate production and leads to increased TCA intermediates and ATP accumulation

As my data suggested that *HNF1B* regulates genes involved in glycolysis in JHOC-5 cells, I assayed changes in medium and intracellular metabolite concentrations over 72 hours in culture using NMR. Two lentiviral clones (577 and 583) were used to stably knock down *HNF1B* expression and were compared to the non-targeting 202 clone; the experiment was performed in triplicate as detailed in section 2.19.1. Compared to clone 202, *HNF1B* expression at the protein level was 63% and 76% lower in cells transfected with clones 577 and 583 respectively on the day of the experiment.

HNF1B knockdown resulted in a significant decrease in lactate excretion in the medium with a corresponding increase in pyruvate uptake (Fig. 5.10). Despite the reduction in *SLC2A1* expression (see section 5.7), glucose uptake from the medium was essentially stable. As expected (Israel & Schwartz 2011), glutamate and alanine mirrored the lactate changes, showing decreased excretion in the medium (Fig. 5.10). Other tested amino acids (glutamine, leucine, isoleucine, valine) showed minor, non-significant changes. The changes in the medium metabolic profile are most consistent with increased utilisation of pyruvate and glutamate (via α -ketoglutarate) in the TCA cycle and, therefore, less conversion of pyruvate to lactate or alanine. This was supported by increased intracellular concentrations of TCA intermediates such as citrate, succinate and fumarate (Fig. 5.11). Intracellular pyruvate and lactate levels were stable, strengthening the conclusion that after *HNF1B* knockdown less lactate is produced and pyruvate preferentially enters the TCA cycle. At the same time, intracellular glucose showed a non-significant increase with cellular glucose levels increasing possibly because of less glycogen accumulation (see section 5.9). Concentrations of membrane building blocks (taurine, choline, phosphocholine) and multiple amino acids (leucine, isoleucine, lysine, methionine, threonine, phenylalanine, glycine and serine) also significantly increased (Fig. 5.11; data not shown for serine and glycine). Even more importantly, the overall energetic state of the cells appeared more favourable with increases in intracellular creatine, phosphocreatine and ATP (Fig. 5.11). These results imply that *HNF1B* contributes to a pro-proliferative Warburg effect in JHOC-5 cells and its knockdown leads to

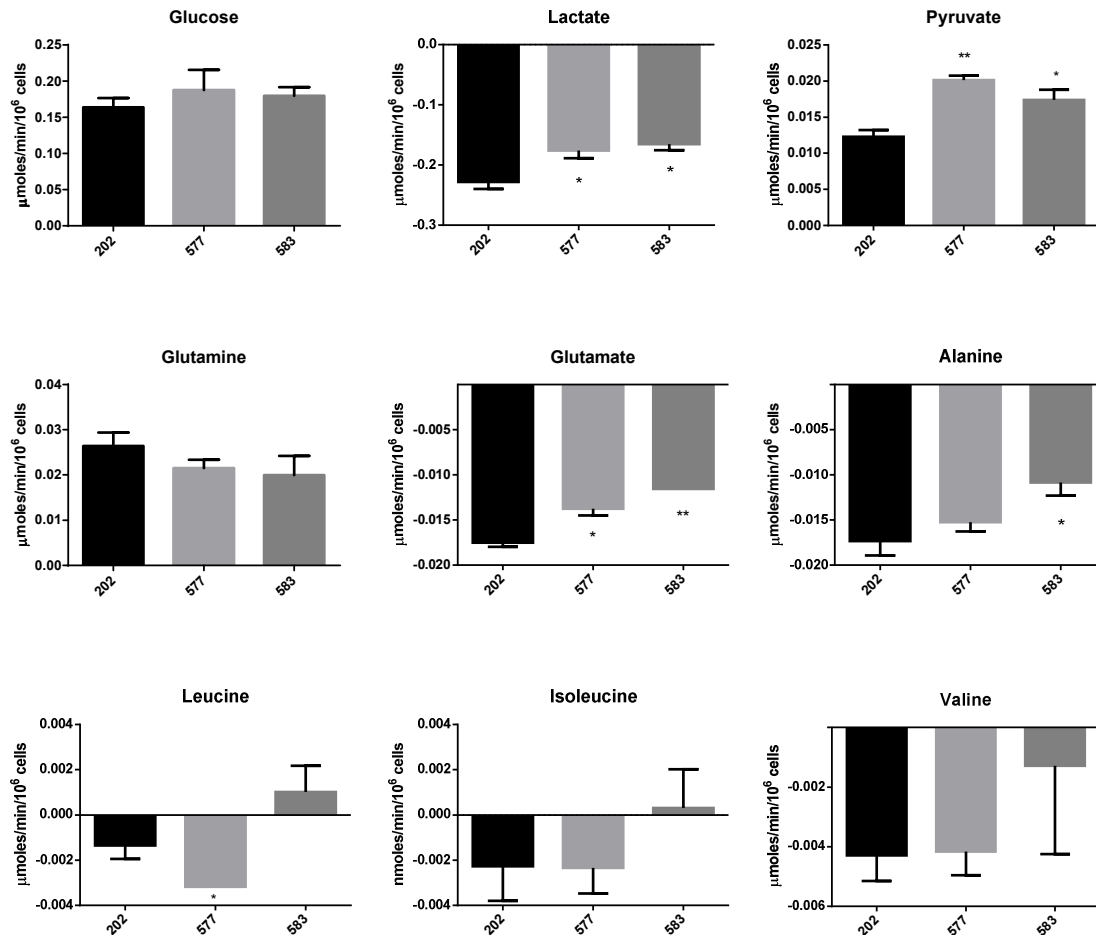


Figure 5.10. Effect of *HNF1B* knockdown on metabolites in the culture medium

Changes in metabolite concentrations in the medium after 72 hours in JHOC-5 cells stably transfected with non-targeting shRNA (202) or shRNA targeting *HNF1B* (577 and 583). Cells were cultured in DMEM medium with 3 flask replicates per clone. Positive values indicate uptake from the medium (i.e. the concentration at 72 hours is lower than the baseline) whereas negative values indicate release in the medium (i.e. the concentration at 72 hours is higher than the baseline).

the cells reverting to oxidative phosphorylation and replenishing intracellular metabolites such as amino acids, membrane building blocks and ATP.

5.9. *HNF1B* drives glycogen accumulation in JHOC-5 and IOSE4 cells

The role of *HNF1B* in glucose metabolism through regulation of glycolytic pathways (Tanaka et al. 2004; Thomas et al. 2004), has led many to propose that *HNF1B* overexpression drives glycogen accumulation in OCCC (Uekuri et al. 2013). However, this has not been directly demonstrated before. I measured glycogen content, using a colorimetric assay (see section 2.24.1 for details), in JHOC-5 and TOV21G cells stably transfected with lentiviruses carrying non-targeting (clone 202) or *HNF1B*-targeting (clones 577, 578, 582 and 583) shRNA,

following puromycin selection, in 3 separate experiments. *HNF1B* knockdown significantly decreased glycogen in JHOC-5 cells by 52% ($p=0.04$) and 77% ($p=0.003$) for clones 577 and 583 respectively (Fig. 5.12A). Conversely, in TOV21G cells there was a non-significant increase in glycogen content (30%, $p=0.39$ for clone 578; 7%, $p=0.9$ for clone 582).

I then interrogated the gene expression data (see section 5.4) for changes in expression of the core glycogen metabolism genes *PYGL* and *GYS1* as well as the accessory genes *PGM1*, *PGM2*, *PGM3*, *UGP1*, *UGP2* and *GBE1*. In JHOC-5 cells, *PYGL*, *PGM3* and *UGP2* showed significantly decreased expression following *HNF1B* knockdown. Conversely, in TOV21G cells *PGM1* and *GBE1* expression was increased following *HNF1B* knockdown. The significant reduction in *PYGL* expression was confirmed at the protein level in JHOC-5 cells, whereas TOV21G cells showed a non-significant trend towards reduced expression (Fig. 5.12D). These results suggest that *HNF1B* directly regulates glycogen content in JHOC-5 but not TOV21G cells. Taking into account the changes in expression of glycolytic pathway-related genes (see section 5.7) as well, it appears that glucose handling, and the role of *HNF1B* in it, differs significantly between JHOC-5 and TOV21G cells.

Intriguingly, glycogen content remained stable or increased 72 hours after siRNA-mediated *HNF1B* knockdown in a panel of 6 OCCC cell lines, including JHOC-5 (Fig. 5.12B), implying complex time-dependent effects of *HNF1B* regulation of metabolism with changes in metabolites immediately after knockdown possibly not accurately reflecting the steady state (which is reflected in the gene expression arrays and metabolite measurement experiments).

In accordance with the results obtained in JHOC-5 cells, expression of *HNF1B* in IOSE4 cells, increased glycogen content by 74% ($p=0.047$, $n=5$) (Fig. 5.12C). Therefore, it can be concluded that *HNF1B* directly regulates glycogen content, at least in a subset of cell lines.

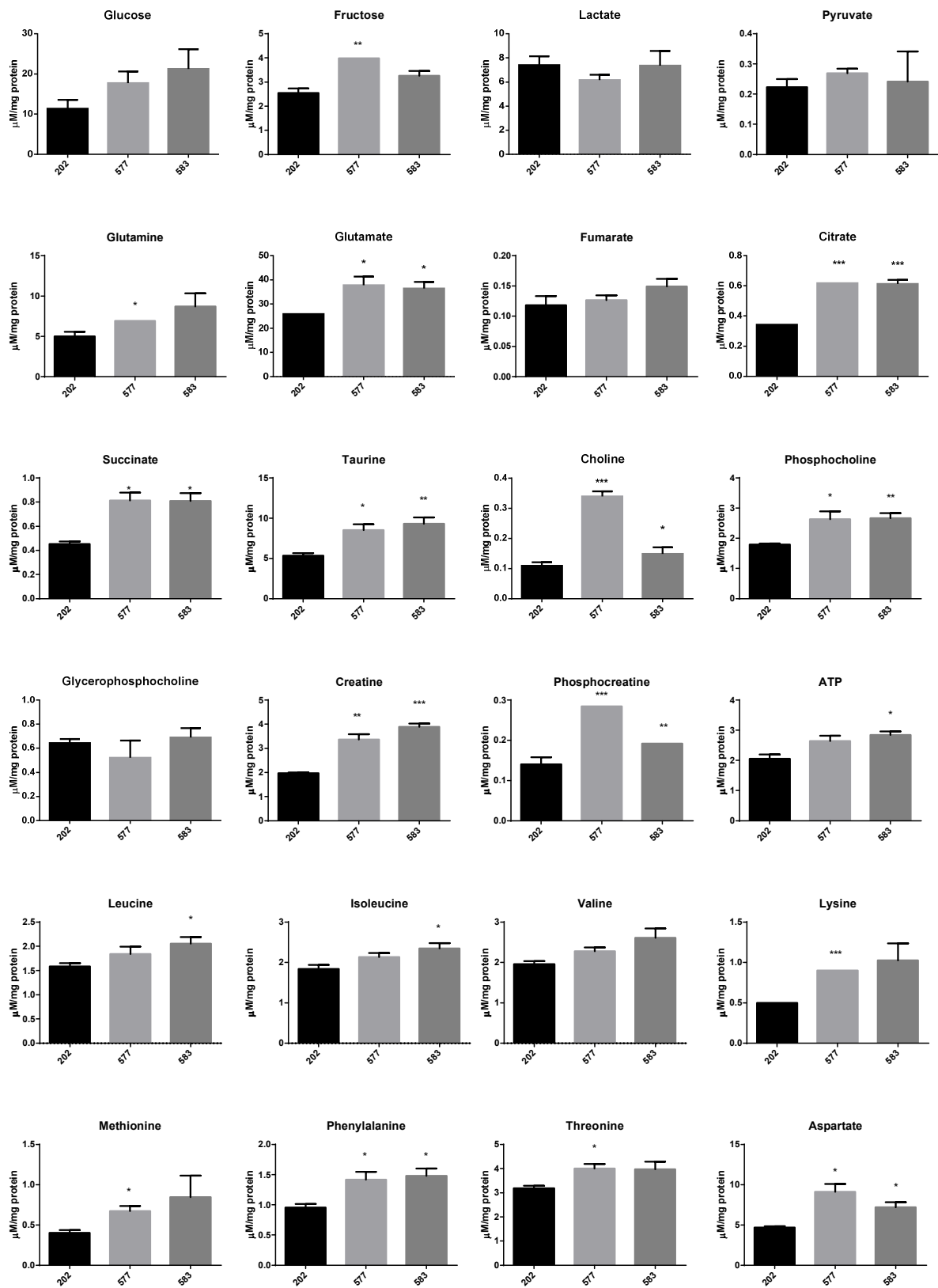


Figure 5.11. Effect of *HNF1B* knockdown on intracellular metabolites

Changes in intracellular metabolite concentrations after 72 hours in JHOC-5 cells stably transfected with non-targeting shRNA (202) or shRNA targeting *HNF1B* (577 and 583). Cells were cultured in DMEM medium with 3 flask replicates per clone and values corrected for protein content.

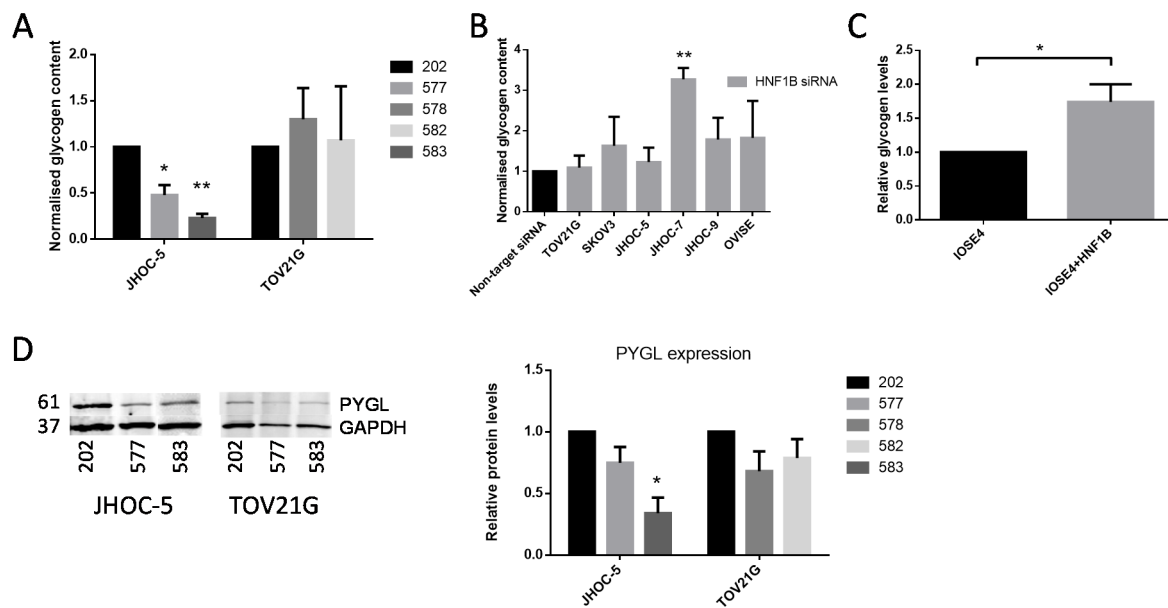


Figure 5.12. HNF1B expression drives glycogen accumulation

A) Glycogen content of JHOC-5 and TOV21G cells stably transfected with non-targeting shRNA (202) or shRNA targeting *HNF1B* (577 and 583 for JHOC-5; 578 and 582 for TOV21G) (n=3). B) Glycogen content of 6 OCCC cell lines 72 hours after siRNA *HNF1B* knockdown (n=2). C) Glycogen content of parental IOSE4 and IOSE4 cells overexpressing HNF1B (IOSE4+HNF1B) (n=5). D) Effect of *HNF1B* knockdown on PYGL protein expression. A representative immunoblot is shown on the left and the mean \pm S.E. expression on the right (n=3). Reduction is significant only for JHOC-5 clone 583 (p=0.03).

5.10. Discussion

My results add to the literature suggesting that HNF1B overexpression, apart from its utility as a diagnostic IHC marker, is a major driver of OCCC. I have shown that *HNF1B* drives proliferation in a wide panel of *bona fide* OCCC cell lines, possibly through effects on interactions with the microenvironment (regulation of EMT and adhesion) and on cellular metabolism. Of considerable interest is the observation that, counter-intuitively, *HNF1B* knockdown increases migration and invasion while reversing the Warburg effect and the direct demonstration that *HNF1B* drives glycogen accumulation.

With regards to proliferation, consistent results were obtained between stable *HNF1B* knockdown using lentiviruses to deliver shRNA in JHOC-5 and TOV21G cells (Fig. 5.1C) and siRNA in a wider panel of 6 OCCC cell lines (Fig. 5.1E). Only JHOC-7 cells were resistant to *HNF1B* knockdown, consistent with the resistance showed by this line to environmental and metabolism manipulations to be described in the following chapter. The lack of any effect on the *HNF1B* non-expressing PEO1 and IOSE4 cell lines, provides some assurances that the

observed changes in proliferation are not due to off-target shRNA or siRNA effects. My results are consistent with those reported previously in both ovarian (Tomassetti et al. 2008; Tsuchiya et al. 2003) and prostate (Grisanzio et al. 2012) cancer cell lines and contrast with the observed increase in proliferation following *HNF1B* knockdown in RMG-I and RMG-II cells (Okamoto et al. 2013). Whether this is due to the specific experimental design and assays used by these authors or to genuine differences in response among the cell lines requires further investigation. However, the increase in proliferation observed in RMG-I and RMG-II cells is inconsistent with the large body of work already mentioned. Further support for this is provided by my finding of increased proliferation in IOSE4+HNF1B compared with the parental IOSE4 cells (Fig. 5.1H).

Gene expression analysis showed that *HNF1B* regulated a large set of genes in both JHOC-5 (n=2919) and TOV21G (n=3630) even with a stringent FDR 0.01 threshold. A limitation is that the array results were not formally validated by qRT-PCR as validating expression changes even for a few of the genes would vastly inflate the costs of the experiment. Nevertheless, in the few cases where array results were compared with qRT-PCR results (for *HNF1B* itself, *CTNNB1*, *SNAI1* and *CDH1*) or protein expression (for PYGL and vimentin), concordance was observed. Use of a stringent FDR threshold as well as the extreme p value accompanying the overlap between genes showing differential expression in JHOC-5 and TOV21G cells (1.8×10^{-270}), provide reassurance that the array results are robust. More importantly, the array predictions regarding regulation of EMT were confirmed by functional assays but, obviously, more extensive confirmation of the array results at the protein level is needed. The number of *HNF1B*-regulated genes in my study was much higher than previously reported (Senkel et al. 2005; Tomassetti et al. 2008). This is probably due to the number of replicates used in my experiment (4 flask replicates run in duplicate) which increased power. In addition, progress in microarray technology and analysis pipelines over the past decade has allowed changes of smaller magnitude to be reliably called as significant.

My results support and expand on those previously reported. Senkel *et al* (2005) reported a list of 15 genes that were *HNF1B*-regulated in HEK293 cells and also part of an OCCC signature. The overlap between that 15-gene list and *HNF1B*-regulated genes in JHOC-5 and TOV21G was significant for both cell lines (9 common genes in JHOC-5, $p=3.4 \times 10^{-5}$; 8 common genes in TOV21G, $p=0.001$). There was also a highly statistically significant overlap between the *HNF1B*-driven expression signature in RMG-II (Okamoto et al. 2013) and that in JHOC-5 ($p=5.86 \times 10^{-11}$) and TOV21G cells ($p=1.69 \times 10^{-7}$), implying that despite the atypical

effect on proliferation in RMG-II, *HNF1B* orchestrates a similar transcriptional programme in all 3 cell lines. Among the 29 genes regulated by *HNF1B* in all 3 cell lines, chemokines and genes implicated in extracellular matrix components and interactions appear prominent (e.g. *CXCR4*, *CCL20*, *GPC4*, *TIMP2*, *DSE*, *GCNT1*, *RELN*), as do growth factor receptors (e.g. *FGFR1*, *IGF1R*, *SEMA6A*) in accordance with the MetaCore pathway analysis of my data.

Pathway analysis using MetaCore of *HNF1B*-regulated genes in both JHOC-5 and TOV21G cells individually and their overlap showed enrichment of pathways related to chemokines and adhesion, ECM remodelling, EMT regulation and *WNT*-driven cytoskeletal remodelling. These results are entirely in agreement with the report that *HNF1B* regulated adhesion, cytoskeletal and ECM-related genes in SKOV3 cells (Tomassetti et al. 2008). Importantly, that report showed that *HNF1B* repressed proteins associated with EMT and promoted E-cadherin expression (Tomassetti et al. 2008). The change of morphology in IOSE4 cells upon *HNF1B* induction (Fig. 5.1F) is consistent with effects of *HNF1B* on adhesion and interactions with the micro-environment. Similarly, my data show that siRNA-mediated *HNF1B* knockdown increases EMT markers such as *SNAI1* and vimentin while suppressing *CDH1*.

The migration and invasion assays clearly show that, despite its pro-proliferative effect, *HNF1B* suppresses migration in both OCCC cell lines and in IOSE and additionally invasion in JHOC-5 cells. This is an extremely important observation that hints at trade-offs between proliferative and metastatic potential during OCCC tumour evolution and requires *in vivo* validation. Moreover, these results raise the intriguing possibility that *HNF1B* expression in OCCC may underlie the frequent presentation of OCCC as early stage disease, in stark contrast to HGS. My data also supports the report that *HNF1B* is the driver behind another well-recognised OCCC clinical manifestation, that of increased VTE risk (Cuff et al. 2013), as it modulates the expression of multiple genes involved in the clotting cascade.

My analysis also reveals some of the limitations of over-reliance on pathway and network analysis predictions. Counter-intuitively, angiogenesis and blood morphogenesis emerged as *HNF1B*-regulated networks in my dataset. Closer examination of the gene lists revealed that this is probably a false positive finding due to changes in expression of pleiotropic transcription factors such as *JUN*, *FOS* and *SP1*. Nevertheless, it would be important to study the effects of *HNF1B* knockdown on angiogenesis in xenograft models. Similar considerations apply to the reported *HNF1B* regulation of an ESR nuclear network in my data. However, one of the main unanswered questions in OCCC carcinogenesis is how the switch from the oestrogen-

dependent endometriosis state to the oestrogen-independent one of OCCC happens. Mechanistic studies of *HNF1B* activation in endometriosis using the Cheng GEMM (Cheng et al. 2011), as well as studies of oestrogen signalling in IOSE4 and IOSE4+HNF1B cells, may help clarify whether *HNF1B* overexpression promotes oestrogen independence.

Another interesting observation from the gene expression data is that *HNF1B* modifies the expression of multiple SWI/SNF components, but not *ARID1A* itself, in the *ARID1A* wild-type JHOC-5 but not the *ARID1A*-mutant TOV21G cell line. This could imply that induction of HNF1B expression may compensate for wild-type *ARID1A* in a subset of tumours. The picture becomes more complicated when one considers that, in my mouse uterus (but not the MEF) data, *Arid1a* positively regulates *Hnf1b* expression, an observation repeated after *ARID1A* knockdown in the IOSE4+HNF1B cells (data not shown). Clearly, more information regarding *HNF1B* and *ARID1A* interactions is needed, as the possibility exists for reciprocal regulatory loops and temporal dependencies of their changes in OCCC carcinogenesis.

Additionally, the gene expression data and the metabolic profiling studies in JHOC-5 cells confirm previous observations about the role of *HNF1B* in glycolysis (Tanaka et al. 2004; Thomas et al. 2004). Stable reduction of HNF1B protein levels in JHOC-5 cells was able to reverse the Warburg effect phenotype with reduction of lactate, glutamate and alanine excretion in the medium and increased pyruvate uptake, coupled with increases in intracellular glucose, TCA cycle intermediates, amino acid and membrane building blocks and a more favourable energetic state, as manifested by increased phosphocreatine and ATP levels. In short, *HNF1B* knockdown changes the metabolic profile of JHOC-5 cells to one that more closely resembles normal metabolism, while reducing proliferation. A limitation of my approach is that it provides a static picture of changes in metabolite concentrations after stable *HNF1B* knockdown; the observed concentrations are probably the aggregate result of changes in fluxes through multiple metabolic pathways. It will be important, in future studies, to investigate changes in carbon and phosphate handling directly. However, my results are generally in agreement with those reported by Okamoto *et al* while the current project was underway. These authors showed that *HNF1B* knockdown in RMG-I and RMG-II cells reduced lactate excretion and glycolytic flux (Okamoto et al. 2013). However, contrary to my data, they also showed reduced glucose uptake. Whether this is due to differences in experimental setup or real differences in the metabolic wiring of the cell lines tested is unclear. Nevertheless, my data provide a more detailed picture of changes in multiple metabolites and, for the first time, demonstrate direct control of intracellular glycogen accumulation by *HNF1B* in JHOC-5 and

IOSE4 cells. The fact that transient knockdown had a null or opposite effect of glycogen levels emphasises the importance of allowing enough time for steady states to be re-established following metabolism perturbations. It should be noted that *HNF1B* knockdown had a much more mixed effect on glycolytic pathway gene expression in TOV21G cells and did not affect glycogen levels. Therefore, it appears that *HNF1B* regulation of metabolism is fairly similar in RMG-I, RMG-II and JHOC-5 but differs in TOV21G cells. TOV21G shows microsatellite instability and is hyper-mutated (Domcke et al. 2013), facts that may have disrupted additional metabolism-related genes, causing these differences. Examination of a wider panel of OCCC cell lines will help to clarify these patterns.

Further *in vivo* work is needed to confirm and expand on my observations. The stably transfected cell lines could be used in xenograft experiments with metastatic dissemination and survival as endpoints. In similar experiments, FDG-PET and spectroscopy could be used to assay metabolite changes and tumour electron microscopy to detect changes in glycogen accumulation. The xenograft approach would also allow for the effect of HNF1B on IL6 and inflammation in the tumour microenvironment to be studied in detail.

To summarise, *HNF1B* is shown to be one of the major drivers of OCCC with a multitude of effects on proliferation, EMT and interactions with the microenvironment, and cancer cell metabolism. Almost all the presented work was conducted in cancer cell lines; it will be useful to study the effects of *HNF1B* expression induction in pre-malignant endometriotic cells, something that is possible using the Cheng endometriosis mouse model that enables genetic manipulation *ex vivo* during the transplantation step. Preparatory work for this has begun in the Charnock-Jones laboratory. Another extremely interesting and related question is whether *HNF1B* expression is induced as a stochastic event in endometriosis, eventually leading to OCCC, or is it that endometrial cells already expressing *HNF1B* confer a proliferative advantage and are at higher risk of malignant transformation in the stressful environment of an endometriotic cyst. Answering this question may help identify a subgroup of women with endometriosis at increased risk of malignancy, in whom preventive and screening efforts could be focused.

6. TARGETING GLYCOGEN METABOLISM MAY BE A NOVEL THERAPEUTIC STRATEGY IN OCCC

6.1. Introduction

Glycogen accumulation is the defining morphological characteristic of OCCC and is thought to represent an adaptive response to the hypoxic and oxidative environment of the endometriotic cysts inside which OCCC develops (Iida et al. 2012; Yamada et al. 2011). Previous reports have suggested that, because of this, OCCC cell lines are more resistant to hypoxia and glucose deprivation than HGS ones (Stany et al. 2011). HIF1 α induction in hypoxia is thought to promote glycogen accumulation in a wide variety of cell types (Favaro et al. 2012; Pelletier et al. 2012; Pescador et al. 2010). However, as I have shown in section 5.9, and others have suggested (Okamoto et al. 2013; Uekuri et al. 2013), HNF1B expression in OCCC also causes glycogen accumulation. Whether hypoxia and HIF1 α further regulate glycogen accumulation in the setting of HNF1B overexpressing OCCC is presently unclear. Furthermore, it is not known whether glycogen accumulation represents a static glucose store, to be used under conditions of nutrient deprivation, or continuous flux of glucose through glycogen is required for optimal cell growth and proliferation.

In this part of my project, I first tested the hypothesis that OCCC is more resistant to hypoxia and glucose deprivation in a panel of 10 EOC cell lines. After assaying the glycogen content of OCCC cell lines, I asked whether *HIF1A* knockdown had an effect on cellular glycogen accumulation in HNF1B expressing OCCC cells. I then asked whether perturbing glycogen metabolism in OCCC cell lines by targeting the rate-limiting enzymes glycogen phosphorylase (PYGL) and synthase (GYS1), would have an effect on cellular proliferation and metabolism and whether that effect would still be evident under normal, glucose-rich culture conditions. While this work was ongoing, work from Prof. Adrian Harris' group suggested that *PYGL* knockdown resulted in decreased proliferation due to senescence induction in U87 glioblastoma and MCF-7 breast cancer cells (Favaro et al. 2012), thus providing support to the concept that glycogen can be a valid therapeutic target in cancer.

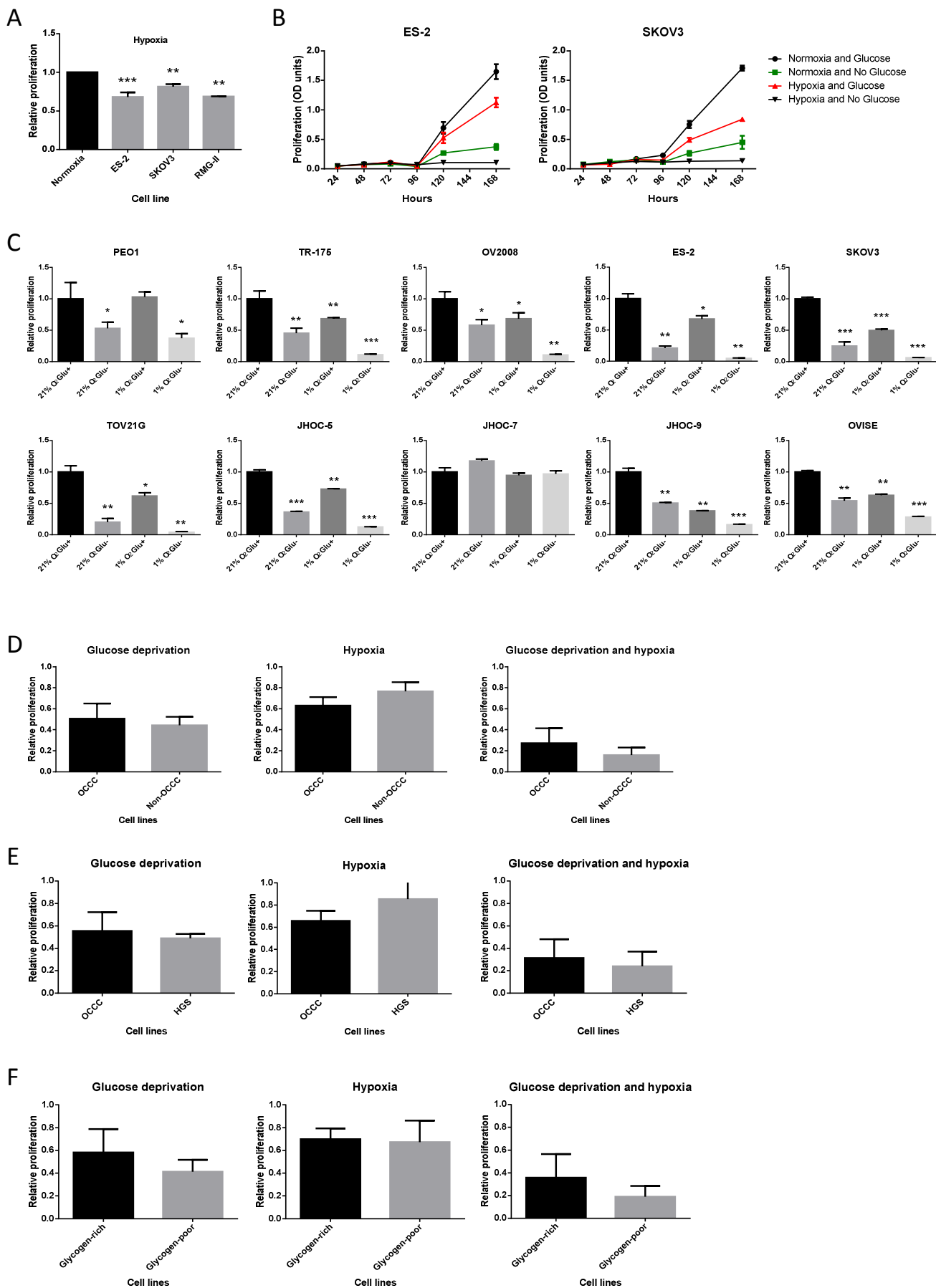
6.2. OCCC cell lines are not more resistant to hypoxia or glucose deprivation

I first studied the effects on proliferation of culturing cells in hypoxia (1% O₂) in ES-2, SKOV3 and RMG-II cells, using ViCell to count cell numbers as detailed in section 2.23.3. In 4 (RMG-II) or 6 (ES-2, SKOV3) separate experiments, culture in 1% O₂ for 96 hours significantly reduced proliferation by 31% (p=0.01), 32% (p=0.001) and 19% (p=0.002) in RMG-II, ES-2 and SKOV3 cells respectively (Fig. 6.1A). However, these experiments required plating a large number of cells (1-2x10⁶) to enable accurate cell counting, making screening of a large panel of cell lines, conditions and timepoints problematic. Therefore, I switched to using the SRB proliferation assay, plating 1000 cells per well in 96-well plates. To eliminate medium effects, all cell lines were cultured in DMEM supplemented with 10% FBS, 50U/ml penicillin and 50µg/ml streptomycin. For glucose deprivation experiments glucose-free DMEM with the same supplements was used. As FBS contains approximately 7mM glucose (personal communication with Life Technologies), cells cultured under glucose deprivation are exposed to ~0.7mM glucose whereas cells cultured under normal conditions (NC) are exposed to 25mM. Experiments were performed with 4 technical replicates per each of 4 biological (flask) replicates. Due to low cell numbers used, differences in proliferation were not apparent until 120 hours after plating and were maximal at 168 hours (Fig. 6.1B).

I then assessed the effects of hypoxia, glucose deprivation, or both on proliferation at 168 hours in 10 cell lines. As can be seen from Fig. 6.1C, hypoxia, glucose deprivation, or both, significantly decreased proliferation in all cell lines tested with the exception of JHOC-7 for all 3 manipulations and PEO1 for hypoxia. Considering all cell lines together, hypoxia had a smaller effect on proliferation (mean reduction 31%) than glucose deprivation (mean reduction 52%, p=0.028 for the comparison of glucose deprivation to hypoxia); combined hypoxia and

Figure 6.1. Effect of hypoxia and glucose deprivation on EOC cell line proliferation

A) Mean ±S.E. proliferation of ES-2, SKOV3 and RMG-II cells under hypoxia (1% O₂), relative to normoxia as assessed by ViCell after 96 hours in culture (n=6 for ES-2 and SKOV-3, n=4 for RMG-II). B) Mean ±S.E. proliferation of ES-2 and SKOV3 cells under normal culture conditions, glucose deprivation, hypoxia or both, as assessed by the SRB assay every 24 hours up to 168 hours (n=4). C) Mean ±S.E. proliferation of 10 EOC cell lines under glucose deprivation, hypoxia or both, relative to normal culture conditions as assessed by the SRB assay after 168 hours in culture (n=4). D) Mean ±S.E. proliferation under glucose deprivation, hypoxia or both, relative to normal culture conditions comparing OCCC (SKOV3, TOV21G, JHOC-5, JHOC-7, JHOC-9 and OWISE) and non-OCCC (PEO1, TR-175, ES-2 and OV2008) cell lines. E) Mean ±S.E. proliferation under glucose deprivation, hypoxia or both, relative to normal culture conditions comparing OCCC and HGS (PEO1 and TR-175) cell lines. F) Mean ±S.E. proliferation under glucose deprivation, hypoxia or both, relative to normal culture conditions comparing glycogen-rich (SKOV3, JHOC-5, JHOC-7 and OWISE) and glycogen-poor (PEO1, TOV21G and JHOC-9) cell lines.



glucose deprivation markedly decreased proliferation (mean reduction 77%, $p < 0.001$ for the comparison of combined hypoxia and glucose deprivation to either condition alone). I subsequently compared the 6 OCCC cell lines (TOV21G, JHOC-5, JHOC-7, JHOC-9, OVISE and SKOV3) with the 4 non-OCCC cell lines (PEO1, TR-175, OV2008 and ES-2). Glucose deprivation decreased proliferation by 49% in OCCC and by 56% in non-OCCC cell lines ($p = 0.75$; Fig. 6.1D). Hypoxia decreased proliferation by 37% in OCCC and 23% in non-OCCC cell lines ($p = 0.29$; Fig. 6.1D). Combined hypoxia and glucose deprivation decreased proliferation by 73% and 84% respectively ($p = 0.56$; Fig. 6.1D). Results were very similar when the 6 OCCC cell lines were compared to the 2 HGS cell lines PEO1 and TR-175 (Fig. 6.1E).

I next asked whether high glycogen content could modify the response to hypoxia and glucose deprivation. Glycogen content was available for 7 of the 10 cell lines (see section 6.3). In the comparison of glycogen-rich (SKOV3, JHOC-5, JHOC-7 and OVISE) and glycogen-poor (PEO1, TOV21G and JHOC-9) cell lines (Fig. 6.1F), no differential effect of hypoxia (mean reduction in proliferation 30% and 33%, $p = 0.9$) was seen. Glucose deprivation decreased proliferation by 42% in glycogen-rich and 59% in glycogen-poor cell lines, although this was not statistically significant ($p = 0.54$). Similarly, combined hypoxia and glucose deprivation decreased proliferation by 64% and 81% in glycogen-rich and glycogen-poor cell lines respectively ($p = 0.54$).

To summarise, I found no evidence that OCCC cell lines are more resistant than other EOC cell lines to hypoxia, glucose deprivation or both combined. Examination of a larger panel of cell lines is needed to clarify whether glycogen-rich cell lines are more resistant to glucose deprivation than glycogen-poor ones, as a non-statistically significant trend was observed.

6.3. OCCC cell lines contain large amounts of glycogen which is utilized under glucose deprivation

Glycogen accumulation is one of the defining characteristics of OCCC. To test whether OCCC cell lines contain detectable amounts of glycogen, I first assayed glycogen content of EOC cell lines using the qualitative PAS/PAS-diastrase stain. This showed glycogen accumulation in all 4 cell lines assayed (purple-magenta PAS staining changing to light pink after diastrase treatment; Fig. 6.2A-D). Even using this non-quantitative method, it is evident that some cell lines such as PEO1 (Fig. 6.2A) or TOV21G (Fig. 6.2C) contain much less glycogen than others such as SKOV3 (Fig. 6.2B) or JHOC-5 (Fig. 6.2D). It is important to note that the HGS cell line

PEO1 contains detectable amounts of glycogen, albeit in lesser quantities than many OCCC cell lines, in accordance with previous reports showing glycogen accumulation in multiple cell types, including glioblastoma and breast cancer cell lines (Favaro et al. 2012). To provide quantitative estimates of glycogen content, I utilised a colorimetric glycogen assay (see section 2.24.1 for details). As can be seen in Fig. 6.2E, the assay is linear over a 40-fold range of tested cell numbers. Seven cell lines were tested in 3 separate experiments and glycogen content ranged from 0.11 to 1.12 $\mu\text{g}/10^5$ cells with 4 OCCC cell lines (SKOV3, JHOC-5, JHOC-7 and OVISE) exhibiting very high glycogen content of approximately 1 $\mu\text{g}/10^5$ cells (Fig. 6.2F).

Glucose deprivation for 24 hours significantly decreased glycogen content (Fig. 6.2G). Glycogen levels tended to decrease more in glycogen-poor cell lines (99.7% in PEO1, 98.6% in TOV21G, 91% in JHOC-9; n=2 per cell line) compared with the glycogen-rich ones (48% in JHOC-7, 72% in JHOC-5, 76% in SKOV3, 93% in OVISE; n=2 per cell line). These results on the one hand serve as indirect validation of the glycogen assay and, on the other, show that intracellular glycogen can readily be utilised by these cells under conditions of nutritional stress.

Culture in 1% O₂ for 96 hours increased glycogen content in all 7 cell lines in accordance with observations in other cell types (Favaro et al. 2012; Pelletier et al. 2012; Pescador et al. 2010). The increase in glycogen levels ranged from 1.6 to 6.7-fold (n=2 per cell line) with a trend for more pronounced increases in glycogen-poor cell lines (Fig. 6.2H).

6.4. *HIF1A* is constitutively expressed and contributes to glycogen accumulation in OCCC cell lines

As shown above, many OCCC cell lines contain up to 10-fold more glycogen than a representative HGS line, PEO1. I have already shown that stable HNF1B expression is a driver for glycogen accumulation, at least in some cell lines (see section 5.9). However, it is not presently known what other factors contribute to the exceptionally high glycogen levels in OCCC. Since HIF1 α induction under hypoxia has been reported to lead to glycogen accumulation (Pelletier et al. 2012; Pescador et al. 2010), I first investigated whether glycogen accumulation is under *HIF1A* control in OCCC cell lines. Unfortunately, I was not able to reliably detect and quantify HIF1 α expression by immunoblots and, therefore, only report expression at the mRNA level, accepting that mRNA and protein expression and stability may differ. Interestingly, *HIF1A* was constitutively expressed in the 3 OCCC cell lines tested

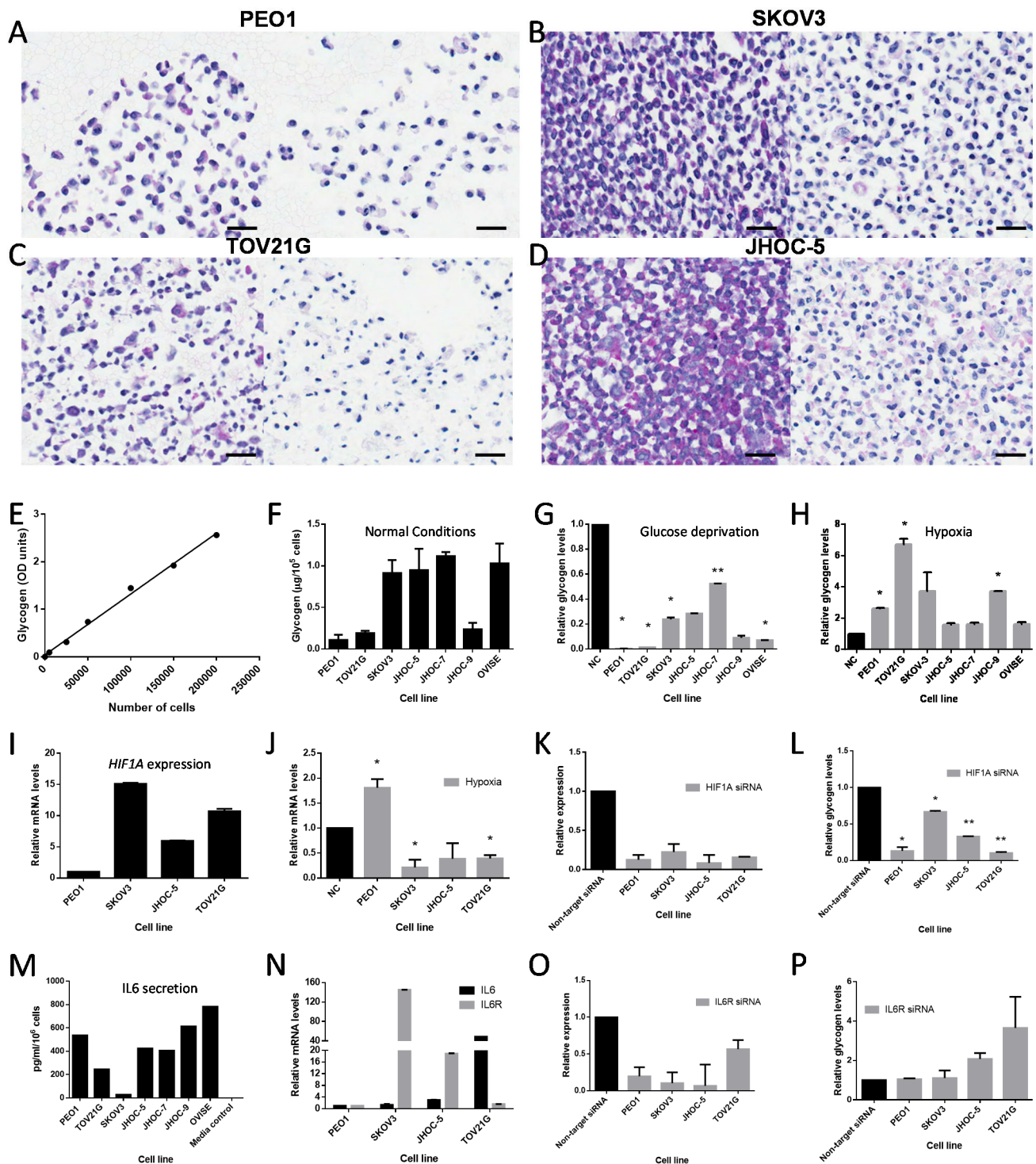
(SKOV3, JHOC-5, TOV21G) under normoxia with mRNA levels 6-15-fold higher than PEO1 (Fig. 6.2I). Culture under hypoxia for 72 hours induced, as expected, *HIF1A* expression in PEO1 but not in the OCCC cell lines, which showed a trend towards reduced mRNA levels (Fig. 6.2J). Treatment with siRNA, under hypoxia, successfully depleted *HIF1A* levels by 78-92% (Fig. 6.2K) and reduced proliferation in all 4 cell lines (by 39% to 81%) as assessed with the SRB assay (data not shown). *HIF1A* knockdown under hypoxia markedly depleted glycogen levels by 90% in TOV21G, 87% in PEO1, 67% in JHOC-5 and 33% in SKOV3 (Fig. 6.2L). It appears, therefore, that constitutive *HIF1A* expression in OCCC cell lines is one of the drivers of glycogen accumulation. This constitutive *HIF1A* expression may be driven by HNF1B, at least in some OCCC cell lines, as my gene expression data (see section 5.4) show that *HNF1B* knockdown significantly decreased *HIF1A* expression in TOV21G (by 40%) but not in JHOC-5 cells.

IL6 has been proposed to lead to HIF1 α induction in OCCC via STAT3 (Anglesio et al. 2011b), so I investigated whether the IL6-IL6R axis also contributes to glycogen accumulation. IL6 was detected in the medium supernatant at concentrations varying from 27 in SKOV3 to 783pg/ml/10⁶ cells in OVISE (Fig. 6.2M). Interestingly, PEO1 cells also secreted considerable amounts of IL6 in the medium (Fig. 6.2M). Compared to PEO1, *IL6* mRNA levels were increased by 1.3, 3 and 49-fold in SKOV3, JHOC-5 and TOV21G cells whereas the corresponding *IL6R* levels were 145, 19 and 1.6-fold higher (Fig. 6.2N). These results show considerable activation of IL6 signalling in OCCC cell lines, consistent with previous observations (Anglesio et al. 2011b). Treatment with siRNA successfully depleted *IL6R* levels by 43-93% (Fig. 6.2O) and modestly reduced proliferation in PEO1, SKOV3 and TOV21G (by

Figure 6.2. Glycogen content of ovarian cell lines under normal culture conditions, hypoxia and glucose deprivation and effect of HIF1 α and interleukin-6 on glycogen accumulation

A-D) PAS (left panels) and PAS-Diastase (right panels) staining of PEO1 (A), SKOV3 (B), TOV21G (C) and JHOC-5 (D) cells (bar=50 μ m). E) Results of colorimetric glycogen assay in TOV21G cells showing the assay is linear over the tested range (n=1 biological replicate run in duplicate). F) Mean \pm S.E. absolute glycogen content of 7 cell lines under normal culture conditions (n=3). G-H) Mean \pm S.E. relative glycogen content of 7 cell lines after 24 hours of glucose deprivation (G) or 96 hours of hypoxia (H). (NC= normal culture conditions) (n=2). I) Mean \pm S.E. *HIF1A* mRNA levels in NC normalised to PEO1 in OCCC cell lines (n=3). J) Mean \pm S.E. *HIF1A* mRNA levels in hypoxia relative to NC in OCCC cell lines (n=3). K) Mean \pm S.E. *HIF1A* mRNA levels relative to non-target siRNA 72 hours after siRNA-mediated *HIF1A* knockdown in hypoxia (n=3). L) Mean \pm S.E. glycogen levels in PEO1, SKOV3, JHOC-5 and TOV21G cells, 72 hours after *HIF1A* siRNA knockdown in hypoxia (n=2). M) IL6 concentration in medium after culture for 72 hours (n=1 biological replicate run in triplicate). N) Mean \pm S.E. *IL6* and *IL6R* mRNA levels normalised to PEO1 in OCCC cell lines (n=3). O) Mean \pm S.E. *IL6R* mRNA levels relative to non-target siRNA 72 hours after siRNA-mediated *IL6R* knockdown (n=3). P) Mean \pm S.E. glycogen levels in PEO1, SKOV3, JHOC-5 and TOV21G cells, 72 hours after *IL6R* siRNA knockdown (n=2).

17%, 26% and 33% respectively) but not JHOC-5 cells as assessed with the SRB assay (data not shown). However, *IL6R* knockdown did not affect glycogen levels in PEO1 and SKOV3 cells whereas JHOC-5 and TOV21G showed a non-significant increase in glycogen content (Fig. 6.2P). To summarise, these results show that, in addition to *HNF1B*, constitutive *HIF1A* expression contributes to the glycogen accumulation phenotype in OCCC. The IL6-IL6R axis appears to be activated in OCCC but does not directly lead to glycogen accumulation.



6.5. The rate-limiting glycogen metabolism enzymes glycogen phosphorylase and synthase are highly expressed in OCCC

Since the accumulated glycogen in OCCC cell lines is rapidly broken down by the cells following glucose deprivation (see section 6.3), I asked whether the two glycogen metabolism rate-limiting enzymes, glycogen phosphorylase (PYGL) and synthase (GYS1) are constitutively expressed in OCCC. PYGL is the main glycogen breakdown enzyme and, compared to PEO1, *PYGL* mRNA levels were 31.3, 4.8 and 2.7-fold higher in SKOV3, TOV21G and JHOC-5 cells respectively (Fig. 6.3A). PYGL protein expression in PEO1 and 6 OCCC cell lines was assessed in 3 separate experiments and a representative immunoblot is shown in Fig. 6.3B. Quantification of protein expression showed that, compared to PEO1, PYGL levels were 1.6 to 13.8-fold higher in OCCC cell lines (Fig. 6.3C). Hypoxia has been reported to induce PYGL expression in U87 glioblastoma cells (Favaro et al. 2012). However, PYGL levels showed no consistent trend and small absolute changes in the 6 OCCC cell lines after 96 hours in 1% O₂ whereas they modestly increased in PEO1 (Fig. 6.3D-E). To investigate the possibility that transient induction occurs at earlier time-points, PYGL expression was assayed in JHOC-5 and TOV21G cells 1, 4, 8, 24 and 48 hours after placement in 1% O₂. Again, no consistent PYGL induction was seen (Fig. 6.3F). Similarly to PYGL, GYS1 protein expression in PEO1 and 6 OCCC cell lines was also assessed in 3 separate experiments and a representative immunoblot is shown in Fig. 6.3G. GYS1 showed a narrower expression range with protein levels in the 6 OCCC cell lines varying from 2.2-fold lower in TOV21G to 3.9-fold higher in OVISE compared with PEO1 (Fig. 6.3H).

The observed constitutive PYGL expression in OCCC, together with the rapid utilisation of glycogen after glucose deprivation, suggest that the glycogen stores are not static and raise the possibility that glycogen plays an active role in OCCC cellular metabolism, even under normal culture conditions.

6.6. *PYGL* knockdown significantly decreases cellular proliferation

To investigate the role of glycogen in OCCC cellular metabolism, I then proceeded to inhibit glycogen breakdown by knocking down *PYGL* in 6 OCCC cell lines and PEO1. Treatment with siRNA reduced PYGL protein levels by 62-100% (Fig. 6.4A-B) and increased glycogen levels in all 7 cell lines even under NC with 25mM glucose in the medium (Fig. 6.4C). Across the 7 cell lines, the mean increase in glycogen levels was 3.5-fold (p=0.026). I repeated the glycogen assay after glucose deprivation in 5 of the cell lines and the results were unchanged

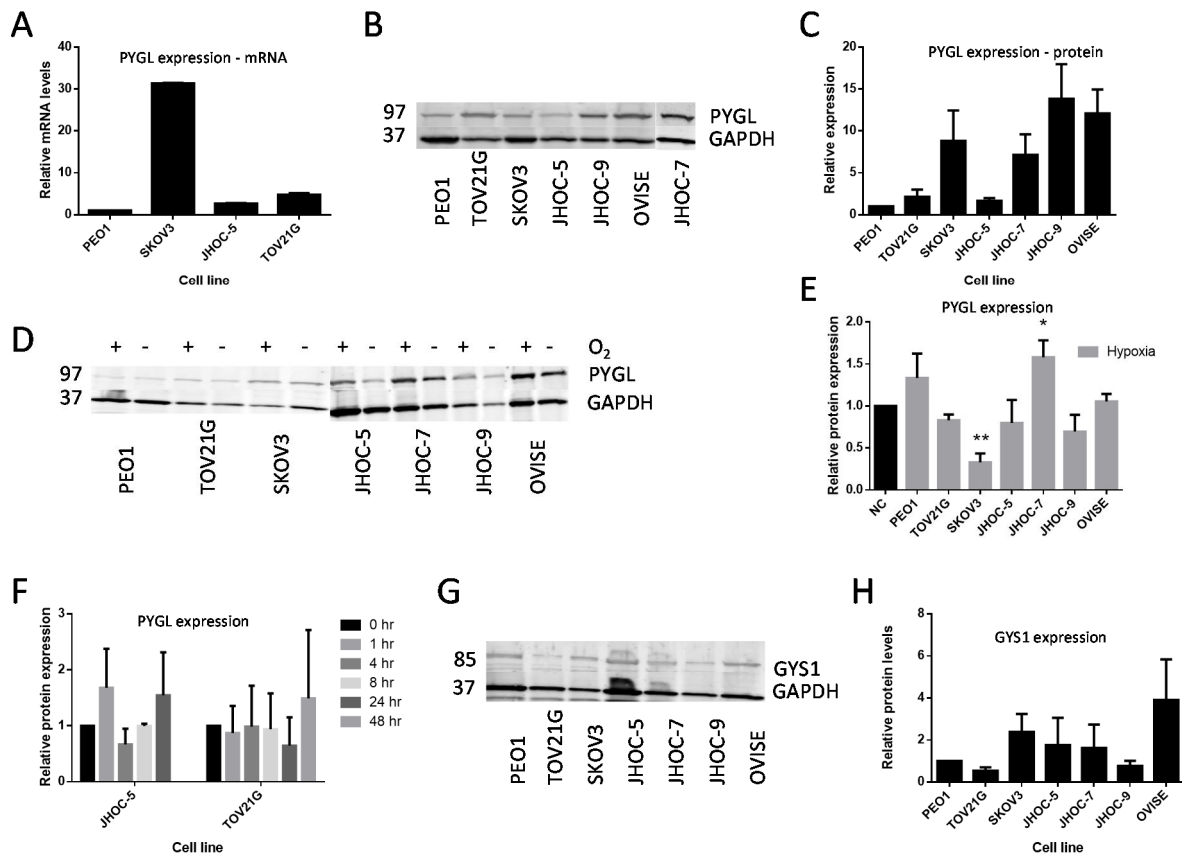


Figure 6.3. PYGL and GYS1 expression in OCCC cell lines

A) Mean \pm S.E. PYGL mRNA levels in OCCC cell lines normalised to PEO1 (n=3). B) Representative immunoblot showing PYGL expression in OCCC cell lines. C) Mean \pm S.E. PYGL protein expression quantification in OCCC cell lines normalised to PEO1 (n=3). D) Representative immunoblot showing changes in PYGL expression after culture for 96 hours in hypoxia (1% O₂) (“+” = 21% O₂, “-” = 1%O₂). E) Mean \pm S.E. change in PYGL expression after culture for 96 hours in hypoxia. (NC= normal culture conditions) (n=3). F) Time course of changes in PYGL expression after placement of JHOC-5 and TOV21G in hypoxia (mean \pm S.E.; n=2). G) Representative immunoblot showing GYS1 expression in OCCC cell lines. H) Mean \pm S.E. GYS1 protein expression quantification in OCCC cell lines normalised to PEO1 (n=3).

(Fig. 6.4D) with a mean 3.8-fold increase in glycogen levels (p=0.11). However, the increase in glycogen levels detected by the colorimetric assay, was not apparent by the qualitative PAS staining (Fig. 6.4E). The implications of these observations are two-fold: first, they show that siRNA PYGL inhibition results in decreased PYGL activity, although additional off-target effects cannot be excluded. More importantly, they suggest that PYGL is not only expressed but, also, constitutively active and that glycogen stores are continuously turned-over, even when plentiful glucose is available from the medium as, otherwise, PYGL inhibition shouldn't have an effect on glycogen levels under NC. This observation applies to both the OCCC cell lines and PEO1, although glycogen and PYGL levels in the latter were lower.

Therefore, I next investigated the effects of *PYGL* knockdown under NC, glucose deprivation and hypoxia. My hypothesis was that *PYGL* knockdown would decrease proliferation under all 3 conditions with the effects being more pronounced under glucose deprivation compared with NC. In all experiments, 1000 cells were plated per well in 96-well plates with 4-technical replicates per each of 4 biological (flask) replicates and the SRB assay was performed after 168 hours. An overview of the results is presented in Table 6.1 and in Fig. 6.4F-H. *PYGL* knockdown dramatically decreased proliferation in 6 of the 7 cell lines under all 3 conditions tested, with the reduction in proliferation exceeding 90% in PEO1 and JHOC-5 cells. The only exception was JHOC-7 which showed no change in proliferation under NC and glucose

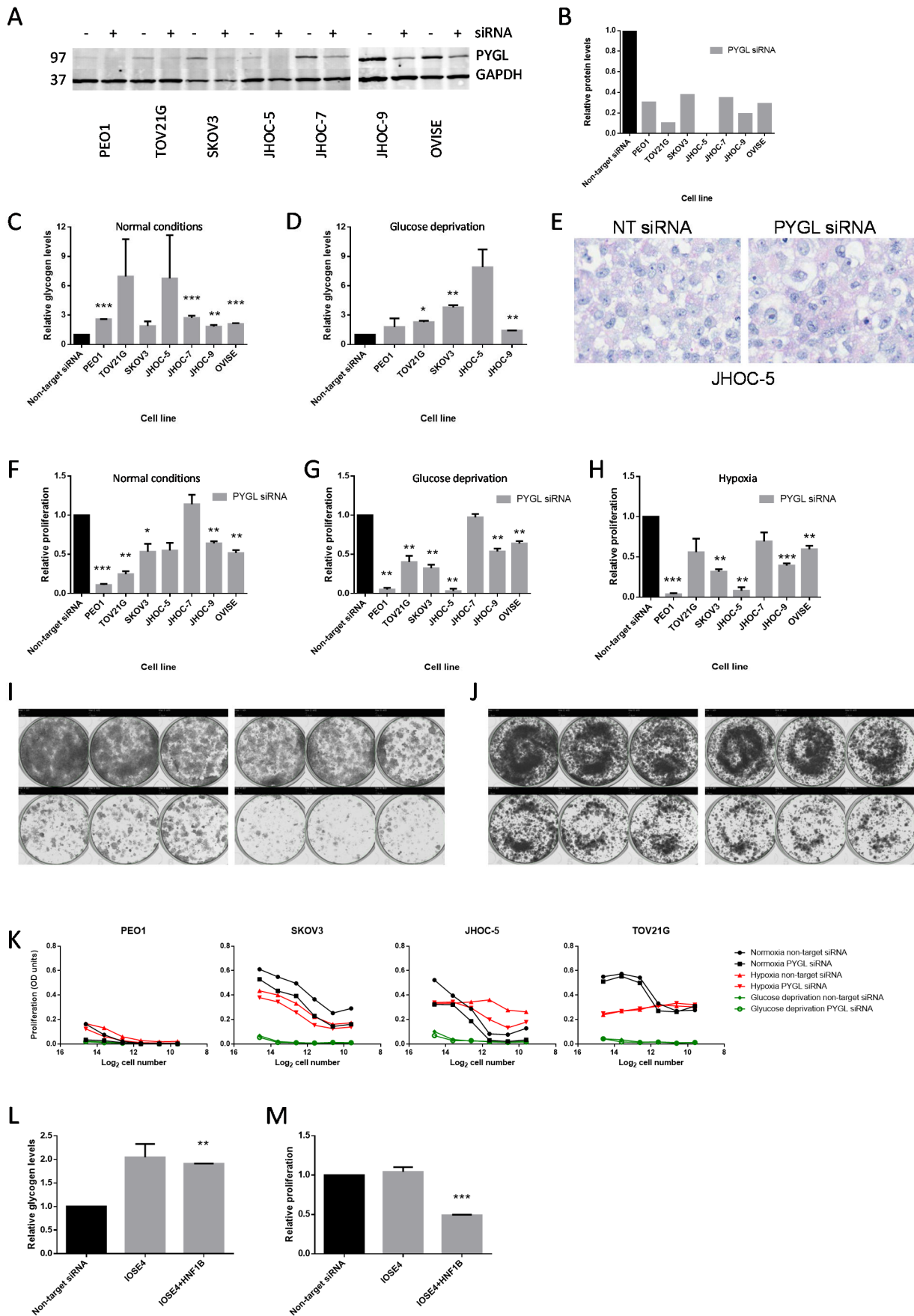
Table 6.1. Relative proliferation of 6 OCCC cell lines and PEO1 after glycogen metabolism perturbation

Cell line	<i>PYGL</i> siRNA (normal conditions)	<i>PYGL</i> siRNA (glucose deprivation)	<i>PYGL</i> siRNA (hypoxia)	<i>GYS1</i> siRNA	R3401 (<i>PYGL</i> inh)
PEO1	11%***	5%**	4%***	47%**	8%***
TOV21G	25%**	40%**	56%	44%**	4%***
SKOV-3	53%*	32%**	32%**	56%*	3%***
JHOC-5	55%	3%**	8%**	75%	2%**
JHOC-7	114%	97%	69%	120%	25%**
JHOC-9	64%**	54%**	39%***	78%***	3%**
OVISE	51%**	64%**	60%**	59%*	10%**
MEAN	53%**	42%**	38%***	69%*	8%***

*=0.01<p≤0.05; **=0.001<p0.01; ***=p≤0.001

Figure 6.4. Effect of *PYGL* knockdown on proliferation in EOC cell lines

A) Representative immunoblot showing *PYGL* expression following siRNA treatment in 7 EOC cell lines. B) Relative *PYGL* expression 72 hours after siRNA treatment in 7 EOC cell lines. C-D) Mean ±S.E. relative glycogen levels 72 hours after siRNA *PYGL* knockdown under normal culture conditions (C) (n=4) or glucose deprivation (D) (n=2). E) PAS staining of JHOC-5 cells 96 hours after non-target (left panel) or *PYGL* (right panel) siRNA treatment. F-H) Relative mean ±S.E. proliferation by the SRB assay in 7 EOC cell lines 168 hours after *PYGL* knockdown under normal culture conditions (F), glucose deprivation (G) or hypoxia (H). 1,000cells/well, 4 technical replicates per each flask replicate (n=4). I) Colony Forming Assay for JHOC-5 cells cultured in limiting dilutions under normal culture conditions for 14 days. In each 6-well plate cell numbers plated (from top left to bottom right) were 25000, 12500, 6250, 3125, 1565 and 782. Left panel: non-target siRNA; right panel: *PYGL* siRNA. J) Colony Forming Assay for SKOV3 cells. Set-up identical to that in (I). K) Cumulative results of the colony forming assays in PEO1, SKOV3, JHOC-5 and TOV21G cells under normal conditions, hypoxia and glucose deprivation. Cell numbers plated identical to (I). L) Mean ±S.E. relative glycogen levels 72 hours after siRNA *PYGL* knockdown under normal culture conditions in IOSE4 and IOSE4+HNF1B cells (n=2). M) Relative mean ±S.E. proliferation by the SRB assay in IOSE4 and IOSE4+HNF1B cell lines 168 hours after *PYGL* knockdown under normal culture conditions. 1000cells/well, 4 technical replicates per each flask replicate (n=4).



deprivation and a small non-significant reduction under hypoxia. Across all 7 cell lines, the mean reduction in proliferation was 47%, 58% and 62% under NC, glucose deprivation and hypoxia respectively. I replicated the results of the proliferation assay in a colony forming assay where limiting dilutions of PEO1, SKOV3, JHOC-5 and TOV21G cells were plated and cultured for 14 days under NC, glucose deprivation and hypoxia (see section 2.23.5). Representative plates are shown in Fig. 6.4I-J and the results of cell number quantification by the SRB assay in Fig. 6.4K. The latter was performed as the colonies were too confluent and ill-defined to be reliably enumerated by the GelCount scanner software. Consequently, the results in Fig 6.4K reflect total cell numbers rather than numbers of individual colonies. Overall, *PYGL* knockdown again decreased cell numbers, especially under NC and hypoxia. Very few colonies were seen under glucose deprivation in both the non-target and the *PYGL* siRNA treated wells, implying a detrimental effect of glucose deprivation under the very low seeding density conditions of this experiment. The smaller magnitude of the effect of *PYGL* knockdown under NC and hypoxia in this experiment compared with the classic proliferation assay, could be due to recovery of *PYGL* expression as cell numbers were assayed 17 days, compared with 7, after knockdown. This hypothesis however, was not directly tested.

The results observed in the EOC cell lines prompted me to investigate whether *PYGL* knockdown had similar effects in the non-malignant IOSE4 and IOSE4+HNF1B cells. siRNA *PYGL* knockdown approximately doubled the glycogen content of these cells (Fig. 6.4L). Knockdown significantly decreased proliferation in IOSE4+HNF1B cells by 51% ($p=0.0005$, $n=4$) but had no effect in IOSE4 cells ($p=0.64$, $n=4$) (Fig. 6.4M).

The results presented in this section, show that glycogen actively participates in the cellular metabolism of all cells, even in conditions where plentiful glucose is available as an energy source. *PYGL* knockdown disrupts glycogen breakdown and markedly decreases proliferation. The lack of an effect on IOSE4 cells provides some preliminary evidence that disruption of glycogen breakdown may be selective for cancer cells.

6.7. *GYS1* knockdown and small molecule inhibitors of glycogen metabolism also decrease cancer cell line proliferation

Although *PYGL* siRNA successfully inhibited *PYGL* as evidenced by the immunoblots (Fig. 6.4A-B) and the increase in glycogen levels (Fig. 6.4C-D), it cannot be excluded that the effect on proliferation is mediated by a secondary, off-target effect. To control for this possibility, I

also checked the effects of *GYS1* knockdown and small molecule inhibitors of glycogen metabolism. The rationale was that, if these interventions consistently showed an effect both on glycogen levels and proliferation, it would be very unlikely that they all shared an off-target effect on proliferation and the most parsimonious explanation would be that it is the perturbation in glycogen metabolism that reduces proliferation.

I first used siRNA to knock down *GYS1* expression under NC. Treatment with siRNA successfully decreased *GYS1* protein expression by 60-94% in all 7 cell lines (Fig. 6.5A). Knockdown also showed the expected reduction in glycogen levels, as glycogen synthesis was inhibited. Glycogen levels decreased 72 hours after knockdown by a mean 56% in 5 of the 7 cell lines whereas there was no change in PEO1 and an unexpected increase in JHOC-7 (Fig. 6.5B). Consistent with this, proliferation was decreased in all cell lines by a mean 31%, except for JHOC-7 (Table 6.1 and Fig. 6.5C).

I then used the small molecule R3401 to inhibit PYGL. The half maximal inhibitory concentration (IC_{50}) was calculated in JHOC-5 and TOV21G cells using 4 biological (flask) replicates and found to be 52 and 66 μ M respectively (Fig. 6.5D). At a concentration of 50 μ M, R3401 modestly increased glycogen levels by 16-72% (Fig. 6.5E), consistent with reports that PYGL phosphorylase activity is inhibited by approximately 60% at 125 μ M (Bergans et al. 2000). Treatment with 150 μ M R3401 resulted in a dramatic decrease in proliferation in all 7 cell lines, including the otherwise resistant JHOC-7 (Table 6.1 and Fig. 6.5F). The discrepancy between the concentrations needed to inhibit PYGL and the observed IC_{50} in the cell lines imply that part of this anti-proliferative effect may be mediated by targets other than PYGL.

I next tried a second PYGL small molecule inhibitor, sc-203975. This compound exhibited poor solubility which limited testing to concentrations up to 1 μ M as at higher concentrations the DMSO vehicle had a substantial impact on cell viability by itself (e.g. no growth of SKOV3 or PEO1 cells when treated with 5% DMSO). At concentrations of 0.5 and 1 μ M, sc-203975 showed no effect on either glycogen content (Fig. 6.5G) or proliferation (Fig. 6.5H). A third small molecule PYGL inhibitor, DAB, showed no effect on proliferation in TOV21G and JHOC-5 cells in concentrations up to 800 μ M (Fig. 6.5I). Treatment with 800 μ M DAB for 72 hours increased glycogen content in PEO1 cells but not in SKOV3, JHOC-5 or TOV21G cells, implying insufficient PYGL inhibition in the OCCC cell lines (Fig. 6.5J). In accordance with its effects on glycogen, 800 μ M DAB significantly decreased proliferation in PEO1 cells by 53% ($p=0.006$) but showed no effect in the 3 OCCC cell lines (Fig. 6.5K).

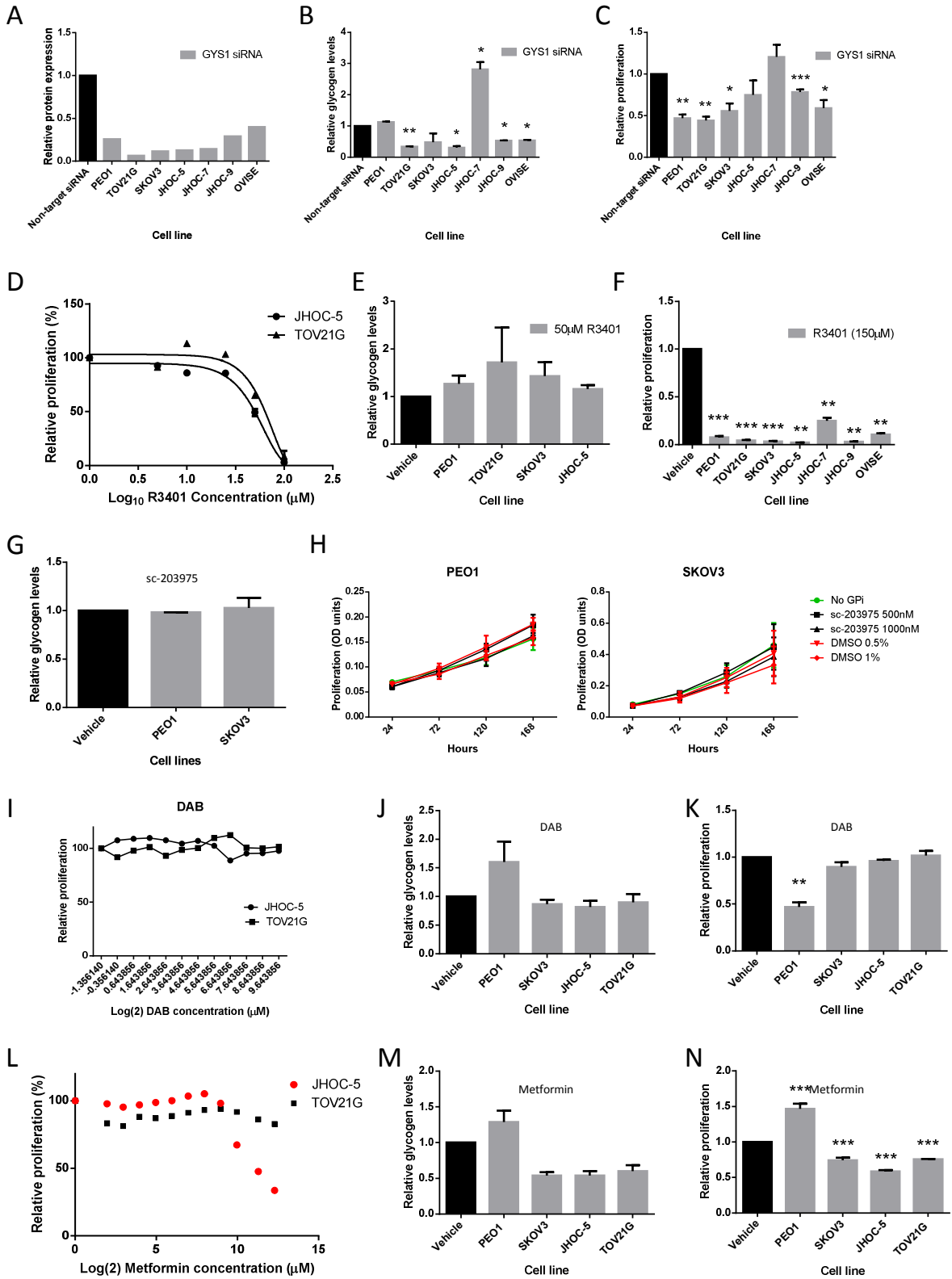
Metformin has pleiotropic effects on carbohydrate metabolism, including a reduction in hepatic glycogen synthesis through effects on GYS1 regulatory proteins (Polakof et al. 2011; Radziuk et al. 2003). Therefore, I investigated the effect of metformin on glycogen content and proliferation in OCCC cell lines. Treatment with up to 5mM metformin very modestly affected proliferation in TOV21G cells without a clear dose-response relationship, whereas a reduction in proliferation was seen in JHOC-5 cells at concentrations above 1mM (Fig. 6.5L). Treatment with 4mM metformin for 72 hours reduced the glycogen content of SKOV3, JHOC-5 and TOV21G cells by 40-46% (Fig. 6.5M). This was accompanied by a modest, but statistically significant, 24-41% decrease in proliferation (Fig. 6.5N). Interestingly, both glycogen levels and proliferation increased in PEO1 cells (Fig. 6.5M-N), implying context-dependent effects of metformin on carbohydrate metabolism.

6.8. *PYGL* Inhibition causes G2/M arrest but not induction of apoptosis or senescence

An interesting question is how inhibition of glycogen metabolism can affect proliferation in a nutrient rich environment. *PYGL* knockdown has been reported to induce senescence in U87 cells (Favaro et al. 2012) but is not known if this mechanism is operating in OCCC too. I, therefore, investigated the mechanism underlying the reduction in proliferation after *PYGL*

Figure 6.5. Effect of glycogen metabolism perturbations on proliferation

A) Relative GYS1 expression 72 hours after siRNA treatment in 7 EOC cell lines. B) Relative mean \pm S.E. glycogen levels 72 hours after siRNA *GYS1* knockdown under normal culture conditions (n=2). C) Relative mean \pm S.E. proliferation by the SRB assay in 7 EOC cell lines 168 hours after *GYS1* knockdown under normal culture conditions. 1,000cells/well, 4 technical replicates per each flask replicate (n=4). D) IC₅₀ curves, as determined by the SRB assay after 168 hours, for R3401 treatment of JHOC-5 and TOV21G cells. 1000cells/well, 4 technical replicates per each flask replicate (n=4). E) Mean \pm S.E. glycogen levels 72 hours after treatment with vehicle (0.17% DMSO) or 50 μ M R3401 (n=2). F) Relative mean \pm S.E. proliferation by the SRB assay in 7 EOC cell lines 168 hours after 150 μ M R3401 treatment under normal culture conditions. 1,000cells/well, 4 technical replicates per each flask replicate (n=4). G) Mean \pm S.E. glycogen levels 72 hours after treatment with vehicle (1% DMSO) or 1 μ M sc-203975 (n=2). H) Relative mean \pm S.E. proliferation by the SRB assay in PEO1 and SKOV3 cells 168 hours after 0.5 and 1 μ M sc-203975 treatment under glucose deprivation. 1,000cells/well, 4 technical replicates per each flask replicate (n=4). I) IC₅₀ curves, as determined by the SRB assay after 168 hours, for DAB treatment of JHOC-5 and TOV21G cells. 1,000cells/well, (n=4). J) Mean \pm S.E. glycogen levels 72 hours after treatment of 4 EOC cell lines with vehicle (8% water) or 800 μ M DAB (n=2). K) Relative mean \pm S.E. proliferation by the SRB assay in 4 EOC cell lines 168 hours after 800 μ M DAB treatment under normal culture conditions. 1,000cells/well, 4 technical replicates per each flask replicate (n=4). L) IC₅₀ curves, as determined by the SRB assay after 168 hours, for metformin treatment of JHOC-5 and TOV21G cells. 1,000cells/well, (n=4). M) Mean \pm S.E. glycogen levels 72 hours after treatment of 4 EOC cell lines with vehicle (8% water) or 4mM metformin (n=2). N) Relative mean \pm S.E. proliferation by the SRB assay in 4 EOC cell lines 168 hours after 4mM metformin treatment under normal culture conditions. 1,000cells/well, 4 technical replicates per each flask replicate (n=4).



siRNA knockdown in SKOV3, JHOC-5 and TOV21G cells. *PYGL* knockdown did not induce apoptosis, as evidenced by a lack of an increase in caspase-3 (Fig. 6.6A) and caspase-8 (data not shown) staining and a negative TUNEL assay (Fig. 6.6B) in all 3 cell lines. β -galactosidase staining after 24 hours X-gal incubation in the 3 cell lines and, additionally, in PEO1, did not show induction of senescence (Fig. 6.6C; TOV21G shows small numbers of senescent cells after non-target siRNA treatment that do not further increase with *PYGL* siRNA treatment).

Cell cycle analysis after *PYGL* siRNA knockdown showed modest accumulation of cells in G2/M in JHOC-5 and TOV21G but not in SKOV3 cells (Fig. 6.7A). The percentage of cells in G2/M in JHOC-5, TOV21G and SKOV3 was 21%, 16% and 46% after non-target siRNA treatment and 32% ($p < 0.0001$), 21% ($p = 0.002$) and 46% ($p = 0.66$) after *PYGL* siRNA treatment respectively. Subsequently, I investigated whether *PYGL* knockdown affected the expression of proteins involved in the G2/M checkpoint in JHOC-5 and TOV21G cells. Cdc25 expression was reduced in JHOC-5 and Cyclin B1 expression was reduced in TOV21G cells whereas Chk1 expression was unchanged (Fig. 6.7B); both observed changes are consistent with delayed cell cycle progression. Cdc2 (also known as Cdk1) was expressed in both JHOC-5 and TOV21G cells, but Y15-phosphorylated Cdc2 was only detected in the latter (Fig. 6.7B). Consistent with inhibition of cell cycle progression at the G2/M checkpoint, the ratio of phosphorylated-to-total Cdc2 was increased after *PYGL* knockdown in TOV21G cells (Fig. 6.7C). Of these proteins, only Cdc2 could be detected in the proteomics screen (see section 6.11). Consistent with the immunoblot results, no significant change in total Cdc2 levels was seen by MS.

6.9. *PYGL* inhibition does not have a major effect on glycolysis, the TCA cycle or ATP production

Inhibition of glycogen metabolism could affect intracellular glucose-6-phosphate levels which sits at the branch point between glucose breakdown and glycogen synthesis (see section 1.4). Altered glucose-6-phosphate levels, in turn, could have a knock-on effect on glycolysis, the TCA cycle and associated pathways such as the pentose phosphate pathway and lipid synthesis. Therefore, using NMR (see section 2.19.1), I measured changes in medium and intracellular metabolite concentrations 96 hours after *PYGL* knockdown. Treatment with siRNA decreased *PYGL* mRNA levels by 81-85%. However, no major changes were seen in metabolite uptake from or excretion in the medium with the exception of a small reduction in pyruvate uptake that was only significant in JHOC-5 cells (Fig. 6.8A-B). Consistent with the

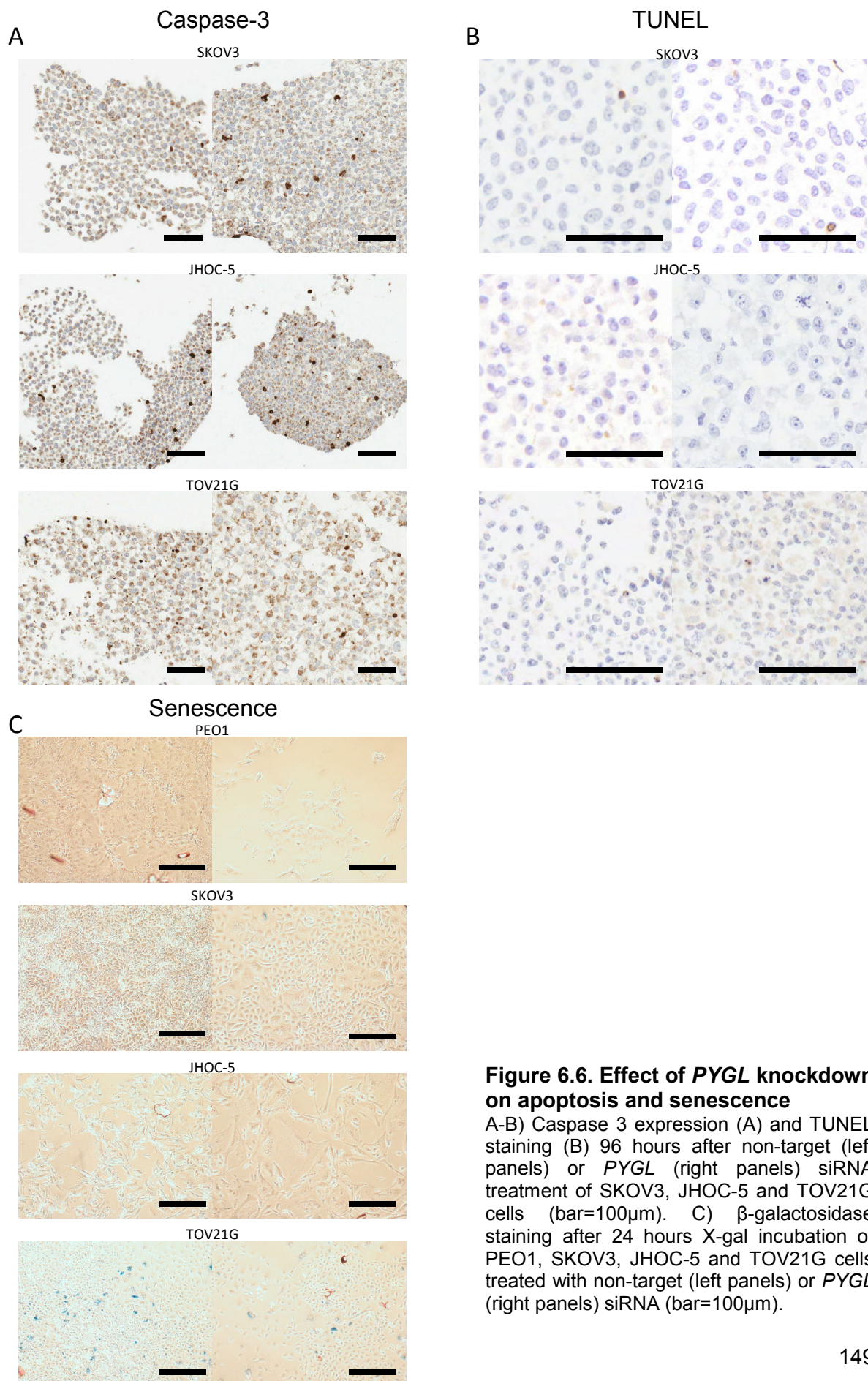


Figure 6.6. Effect of *PYGL* knockdown on apoptosis and senescence

A-B) Caspase 3 expression (A) and TUNEL staining (B) 96 hours after non-target (left panels) or *PYGL* (right panels) siRNA treatment of SKOV3, JHOC-5 and TOV21G cells (bar=100μm). C) β-galactosidase staining after 24 hours X-gal incubation of PEO1, SKOV3, JHOC-5 and TOV21G cells treated with non-target (left panels) or *PYGL* (right panels) siRNA (bar=100μm).

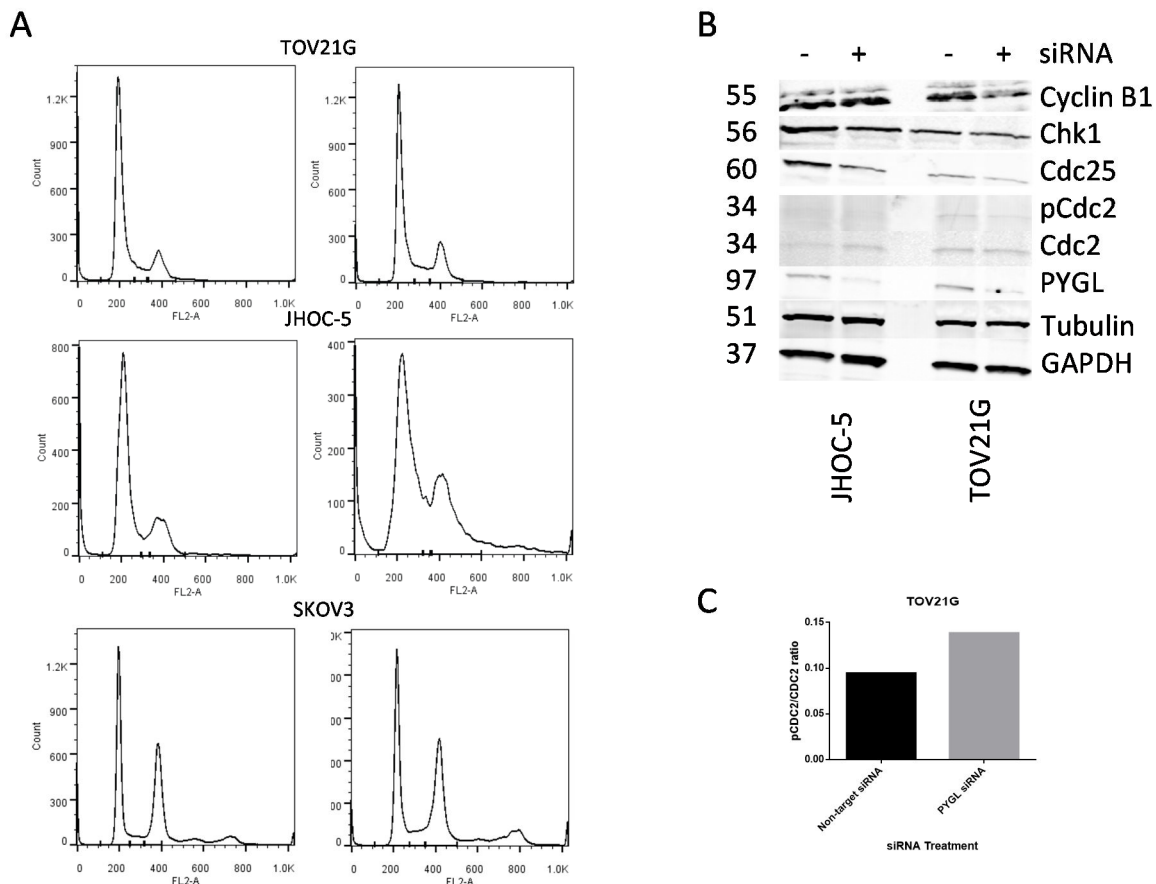


Figure 6.7. Effect of *PYGL* knockdown on cell cycle progression

A) Cell cycle phase distribution of TOV21G, JHOC-5 and SKOV3 cells 96 hours after non-target (left panels) or *PYGL* (right panels) siRNA treatment. B) Immunoblot showing Cyclin B1, Chk1, Cdc25, Cdc2 and pCdc2 (Tyr15) expression in JHOC-5 and TOV21G cells 72 hours after non-target (-) and *PYGL* (+) siRNA treatment. C) Quantitative assessment of the pCdc2/Cdc2 ratio for TOV21G cells (JHOC-5 cells did not show pCdc2 expression).

lack of an effect on glucose uptake, *SLC2A1* mRNA levels were not affected by *PYGL* knockdown (Fig. 6.8C). Assessment of intracellular metabolite concentrations showed no changes in the major glycolytic molecules glucose, lactate and pyruvate, except for a small but significant increase in pyruvate seen in JHOC-5 cells (Fig. 6.9). Decreased concentrations of some (succinate, acetate) but not other (fumarate, citrate) intermediaries of the TCA cycle were seen in both cell lines. Interestingly, intracellular glutamine, which can serve as an alternate substrate in the TCA cycle showed a large, but not significant, increase in TOV21G cells (Fig. 6.9). No change was observed in membrane building blocks such as choline and phosphocholine, or the overall energetic state of the cells as measured by phosphocreatine and ATP concentrations, whereas the concentrations of some amino acids (phenylalanine, methionine, leucine) was increased in JHOC-5 cells (Fig. 6.9).

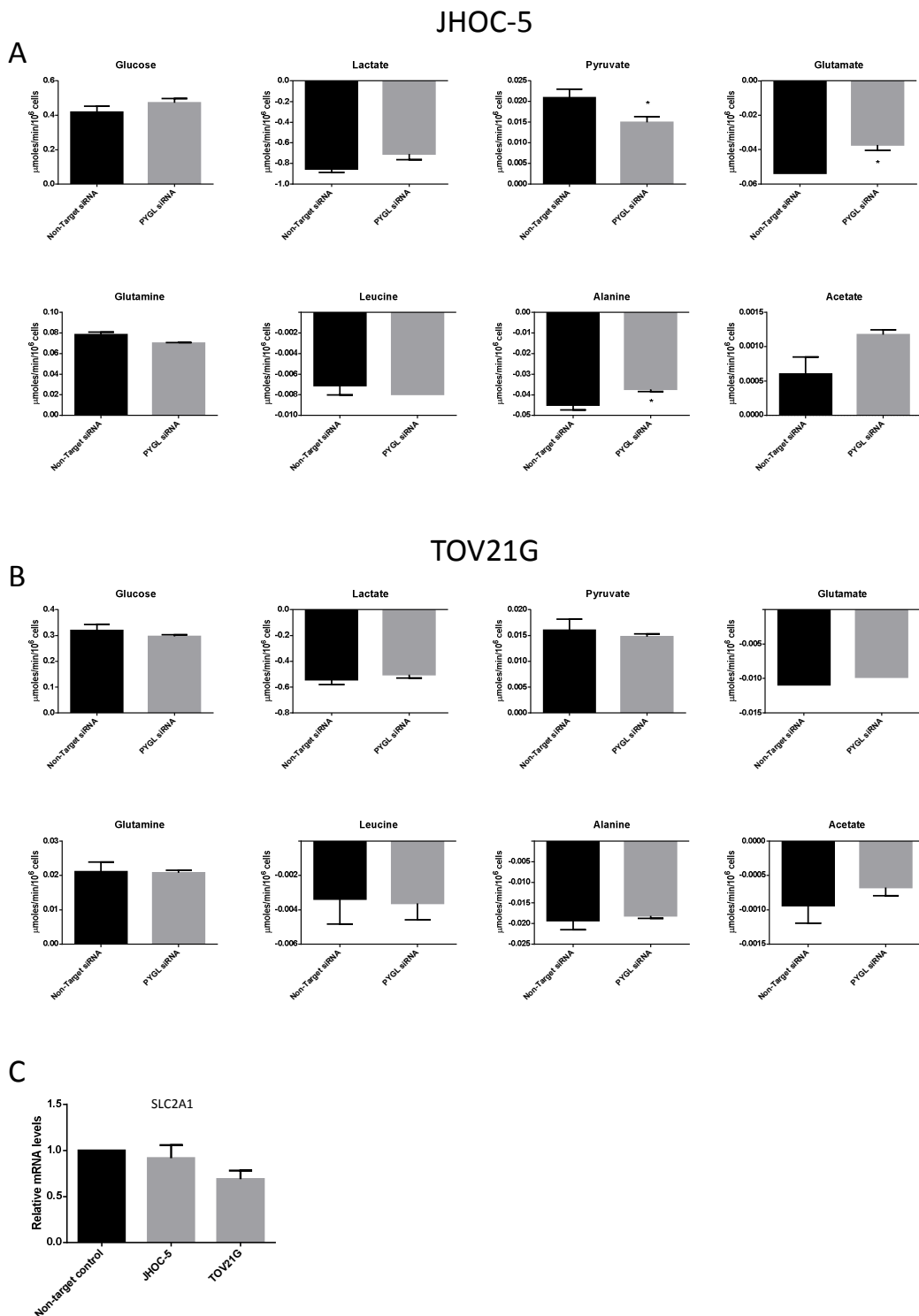


Figure 6.8. Effect of *PYGL* knockdown on metabolites in the culture medium

A-B) Changes in metabolite concentrations in the medium 96 hours after siRNA-mediated *PYGL* knockdown in JHOC-5 (A) and TOV21G (B) cells. Cells were cultured in DMEM medium with 3 flask replicates per cell line. Positive values indicate uptake from the medium (i.e. the concentration at 96 hours is lower than the baseline) whereas negative values indicate release in the medium (i.e. the concentration at 96 hours is higher than the baseline). C) Change in *SLC2A1* mRNA levels 72 hours after siRNA-mediated *PYGL* knockdown in JHOC-5 and TOV21G cells (n=2).

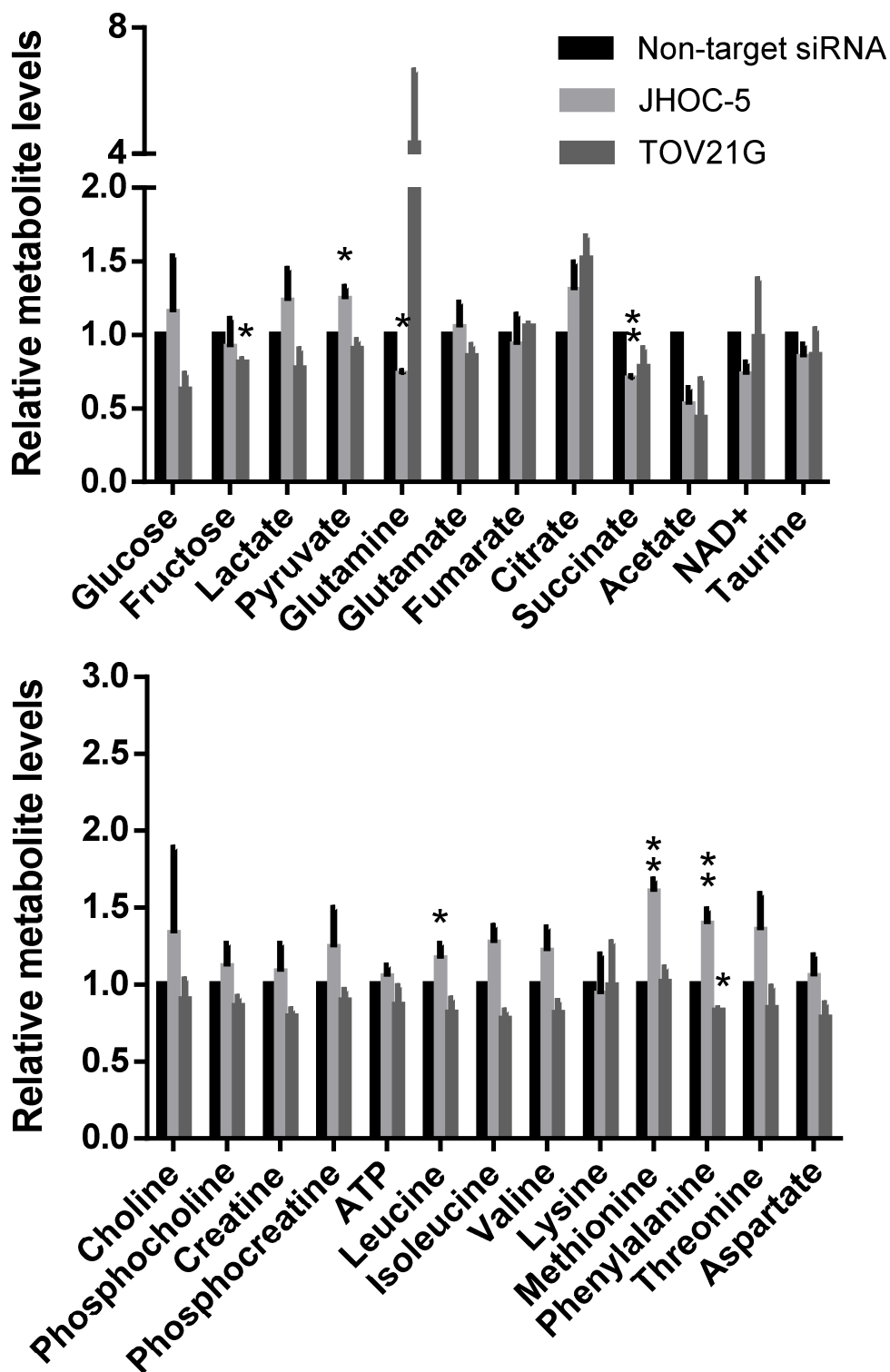


Figure 6.9. Effect of *PYGL* knockdown on intracellular metabolites

Relative changes in intracellular metabolite concentrations 96 hours after siRNA-mediated *PYGL* knockdown in JHOC-5 and TOV21G cells. Cells were cultured in DMEM medium with 3 flask replicates per cell line and values corrected for protein content.

6.10. *PYGL* knockdown impairs lipid metabolism but does not result in ROS accumulation or induction of the unfolded protein response (UPR) pathway

Glucose-1-phosphate (G-1-P), the main product of glycogen breakdown, interacts with L-FABP to modulate PPAR α function (Hostetler et al. 2010). PPAR α is the main regulator of lipid β -oxidation (Dreyer et al. 1993) and I, therefore, hypothesised that *PYGL* knockdown would inhibit PPAR α and result in lipid accumulation. CARS was used to image lipid droplets (see section 2.19.2) in a label-free manner. Consistent with the hypothesis, lipid droplet content 96

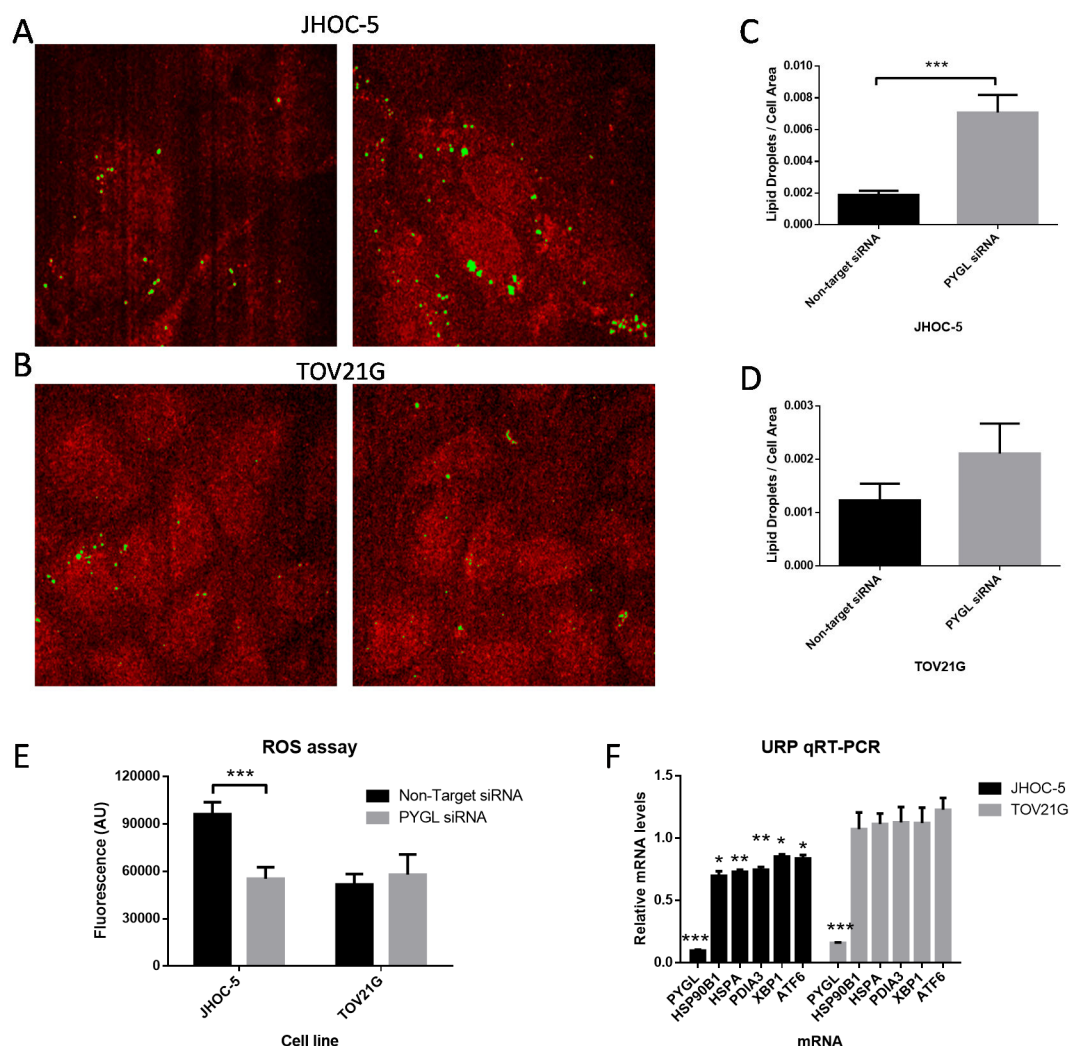


Figure 6.10. Effect of *PYGL* knockdown on lipid droplet, reactive oxygen species (ROS) accumulation and the unfolded protein response

A-B) Lipid droplet imaging (green) in JHOC-5 (A) and TOV21G (B) cells treated with non-target (left panels) or *PYGL* (right panels) siRNA. C-D) Quantitative assessment of lipid droplet accumulation in JHOC-5 (C) and TOV21G (D) cells treated with non-target or *PYGL* siRNA (n=10 75x75 μ m areas scanned per sample). E) Mean \pm S.E. ROS accumulation 96 hours after siRNA-mediated *PYGL* knockdown in JHOC-5 and TOV21G cells (n=5). F) Relative mean \pm S.E. changes in mRNAs involved in the unfolded-protein response after siRNA *PYGL* knockdown (n=3 flask replicates per cell line).

hours after *PYGL* knockdown was increased in JHOC-5 cells 3.77-fold ($p=0.0002$) with a non-significant trend (1.72-fold, $p=0.19$) in TOV21G cells (Fig. 6.10A-D).

Impaired lipid oxidation or pentose phosphate pathway function after *PYGL* knockdown could alter the cellular ROS content. However, *PYGL* siRNA treatment did not result in any change in intracellular ROS in TOV21G cells (difference 9%, $p=0.43$) and decreased the ROS content of JHOC-5 cells by 43% ($p=0.0008$) (Fig. 6.10E). As increased ROS production generally induces apoptosis or senescence, the lack of ROS induction by *PYGL* knockdown is consistent with the results of the apoptosis and senescence assays reported in section 6.8 but suggest that any potential defect in lipid oxidation does not result in marked alterations of the cellular redox state.

Another potential mechanism through which *PYGL* knockdown could affect proliferation is aberrant N-glycosylation of target proteins and induction of the unfolded-protein response (UPR) (Lecca et al. 2005; Philips et al. 2014). I therefore tested whether *PYGL* knockdown induced the expression of 5 core UPR genes (*HSP90B1*, *HSPA5*, *PDIA3*, *XBP1* and *ATF6*). Contrary to my hypothesis, I found that expression of these genes was modestly (mean decrease 15-30%) but statistically significantly decreased in JHOC-5 cells whereas it did not change in TOV21G cells (Fig. 6.10F).

6.11. *PYGL* knockdown does not markedly perturb the proteome but results in changes in Protein Kinase A signalling

To gain further insights as to how *PYGL* knockdown affects proliferation, I tested its effects on the proteome in an agnostic manner. MS/MS was performed (see section 2.31 for details) in JHOC-5 and TOV21G cells 72 hours after siRNA *PYGL* knockdown using 3 flask replicates per cell line. 2776 proteins could be reproducibly detected and their differential expression after knockdown was assessed. As can be seen in Fig 6.11A, using a stringent threshold of corrected $p=0.05$, very few proteins showed change in expression, and these were mostly of low abundance.

With a less stringent threshold of $p=0.1$, 100 proteins were differentially expressed in JHOC-5 cells with the majority showing decreased expression after knockdown (Fig. 6.11B). Peroxiredoxin-3 (PRDX3), a protein with anti-oxidant function was significantly up-regulated,

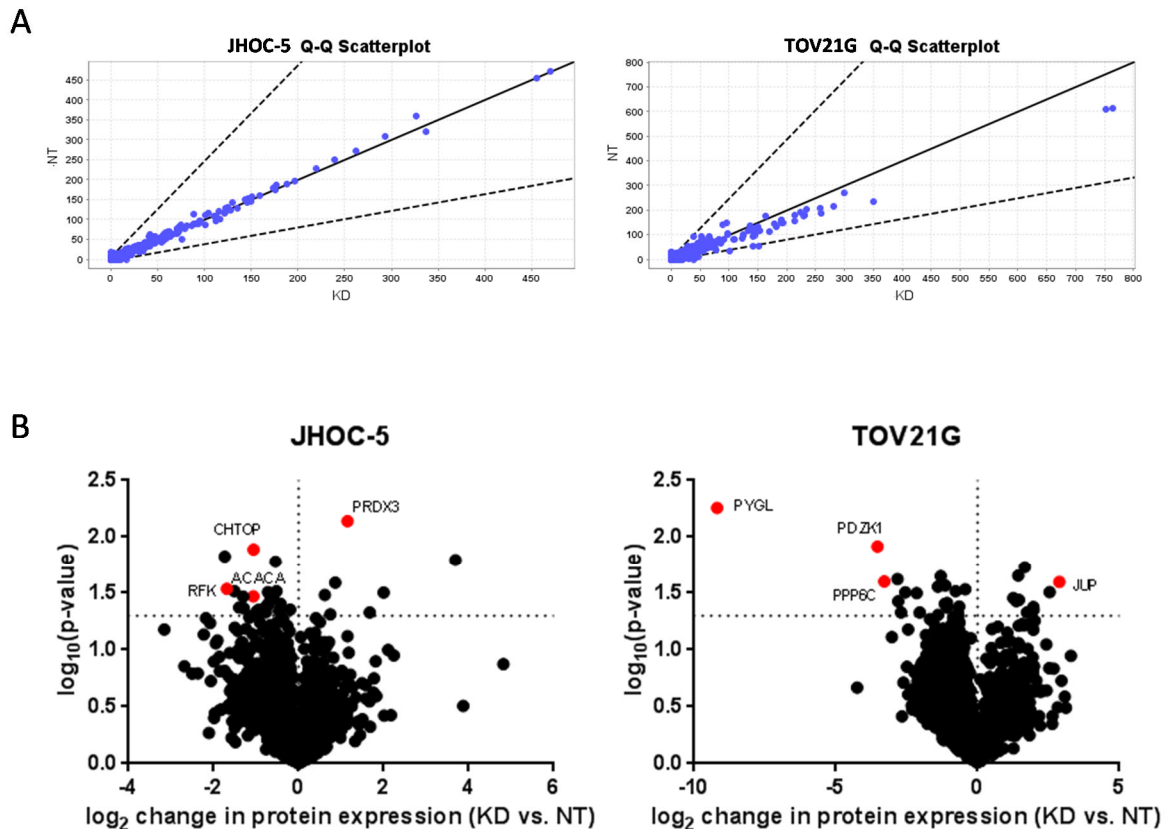


Figure 6.11. Effect of *PYGL* knockdown on cellular proteomics

MS/MS was used to assay 2776 proteins in non-target (NT) and *PYGL*-siRNA (KD) treated JHOC-5 and TOV21G cells ($n=3$ flask replicates). A) Q-Q scatterplots. Dotted lines delineate corrected 95% confidence intervals. B) Volcano plots. Horizontal dotted lines mark $p=0.05$.

a fact that could explain the reduction in ROS content seen upon knockdown in these cells (see section 6.10). Using MetaCore, pathways (Table A.15 in the Appendix) and metabolic networks (Table A.16 in the Appendix) related to protein kinase A (PKA) were significantly enriched among these 100 *PYGL*-regulated proteins driven by a significant increase in the expression of the catalytic subunit *PRKACA* and a concomitant decrease in that of the regulatory subunit *PRKAR2B* (54% and 38% respectively).

Similarly, in TOV21G cells, 111 proteins were differentially expressed, with *PDZK1* (PDZ Domain Containing 1), a protein involved in ion transport and *PPP6C* (Protein Phosphatase 6, Catalytic Subunit), a protein that regulates cell cycle progression, being among the top hits (Fig. 6.11B). As in JHOC-5, pathways related to PKA were significantly enriched among *PYGL*-regulated proteins (Table A.17 in the Appendix), driven in this instance by a 52%

decrease in the expression of the alternative regulatory subunit PRKAR2A. No enriched metabolic networks were identified at an FDR threshold of 0.1.

Table 6.2. PYGL-regulated proteins in both JHOC-5 and TOV21G cells

Protein	Full Name	Function	LFC JHOC-5	LFC TOV21G
EIF2AK2	Eukaryotic Translation Initiation Factor 2-Alpha Kinase 2	Inhibits protein synthesis	-0.53	-0.77
PRCP	Prolylcarboxypeptidase (Angiotensinase C)	Cleaves C-terminal amino acids in peptides such as angiotensin II, III and des-Arg9-bradykinin	-0.71	-0.79
ACACA	Acetyl-CoA Carboxylase Alpha	Catalyses the carboxylation of acetyl-CoA to malonyl-CoA, the rate-limiting step in fatty acid synthesis	-1.06	-1.02
ERLIN1	ER Lipid Raft Associated 1	Mediates the endoplasmic reticulum-associated degradation (ERAD) of inositol 1,4,5-trisphosphate receptors (IP3Rs)	-0.44	-1.07
VPS25	Vacuolar Protein Sorting 25 Homolog (S. Cerevisiae)	Sorts ubiquitinated membrane proteins during endocytosis	-0.64	-1.09
MGEA5	Meningioma Expressed Antigen 5 (Hyaluronidase)	Removes O-GlcNAc modifications on serine and threonine residues	-1.50	-1.19
CCDC22	Coiled-Coil Domain Containing 22	Regulates of NF-kB by interacting with COMMD (copper metabolism Murr1 domain-containing) proteins	-0.90	-1.21
ENO2	Enolase 2 (Gamma, Neuronal)	Glycolysis	-0.91	-1.23
ERAP1	Endoplasmic Reticulum Aminopeptidase 1	Trims HLA class I-binding precursors so that they can be presented on MHC class I molecules	-0.72	-1.25
CHTOP	Chromatin Target Of PRMT1	Cell cycle progression; interaction with protein arginine methyltransferases; role in the activation of estradiol-dependent transcription	-1.06	-1.49
PPP1R21	Protein Phosphatase 1, Regulatory Subunit 21		-3.16	-2.80
RFK	Riboflavin Kinase	Phosphorylation of riboflavin to form flavin-mononucleotide (FMN), hence rate-limiting enzyme in the synthesis of FAD	-1.69	-3.02

Protein functions imported from www.genecards.org; LFC: Log₂ fold change.

There was a significant overlap between the 100 *PYGL*-regulated proteins in JHOC-5 and the 111 in TOV21G cells, with 12 proteins showing concordant significant changes ($p=4.97 \times 10^{-4}$). Table 6.2 summarises these proteins and their function. It is interesting to note that all 12 show decreased expression upon *PYGL* knockdown. Although no specific pathways were enriched, some of these proteins' functions such as involvement in lipid synthesis (*ACACA*), post-translational glycosylation (*MGEA5*), glycolysis (*ENO2*), endoplasmic-reticulum associated degradation (ERAD) (*ERLIN1*) and the cellular redox state (*RFK*) could be relevant to *PYGL*'s effect on proliferation.

6.12. Discussion

In this chapter, I have shown that, contrary to previous publications, OCCC cell lines are not more resistant to hypoxia or glucose deprivation. Driven by *HNF1B* overexpression and constitutive *HIF1 α* expression, they accumulate large amounts of glycogen, which they can access under conditions of nutrient deprivation. Importantly, my results show that glycogen is continuously being turned-over and that perturbing glycogen metabolism by inhibiting either its breakdown or its synthesis has a pronounced effect on cellular proliferation, even when plentiful glucose is available to be utilised as a fuel source. The reduction in proliferation after glycogen breakdown inhibition is not due to increased apoptosis or senescence but could be due to G2/M checkpoint activation mediated by changes in lipid metabolism and PKA signalling.

As OCCC arises from the hypoxic and iron-rich oxidative environment of endometriotic cysts, many authors have postulated that resistance to hypoxia and nutrient deprivation underlies its chemoresistance (Iida et al. 2012; Yamada et al. 2011). Stany *et al* (2011) reported that ES-2 and TOV21G cells were more resistant to combined hypoxia (1% O_2) and glucose deprivation (0.7mM glucose) than the HGS cell lines OVCA420 and OVCA429 using the CellTiter Blue assay at 72 hours. In contrast, using a panel of 6 OCCC and 4 non-OCCC cell lines, I found no difference in sensitivity to glucose deprivation, hypoxia or their combination with the SRB assay at 168 hours. The results were unchanged when I compared the 6 OCCC cell lines only with the 2 HGS cell lines. I used ES-2 cells as a non-OCCC cell line whereas Stany *et al* used it as an OCCC cell model. There is compelling evidence that ES-2 is not OCCC as it has *TP53* and *BRAF* mutations in the absence of *ARID1A* and *PIK3CA* mutations (Domcke et al. 2013), does not express *HNF1B*, both according to my results (see section 5.2) and others (Anglesio et al. 2013), and forms undifferentiated tumours when engrafted in immunosuppressed mice (Shaw et al. 2004). Both the CellTiter Blue (Niles et al. 2009) and the SRB (Vichai & Kirtikara

2006) assays are well validated and both Stany *et al* and I plated similar numbers of cells; therefore, the most likely explanation for the discrepant results is the limited number of cell lines tested by these authors and the shorter timeframe utilised. Interestingly, in my data there was a trend for glycogen-rich cell lines to be more resistant to glucose deprivation but not to hypoxia. In glycogen-poor cell lines, glycogen stores were depleted after 24 hours of glucose deprivation but most glycogen-rich cell lines still showed considerable residual glycogen stores (Fig. 6.2G) which may have been sufficient to sustain proliferation for longer. Furthermore, it has been recently reported that, in a large panel of cancer cell lines, impaired glucose uptake and mutations affecting mitochondrial complex I function are the main determinants of sensitivity to glucose deprivation (Birsoy et al. 2014). It will be interesting to investigate whether these mechanisms are operative in OCCC cell lines and whether the phenotype is modulated by glycogen.

Using a colorimetric glycogen assay, I have shown that many OCCC cell lines have a glycogen content that is 10-fold higher than the HGS cell line PEO1. Far from being an inert pool, this glycogen is readily utilised when the cells are deprived of glucose. An unanswered question is what drives this profound glycogen accumulation in OCCC cells. Hypoxia and HIF1 α induction have been consistently reported to cause glycogen accumulation in cancer cells (Favaro et al. 2012; Pelletier et al. 2012; Pescador et al. 2010). However, this does not explain why OCCC cells accumulate glycogen to a much greater extent than other cancer cells. My data show that *HIF1A* mRNA is detectable in OCCC cell lines cultured in 21% O₂ at levels 6- to 15-fold higher than in PEO1 and do not increase further under hypoxia. Additionally, *HIF1A* knockdown resulted in a significant decrease in glycogen content. IL6 has been reported to lead to HIF1 α induction in OCCC (Anglesio et al. 2011b). Although my results show that the IL6-IL6R axis is active in OCCC cell lines, IL6R knockdown did not affect the glycogen content of the cells, implying that other factors contribute to constitutive HIF1 α expression in OCCC. One of those factors could be HNF1B, as *HNF1B* knockdown significantly decreased *HIF1A* expression in TOV21G cells. As shown in section 5.9, HNF1B overexpression also drives glycogen accumulation. Therefore, it appears that constitutive HIF1 α and HNF1B expression, acting synergistically, are behind the high glycogen content that characterises OCCC cells.

The 2 rate limiting enzymes for glycogen metabolism, PYGL and GYS1, are expressed at high levels in the OCCC cell lines, even under normal culture conditions and, PYGL at least, is not further induced in hypoxia (Fig. 6.3). These observations imply that glycogen turn-over occurs in OCCC even under normal culture conditions. While this project was underway, it was shown

that *PYGL* knockdown reduced proliferation in U87 and MCF-7 cells cultured in hypoxia (0.1% O₂) and 5 or 25mM glucose (Favaro et al. 2012). I hypothesised that in OCCC with its constitutive *PYGL* expression, an effect of *PYGL* knockdown would be evident under normal culture conditions as well. Remarkably, *PYGL* knockdown dramatically decreased proliferation in 5 of the 6 OCCC cell lines tested under all culture conditions (normal, hypoxia, glucose deprivation) and this effect was also seen in the HGS cell line PEO1. The results obtained with the SRB assay were then replicated using a colony forming assay. It is, however, conceivable that these observations are due to an off-target effect of the *PYGL* siRNA. The fact that similar findings were observed using shRNA by Favaro *et al* (2012) and that *PYGL* knockdown increased glycogen levels in accordance with predictions suggest that the observations are due, at least partly, to an on-target effect. As I showed in the previous chapter, *HNF1B* is a major driver of proliferation and the Warburg effect in OCCC cell lines. The fact that *PYGL* knockdown had no effect in the non-malignant IOSE4 cells but decreased proliferation in the *HNF1B* overexpressing isogenic IOSE4+HNF1B cell line suggests on the one hand that the siRNA used is not indiscriminately toxic to cells and, on the other, that *PYGL* function is necessary for cancer, but not normal, cell metabolism.

To validate the siRNA findings, I then tested 3 different small molecule *PYGL* inhibitors. R3401 modestly increased glycogen levels at a 50µM dose and dramatically decreased proliferation at a 150µM dose, which is the dose previously used in glycogen metabolism experiments in rat hepatocytes (Bergans et al. 2000), in all 7 cell lines. There are 2 potential explanations for these observations: either that more complete *PYGL* inhibition at high R3401 doses has an even greater effect on proliferation than siRNA knockdown, or that R3401 has significant off-target effects. The fact that cytotoxicity occurred at doses that have little impact on *PYGL* activity (Bergans et al. 2000) supports the latter. Assessing glycogen levels after treatment with 150µM R3401 would have been informative but it was not possible to perform that experiment due to the very low cell yield after exposure to that R3401 dose. sc-203975 exhibited poor solubility that precluded treatment of the cell lines with doses above 1µM. However, at the doses tested, no effect on glycogen or proliferation was seen. The results observed with DAB are interesting because, at an 800µM dose, glycogen was only increased in PEO1 cells that have low *PYGL* expression, but not in SKOV3, JHOC-5 or TOV21G cells. Mirroring this, proliferation was decreased in PEO1 but not in the 3 OCCC cell lines. Taking the 3 small molecule putative *PYGL* inhibitors together, it appears that effects on glycogen and proliferation are correlated, providing further support to the conclusion that the results observed with the siRNA are not due to off-target effects. Additionally, inhibition of the brain isoform of glycogen phosphorylase, *PYGB*, also decreases proliferation in a panel of cell lines

(Schnier et al. 2003) and sensitises cells to glucose starvation (Philips et al. 2014), further supporting the role of glycogen phosphorylase in sustaining cancer cell proliferation. Furthermore, if glucose flux through glycogen and access to glycogen stores is indeed important for continued proliferation in cancer cell lines, then inhibition of glycogen synthesis should have a similar effect on proliferation. Indeed, siRNA knockdown of *GYS1* resulted in reductions in both glycogen and proliferation, albeit of lesser magnitude compared to *PYGL* knockdown.

Metformin has pleiotropic effects on glucose metabolism and its effects on cancer cell metabolism and proliferation are the subject of considerable research efforts (Ben Sahra et al. 2010). Reports have suggested an effect on both glycogen synthesis through *GYS1* regulation (Radziuk et al. 2003) and on glycogenolysis (Ben Sahra et al. 2010). Treatment of SKOV3, JHOC-5 and TOV21G cells with 4mM metformin resulted in significant reductions in both glycogen content and proliferation (Fig 6.5M-N), consistent with an effect on *GYS1*. However, it is not possible to determine from these data how much of metformin's anti-proliferative effect is mediated through inhibition of glycogen metabolism compared with its other actions on targets such as mTOR (Del Barco et al. 2011). It should also be noted that metformin had the opposite effect on PEO1 cells with increases in both glycogen content and proliferation. Similarly, it was recently reported that some *MYC*-driven cell lines are dependent on AMPK signalling (which is activated by metformin) for continuing proliferation and survival (Liu et al. 2012). These observations should temper the enthusiasm for uncritical testing of metformin in a wide variety of tumours without consideration of the genomic and metabolic cellular context. Furthermore, I treated cells with 4mM metformin, a dose very similar to that used by other researchers in uterine serous (Sarfstein et al. 2013) or triple-negative breast (Deng et al. 2012) cancers. However, the peak plasma concentrations in patients with diabetes do not exceed 30 μ M⁷, raising concerns about the applicability of cell line-derived observations in clinical practice.

Taken together, my data show that perturbing glycogen metabolism, especially by inhibiting *PYGL*, is a valid therapeutic strategy. I was not able to perform animal studies to *in vivo* validate my findings. However, decreased tumour growth after *PYGL* knockdown was seen using U87 xenografts (Favaro et al. 2012), alleviating concerns that the cell line observations are an artefact of 2D culture on plastic. Two cell lines, PEO1 and JHOC-7, deserve special mention. The former provides evidence that targeting glycogen metabolism is applicable to a

⁷ Metformin Summary of Product Characteristics (SPC); accessed at www.medicines.org.uk

wide variety of tumours and not just the glycogen-rich OCCC, corroborating previous findings in glioblastoma and breast cancer cell lines (Favaro et al. 2012) and a very recent report in UMUC3 bladder cancer cells (Guin et al. 2014). On the other hand, JHOC-7 was resistant to *PYGL*, *GYS1* or *HNF1B* knockdown, hypoxia, glucose deprivation and even combined hypoxia and glucose deprivation. More detailed characterisation of this line may provide new insights into mechanisms of resistance to metabolism perturbations.

An interesting question is how inhibiting *PYGL* affects proliferation. *PYGL* knockdown was shown to induce senescence in U87 cells (Favaro et al. 2012). However, I did not observe senescence induction in PEO1, SKOV-3, JHOC-5 or TOV21G cells. The low but readily detectable background senescence rate in TOV21G cells provided a useful internal positive control for the assay (Fig. 6.6C) and, therefore, my findings are unlikely to be due to an insensitive assay. Additionally, there was no induction of apoptosis in multiple assays (caspase-3 and caspase-8 IHC, TUNEL assay). Using flow cytometry, I observed an accumulation of cells in G2/M in JHOC-5 and TOV21G, but not in SKOV-3 cells, that could be the proximal reason for the decreased proliferation. The flow cytometry results were corroborated by changes in expression of proteins involved in the G2/M checkpoint. Nevertheless, it is not clear why knocking down *PYGL* would induce a G2/M arrest. To gain further insights, I measured changes in medium and intracellular metabolites after *PYGL* knockdown. In marked contrast to the effect of *HNF1B* knockdown (see section 5.8), *PYGL* knockdown did not affect glucose uptake, glycolysis, most TCA cycle metabolites and the overall cellular energetic state. However, lipid droplet accumulation was seen, predominantly in JHOC-5, but also in TOV21G cells, consistent with an inhibitory effect on PPAR α mediated by altered glucose-1-phosphate levels (Hostetler et al. 2010). Reduced lipid β -oxidation can explain the small reductions seen in intracellular acetate and succinate. Furthermore, impaired lipid metabolism has been linked to G2/M arrest (Joe et al. 2010; Wu et al. 2012) and oxidative stress (Biswas et al. 2012) that could explain the effect on proliferation. The latter though does not seem to be mediating the effects of *PYGL* knockdown in OCCC, as ROS levels were reduced rather than increased in JHOC-5 and showed no change in TOV21G cells.

Another potential mechanism, through which glycogen metabolism perturbations could affect proliferation, is impaired or aberrant protein glycosylation (Tegtmeyer et al. 2014) leading to UPR induction (Chakrabarti et al. 2011; Lecca et al. 2005). However, in my study, core UPR genes did not show increased expression by qRT-PCR. These results do not support UPR

induction as the mechanism for the observed decreased proliferation but do not entirely exclude the possibility that aberrant glycosylation of some proteins or lipids may occur.

Agnostic proteome analysis is a powerful tool in the search for changes in metabolism-associated proteins that could explain the effects on proliferation. Out of 2776 assessed proteins, only 12 showed concordant changes in expression, a decrease in all cases, after *PYGL* knockdown. Some of these proteins could potentially explain the observed phenotype. For example, *MGEA5* and *ERLIN1* changes could lead to aberrant glycosylation and ERAD (Li et al. 2010; Lu et al. 2011), *RFK* to altered redox state (Park et al. 2012) or *ENO2* to reduced glycolysis. However, in every one of these cases, other assays such as TUNEL and caspase-3 imaging for apoptosis and measurements of total cell ROS, glucose, pyruvate and lactate are not supportive. Nevertheless, the proteomic data suggest that PKA signalling is perturbed following *PYGL* knockdown. PKA regulates lipid metabolism (Ermisch et al. 2011; Rodriguez-Cuenca et al. 2012) as well the G2/M checkpoint through phosphorylation of Cdc25b (Cui et al. 2008) and effects on the centrosome (Terrin et al. 2012). PKA also regulates Cyclin D2 (Muñiz et al. 2006) while *PRKACA* mutations and fusions have recently been implicated in adrenal adenomas (Beuschlein et al. 2014) and fibrolamellar hepatocellular carcinomas (Honeyman et al. 2014) providing further links between *PRKACA* and proliferation.

Based on the above, a plausible explanation for the effect of *PYGL* knockdown on proliferation is aberrant PKA signalling leading to perturbed lipid metabolism and activation of the G2/M checkpoint. Another possibility is that low glucose-1-phosphate levels impair lipid oxidation and that in turn activates the G2/M checkpoint. In this scenario, impaired lipid synthesis due to reduction in *ACACA* expression could be contributory and the observed PKA changes are a compensatory response to the decreased *PYGL* expression. PKA is the prototypical cAMP-dependent kinase (Cho-Chung et al. 1995) and is known to regulate *GYS1* directly (Bouché et al. 2004) and indirectly through *GSK3* (Pearce et al. 2010). More importantly, it can indirectly activate *PYGL* through its effect on phosphorylase kinase (Bouché et al. 2004; Brushia & Walsh 1999; Ortmeyer 1997). It is therefore of extreme interest to further explore whether *PYGL* knockdown affects the cellular cAMP pool and whether the observed changes in PKA signalling accentuate or attenuate the effect on proliferation. It should be also kept in mind, that *PYGL* may exert its effects partly through non-enzymatic mechanisms, as was recently demonstrated for the glycogen debranching enzyme *AGL*. The latter was shown to contribute to bladder cancer cell line proliferation through effects on glycine synthesis that were independent of its enzymatic activity (Guin et al. 2014). Glucose flux experiments using

radiolabelled glucose molecules would be useful in clarifying the effects of *PYGL* knockdown on carbon handling and knock-on effects on pathways such as the pentose phosphate shunt. Additionally, more detailed *in vivo* studies are required as well as further characterisation and medicinal chemistry optimisation of *PYGL* inhibitors, currently under development as potential antidiabetic drugs (Agius 2010; Chrysina et al. 2011).

To summarise, my results show a marked dependence of OCCC cell lines on intact glycogen metabolism for sustained proliferation. Constitutive HIF1 α and HNF1B expression drive glycogen accumulation and inhibition of glycogenolysis results in G2/M arrest and a dramatic reduction in proliferation. Importantly, although the high glycogen content makes OCCC a useful model system, these observations seem to apply to a wider variety of cell lines, raising the possibility that reliance on glycogen metabolism is an underexplored vulnerability of cancer cells in general. Germline *PYGL* mutations are the cause of Glycogenosis Type VI (Burwinkel et al. 1998), a glycogen storage disorder with a relatively benign course (Ozen 2007), suggesting that *PYGL* inhibition in adult cancer patients may be feasible without excessive toxicity, a hypothesis supported by the lack of an effect of *PYGL* knockdown in non-malignant IOSE4 cells.

7. CONCLUSIONS AND FUTURE DIRECTIONS

The work presented in this thesis investigated the consequences of 3 signature events in OCCC pathogenesis: *ARID1A* mutations, HNF1B overexpression and glycogen accumulation. Experiments were carried out in a variety of systems including mouse uterus, reflecting the putative tissue of origin, mouse fibroblasts, immortalised human ovarian surface epithelium and cancer cell lines.

ARID1A mutations occur at high frequency in uterus-derived cancers, including OCCC, OEAC and high-grade endometrial endometrioid cancer. When this project started in 2011, knowledge about ARID1A function in most tissues and contexts was limited but included a report that ARID1A was necessary for ER-mediated transactivation in breast cancer cell lines (Inoue et al. 2002). Therefore, I considered it was important to investigate the relationship between ARID1A and hormonal regulation of the uterus. I found limited evidence that *Arid1a* itself is hormonally regulated in the mouse uterus and no strong evidence, apart from moderate correlation between *Arid1a* and ER expression in the uterine stroma, that *Arid1a* regulates hormonal responses. Examining *ARID1A*-driven transcriptional programmes in mouse uterus, MEFs and human IOSE cells, I described a “core” set of *ARID1A*-regulated genes, centred on the G2/M checkpoint. Interestingly, preliminary evidence of an increase in proliferation after knocking-out *Arid1a* in the uterine epithelium, suggests a growth advantage for an endometrial clone acquiring an *Arid1a* mutation.

Much work needs to be done to extend on these observations. First, the predictions from the gene expression arrays need to be validated at the protein level. An expedient way to achieve this would be to create MEFs from *ROSA26^{Cre-ERT2}-Arid1a^{fl/fl}* mice and use tamoxifen to *in vitro* knock out *Arid1a*. If *Arid1a* regulation of targets such as Aurora kinases, Polo-like kinases and Cyclins B and D is confirmed, the effect of inhibitors could be tested in the MEFs and OCCC cell lines carrying *ARID1A* mutations *in vitro* and *in vivo*. Meanwhile, our understanding of *Arid1a*'s role would be improved by ChIP-seq studies in MEFs and uterus samples. Preparatory work has begun to optimise ChIP-seq protocols using antibodies against *Arid1a* and constitutive Swi/Snf components such as BAF155. BAF155 ChIP-seq with or without *Arid1a* knockout, correlated with the transcriptomic data, would provide valuable insights into *Arid1a* regulation of gene expression and the consequences of its loss. Finally, the role of *Arid1a* in the regulation of hormonal responses in the uterus should be studied in more detail

using the current tamoxifen-driven *ROSA26^{Cre-ERT2}* GEMM in addition to models of stromal *Arid1a* loss, perhaps driven by *Amhr2-Cre*.

My studies expand on the previously reported data regarding the role of HNF1B in OCCC proliferation and metabolism. I was able to show that HNF1B expression promotes proliferation in all OCCC cell lines tested and, additionally, in IOSE. Furthermore, in accordance with other studies (Okamoto et al. 2013), I found that HNF1B is a major driver of the Warburg effect phenotype and that its overexpression directly leads to glycogen accumulation. However, the growth and metabolic advantage of HNF1B-overexpressing cells, particularly important considering OCCC's origin in the oxidative and hypoxic environment of endometriotic cysts, is counter-balanced by a reduction in their metastatic and invasive potential. This important observation, only hinted at by previous work (Tomassetti et al. 2008), for the first time provides a biological explanation for the frequent early stage clinical presentation of OCCC.

Important future work should aim to clarify whether HNF1B overexpression in benign endometriosis increases the risk of OCCC development. Given the rarity of OCCC, this would be a significant undertaking, necessitating an international collaboration in order to assemble an adequate number of cases and matched controls with available endometriotic tissue. However, if HNF1B overexpression in endometriosis substantially increases OCCC risk, it could potentially form the basis of a screening programme. Given my observations regarding migration and invasion, it would be interesting to investigate whether there is reduced HNF1B expression in advanced stage or recurrent OCCC. With that in mind, construction of a tissue microarray with sufficient representation of advanced stage cases has begun. Additionally, potential interactions and cross-regulatory loops between *ARID1A* and *HNF1B* require further study as my results suggest that *ARID1A* loss would suppress HNF1B expression and that HNF1B regulates various SWI/SNF components in an *ARID1A* non-mutated cell line. Furthermore, as *HNF1B* in my data regulated transcription factors involved in oestrogen signalling, it would be important to study whether HNF1B overexpression leads to loss of hormonal dependence in endometriosis. Finally, given its universal expression in OCCC, HNF1B could be a therapeutic target. So far, it has been proven difficult to target transcription factors but innovative work at our laboratory, led by Ms. Mareike Wiedmann, is exploring the feasibility of modulating HNF1B function by blocking its nuclear import signal.

Glycogen accumulation remains the most understudied cardinal feature of OCCC. I have shown that constitutive *HNF1B* and *HIF1A* expression in OCCC are driving this accumulation. Importantly, my results suggest that the accumulated glycogen does not constitute an inert fuel store, to be accessed only when the cells are under nutritional stress. Inhibition of glycogen breakdown resulted in a dramatic decrease in proliferation, even in the presence of plentiful extracellular glucose, implying a necessity for glucose flux through glycogen for sustained cellular growth. Given the fact that similar findings have been observed in cell lines with a lesser magnitude of glycogen accumulation [PEO1 in my studies, U87 and MCF-7 in the report by Favaro *et al* (2012)], and that germline *PYGL* mutations exhibit a mild phenotype, targeting glycogen breakdown may prove to be a valid treatment strategy for many cancers.

In the first instance, my *in vitro* findings need to be validated with *in vivo* xenograft studies. The small molecule inhibitors I tested so far, exhibit considerable limitations such as probable off-target effects (R3401), poor solubility (sc-203975) or insufficient activity (DAB). However, *PYGL* inhibitors continue to be developed as anti-diabetes agents (Gaboriaud-Kolar & Skaltsounis 2013; Kun *et al.* 2014); investigation of such compounds as anticancer agents should be a priority.

Taking into account the interplay between *ARID1A* and *HNF1B*, a speculative model of OCCC pathogenesis can be constructed (Fig. 7.1A). In this model, by chance, some endometriotic cysts contain *HNF1B* overexpressing cells, known to normally occur in the secretory endometrium. These cells have a growth advantage within the endometriotic cyst and expand. Accumulation of mutations in other genes such as in *ARID1A*, or in some cases modulation of other chromatin remodellers by *HNF1B* itself, eventually lead to invasive OCCC. In this model, *ARID1A* mutations are a later event and are not necessary for OCCC development. Additionally, *HNF1B* regulation of transcription factors such *FOXA1* or *FOS* confers hormone independence. In an alternative model, *ARID1A* mutations occur first, promoting growth within the cyst; at that point either an OCCC or an OEAC can eventually develop. *HNF1B* overexpression occurs later, in a subset of *ARID1A*-driven atypical endometriosis, conferring hormone independence and leading to OCCC, whereas other mutations lead to hormone-dependent OEAC (Fig. 7.1B).

The predictions of these models should be testable using the Cheng endometriosis mouse model developed by the Charnock-Jones laboratory. As previously discussed, this model is based on local activation of oncogenic *Kras* in the endometrium of donor mice which is then

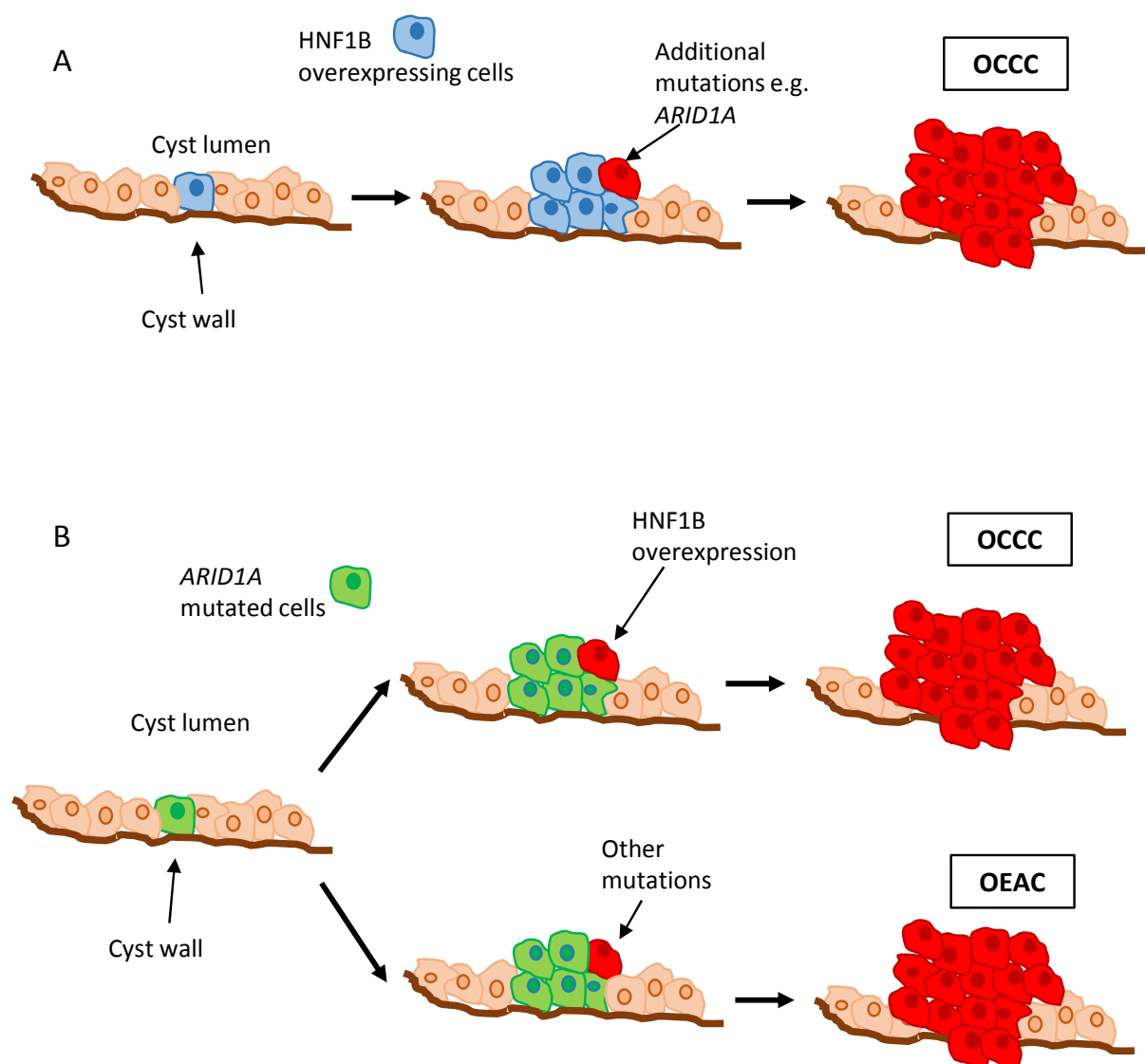


Figure 7.1. Models of OCCC development

A) In this model, HNF1B overexpression is the initiating event with *ARID1A* mutations occurring as a later event in a subset of OCCC. B) In an alternative model, *ARID1A* mutations occur first, predisposing to endometriosis-related cancer, either OCCC or OEAC. HNF1B overexpression in a subset of *ARID1A*-mutant cells leads to OCCC whereas other events (e.g. PTEN loss) lead to OEAC.

harvested and subcutaneously implanted in donor mice. We have begun preparatory work aiming to knock down *Arid1a* or overexpress *Hnf1b* using lentiviruses to transfect the endometrial fragments prior to implantation. If successful, this could lead to a GEMM of OCCC that will greatly facilitate future studies in the pathogenesis and treatment of OCCC.

In conclusion, the work carried out in this thesis has contributed to the functional characterisation of OCCC driver events. The insights gained will help design better OCCC models and develop therapeutic strategies for this chemoresistant malignancy.

Appendix

Table A.1. Pathways enriched in “High *Arid1a*” compared with “Low *Arid1a*” mouse uterine samples

Pathway	p value	FDR
Cell cycle - Role of Nek in cell cycle regulation	4.925E-08	3.32E-05
Cell cycle - Spindle assembly and chromosome separation	6.207E-06	0.002089
Cell cycle - Role of APC in cell cycle regulation	3.555E-05	0.005981
Cell cycle - Start of DNA replication in early S phase	3.555E-05	0.005981
Cytoskeleton remodelling - TGF, WNT and cytoskeletal remodelling	9.553E-05	0.01101
Cell cycle - The metaphase checkpoint	9.817E-05	0.01101
Apoptosis and survival - Granzyme A signaling	1.473E-04	0.01304
Development - PIP3 signaling in cardiac myocytes	1.744E-04	0.01304
Development - HGF signaling pathway	1.744E-04	0.01304
Development - Thromboxane A2 pathway signaling	2.510E-04	0.01689
LRRK2 in neurons in Parkinson's disease	3.023E-04	0.01844
Apoptosis and survival - BAD phosphorylation	3.473E-04	0.01844
Protein folding - Membrane trafficking and signal transduction of G-alpha (i) heterotrimeric G-protein	3.732E-04	0.01844
Cytoskeleton remodelling - Cytoskeleton remodelling	3.836E-04	0.01844
Apoptosis and survival - Endoplasmic reticulum stress response pathway	4.898E-04	0.0206
Translation - Regulation of EIF4F activity	4.898E-04	0.0206
Cell adhesion - Tight junctions	5.705E-04	0.02259
Apoptosis and survival - NGF activation of NF-kB	7.438E-04	0.02781
Hypoxia-induced EMT in cancer and fibrosis	8.790E-04	0.03113

Pathways list created and statistical analysis performed using MetaCore

Table A.2. Process networks enriched in “High *Arid1a*” compared with “Low *Arid1a*” mouse uterine samples

Process Network	p value	FDR
Cell cycle – Mitosis	1.56E-05	0.001224
Protein folding - Response to unfolded proteins	1.21E-05	0.001224
Cell cycle – Core	2.85E-05	0.00149
Protein folding - Folding in normal condition	3.874E-04	0.0152
Cytoskeleton - Spindle microtubules	7.773E-04	0.01743
Proteolysis - Ubiquitin-proteasomal proteolysis	7.537E-04	0.01743
Cell cycle - S phase	7.35E-04	0.01743
Cell cycle - G2-M	0.001214	0.02383

Process networks list created and statistical analysis performed using MetaCore

Table A.3. Top 30 pathways enriched in *Arid1a*-regulated genes in MEFs

Pathway	p value	FDR
Cytoskeleton remodelling - TGF, WNT and cytoskeletal remodelling	6.945E-09	2.796E-06
Cell cycle - Spindle assembly and chromosome separation	8.272E-09	2.796E-06
Cell cycle - The metaphase checkpoint	3.534E-08	6.495E-06
Cell adhesion - Chemokines and adhesion	4.683E-08	6.495E-06
Cell cycle - Role of Nek in cell cycle regulation	4.804E-08	6.495E-06
Cytoskeleton remodelling - Cytoskeleton remodeling	7.252E-08	8.171E-06
Cytoskeleton remodelling - Regulation of actin cytoskeleton by Rho GTPases	4.491E-07	4.337E-05
Cell cycle - Initiation of mitosis	1.275E-06	1.077E-04
Cell cycle - Chromosome condensation in prometaphase	1.606E-06	1.207E-04
Cell cycle - Regulation of G1/S transition (part 2)	2.051E-06	1.387E-04
Development - Alpha-2 adrenergic receptor activation of ERK	4.581E-06	2.455E-04
LRRK2 in neurons in Parkinson's disease	4.709E-06	2.455E-04
Immune response - IL-1 signaling pathway	4.721E-06	2.455E-04
Immune response - IL-33 signaling pathway	6.258E-06	3.022E-04
Development - VEGF signaling via VEGFR2 - generic cascades	7.255E-06	3.227E-04
Regulation of CFTR activity (norm and CF)	8.010E-06	3.227E-04
Blood coagulation - GPCRs in platelet aggregation	8.114E-06	3.227E-04
Development - Role of IL-8 in angiogenesis	9.206E-06	3.457E-04
Immune response - HSP60 and HSP70/ TLR signaling pathway	1.401E-05	4.983E-04
Development - S1P2 and S1P3 receptors in cell proliferation and differentiation	1.671E-05	5.647E-04
Development - Beta-adrenergic receptors transactivation of EGFR	1.822E-05	5.843E-04
Cytoskeleton remodelling - Integrin outside-in signaling	1.901E-05	5.843E-04
Immune response - CD28 signaling	2.261E-05	6.645E-04
Normal and pathological TGF-beta-mediated regulation of cell proliferation	3.051E-05	7.465E-04
Signal transduction - Activin A signaling regulation	3.051E-05	7.465E-04
Chemotaxis - Inhibitory action of lipoxins on IL-8- and Leukotriene B4-induced neutrophil migration	3.131E-05	7.465E-04
Development - EGFR signaling pathway	3.234E-05	7.465E-04
Neurophysiological process - Receptor-mediated axon growth repulsion	3.312E-05	7.465E-04
Development - Thrombopoietin-regulated cell processes	3.312E-05	7.465E-04
Transcription - P53 signaling pathway	3.313E-05	7.465E-04

Pathways list created and statistical analysis performed using MetaCore

Table A.4. Process networks enriched in *Arid1a*-regulated genes in MEFs

Process Network	p value	FDR
Cell cycle – Mitosis	6.366E-11	1.012E-08
Cytoskeleton - Regulation of cytoskeleton rearrangement	3.817E-08	3.035E-06
Cell cycle – Core	8.253E-07	4.374E-05
Transcription - Chromatin modification	1.486E-06	5.909E-05
Cytoskeleton - Spindle microtubules	6.152E-06	1.956E-04
Cytoskeleton - Actin filaments	8.622E-06	2.285E-04
Cell cycle - G2-M	2.324E-05	5.279E-04
Cell adhesion - Integrin-mediated cell-matrix adhesion	3.054E-05	6.07E-04
Signal transduction - Androgen receptor nuclear signalling	1.335E-04	0.002358
Cell cycle - G1-S Growth factor regulation	2.453E-04	0.003108
Development - Hemopoiesis, Erythropoietin pathway	2.541E-04	0.003108
Apoptosis - Apoptotic nucleus	2.426E-04	0.003108
Development - Regulation of angiogenesis	3.588E-04	0.003804
Development - Skeletal muscle development	3.443E-04	0.003804
Development – Neurogenesis - Axonal guidance	3.887E-04	0.003863
Cell cycle - G1-S Interleukin regulation	4.212E-04	0.00394
Inflammation - Amphoterin signalling	5.244E-04	0.004388
Signal transduction - WNT signalling	5.106E-04	0.004388
Cell adhesion – Cadherins	7.189E-04	0.005715
Cytoskeleton - Cytoplasmic microtubules	7.807E-04	0.005911
Translation - Regulation of initiation	8.199E-04	0.005926
Proliferation - Positive regulation cell proliferation	0.001042	0.007202
Development - Blood vessel morphogenesis	0.001108	0.007343
Cell adhesion - Amyloid proteins	0.001803	0.01146
DNA damage - DBS repair	0.001983	0.01213
Cell cycle - G0-G1	0.002299	0.01354
Reproduction - Feeding and Neurohormone signalling	0.004337	0.02378
Cell cycle - S phase	0.005241	0.02567
Immune response - TCR signalling	0.00505	0.02567
Inflammation - Innate inflammatory response	0.005328	0.02567
Immune response - BCR pathway	0.005538	0.0259
Signal transduction - NOTCH signalling	0.006639	0.02932
Signal Transduction - TGF-beta, GDF and Activin signalling	0.008502	0.03379
Cell adhesion - Attractive and repulsive receptors	0.009803	0.03791
Signal transduction - ERBB-family signalling	0.01001	0.03791

Process networks list created and statistical analysis performed using MetaCore

Table A.5. Pathways enriched in *Arid1a*-regulated genes in both mouse uterus and MEFs

Pathway	p value	FDR
Cell cycle - Role of Nek in cell cycle regulation	3.322E-08	1.19E-05
Cell cycle - Spindle assembly and chromosome separation	4.476E-08	1.19E-05
Cell cycle - The metaphase checkpoint	1.434E-06	2.55E-04
Cell cycle - Role of APC in cell cycle regulation	8.693E-05	0.01158
Apoptosis and survival - Granzyme A signalling	6.131E-04	0.04668
Cytoskeleton remodelling - RalA regulation pathway	6.131E-04	0.04668
Cell adhesion - Gap junctions	6.131E-04	0.04668

Pathways list created and statistical analysis performed using MetaCore

Table A.6. Process networks enriched in *Arid1a*-regulated genes in both mouse uterus and MEFs

Process Network	p value	FDR
Cell cycle – Mitosis	1.473E-10	2.254E-08
Cytoskeleton - Spindle microtubules	6.792E-06	5.057E-04
Cell cycle – Core	1.322E-05	5.057E-04
Cytoskeleton - Cytoplasmic microtubules	1.322E-05	5.057E-04
Transcription - Chromatin modification	1.815E-04	0.005553
Cell cycle - G2-M	4.003E-04	0.01021
Cell cycle – Meiosis	0.001377	0.02658
Reproduction - Spermatogenesis, motility and copulation	0.00139	0.02658

Process networks list created and statistical analysis performed using MetaCore

Table A.7. Top 30 pathways enriched in *ARID1A*-regulated genes in IOSE4 cells

Pathway	p value	FDR
Cell cycle - Role of APC in cell cycle regulation	5.480E-11	4.302E-08
Cell cycle - Regulation of G1/S transition (part 1)	3.341E-10	1.311E-07
Cell cycle - Role of SCF complex in cell cycle regulation	7.655E-10	1.718E-07
Cell cycle - The metaphase checkpoint	8.755E-10	1.718E-07
Cell cycle - Chromosome condensation in prometaphase	2.251E-09	3.534E-07
Cytoskeleton remodeling -TGF, WNT and cytoskeletal remodeling	4.966E-09	6.497E-07
DNA damage - ATM / ATR regulation of G2 / M checkpoint	1.063E-08	1.093E-06
Cell cycle - Spindle assembly and chromosome separation	1.114E-08	1.093E-06
Cell cycle - Influence of Ras and Rho proteins on G1/S transition	1.310E-08	1.142E-06
Cell cycle - Transition and termination of DNA replication	4.149E-08	3.257E-06
DNA damage - ATM/ATR regulation of G1/S checkpoint	5.257E-08	3.668E-06
Cell cycle - Initiation of mitosis	5.607E-08	3.668E-06
Normal and pathological TGF-beta-mediated regulation of cell proliferation	9.156E-08	5.437E-06
Cytoskeleton remodeling - Cytoskeleton remodeling	9.696E-08	5.437E-06
Development - TGF-beta-dependent induction of EMT via RhoA, PI3K and ILK.	1.419E-07	7.429E-06
Aberrant B-Raf signaling in melanoma progression	7.832E-07	3.843E-05
Development - Notch Signaling Pathway	1.357E-06	6.267E-05
Immune response - TLR2 and TLR4 signaling pathways	1.509E-06	6.581E-05
Development - TGF-beta-dependent induction of EMT via SMADs	1.691E-06	6.986E-05
Development - PEDF signaling	2.351E-06	9.229E-05
Development - VEGF signaling via VEGFR2 - generic cascades	2.569E-06	9.604E-05
Development - PDGF signaling via STATs and NF-kB	2.794E-06	9.969E-05
IL-6 signaling in multiple myeloma	4.570E-06	1.560E-04
Development - NOTCH1-mediated pathway for NF-KB activity modulation	6.657E-06	2.177E-04
Development - WNT signaling pathway. Part 1. Degradation of beta-catenin in the absence WNT signaling	1.003E-05	3.151E-04
Cytoskeleton remodeling - Integrin outside-in signaling	1.094E-05	3.303E-04
Immune response - HSP60 and HSP70/ TLR signaling pathway	1.147E-05	3.334E-04
Neurophysiological process - Receptor-mediated axon growth repulsion	1.387E-05	3.889E-04
Apoptosis and survival - Granzyme B signaling	1.699E-05	4.446E-04
Cell cycle - Role of Nek in cell cycle regulation	1.699E-05	4.446E-04

Pathways list created and statistical analysis performed using MetaCore

Table A.8. Process networks enriched in *ARID1A*-regulated genes in IOSE4 cells

Process Network	p value	FDR
Cell cycle - Mitosis	1.615E-14	2.584E-12
Cell cycle - Core	5.416E-13	4.333E-11
Cell cycle - G2-M	8.232E-13	4.391E-11
Cytoskeleton - Spindle microtubules	2.635E-09	1.054E-07
Cell cycle - S phase	6.152E-09	1.969E-07
Cell adhesion - Integrin-mediated cell-matrix adhesion	1.151E-07	3.069E-06
Signal transduction - NOTCH signaling	6.476E-07	1.480E-05
Cell cycle - G1-S	1.326E-06	2.652E-05
Development – EMT-regulation of epithelial-to-mesenchymal transition	2.008E-06	3.571E-05
Signal transduction - WNT signaling	4.078E-06	6.524E-05
DNA damage checkpoint	5.226E-06	7.601E-05
Cell adhesion - Platelet-endothelium-leucocyte interactions	1.091E-04	1.454E-03
Signal Transduction - TGF-beta, GDF and Activin signaling	1.556E-04	1.915E-03
Development - Regulation of angiogenesis	1.817E-04	2.077E-03
Inflammation - IL-10 anti-inflammatory response	2.018E-04	2.153E-03
Inflammation - MIF signaling	2.856E-04	2.856E-03
Development - Blood vessel morphogenesis	3.467E-04	3.263E-03
Cell cycle - G1-S Growth factor regulation	6.033E-04	5.363E-03
Cytoskeleton - Intermediate filaments	8.130E-04	6.847E-03
Cell adhesion - Amyloid proteins	1.092E-03	8.382E-03
Apoptosis - Anti-Apoptosis mediated by external signals via PI3K/AKT	1.100E-03	8.382E-03
Development - Hemopoiesis, Erythropoietin pathway	1.258E-03	9.149E-03

Process networks list created and statistical analysis performed using MetaCore

Table A.9. Pathways enriched in *ARID1A*-regulated genes in JHOC-5 OCCC cells

Pathway	p value	FDR
Cell adhesion - ECM remodeling	9.422E-06	0.0048
Immune response - IL-1 signaling pathway	2.546E-04	0.065
Role and regulation of Prostaglandin E2 in gastric cancer	4.634E-04	0.073
Transcription - NF-kB activation pathways	5.768E-04	0.073
Expression targets of Tissue factor signaling in cancer	9.412E-04	0.073
Transcription - Role of AP-1 in regulation of cellular metabolism	0.001	0.073
Immune response - Role of PKR in stress-induced antiviral cell response	0.0011	0.073
Development - Prolactin receptor signaling	0.0012	0.073
Apoptosis and survival - TNFR1 signaling pathway	0.0018	0.091
Immune response - IL-15 signaling	0.0019	0.091
Apoptosis and survival - FAS signaling cascades	0.002	0.091

Pathways list created and statistical analysis performed using MetaCore

Table A.10. Process networks enriched in *ARID1A*-regulated genes in JHOC-5 OCCC cells

Process Network	p value	FDR
Blood coagulation	1.403E-04	0.021
Cell adhesion - Cell-matrix interactions	2.716E-04	0.021
Proteolysis - Connective tissue degradation	0.0011	0.056
Development - Regulation of angiogenesis	0.0014	0.056
Inflammation - Interferon signaling	0.0021	0.064
Cell adhesion - Platelet-endothelium-leucocyte interactions	0.0028	0.07
Immune response - Th17-derived cytokines	0.0032	0.07
Proteolysis - ECM remodeling	0.0046	0.089

Process networks list created and statistical analysis performed using MetaCore

Table A.11. Top 30 pathways enriched in *HNF1B*-regulated genes in JHOC-5 cells

Pathway	p value	FDR
Development - Regulation of epithelial-to-mesenchymal transition (EMT)	9.911E-11	6.353E-08
Development - WNT signaling pathway. Part 2	1.831E-10	6.353E-08
Cell adhesion - Chemokines and adhesion	4.281E-10	9.904E-08
Cell adhesion - ECM remodeling	5.123E-09	8.889E-07
Immune response - IL-17 signaling pathways	2.217E-08	3.078E-06
Cytoskeleton remodelling - TGF, WNT and cytoskeletal remodeling	3.482E-08	4.027E-06
Development - TGF-beta-dependent induction of EMT via RhoA, PI3K and ILK.	9.164E-08	8.239E-06
DNA damage - Brca1 as a transcription regulator	9.621E-08	8.239E-06
Cell cycle - Regulation of G1/S transition (part 1)	1.068E-07	8.239E-06
Cytoskeleton remodelling - Cytoskeleton remodeling	1.898E-07	1.317E-05
Immune response - IL-1 signaling pathway	2.387E-07	1.445E-05
Immune response - HMGB1/RAGE signaling pathway	2.498E-07	1.445E-05
Immune response - HSP60 and HSP70/ TLR signaling pathway	3.568E-07	1.774E-05
Neurophysiological process - Receptor-mediated axon growth repulsion	3.580E-07	1.774E-05
Cell cycle - ESR1 regulation of G1/S transition	4.697E-07	2.167E-05
Immune response - MIF-induced cell adhesion, migration and angiogenesis	5.292E-07	2.167E-05
Immune response - IL-18 signaling	5.504E-07	2.167E-05
Immune response - MIF-mediated glucocorticoid regulation	5.621E-07	2.167E-05
Immune response - Role of PKR in stress-induced antiviral cell response	9.779E-07	3.572E-05
Development - TGF-beta-dependent induction of EMT via SMADs	1.193E-06	3.966E-05
Apoptosis and survival - Role of PKR in stress-induced apoptosis	1.252E-06	3.966E-05
Apoptosis and survival - Role of IAP-proteins in apoptosis	1.257E-06	3.966E-05
Development - VEGF signaling via VEGFR2 - generic cascades	1.553E-06	4.687E-05
Immune response - CCL2 signaling	1.738E-06	5.027E-05
DNA damage - ATM/ATR regulation of G1/S checkpoint	2.014E-06	5.59E-05
PGE2 pathways in cancer	2.390E-06	6.106E-05
Cell cycle - Nucleocytoplasmic transport of CDK/Cyclins	2.395E-06	6.106E-05
Development - Role of IL-8 in angiogenesis	2.464E-06	6.106E-05
Regulation of metabolism - Bile acids regulation of glucose and lipid metabolism via FXR	2.791E-06	6.678E-05
Apoptosis and survival - Regulation of Apoptosis by Mitochondrial Proteins	3.152E-06	7.291E-05

Pathways list created and statistical analysis performed using MetaCore

Table A.12. Process networks enriched in *HNF1B*-regulated genes in JHOC-5 cells

Process Network	p value	FDR
Cell cycle - Mitosis	9.885E-07	0.0001027
Immune response - Antigen presentation	1.292E-06	0.0001027
Reproduction - Feeding and Neurohormone signaling	3.568E-06	0.0001891
Development – EMT - Regulation of epithelial-to-mesenchymal transition	5.066E-06	0.0002014
Cell adhesion - Integrin-mediated cell-matrix adhesion	1.240E-05	0.0003943
Signal transduction - ESR1-nuclear pathway	1.714E-05	0.0004542
Transcription - Chromatin modification	2.179E-05	0.0004949
Signal transduction - WNT signaling	3.618E-05	0.0007191
Development - Regulation of angiogenesis	5.020E-05	0.0008371
DNA damage - Checkpoint	5.265E-05	0.0008371
Inflammation - MIF signaling	1.018E-04	0.001472
Apoptosis - Apoptotic nucleus	1.391E-04	0.001843
Development - Blood vessel morphogenesis	1.899E-04	0.002115
Inflammation - Amphoterin signaling	1.913E-04	0.002115
Inflammation - Interferon signaling	2.057E-04	0.002115
Cell adhesion - Attractive and repulsive receptors	2.180E-04	0.002115
Cell adhesion - Cell junctions	2.262E-04	0.002115
Development - Hedgehog signaling	2.786E-04	0.002461
Cell cycle - G2-M	3.861E-04	0.003231
Development – Neurogenesis - Axonal guidance	4.422E-04	0.003515
Cell cycle - G1-S Growth factor regulation	5.505E-04	0.004168
Cardiac development - Role of NADPH oxidase and ROS	5.970E-04	0.004314
Reproduction - FSH-beta signaling pathway	6.430E-04	0.004445
Cytoskeleton - Regulation of cytoskeleton rearrangement	6.865E-04	0.004548
Proliferation - Negative regulation of cell proliferation	7.850E-04	0.004993
Apoptosis - Death Domain receptors & caspases in apoptosis	9.906E-04	0.005953
Proteolysis - Connective tissue degradation	0.001052	0.005953
Cardiac development - Wnt_beta-catenin, Notch, VEGF, IP3 and integrin signalling	0.001059	0.005953
Protein folding - ER and cytoplasm	0.001086	0.005953
Apoptosis - Apoptotic mitochondria	0.001156	0.006127
Signal transduction - Androgen receptor nuclear signaling	0.001592	0.008164
Cell cycle - S phase	0.001739	0.008428
Cytoskeleton - Spindle microtubules	0.001749	0.008428
Cell cycle - G1-S	0.001824	0.00853

Process networks list created and statistical analysis performed using MetaCore

Table A.13. Top 30 pathways enriched in *HNF1B*-regulated genes in TOV21G cells

Pathway	p value	FDR
Cell adhesion - Chemokines and adhesion	1.091E-15	7.704E-13
Cytoskeleton remodelling - Cytoskeleton remodeling	8.065E-14	2.847E-11
Cytoskeleton remodelling - TGF, WNT and cytoskeletal remodelling	3.093E-12	7.278E-10
Development - Regulation of epithelial-to-mesenchymal transition (EMT)	1.862E-10	3.287E-08
Cell adhesion - Histamine H1 receptor signaling in the interruption of cell barrier integrity	4.294E-10	6.063E-08
Neurophysiological process - Receptor-mediated axon growth repulsion	1.916E-08	2.254E-06
Cell adhesion - Cadherin-mediated cell adhesion	2.340E-08	2.36E-06
Muscle contraction - Regulation of eNOS activity in endothelial cells	3.816E-08	3.368E-06
Cell adhesion - ECM remodeling	9.668E-08	7.181E-06
Development - VEGF signaling via VEGFR2 - generic cascades	1.017E-07	7.181E-06
Cell cycle - Regulation of G1/S transition (part 1)	1.139E-07	7.31E-06
Development - WNT signaling pathway. Part 2	1.486E-07	8.742E-06
Cell cycle - Role of SCF complex in cell cycle regulation	1.979E-07	1.038E-05
Immune response - C5a signaling	2.059E-07	1.038E-05
Development - Gastrin in cell growth and proliferation	2.433E-07	1.145E-05
Development - Thromboxane A2 pathway signaling	6.674E-07	2.945E-05
G-protein signalling - Regulation of p38 and JNK signaling mediated by G-proteins	1.120E-06	4.313E-05
Cell cycle - Start of DNA replication in early S phase	1.161E-06	4.313E-05
DNA damage - ATM/ATR regulation of G1/S checkpoint	1.161E-06	4.313E-05
Development - S1P2 and S1P3 receptors in cell proliferation and differentiation	1.735E-06	6.124E-05
LRRK2 in neurons in Parkinson's disease	1.964E-06	6.343E-05
Cytoskeleton remodelling - Regulation of actin cytoskeleton by Rho GTPases	1.977E-06	6.343E-05
Muscle contraction - S1P2 receptor-mediated smooth muscle contraction	2.522E-06	7.742E-05
Cytoskeleton remodelling - Fibronectin-binding integrins in cell motility	4.262E-06	1.162E-04
Immune response - MIF-induced cell adhesion, migration and angiogenesis	4.429E-06	1.162E-04
Development - TGF-beta-dependent induction of EMT via RhoA, PI3K and ILK.	4.429E-06	1.162E-04
Immune response - CCL2 signaling	4.445E-06	1.162E-04
Development - TGF-beta-dependent induction of EMT via SMADs	5.196E-06	1.31E-04
Reproduction - GnRH signaling	6.248E-06	1.518E-04
Signal transduction - PKA signaling	6.448E-06	1.518E-04

Pathways list created and statistical analysis performed using MetaCore

Table A.14. Process networks enriched in *HNF1B*-regulated genes in TOV21G cells

Process Network	p value	FDR
Cell adhesion - Integrin-mediated cell-matrix adhesion	1.348E-09	2.157E-07
Development - Regulation of angiogenesis	6.030E-09	4.824E-07
Cytoskeleton - Regulation of cytoskeleton rearrangement	1.423E-08	7.591E-07
Cell cycle - S phase	6.168E-08	2.467E-06
Cytoskeleton - Actin filaments	1.850E-07	5.919E-06
Development – EMT - Regulation of epithelial-to-mesenchymal transition	6.537E-07	1.743E-05
Development - Blood vessel morphogenesis	2.029E-06	4.638E-05
Signal transduction - WNT signaling	2.766E-06	5.347E-05
Development – Neurogenesis - Axonal guidance	3.008E-06	5.347E-05
Reproduction - FSH-beta signaling pathway	1.379E-05	2.033E-04
Signal Transduction - Cholecystokinin signaling	1.398E-05	2.033E-04
Development - Ossification and bone remodeling	6.702E-05	8.936E-04
Cell adhesion - Cadherins	9.093E-05	0.001119
Cell cycle - Core	1.371E-04	0.001567
Proliferation - Negative regulation of cell proliferation	1.848E-04	0.001809
Cell cycle - G1-S Growth factor regulation	1.856E-04	0.001809
Signal transduction - NOTCH signaling	1.922E-04	0.001809
Cell cycle - G1-S	2.116E-04	0.001881
Reproduction - Feeding and Neurohormone signaling	2.268E-04	0.00191
Cell adhesion - Amyloid proteins	3.378E-04	0.002577
Cell adhesion - Cell junctions	3.382E-04	0.002577
DNA damage - Checkpoint	4.460E-04	0.003141
Cardiac development - BMP_TGF_beta_signaling	4.516E-04	0.003141
Cell adhesion - Leucocyte chemotaxis	5.012E-04	0.003341
Signal Transduction - TGF-beta, GDF and Activin signaling	5.623E-04	0.003599
Inflammation - Protein C signaling	6.222E-04	0.003829
Inflammation - Interferon signaling	9.374E-04	0.005555
Signal transduction - ESR1-nuclear pathway	0.001388	0.007933
Signal Transduction - BMP and GDF signaling	0.001458	0.008044
Cell cycle - G0-G1	0.001726	0.009205
Cell adhesion - Integrin priming	0.001869	0.009649

Process networks list created and statistical analysis performed using MetaCore

Table A.15. Pathways enriched in *PYGL*-regulated proteins in JHOC-5 cells

Pathway	p value	FDR
Non-genomic action of Retinoic acid in cell differentiation	8.979E-07	2.927E-04
cAMP signalling	2.762E-06	4.501E-04
Regulation of lipid metabolism by niacin and isoprenaline	6.512E-06	5.927E-04
ACM regulation of nerve impulse	7.273E-06	5.927E-04
Regulation of CFTR activity (normal and CF)	2.949E-05	1.735E-03
Constitutive and regulated NMDA receptor trafficking	3.193E-05	1.735E-03
Erk Interactions: Inhibition of Erk	4.673E-05	2.176E-03
BAD phosphorylation	1.089E-04	4.436E-03
MIF - the neuroendocrine-macrophage connector	1.559E-04	5.648E-03
CREB pathway	1.998E-04	5.857E-03
Corticoliberin signalling via CRHR1	2.162E-04	5.857E-03
Histamine signalling in dendritic cells	2.162E-04	5.857E-03
PKA signalling	2.335E-04	5.857E-03
Beta-adrenergic receptors signalling via cAMP	2.519E-04	5.865E-03
Ca(2+)-dependent NF-AT signalling in cardiac hypertrophy	3.595E-04	7.672E-03
Role of Parkin in the Ubiquitin-Proteasomal Pathway	3.766E-04	7.672E-03
Signalling of Beta-adrenergic receptors via Beta-arrestins	4.796E-04	8.993E-03
Activity-dependent synaptic AMPA receptor removal	4.966E-04	8.993E-03

Pathways list created and statistical analysis performed using MetaCore

Table A.16. Metabolic networks enriched in *PYGL*-regulated proteins in JHOC-5 cells

Metabolic Network	p value	FDR
Phosphatidylcholine pathway	3.220E-03	8.935E-02
L-arginine pathways and transport	5.206E-03	8.935E-02
Lyso-Phosphatidylserine pathway	6.701E-03	8.935E-02

Metabolic networks list created and statistical analysis performed using MetaCore

Table A.17. Pathways enriched in *PYGL*-regulated proteins in TOV21G cells

Pathway	p value	FDR
PKA signalling	2.508E-04	4.135E-02
Regulation of CFTR activity (normal and CF)	5.007E-04	4.135E-02
Cadherin-mediated cell adhesion	5.063E-04	4.135E-02

Pathways list created and statistical analysis performed using MetaCore

References

Abe A, Minaguchi T, Ochi H et al., 2013. PIK3CA overexpression is a possible prognostic factor for favorable survival in ovarian clear cell carcinoma. *Human Pathology*, 44(2):199–207.

Agius L, 2010. Physiological control of liver glycogen metabolism: lessons from novel glycogen phosphorylase inhibitors. *Mini Reviews in Medicinal Chemistry*, 10(12):1175–87.

Ahmed AA, Etemadmoghadam D, Temple J et al., 2010. Driver mutations in TP53 are ubiquitous in high grade serous carcinoma of the ovary. *The Journal of Pathology*, 221(1): 49–56.

Ali AY, Abedini MR & Tsang BK, 2012. The oncogenic phosphatase PPM1D confers cisplatin resistance in ovarian carcinoma cells by attenuating checkpoint kinase 1 and p53 activation. *Oncogene*, 31(17):2175–86.

Andersen CL, Jensen JL & Ørntoft TF, 2004. Normalization of real-time quantitative reverse transcription-PCR data: a model-based variance estimation approach to identify genes suited for normalization, applied to bladder and colon cancer data sets. *Cancer Research*, 64(15):5245–50.

Anglesio MS, Carey MS, Köbel M et al., 2011a. Clear cell carcinoma of the ovary: a report from the first Ovarian Clear Cell Symposium, June 24th, 2010. *Gynecologic Oncology*, 121(2):407–15.

Anglesio MS, George J, Kulbe H et al., 2011b. IL6-STAT3-HIF signaling and therapeutic response to the angiogenesis inhibitor sunitinib in ovarian clear cell cancer. *Clinical Cancer Research*, 17(8):2538–48.

Anglesio MS, Wiegand KC, Melnyk N et al., 2013. Type-specific cell line models for type-specific ovarian cancer research. *PloS One*, 8(9):e72162.

Appleman LJ, 2011. MET signaling pathway: a rational target for cancer therapy. *Journal of Clinical Oncology*, 29(36):4837–8.

Ayhan A, Mao TL, Seckin T et al., 2012. Loss of ARID1A expression is an early molecular event in tumor progression from ovarian endometriotic cyst to clear cell and endometrioid carcinoma. *International Journal of Gynecological Cancer*, 22(8):1310–15.

Del Barco S, Vazquez-Martin A, Cufí S et al., 2011. Metformin: multi-faceted protection against cancer. *Oncotarget*, 2(12):896–917.

Barlow DH & Kennedy S, 2005. Endometriosis: New genetic approaches and therapy. *Annual Review of Medicine*, 56:345–56.

Bast RC, Hennessey B & Mills GB, 2009. The biology of ovarian cancer: new opportunities for translation. *Nature Reviews Cancer*, 9(6):415–28.

Begley CG & Ellis LM, 2012. Drug development: raise standards for preclinical cancer research. *Nature*, 483(7391):531–3.

Bergans N, Stalmans W, Goldmann S & Vanstapel F, 2000. Molecular mode of inhibition of glycogenolysis in rat liver by the dihydropyridine derivative, BAY R3401: inhibition and inactivation of glycogen phosphorylase by an activated metabolite. *Diabetes*, 49(9):1419–26.

Bergman MD, Schachter BS, Karelus K et al., 1992. Up-regulation of the uterine estrogen receptor and its messenger ribonucleic acid during the mouse estrous cycle: the role of estradiol. *Endocrinology*, 130(4):1923–30.

Bernardini L, Gimelli S, Gervasini C et al., 2009. Recurrent microdeletion at 17q12 as a cause of Mayer-Rokitansky-Kuster-Hauser (MRKH) syndrome: two case reports. *Orphanet Journal of Rare Diseases*, 4:25.

Berns K, Gennissen A, Hijmans EM et al., 2013. Loss of ARID1A confers resistance to multiple targeted cancer drugs through activation of AKT signaling. *European Journal of Cancer*, 49(Suppl3):S16–7.

Beuschlein F, Fassnacht M, Assié G et al., 2014. Constitutive activation of PKA catalytic subunit in adrenal Cushing's syndrome. *The New England Journal of Medicine*, 370(11):1019–28.

Bingham C, Ellard S, Cole TR et al., 2002. Solitary functioning kidney and diverse genital tract malformations associated with hepatocyte nuclear factor-1beta mutations. *Kidney International*, 61(4):1243–51.

Birnbaum DJ, Adélaïde J, Mamessier E et al., 2011. Genome profiling of pancreatic adenocarcinoma. *Genes, Chromosomes & Cancer*, 50(6):456–65.

Birsoy K, Possemato R, Lorbeer FK et al., 2014. Metabolic determinants of cancer cell sensitivity to glucose limitation and biguanides. *Nature*, 508(7494):108–12.

Biswas S, Lunec J & Bartlett K, 2012. Non-glucose metabolism in cancer cells - is it all in the fat? *Cancer Metastasis Reviews*, 31(3-4):689–98.

Bosse T, ter Haar NT, Seeber LM et al., 2013. Loss of ARID1A expression and its relationship with PI3K-Akt pathway alterations, TP53 and microsatellite instability in endometrial cancer. *Modern Pathology*, 26(11):1525–35.

Bouché C, Serdy S, Kahn CR & Goldfine AB, 2004. The cellular fate of glucose and its relevance in type 2 diabetes. *Endocrine Reviews*, 25(5):807–30.

Bourgo RJ, Siddiqui H, Fox S et al., 2009. SWI/SNF deficiency results in aberrant chromatin organization, mitotic failure, and diminished proliferative capacity. *Molecular Biology of the Cell*, 20(14):3192–9.

Bronson FH & Hamilton TH, 1971. Concentrations of nucleic acids and protein in the mouse oviduct during the oestrous cycle and after steroid replacement. *Journal of Reproduction and Fertility*, 25(2):283–6.

Brushia, RJ & Walsh DA, 1999. Phosphorylase kinase: the complexity of its regulation is reflected in the complexity of its structure. *Frontiers in Bioscience*, 4:D618–41.

Bulun SE, 2009. Endometriosis. *The New England Journal of Medicine*, 360(3):268–79.

Burwinkel B, Bakker HD, Herschkovitz E et al., 1998. Mutations in the liver glycogen phosphorylase gene (PYGL) underlying glycogenosis type VI. *American Journal of Human Genetics*, 62(4):785–91.

Campbell EA, O'Hara L, Catalano RD et al., 2006. Temporal expression profiling of the uterine luminal epithelium of the pseudo-pregnant mouse suggests receptivity to the fertilized egg is associated with complex transcriptional changes. *Human Reproduction*, 21(10):2495–513.

Cancer Statistics England, 2011. Cancer Statistics Registrations, England (Series MB1). <http://www.ons.gov.uk/ons/rel/vsob1/cancer-statistics-registrations--england--series-mb1-/index.html>. Accessed on 13 Dec 2013.

Centenera MM, Gillis JL, Hanson AR et al., 2012. Evidence for efficacy of new Hsp90 inhibitors revealed by ex vivo culture of human prostate tumors. *Clinical Cancer Research*, 18(13):3562–70.

Chakrabarti A, Chen AW & Varner JD, 2011. A review of the mammalian unfolded protein response. *Biotechnology and Bioengineering*, 108(12):2777–93.

Cheng CW, Licence D, Cook E et al., 2011. Activation of mutated K-ras in donor endometrial epithelium and stroma promotes lesion growth in an intact immunocompetent murine model of endometriosis. *The Journal of Pathology*, 224(2):261–9.

Cheung LW, Hennessy BT, Li J et al., 2011. High frequency of PIK3R1 and PIK3R2 mutations in endometrial cancer elucidates a novel mechanism for regulation of PTEN protein stability. *Cancer Discovery*, 1(2):170–85.

Cho-Chung YS, Pepe S, Clair T et al., 1995. cAMP-dependent protein kinase: role in normal and malignant growth. *Critical Reviews in Oncology / Hematology*, 21(1-3):33–61.

Chrysin ED, Chajistamatiou A & Chegkazi M, 2011. From structure-based to knowledge-based drug design through x-ray protein crystallography: sketching glycogen phosphorylase binding sites. *Current Medicinal Chemistry*, 18(17):2620–9.

Chung D & Das SK, 2011. Mouse primary uterine cell coculture system revisited: ovarian hormones mimic the aspects of in vivo uterine cell proliferation. *Endocrinology*, 152(8):3246–58.

Contreras CM, Gurumurthy S, Haynie JM et al., 2008. Loss of Lkb1 provokes highly invasive endometrial adenocarcinomas. *Cancer Research*, 68(3):759–66.

Contreras CM, Akbay EA, Gallardo TD et al., 2010. Lkb1 inactivation is sufficient to drive endometrial cancers that are aggressive yet highly responsive to mTOR inhibitor monotherapy. *Disease Models & Mechanisms*, 3(3-4):181–93.

Cooke PS, Buchanan DL, Young P et al., 1997. Stromal estrogen receptors mediate mitogenic effects of estradiol on uterine epithelium. *Proceedings of the National Academy of Sciences of the United States of America*, 94(12):6535–40.

Courtney KD, Corcoran RB & Engelman JA, 2010. The PI3K pathway as drug target in human cancer. *Journal of Clinical Oncology*, 28(6):1075–83.

Coward J, Kulbe H, Chakravarty P et al., 2011. Interleukin-6 as a therapeutic target in human ovarian cancer. *Clinical Cancer Research*, 17(18):6083–96.

Crotzer DR, Sun CC, Coleman RL et al., 2007. Lack of effective systemic therapy for recurrent clear cell carcinoma of the ovary. *Gynecologic Oncology*, 105(2):404–8.

Cuff J, Salari K, Clarke N et al., 2013. Integrative bioinformatics links HNF1B with clear cell carcinoma and tumor-associated thrombosis. *PloS One*, 8(9):e74562.

Cui C, Zhao H, Zhang Z et al., 2008. CDC25B acts as a potential target of PRKACA in fertilized mouse eggs. *Biology of Reproduction*, 79(5):991–8.

Cummings AM & Metcalf JL, 1995. Induction of endometriosis in mice: a new model sensitive to estrogen. *Reproductive Toxicology*, 9(3):233–8.

Cunha GR, Cooke PS & Kurita T, 2004. Role of stromal-epithelial interactions in hormonal responses. *Archives of Histology and Cytology*, 67(5):417–34.

Daikoku T, Hirota Y, Tranguch S et al., 2008. Conditional loss of uterine Pten unfailingly and rapidly induces endometrial cancer in mice. *Cancer Research*, 68(14):5619–27.

Daikoku T, Jackson L, Besnard V et al., 2011. Cell-specific conditional deletion of Pten in the uterus results in differential phenotypes. *Gynecologic Oncology*, 122(2):424–9.

Deng XS, Wang S, Deng A et al., 2012. Metformin targets Stat3 to inhibit cell growth and induce apoptosis in triple-negative breast cancers. *Cell Cycle*, 11(2):367–76.

Dinulescu DM, Ince TA, Quade BJ et al., 2005. Role of K-ras and Pten in the development of mouse models of endometriosis and endometrioid ovarian cancer. *Nature Medicine*, 11(1):63–70.

Domcke S, Sinha R, Levine DA et al., 2013. Evaluating cell lines as tumour models by comparison of genomic profiles. *Nature Communications*, 4:2126.

Dreyer C, Keller H, Mahfoudi A et al., 1993. Positive regulation of the peroxisomal beta-oxidation pathway by fatty acids through activation of peroxisome proliferator-activated receptors (PPAR). *Biology of the Cell*, 77(1):67–76.

Dubeau L, 2008. The cell of origin of ovarian epithelial tumours. *Lancet Oncology*, 9(12):1191–7.

Dulak AM, Stojanov P, Peng S et al., 2013. Exome and whole-genome sequencing of esophageal adenocarcinoma identifies recurrent driver events and mutational complexity. *Nature Genetics*, 45(5):478–86.

Dykhuisen EC, Hargreaves DC, Miller EL et al., 2013. BAF complexes facilitate decatenation of DNA by topoisomerase II α . *Nature*, 497(7451):624–7.

Ermisch M, Firla B & Steinhilber D, 2011. Protein kinase A activates and phosphorylates ROR α 4 in vitro and takes part in ROR α activation by CaMK-IV. *Biochemical and Biophysical Research Communications*, 408(3):442–6.

Euskirchen GM, Auerbach RK, Davidov E et al., 2011. Diverse roles and interactions of the SWI/SNF chromatin remodeling complex revealed using global approaches. *PLoS Genetics*, 7(3):e1002008.

Fadare O & Liang SX, 2012. Diagnostic utility of hepatocyte nuclear factor 1-beta immunoreactivity in endometrial carcinomas: lack of specificity for endometrial clear cell carcinoma. *Applied Immunohistochemistry & Molecular Morphology*, 20(6):580–7.

Favaro E, Bensaad K, Chong MG et al., 2012. Glucose utilization via glycogen phosphorylase sustains proliferation and prevents premature senescence in cancer cells. *Cell Metabolism*, 16(6):751–64.

Fernandez-Cuesta L, Peifer M, Lu X et al., 2014. Frequent mutations in chromatin-remodelling genes in pulmonary carcinoids. *Nature Communications*, 5:3518.

Ferrè S, Veenstra GJ, Bouwmeester R et al., 2011. HNF-1B specifically regulates the transcription of the γ -subunit of the Na⁺/K⁺-ATPase. *Biochemical and Biophysical Research Communications*, 404(1):284–90.

Flores-Alcantar A, Gonzalez-Sandoval A, Escalante-Alcalde D & Lomelí H, 2011. Dynamics of expression of ARID1A and ARID1B subunits in mouse embryos and in cells during the cell cycle. *Cell and Tissue Research*, 345(1):137–48.

Friboulet L, Olausson KA, Pignon JP et al., 2013. ERCC1 isoform expression and DNA repair in non-small-cell lung cancer. *The New England Journal of Medicine*, 368(12):1101–10.

Fujimoto A, Totoki Y, Abe T et al., 2012. Whole-genome sequencing of liver cancers identifies etiological influences on mutation patterns and recurrent mutations in chromatin regulators. *Nature Genetics*, 44(7):760–4.

Fujimura M, Katsumata N, Tsuda H et al., 2002. HER2 is frequently over-expressed in ovarian clear cell adenocarcinoma: possible novel treatment modality using recombinant monoclonal antibody against HER2, trastuzumab. *Japanese Journal of Cancer Research*, 93(11):1250–7.

Gaboriaud-Kolar N. & Skaltsounis AL, 2013. Glycogen phosphorylase inhibitors: a patent review (2008 - 2012). *Expert Opinion on Therapeutic Patents*, 23(8):1017–32.

Le Gallo M, O'Hara AJ, Rudd ML et al., 2012. Exome sequencing of serous endometrial tumors identifies recurrent somatic mutations in chromatin-remodeling and ubiquitin ligase complex genes. *Nature Genetics*, 44(12):1310–15.

Gao X, Tate P, Hu P et al., 2008. ES cell pluripotency and germ-layer formation require the SWI/SNF chromatin remodeling component BAF250a. *Proceedings of the National Academy of Sciences of the United States of America*, 105(18):6656-61.

García-Pedrero JM, Kiskinis E, Parker MG & Belandia B, 2006. The SWI/SNF chromatin remodeling subunit BAF57 is a critical regulator of estrogen receptor function in breast cancer cells. *The Journal of Biological Chemistry*, 281(32):22656–64.

Gargett CE, 2007. Uterine stem cells: what is the evidence? *Human Reproduction Update*, 13(1):87–101.

Gargett CE, Nguyen HP & Ye L, 2012. Endometrial regeneration and endometrial stem/progenitor cells. *Reviews in Endocrine & Metabolic Disorders*, 13(4):235–51.

Gentleman RC, Carey VJ, Bates DM et al., 2004. Bioconductor: open software development for computational biology and bioinformatics. *Genome Biology*, 5(10):R80.

Giudice LC & Kao LC, 2004. Endometriosis. *Lancet*, 364(9447):1789–99.

Giulino-Roth L, Wang K, MacDonald TY et al., 2012. Targeted genomic sequencing of pediatric Burkitt lymphoma identifies recurrent alterations in antiapoptotic and chromatin-remodeling genes. *Blood*, 120(26):5181–4.

Glasspool RM & McNeish IA, 2013. Clear cell carcinoma of ovary and uterus. *Current Oncology Reports*, 15(6):566–72.

Gounaris I, Charnock-Jones DS & Brenton JD, 2011. Ovarian clear cell carcinoma - bad endometriosis or bad endometrium? *The Journal of Pathology*, 225(2):157–60.

Greenberg CC, Jurczak MJ, Danos AM & Brady MJ, 2006. Glycogen branches out: new perspectives on the role of glycogen metabolism in the integration of metabolic pathways. *American Journal of Physiology Endocrinology and Metabolism*, 291(1):E1–8.

Grisanzio C, Werner L, Takeda D et al., 2012. Genetic and functional analyses implicate the NUDT11, HNF1B, and SLC22A3 genes in prostate cancer pathogenesis. *Proceedings of the National Academy of Sciences of the United States of America*, 109(28):11252–7.

Guan B, Wang TL & Shih IeM, 2011. ARID1A, a factor that promotes formation of SWI/SNF-mediated chromatin remodeling, is a tumor suppressor in gynecologic cancers. *Cancer Research*, 71(21):6718–27.

Guan B, Wang TL & Shih IeM, 2013. Arid1a loss in collaboration with PI3K pathway activation leads to ovarian tumorigenesis in mouse. *Cancer Research*, 73(8-Suppl1):LB-259.

Gui Y, Guo G, Huang Y et al., 2011. Frequent mutations of chromatin remodeling genes in transitional cell carcinoma of the bladder. *Nature Genetics*, 43(9):875–8.

Guin S, Pollard C, Ru Y et al., 2014. Role in tumor growth of a glycogen debranching enzyme lost in glycogen storage disease. *Journal of the National Cancer Institute*, 106(5):dju062.

Hameyer D, Loonstra A, Eshkind L et al., 2007. Toxicity of ligand-dependent Cre recombinases and generation of a conditional Cre deleter mouse allowing mosaic recombination in peripheral tissues. *Physiological Genomics*, 31(1):32–41.

Hashiguchi Y, Tsuda H, Inoue T et al., 2006. PTEN expression in clear cell adenocarcinoma of the ovary. *Gynecologic Oncology*, 101(1):71–5.

Helming KC, Wang X, Wilson BG et al., 2014. ARID1B is a specific vulnerability in ARID1A-mutant cancers. *Nature Medicine*, 20(3):251-4.

Higashiguchi A, Yamada T, Susumu N et al., 2007. Specific expression of hepatocyte nuclear factor-1beta in the ovarian clear cell adenocarcinoma and its application to cytological diagnosis. *Cancer Science*, 98(3):387–91.

Hitzemann R, Bottomly D, Darakjian P et al., 2013. Genes, behavior and next-generation RNA sequencing. *Genes, Brain, and Behavior*, 12(1):1–12.

Ho CM, Huang YJ, Chen TC et al., 2004. Pure-type clear cell carcinoma of the ovary as a distinct histological type and improved survival in patients treated with paclitaxel-platinum-based chemotherapy in pure-type advanced disease. *Gynecologic Oncology*, 94(1):197–203.

Ho CM, Lin MC, Huang SH et al., 2009. PTEN promoter methylation and LOH of 10q22-23 locus in PTEN expression of ovarian clear cell adenocarcinomas. *Gynecologic Oncology*, 112(2):307–13.

Hoffman GR, Rahal R, Buxton F et al., 2014. Functional epigenetics approach identifies BRM/SMARCA2 as a critical synthetic lethal target in BRG1-deficient cancers. *Proceedings of the National Academy of Sciences of the United States of America*, 111(8):3128–33.

Hollander MC, Blumenthal GM & Dennis PA, 2011. PTEN loss in the continuum of common cancers, rare syndromes and mouse models. *Nature Reviews Cancer*, 11(4):289–301.

Honeyman JN, Simon EP, Robine N et al., 2014. Detection of a recurrent DNAJB1-PRKACA chimeric transcript in fibrolamellar hepatocellular carcinoma. *Science*, 343(6174):1010–14.

Hoskins PJ, Le N, Gilks B et al., 2012. Low-stage ovarian clear cell carcinoma: population-based outcomes in British Columbia, Canada, with evidence for a survival benefit as a result of irradiation. *Journal of Clinical Oncology*, 30(14):1656–62.

Hostetler HA, Balanarasimha M, Huang H et al., 2010. Glucose regulates fatty acid binding protein interaction with lipids and peroxisome proliferator-activated receptor α . *Journal of Lipid Research*, 51(11):3103–16.

Huang J, Deng Q, Wang Q et al., 2012. Exome sequencing of hepatitis B virus-associated hepatocellular carcinoma. *Nature Genetics*, 44(10):1117–21.

Iida Y, Aoki K, Asakura T et al., 2012. Hypoxia promotes glycogen synthesis and accumulation in human ovarian clear cell carcinoma. *International Journal of Oncology*, 40(6):2122–30.

Inoue H, Furukawa T, Giannakopoulos S et al., 2002. Largest subunits of the human SWI/SNF chromatin-remodeling complex promote transcriptional activation by steroid hormone receptors. *The Journal of Biological Chemistry*, 277(44):41674–85.

Israël M & Schwartz L, 2011. The metabolic advantage of tumor cells. *Molecular Cancer*, 10:70.

Jeong KW, Lee YH & Stallcup MR, 2009. Recruitment of the SWI/SNF chromatin remodeling complex to steroid hormone-regulated promoters by nuclear receptor coactivator flightless-I. *The Journal of Biological Chemistry*, 284(43):29298–309.

Joe Y, Do MH, Seo E et al., 2010. Fenofibrate antagonizes Chk2 activation by inducing Wip1 expression: implications for cell proliferation and tumorigenesis. *Life Sciences*, 86(19-20):716–21.

Jones S, Wang TL, Shih IeM et al., 2010. Frequent mutations of chromatin remodeling gene ARID1A in ovarian clear cell carcinoma. *Science*, 330(6001):228–31.

Jones S, Li M, Parsons DW et al., 2012. Somatic mutations in the chromatin remodeling gene ARID1A occur in several tumor types. *Human Mutation*, 33(1):100–3.

Joshi A & Ellenson LH, 2011. Adenovirus mediated homozygous endometrial epithelial Pten deletion results in aggressive endometrial carcinoma. *Experimental Cell Research*, 317(11):1580–9.

Kadoch C, Hargreaves DC, Hodges C et al., 2013. Proteomic and bioinformatic analysis of mammalian SWI/SNF complexes identifies extensive roles in human malignancy. *Nature Genetics*, 45(6):592–601.

Kandoth C, Schultz N, Cherniack AD et al., 2013. Integrated genomic characterization of endometrial carcinoma. *Nature*, 497(7447):67–73.

Kasten MM, Clapier CR & Cairns BR, 2011. SnapShot: Chromatin remodeling: SWI/SNF. *Cell*, 144(2):310.e1.

Katagiri A, Nakayama K, Rahman MT et al., 2012. Loss of ARID1A expression is related to shorter progression-free survival and chemoresistance in ovarian clear cell carcinoma. *Modern Pathology*, 25(2):282–8.

Kato N, Sasou S & Motoyama T, 2006. Expression of hepatocyte nuclear factor-1beta (HNF-1beta) in clear cell tumors and endometriosis of the ovary. *Modern Pathology*, 19(1):83–9.

Kato N, Toukairin M, Asanuma I & Motoyama T, 2007. Immunocytochemistry for hepatocyte nuclear factor-1beta (HNF-1beta): a marker for ovarian clear cell carcinoma. *Diagnostic Cytopathology*, 35(4):193–7.

Kato N, Tamura G & Motoyama T, 2008. Hypomethylation of hepatocyte nuclear factor-1beta (HNF-1beta) CpG island in clear cell carcinoma of the ovary. *Virchows Archiv*, 452(2):175–80.

Kayis SA, Atli MO, Kurar E et al., 2011. Rating of putative housekeeping genes for quantitative gene expression analysis in cyclic and early pregnant equine endometrium. *Animal Reproduction Science*, 125(1-4):124–32.

Kobayashi H, Kajiwara H, Kanayama S et al., 2009. Molecular pathogenesis of endometriosis-associated clear cell carcinoma of the ovary (Review). *Oncology Reports*, 22(2):233–40.

Korch C, Spillman MA, Jackson TA et al., 2012. DNA profiling analysis of endometrial and ovarian cell lines reveals misidentification, redundancy and contamination. *Gynecologic Oncology*, 127(1):241–8.

Kornfeld JW, Baitzel C, Könner AC et al., 2013. Obesity-induced overexpression of miR-802 impairs glucose metabolism through silencing of Hnf1b. *Nature*, 494(7435):111–15.

Krosi J, Mamo A, Chagraoui J et al., 2010. A mutant allele of the Swi/Snf member BAF250a determines the pool size of fetal liver hemopoietic stem cell populations. *Blood*, 116(10):1678–84.

Kuhn E, Kurman RJ, Vang R et al., 2012. TP53 mutations in serous tubal intraepithelial carcinoma and concurrent pelvic high-grade serous carcinoma - evidence supporting the clonal relationship of the two lesions. *The Journal of Pathology*, 226(3):421–6.

Kun S, Bokor É, Varga G et al., 2014. New synthesis of 3-(β -D-glucopyranosyl)-5-substituted-1,2,4-triazoles, nanomolar inhibitors of glycogen phosphorylase. *European Journal of Medicinal Chemistry*, 76:567–79.

Kuo KT, Mao TL, Jones S et al., 2009. Frequent activating mutations of PIK3CA in ovarian clear cell carcinoma. *The American Journal of Pathology*, 174(5):1597–601.

Kurman RJ & Shih IeM, 2011. Molecular pathogenesis and extraovarian origin of epithelial ovarian cancer - shifting the paradigm. *Human Pathology*, 42(7):918–31.

Kyo S, Maida Y & Inoue M, 2011. Stem cells in endometrium and endometrial cancer: accumulating evidence and unresolved questions. *Cancer Letters* 308(2):123–33.

Laudanski P, Szamatowicz J, Kowalczyk O et al., 2009. Expression of selected tumor suppressor and oncogenes in endometrium of women with endometriosis. *Human Reproduction*, 24(8):1880–90.

Lecca, MR, Wagner U, Patrignani A et al., 2005. Genome-wide analysis of the unfolded protein response in fibroblasts from congenital disorders of glycosylation type-I patients. *FASEB Journal*, 19(2):240–2.

Lee Y, Medeiros F, Kindelberger D et al., 2006. Advances in the recognition of tubal intraepithelial carcinoma: applications to cancer screening and the pathogenesis of ovarian cancer. *Advances in Anatomic Pathology*, 13(1):1–7.

Lee YY, Kim TJ, Kim MJ et al., 2011. Prognosis of ovarian clear cell carcinoma compared to other histological subtypes: a meta-analysis. *Gynecologic Oncology*, 122(3):541–7.

Li J, Huang CL, Zhang LW et al., 2010. Isoforms of human O-GlcNAcase show distinct catalytic efficiencies. *Biochemistry Biokhimiia*, 75(7):938–43.

Li S, Zhang Y & Xu W, 2013. Developments of polo-like kinase 1 (Plk1) inhibitors as anti-cancer agents. *Mini Reviews in Medicinal Chemistry*, 13(14):2014–25.

Liang H, Cheung LW, Li J et al., 2012. Whole-exome sequencing combined with functional genomics reveals novel candidate driver cancer genes in endometrial cancer. *Genome Research*, 22(11):2120–9.

Lichner Z, Scorilas A, White NM et al., 2013. The chromatin remodeling gene ARID1A is a new prognostic marker in clear cell renal cell carcinoma. *The American Journal of Pathology*, 182(4):1163–70.

Liu L, Ulbrich J, Müller J et al., 2012. Deregulated MYC expression induces dependence upon AMPK-related kinase 5. *Nature*, 483(7391):608–12.

Liu P, Khurana A, Rattan R et al., 2009. Regulation of HSulf-1 expression by variant hepatic nuclear factor 1 in ovarian cancer. *Cancer Research*, 69(11):4843–50.

Love C, Sun Z, Jima D et al., 2012. The genetic landscape of mutations in Burkitt lymphoma. *Nature Genetics*, 44(12):1321–5.

Lowery WJ, Schildkraut JM, Akushevich L et al., 2012. Loss of ARID1A-associated protein expression is a frequent event in clear cell and endometrioid ovarian cancers. *International Journal of Gynecological Cancer*, 22(1):9–14.

Lu JP, Wang Y, Sliter DA et al., 2011. RNF170 protein, an endoplasmic reticulum membrane ubiquitin ligase, mediates inositol 1,4,5-trisphosphate receptor ubiquitination and degradation. *The Journal of Biological Chemistry*, 286(27):24426–33.

Ma Z, Gong Y, Patel V et al., 2007. Mutations of HNF-1beta inhibit epithelial morphogenesis through dysregulation of SOCS-3. *Proceedings of the National Academy of Sciences of the United States of America*, 104(51):20386–91.

Mabuchi S, Kawase C, Altomare DA et al., 2009. mTOR is a promising therapeutic target both in cisplatin-sensitive and cisplatin-resistant clear cell carcinoma of the ovary. *Clinical Cancer Research*, 15(17):5404–13.

Mabuchi S, Hisamatsu T, Kawase C et al., 2011. The activity of trabectedin as a single agent or in combination with everolimus for clear cell carcinoma of the ovary. *Clinical Cancer Research*, 17(13):4462–73.

Madhu B, Waterton JC, Griffiths JR et al., 2006. The response of RIF-1 fibrosarcomas to the vascular-disrupting agent ZD6126 assessed by in vivo and ex vivo 1H magnetic resonance spectroscopy. *Neoplasia*, 8(7):560–7.

Maeda D, Mao TL, Fukayama M et al., 2010. Clinicopathological significance of loss of ARID1A immunoreactivity in ovarian clear cell carcinoma. *International Journal of Molecular Sciences*, 11(12):5120–8.

Mandai M, Yamaguchi K, Matsumura N et al., 2009. Ovarian cancer in endometriosis: molecular biology, pathology, and clinical management. *International Journal of Clinical Oncology*, 14(5):383–91.

Mao TL & Shih leM, 2013. The roles of ARID1A in gynecologic cancer. *Journal of Gynecologic Oncology*, 24(4):376–81.

Martini M, Ciccarone M, Garganese G et al., 2002. Possible involvement of hMLH1, p16(INK4a) and PTEN in the malignant transformation of endometriosis. *International Journal of Cancer*, 102(4):398–406.

Masters JR, 2012. Cell-line authentication: End the scandal of false cell lines. *Nature*, 492(7428):186.

Masuda H, Maruyama T, Hiratsu E et al., 2007. Noninvasive and real-time assessment of reconstructed functional human endometrium in NOD/SCID/gamma c(null) immunodeficient mice. *Proceedings of the National Academy of Sciences of the United States of America*, 104(6):1925–30.

McCluggage WG, 2008. My approach to and thoughts on the typing of ovarian carcinomas. *Journal of Clinical Pathology*, 61(2):152–63.

McConechy MK, Anglesio MS, Kalloger SE et al., 2011. Subtype-specific mutation of PPP2R1A in endometrial and ovarian carcinomas. *The Journal of Pathology*, 223(5):567–73.

Meléndez R, Meléndez-Hevia E & Canela EI, 1999. The fractal structure of glycogen: a clever solution to optimize cell metabolism. *Biophysical Journal*, 77(3):1327–32.

Miki Y, Swensen J, Shattuck-Eidens D et al., 1994. A strong candidate for the breast and ovarian cancer susceptibility gene BRCA1. *Science*, 266(5182):66–71.

Mote PA, Arnett-Mansfield RL, Gava N et al., 2006. Overlapping and distinct expression of progesterone receptors A and B in mouse uterus and mammary gland during the estrous cycle. *Endocrinology*, 147(12):5503–12.

Muñiz LC, Yehia G, Mémin E et al., 2006. Transcriptional regulation of cyclin D2 by the PKA pathway and inducible cAMP early repressor in granulosa cells. *Biology of Reproduction*, 75(2):279–88.

Nagl NG, Patsialou A, Haines DS et al., 2005. The p270 (ARID1A/SMARCF1) subunit of mammalian SWI/SNF-related complexes is essential for normal cell cycle arrest. *Cancer Research*, 65(20):9236–44.

Nagl NG, Zweitzig DR, Thimmapaya B et al., 2006. The c-myc gene is a direct target of mammalian SWI/SNF-related complexes during differentiation-associated cell cycle arrest. *Cancer Research*, 66(3):1289–93.

Nagl NG, Wang X, Patsialou A et al., 2007. Distinct mammalian SWI/SNF chromatin remodeling complexes with opposing roles in cell-cycle control. *The EMBO Journal*, 26(3):752–63.

Nelson GS, Pink A, Lee S et al., 2013. MMR deficiency is common in high-grade endometrioid carcinomas and is associated with an unfavorable outcome. *Gynecologic Oncology*, 131(2):309–14.

Newbold RR, Teng CT, Beckman WC et al., 1992. Fluctuations of lactoferrin protein and messenger ribonucleic acid in the reproductive tract of the mouse during the estrous cycle. *Biology of Reproduction*, 47(5):903–15.

Newbold RR, Hanson RB & Jefferson WN, 1994. Immature mouse uterine tissue in organ culture: estrogen-induced growth, morphology and biochemical parameters. *In Vitro Cellular and Developmental Biology*, 30A(8):519–28.

Ng CK, Cooke SL, Howe K et al., 2012. The role of tandem duplicator phenotype in tumour evolution in high-grade serous ovarian cancer. *The Journal of Pathology*, 226(5):703–12.

Niles AL, Moravec RA & Riss TL, 2009. In vitro viability and cytotoxicity testing and same-well multi-parametric combinations for high throughput screening. *Current Chemical Genomics*, 3:33–41.

Niskakoski A, Kaur S, Renkonen-Sinisalo L et al., 2013. Distinct molecular profiles in Lynch syndrome-associated and sporadic ovarian carcinomas. *International Journal of Cancer*, 133(11):2596–608.

Ohkawa K, Amasaki H, Terashima Y et al., 1977. Clear cell carcinoma of the ovary: light and electron microscopic studies. *Cancer*, 40(6):3019–29.

Okamoto T, Mandai M, Matsumura N et al., 2013. Hepatocyte nuclear factor-1 β (HNF-1 β) promotes glucose uptake and glycolytic activity in ovarian clear cell carcinoma. *Molecular Carcinogenesis*. doi: 10.1002/mc.22072 [Epub ahead of print].

Olave I, Wang W, Xue Y et al., 2002. Identification of a polymorphic, neuron-specific chromatin remodeling complex. *Genes & Development*, 16(19):2509–17.

Ootani A, Li X, Sangiorgi E et al., 2009. Sustained in vitro intestinal epithelial culture within a Wnt-dependent stem cell niche. *Nature Medicine*, 15(6):701–6.

Oram RA, Edghill EL, Blackman J et al., 2010. Mutations in the hepatocyte nuclear factor-1 β (HNF1B) gene are common with combined uterine and renal malformations but are not found with isolated uterine malformations. *American Journal of Obstetrics and Gynecology*, 203(4):364.e1–5.

Ortmeyer HK, 1997. Relationship of glycogen synthase and glycogen phosphorylase to protein phosphatase 2C and cAMP-dependent protein kinase in liver of obese rhesus monkeys. *Obesity Research*, 5(6):613–21.

Ouellette MJ, Hamel L, Tremblay N et al., 1999. Characterization of endoglin on mouse uterine stromal cells. *Journal of reproduction and Fertility*, 117(2):229–39.

Ozen H, 2007. Glycogen storage diseases: new perspectives. *World Journal of Gastroenterology*, 13(18):2541–53.

Park KJ, Lee CH, Kim A et al., 2012. Death receptors 4 and 5 activate Nox1 NADPH oxidase through riboflavin kinase to induce reactive oxygen species-mediated apoptotic cell death. *The Journal of Biological Chemistry*, 287(5):3313–25.

Pearce CL, Templeman C, Rossing MA et al., 2012. Association between endometriosis and risk of histological subtypes of ovarian cancer: a pooled analysis of case-control studies. *The Lancet Oncology*, 13(4):385–94.

Pearce LR, Komander D & Alessi DR, 2010. The nuts and bolts of AGC protein kinases. *Nature Reviews Molecular Cell Biology*, 11(1):9–22.

Pelletier J, Bellot G, Gounon P et al., 2012. Glycogen synthesis is induced in hypoxia by the hypoxia-inducible factor and promotes cancer cell survival. *Frontiers in Oncology*, 2:18.

Perrotti D & Neviani P, 2013. Protein phosphatase 2A: a target for anticancer therapy. *The Lancet Oncology*, 14(6):e229–38.

Pescador N, Villar D, Cifuentes D et al., 2010. Hypoxia promotes glycogen accumulation through hypoxia inducible factor (HIF)-mediated induction of glycogen synthase 1. *PLoS One*, 5(3):e9644.

Pfaffl MW, Tichopad A, Prgomet C & Neuvians TP, 2004. Determination of stable housekeeping genes, differentially regulated target genes and sample integrity: BestKeeper - Excel-based tool using pair-wise correlations. *Biotechnology Letters*, 26(6):509–15.

Pharoah PD, Tsai YY, Ramus SJ et al., 2013. GWAS meta-analysis and replication identifies three new susceptibility loci for ovarian cancer. *Nature Genetics*, 45(4):362–70.

Philips KB, Kurtoglu M, Leung HJ et al., 2014. Increased sensitivity to glucose starvation correlates with downregulation of glycogen phosphorylase isoform PYGB in tumor cell lines resistant to 2-deoxy-D-glucose. *Cancer Chemotherapy and Pharmacology*, 73(2):349–61.

Polakof S, Panserat S, Craig PM et al., 2011. The metabolic consequences of hepatic AMP-kinase phosphorylation in rainbow trout. *PloS One*, 6(5):e20228.

Radziuk J, Bailey CJ, Wiernsperger NF & Yudkin JS, 2003. Metformin and its liver targets in the treatment of type 2 diabetes. *Current Drug Targets Immune, Endocrine and Metabolic Disorders*, 3(2):151–69.

Rahman M, Nakayama K, Rahman MT et al., 2012. Clinicopathologic and biological analysis of PIK3CA mutation in ovarian clear cell carcinoma. *Human Pathology*, 43(12):2197–206.

Rechsteiner M, Zimmermann AK, Wild PJ et al., 2013. TP53 mutations are common in all subtypes of epithelial ovarian cancer and occur concomitantly with KRAS mutations in the mucinous type. *Experimental and Molecular Pathology*, 95(2):235–41.

Reisman D, Glaros S & Thompson EA, 2009. The SWI/SNF complex and cancer. *Oncogene*, 28(14):1653–68.

Rizner TL, 2009. Estrogen metabolism and action in endometriosis. *Molecular and Cellular Endocrinology*, 307(1-2):8–18.

Roach PJ, Depaoli-Roach AA, Hurley TD & Tagliabracci VS, 2012. Glycogen and its metabolism: some new developments and old themes. *The Biochemical Journal*, 441(3):763–87.

Rocca A, Farolfi A, Bravaccini S et al., 2014. Palbociclib (PD 0332991): targeting the cell cycle machinery in breast cancer. *Expert Opinion on Pharmacotherapy*, 15(3):407–20.

Rodriguez-Cuenca S, Carobbio S, Velagapudi VR et al., 2012. Peroxisome proliferator-activated receptor γ -dependent regulation of lipolytic nodes and metabolic flexibility. *Molecular and Cellular Biology*, 32(8):1555–65.

Ross JS, Wang K, Gay L et al., 2014. New routes to targeted therapy of intrahepatic cholangiocarcinomas revealed by next-generation sequencing. *The Oncologist*, 19(3):235–42.

Ben Sahra I, Le Marchand-Brustel Y, Tanti JF & Bost F, 2010. Metformin in cancer therapy: a new perspective for an old antidiabetic drug? *Molecular Cancer Therapeutics*, 9(5):1092–9.

Samartzis EP, Samartzis N, Noske A et al., 2012. Loss of ARID1A/BAF250a-expression in endometriosis: a biomarker for risk of carcinogenic transformation? *Modern Pathology*, 25(6):885–92.

Santen GW, Aten E, Vulto-van Silfhout AT et al., 2013. Coffin-Siris syndrome and the BAF complex: genotype-phenotype study in 63 patients. *Human Mutation*, 34(11):1519–28.

Santen GW, Aten E, Sun Y et al., 2012. Mutations in SWI/SNF chromatin remodeling complex gene ARID1B cause Coffin-Siris syndrome. *Nature Genetics*, 44(4):379–80.

Sarfstein R, Friedman Y, Attias-Geva Z et al., 2013. Metformin downregulates the insulin/IGF-I signaling pathway and inhibits different uterine serous carcinoma (USC) cells proliferation and migration in p53-dependent or -independent manners. *PloS One*, 8(4):e61537.

Sausen M, Leary RJ, Jones S et al., 2013. Integrated genomic analyses identify ARID1A and ARID1B alterations in the childhood cancer neuroblastoma. *Nature Genetics*, 45(1):12–17.

Savvari P, Peitsidis P, Alevizaki M et al., 2009. Paraneoplastic humorally mediated hypercalcemia induced by parathyroid hormone-related protein in gynecologic malignancies: a systematic review. *Onkologie*, 32(8-9):517–23.

Schneider JG, Farhadfar N, Sivapiragasam A et al., 2014. Commercial laboratory testing of excision repair cross-complementation group 1 expression in non-small cell lung cancer. *The Oncologist*, 19(5):459–65.

Schnier JB, Nishi K, Monks A et al., 2003. Inhibition of glycogen phosphorylase (GP) by CP-91,149 induces growth inhibition correlating with brain GP expression. *Biochemical and Biophysical Research Communications*, 309(1):126–34.

Schroder AL, Pelch KE & Nagel SC, 2009. Estrogen modulates expression of putative housekeeping genes in the mouse uterus. *Endocrine*, 35(2):211–19.

Schwartz DR, Kardia SL, Shedden KA et al., 2002. Gene expression in ovarian cancer reflects both morphology and biological behavior, distinguishing clear cell from other poor-prognosis ovarian carcinomas. *Cancer Research*, 62(16):4722–9.

Senkel S, Lucas B, Klein-Hitpass L & Ryffel GU, 2005. Identification of target genes of the transcription factor HNF1beta and HNF1alpha in a human embryonic kidney cell line. *Biochimica et Biophysica Acta*, 1731(3):179–90.

de la Serna IL, Ohkawa Y & Imbalzano AN, 2006. Chromatin remodelling in mammalian differentiation: lessons from ATP-dependent remodellers. *Nature Reviews Genetics*, 7(6):461–73.

Shain AH & Pollack JR, 2013. The spectrum of SWI/SNF mutations, ubiquitous in human cancers. *PloS One*, 8(1):e55119.

Shaw TJ, Senterman MK, Dawson K et al., 2004. Characterization of intraperitoneal, orthotopic, and metastatic xenograft models of human ovarian cancer. *Molecular Therapy*, 10(6):1032–42.

Shen H, Fridley BL, Song H et al., 2013. Epigenetic analysis leads to identification of HNF1B as a subtype-specific susceptibility gene for ovarian cancer. *Nature Communications*, 4:1628.

Siegel R, Ma J, Zou Z & Jemal A, 2014. Cancer statistics, 2014. *CA: a Cancer Journal for Clinicians*, 64(1):9–29.

Soyal SM, Mukherjee A, Lee KY et al., 2005. Cre-mediated recombination in cell lineages that express the progesterone receptor. *Genesis*, 41(2):58–66.

Spurdle AB, Thompson DJ, Ahmed S et al., 2011. Genome-wide association study identifies a common variant associated with risk of endometrial cancer. *Nature Genetics*, 43(5):451–4.

Stany MP, Vathipadiekal V, Ozburn L et al., 2011. Identification of novel therapeutic targets in microdissected clear cell ovarian cancers. *PloS One*, 6(7):e21121.

Stephens PJ, Tarpey PS, Davies H et al., 2012. The landscape of cancer genes and mutational processes in breast cancer. *Nature*, 486(7403):400–4.

Steuwe C, Patel II, Ul-Hasan M et al., 2013. CARS based label-free assay for assessment of drugs by monitoring lipid droplets in tumour cells. *Journal of Biophotonics*, doi: 10.1002/jbio.201300110 [Epub ahead of print].

Stone RL, Nick AM, McNeish IA et al., 2012. Paraneoplastic thrombocytosis in ovarian cancer. *The New England Journal of Medicine*, 366(7):610–8.

Streppel MM, Lata S, DelaBastide M et al., 2014. Next-generation sequencing of endoscopic biopsies identifies ARID1A as a tumor-suppressor gene in Barrett's esophagus. *Oncogene*, 33(3):347–57.

Sugiyama T, Kamura T, Kigawa J et al., 2000. Clinical characteristics of clear cell carcinoma of the ovary: a distinct histologic type with poor prognosis and resistance to platinum-based chemotherapy. *Cancer*, 88(11):2584–9.

Sun H, Gulbagci NT & Taneja R, 2007. Analysis of growth properties and cell cycle regulation using mouse embryonic fibroblast cells. *Methods in Molecular Biology*, 383:311–9.

Takano M, Sasaki N, Kita T et al., 2008a. Survival analysis of ovarian clear cell carcinoma confined to the ovary with or without comprehensive surgical staging. *Oncology Reports*, 19(5):1259–64.

Takano M, Sugiyama T, Yaegashi N et al., 2008b. Low response rate of second-line chemotherapy for recurrent or refractory clear cell carcinoma of the ovary : a retrospective Japan Clear Cell Carcinoma Study. *International Journal of Gynecological Cancer*, 18(5):937–42.

Takano M, Sugiyama T, Yaegashi N et al., 2010. Less impact of adjuvant chemotherapy for stage I clear cell carcinoma of the ovary: a retrospective Japan Clear Cell Carcinoma Study. *International Journal of Gynecological Cancer*, 20(9):1506–10.

Takano M, Kikuchi Y, Kudoh K et al., 2011. Weekly administration of temsirolimus for heavily pretreated patients with clear cell carcinoma of the ovary: a report of six cases. *International Journal of Clinical Oncology*, 16(5):605–9.

Tan DS & Kaye S, 2007. Ovarian clear cell adenocarcinoma : a continuing enigma. *Journal of Clinical Pathology*, 60(4):355–60.

Tan DS, Lambros MB, Rayter S et al., 2009. PPM1D is a potential therapeutic target in ovarian clear cell carcinomas. *Clinical Cancer Research*, 15(7):2269–80.

Tan DS, Iravani M, McCluggage WG et al., 2011. Genomic analysis reveals the molecular heterogeneity of ovarian clear cell carcinomas. *Clinical Cancer Research*, 17(6):1521–34.

Tan DS, Miller RE & Kaye SB, 2013. New perspectives on molecular targeted therapy in ovarian clear cell carcinoma. *British Journal of Cancer*, 108(8):1553–9.

Tan YF, Li FX, Piao YS et al., 2003. Global gene profiling analysis of mouse uterus during the oestrous cycle. *Reproduction*, 126(2):171–82.

Tanaka T, Tomaru Y, Nomura Y et al., 2004. Comprehensive search for HNF-1beta-regulated genes in mouse hepatoma cells perturbed by transcription regulatory factor-targeted RNAi. *Nucleic Acids Research*, 32(9):2740–50.

TCGA, 2011. Integrated genomic analyses of ovarian carcinoma. *Nature*, 474(7353):609–15.

TCGA, 2014. Comprehensive molecular characterization of urothelial bladder carcinoma. *Nature*, 507(7492):315–22.

Terrin A, Monterisi S, Stangherlin A et al., 2012. PKA and PDE4D3 anchoring to AKAP9 provides distinct regulation of cAMP signals at the centrosome. *The Journal of Cell Biology*, 198(4):607–21.

Thomas H, Senkel S, Erdmann S et al., 2004. Pattern of genes influenced by conditional expression of the transcription factors HNF6, HNF4alpha and HNF1beta in a pancreatic beta-cell line. *Nucleic Acids Research*, 32(19):e150.

Tirado-González I, Barrientos G, Tariverdian N et al., 2010. Endometriosis research : animal models for the study of a complex disease. *Journal of Reproductive Immunology*, 86(2):141–7.

Tomassetti A, De Santis G, Castellano G et al., 2008. Variant HNF1 modulates epithelial plasticity of normal and transformed ovary cells. *Neoplasia*, 10(12):1481–92.

Treon SP, Xu L, Yang G et al., 2012. MYD88 L265P somatic mutation in Waldenström's macroglobulinemia. *The New England Journal of Medicine*, 367(9):826–33.

Tronche F & Yaniv M, 1992. HNF1, a homeoprotein member of the hepatic transcription regulatory network. *BioEssays*, 14(9):579–87.

Tsuchiya A, Sakamoto M, Yasuda J et al., 2003. Expression profiling in ovarian clear cell carcinoma: identification of hepatocyte nuclear factor-1 beta as a molecular marker and a possible molecular target for therapy of ovarian clear cell carcinoma. *The American Journal of Pathology*, 163(6):2503–12.

Uekuri C, Shigetomi H, Ono S et al., 2013. Toward an understanding of the pathophysiology of clear cell carcinoma of the ovary (review). *Oncology Letters*, 6(5):1163–73.

Umene K, Banno K, Kisu I et al., 2013. Aurora kinase inhibitors: potential molecular-targeted drugs for gynecologic malignant tumors. *Biomedical Reports*, 1(3):335–40.

Varga-Weisz P, 2001. ATP-dependent chromatin remodeling factors: nucleosome shufflers with many missions. *Oncogene*, 20(24):3076–85.

Vaughan S, Coward JI, Bast RC et al., 2011. Rethinking ovarian cancer: recommendations for improving outcomes. *Nature Reviews Cancer*, 11(10):719–25.

Veras E, Mao TL, Ayhan A et al., 2009. Cystic and adenofibromatous clear cell carcinomas of the ovary: distinctive tumors that differ in their pathogenesis and behavior : a clinicopathologic analysis of 122 cases. *The American Journal of Surgical Pathology*, 33(6):844–53.

Vestergaard AL, Knudsen UB, Munk T et al., 2011. Transcriptional expression of type-I interferon response genes and stability of housekeeping genes in the human endometrium and endometriosis. *Molecular Human Reproduction*, 17(4):243–54.

Vicent GP, Zaurin R, Nacht AS et al., 2009. Two chromatin remodeling activities cooperate during activation of hormone responsive promoters. *PLoS Genetics*, 5(7):e1000567.

Vichai V & Kirtikara K, 2006. Sulforhodamine B colorimetric assay for cytotoxicity screening. *Nature Protocols*, 1(3):1112–16.

Vries RG, Bezrookove V, Zuijderduijn LM et al., 2005. Cancer-associated mutations in chromatin remodeler hSNF5 promote chromosomal instability by compromising the mitotic checkpoint. *Genes & Development*, 19(6):665–70.

Wang DD, Chen YB, Pan K et al., 2012. Decreased expression of the ARID1A gene is associated with poor prognosis in primary gastric cancer. *PloS One*, 7(7):e40364.

Wang K, Kan J, Yuen ST et al., 2011. Exome sequencing identifies frequent mutation of ARID1A in molecular subtypes of gastric cancer. *Nature Genetics*, 43(12):1219–23.

Wang L, Coffinier C, Thomas MK et al., 2004. Selective deletion of the Hnf1beta (MODY5) gene in beta-cells leads to altered gene expression and defective insulin release. *Endocrinology*, 145(8):3941–9.

Wang S, Li J, Zhang A et al., 2011. Selection of reference genes for studies of porcine endometrial gene expression on gestational day 12. *Biochemical and Biophysical Research Communications*, 408(2):265–8.

Watanabe R, Ui A, Kanno S et al., 2014. SWI/SNF factors required for cellular resistance to DNA damage include ARID1A and ARID1B and show interdependent protein stability. *Cancer Research*, 74(9):2465–75.

Wiegand KC, Shah SP, Al-Agha OM et al., 2010. ARID1A mutations in endometriosis-associated ovarian carcinomas. *The New England Journal of Medicine*, 363(16):1532–43.

Wiegand KC, Lee AF, Al-Agha OM et al., 2011. Loss of BAF250a (ARID1A) is frequent in high-grade endometrial carcinomas. *The Journal of Pathology*, 224(3):328–33.

Wiegand KC, Hennessy BT, Leung S et al., 2014a. A functional proteogenomic analysis of endometrioid and clear cell carcinomas using reverse phase protein array and mutation analysis: protein expression is histotype-specific and loss of ARID1A/BAF250a is associated with AKT phosphorylation. *BMC Cancer*, 14:120.

Wiegand KC, Sy K, Kalloger SE et al., 2014b. ARID1A/BAF250a as a prognostic marker for gastric carcinoma: a study of 2 cohorts. *Human Pathology*. doi: 10.1016/j.humpath.2014.02.006 [Epub ahead of print].

Wilson BG, Wang X, Shen X et al., 2010. Epigenetic antagonism between polycomb and SWI/SNF complexes during oncogenic transformation. *Cancer Cell*, 18(4):316–28.

Wilson BG & Roberts CW, 2011. SWI/SNF nucleosome remodellers and cancer. *Nature Reviews Cancer*, 11(7):481–92.

Wooster R, Neuhausen SL, Mangion J et al., 1994. Localization of a breast cancer susceptibility gene, BRCA2, to chromosome 13q12-13. *Science*, 265(5181):2088–90.

Wu JN & Roberts CW, 2013. ARID1A mutations in cancer: another epigenetic tumor suppressor? *Cancer Discovery*, 3(1):35–43.

Wu R, Hendrix-Lucas N, Kuick R et al., 2007. Mouse model of human ovarian endometrioid adenocarcinoma based on somatic defects in the Wnt/beta-catenin and PI3K/Pten signaling pathways. *Cancer Cell*, 11(4):321–33.

Wu YV, Okada T, DeCarolis P et al., 2012. Restoration of C/EBP α in dedifferentiated liposarcoma induces G2/M cell cycle arrest and apoptosis. *Genes, Chromosomes & Cancer*, 51(4):313–27.

Xiao W, Awadallah A & Xin W, 2012. Loss of ARID1A/BAF250a expression in ovarian endometriosis and clear cell carcinoma. *International Journal of Clinical and Experimental Pathology*, 5(7):642–50.

Xu B, Hamada S, Kusuki I et al., 2011. Possible involvement of loss of heterozygosity in malignant transformation of ovarian endometriosis. *Gynecologic Oncology*, 120(2):239–46.

Xue Y, Canman JC, Lee CS et al., 2000. The human SWI/SNF-B chromatin-remodeling complex is related to yeast rsc and localizes at kinetochores of mitotic chromosomes. *Proceedings of the National Academy of Sciences of the United States of America*, 97(24):13015–20.

Yamada Y, Shigetomi H, Onogi A et al., 2011. Redox-active iron-induced oxidative stress in the pathogenesis of clear cell carcinoma of the ovary. *International Journal of Gynecological Cancer*, 21(7):1200–7.

Yamamoto S, Tsuda H, Aida S et al., 2007. Immunohistochemical detection of hepatocyte nuclear factor 1beta in ovarian and endometrial clear-cell adenocarcinomas and nonneoplastic endometrium. *Human Pathology*, 38(7):1074–80.

Yamamoto S, Tsuda H, Takano M et al., 2011. PIK3CA mutation is an early event in the development of endometriosis-associated ovarian clear cell adenocarcinoma. *The Journal of Pathology*, 225(2):189–94.

Yamamoto S, Tsuda H, Takano M et al., 2012a. Loss of ARID1A protein expression occurs as an early event in ovarian clear-cell carcinoma development and frequently coexists with PIK3CA mutations. *Modern Pathology*, 25(4):615–24.

Yamamoto S, Tsuda H, Takano M et al., 2012b. PIK3CA mutations and loss of ARID1A protein expression are early events in the development of cystic ovarian clear cell adenocarcinoma. *Virchows Archiv*, 460(1):77–87.

Yamamoto S, Tsuda H, Miyai K et al., 2012c. Accumulative copy number increase of MET drives tumor development and histological progression in a subset of ovarian clear-cell adenocarcinomas. *Modern Pathology*, 25(1):122–30.

Yamashita Y, Akatsuka S, Shinjo K et al., 2013. Met is the most frequently amplified gene in endometriosis-associated ovarian clear cell adenocarcinoma and correlates with worsened prognosis. *PloS One*, 8(3):e57724.

Yan HB, Wang XF, Zhang Q et al., 2014. Reduced expression of the chromatin remodelling gene ARID1A enhances gastric cancer cell migration and invasion via downregulation of E-cadherin transcription. *Carcinogenesis*, 35(4):867–76.

Yip KS, Suvorov A, Connerney J et al., 2013. Changes in mouse uterine transcriptome in estrus and proestrus. *Biology of Reproduction*, 89(1):13.

Yotova IY, Quan P, Leditznig N et al., 2011. Abnormal activation of Ras/Raf/MAPK and RhoA/ROCKII signalling pathways in eutopic endometrial stromal cells of patients with endometriosis. *Human Reproduction*, 26(4):885–97.

Zang ZJ, Cutcutache I, Poon SL et al., 2012. Exome sequencing of gastric adenocarcinoma identifies recurrent somatic mutations in cell adhesion and chromatin remodeling genes. *Nature Genetics*, 44(5):570–4.

van der Zee M, Jia Y, Wang Y et al., 2013. Alterations in Wnt- β -catenin and Pten signalling play distinct roles in endometrial cancer initiation and progression. *The Journal of Pathology*, 230(1):48–58.

Zeng Y, Liu Z, Yang J et al., 2013. ARID1A is a tumour suppressor and inhibits glioma cell proliferation via the PI3K pathway. *Head & Neck Oncology*, 5(1):6.

Zhang W, Wei Y, Ignatchenko V et al., 2014. Proteomic profiles of human lung adeno and squamous cell carcinoma using super-SILAC and label-free quantification approaches. *Proteomics*, 14(6):795–803.

Zhang X, Yuan H, Deng L et al., 2008. Evaluation of the efficacy of a danazol-loaded intrauterine contraceptive device on adenomyosis in an ICR mouse model. *Human Reproduction*, 23(9):2024–30.

Zhang X, Zhang Y, Yang Y et al., 2012. Frequent low expression of chromatin remodeling gene ARID1A in breast cancer and its clinical significance. *Cancer Epidemiology*, 36(3):288–93.

Zhang Y, Xu X, Zhang M et al., 2014. ARID1A is downregulated in non-small cell lung cancer and regulates cell proliferation and apoptosis. *Tumour Biology*, doi: 10.1007/s13277-014-1755-x [Epub ahead of print].

Zorn KK, Bonome T, Gangi L et al., 2005. Gene expression profiles of serous, endometrioid, and clear cell subtypes of ovarian and endometrial cancer. *Clinical Cancer Research*, 11(18):6422–30.

Zou KH, Tuncali K & Silverman SG, 2003. Correlation and simple linear regression. *Radiology*, 227(3):617–22.